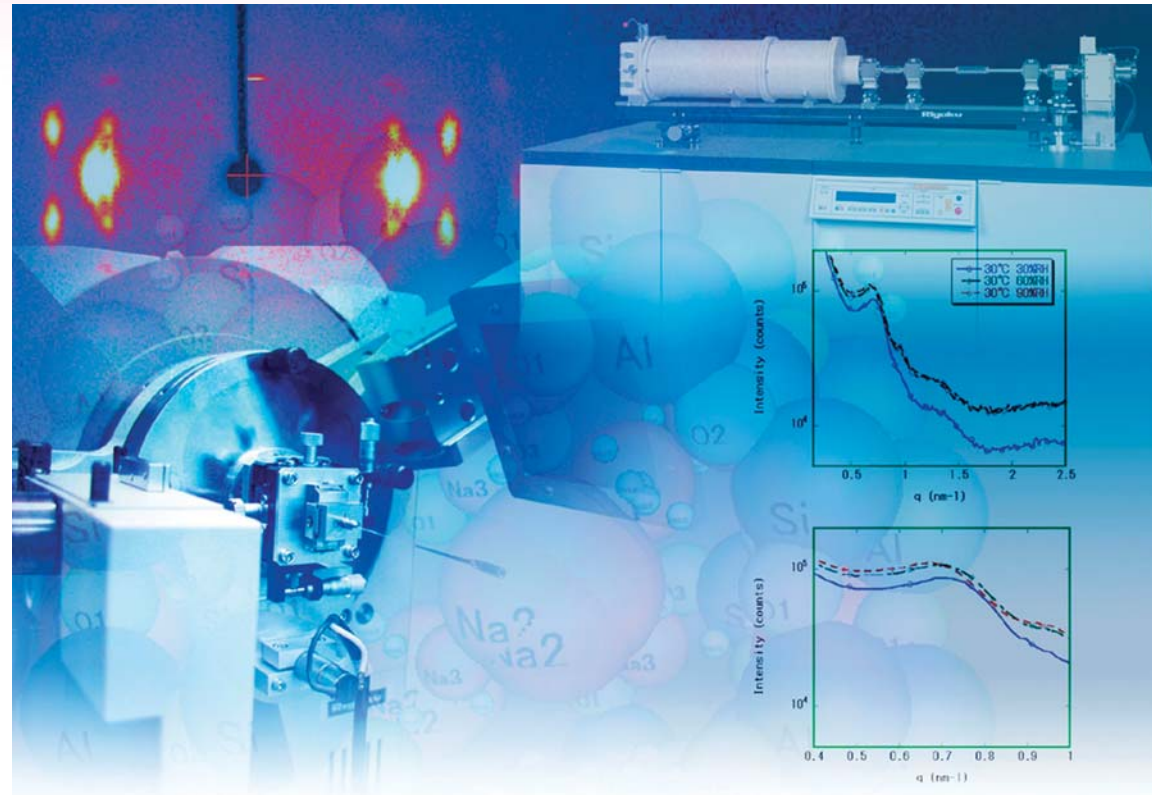


# Bad hair day?

X-ray scattering is the answer!



At Rigaku, we don't just look at the what, we look at the why. Rigaku has multiple systems to meet the dynamic needs of fiber diffraction analysts everywhere.

Rigaku's versatile X-ray scattering systems can be configured with a number of different X-ray sources, from the customizable ultraX rotating anode to the FR-E SuperBright rotating anode or other micro-focus generators. A range of Rigaku detectors can be utilized for wide and small angle scattering, including CCDs, the 300 X 300 mm R-AXIS IV++ imaging plate, and other specialty detectors. For analysts seeking specialized configurations, Rigaku can meet your needs up to 1,000 nm ( $q=0.00034 \text{ \AA}^{-1}$ ).

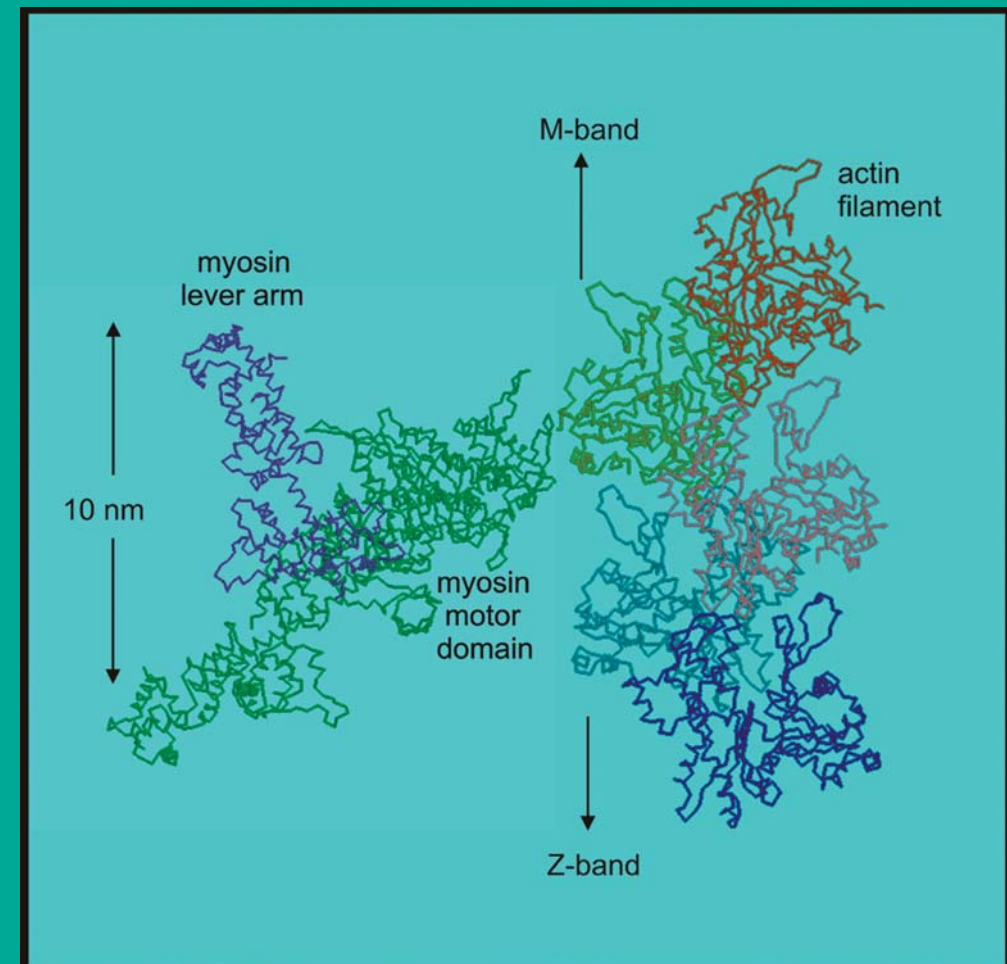
Whether you're looking at hair, Kevlar fibers or anything else that requires X-ray scattering analysis, Rigaku has your system. With over 50 years of XRD expertise, Rigaku is your source for advanced technology and extraordinary results.

Contact Rigaku today for all your fiber diffraction needs

# FIBRE DIFFRACTION REVIEW

*Reports on Progress in Fibre Diffraction  
and Solution Scattering*

*A CCP13 / NCD Publication*



**Molecular Subdomain Configurations Modelled  
from Low-angle X-ray Fibre Diffraction**

Contents, Cover Picture Caption and Production . . . . .	1
The CCP13 Committee Members . . . . .	83
Chairman's Message . . . . .	3
From the Editor . . . . .	84
A North American Fibre Diffraction Network (US-RCN) - Gerald Stubbs . . . . .	5
US-RCN Research Assistant Profile - Wen Bian . . . . .	6

## Meeting Reports

The 2003 CCP13/NCD Workshop in Cambridge, - John Squire . . . . .	7
---	---

## Technical Reports

The non-crystalline diffraction beamline for Diamond – An update, - Nick Terrill . . . . .	9
Facility Report on ISIS, with a brief Introduction to Neutron Scattering, - Steve King . . . . .	15
Report on the Development of ICE: an integrated CCP13 environment for Windows, - Andrew He <i>et al</i> . . . . .	21
Development of CORFUNC, - Matthew Rodman . . . . .	24

## Reviews

Normal-mode-based Refinement of an F-actin Model against Fibre Diffraction Data, - Yinghao Wu & Jianpeng Ma . . . . .	25
The structure of Amyloid, - Sumner Makin and Louise Serpell . . . . .	29

## Original Articles

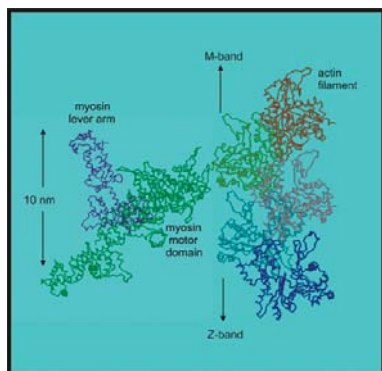
Combined microdrop generation and microdiffraction for biopolymer hydration experiments, - Christian Riek <i>et al</i> . . . . .	36
SANS from Surfactant-Treated Nylon Fibres, - Steve King, D. Bucknall & Richard Heenan . . . . .	41
Modelling Oriented Macromolecular Assemblies from Low-Angle X-ray Fibre Diffraction Data with the Program MOVIE: Insect Flight Muscle as Example, - Hind AL-Khayat <i>et al</i> . . . . .	50

## Expanded Poster-Prize Abstracts

SAXS study of the influence of added clay particles on a block copolymer gel. - Valeria Castelletto & Ian Hamley. . . . .	61
Astringency - A Molecular Model for Polyphenol/Protein Binding - Elisabeth Joebstl <i>et al</i> . . . . .	66
12th Annual Workshop Abstracts . . . . .	70
Summary of Available CCP13/NCD Software . . . . .	81
Instructions to Authors . . . . .	82
14th Annual Workshop - Cardiff University July 2005 . . . . .	inside back cover

## Index of Advertisers

HUBER Diffraktionstechnik . . . . .	2
BrukerAXS . . . . .	4
Spectra Stable Isotope . . . . .	6
Rigaku/MSC . . . . .	back cover



Low-angle X-ray fibre diffraction can be used to determine protein sub-domain positions to very high precision. The approach outlined in AL-Khayat *et al.* (this volume) shows how simulated-annealing parameter searches, using the CCP13 program MOVIE, of myosin cross-bridges in relaxed insect flight muscle against observed X-ray diffraction data have led to the first *in situ* atomic model of the pre-powerstroke conformation for the myosin head. This turned out to be remarkably comparable to a crystallographically-determined structure for a similar head conformation of truncated vertebrate smooth muscle myosin solved using molecular replacement methodology by Dominguez *et al.* (1998: *Cell* 94, 559-571). The transition from the head shape in relaxed insect muscle to the different head shape in rigor may be revealing the working stroke of the myosin head involved in muscle contraction and force generation.

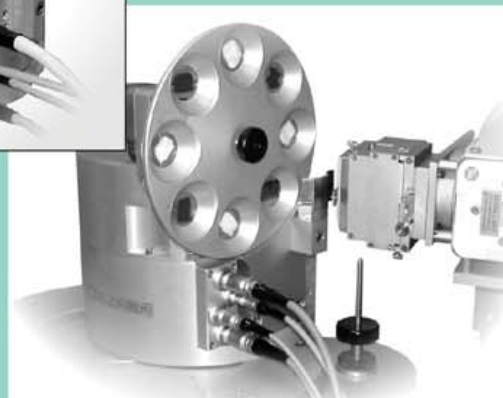
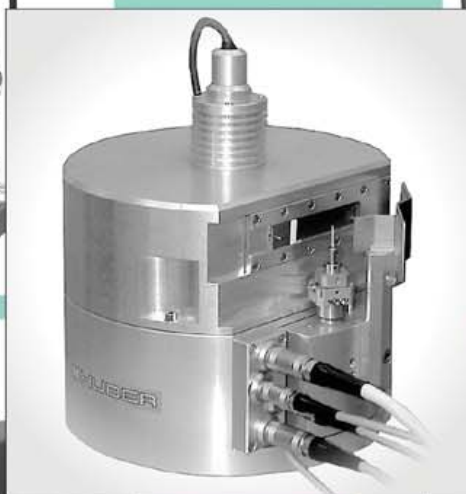
### Fibre Diffraction Review Editorial Office

**Editor:** Prof. John Squire - Biological Structure and Function Section, Biomedical Sciences Division, Imperial College, London SW7 2AZ.

**Production:** Dr Andrew He - Biological Structure and Function Section, Biomedical Sciences Division, Imperial College, London SW7 2AZ.

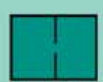
# ***SPEED...***

## **in X-ray Powder Diffractometry**



## **HUBER Imaging Plate Guinier Camera 670**

- ☑ A factor of more than 100 faster compared to conventional step scan
- ☑ X-ray powder diffraction in  $45^\circ$  (asymmetric) transmission,  $0^\circ$  to  $100^\circ$  2-theta
- ☑ Bulk samples in  $17^\circ$  (fixed grazing incidence) reflection,  $50^\circ$  to  $150^\circ$  2-theta
- ☑ Plane foil or capillary samples. 8-fold sample changer for plane foil samples
- ☑ Vertical mount for liquids,  $0^\circ$  to  $20^\circ$  (adjustable grazing incidence) reflection
- ☑ Focussing monochromatic radiation,  $K\alpha_1$ , stripping not required
- ☑ Range of Bragg angles  $100^\circ$  2-theta, 20001 steps @  $0.005^\circ$
- ☑ Laser scans signals @ 16 Bit A/D resolution. Linear dynamic range up to 200,000 counts
- ☑ Creates all common ASCII file types ready for data evaluation like Rietveld-Refinement
- ☑ Low-temperature attachment: Closed cycle He-refrigerator, 10 to 320 K
- ☑ Hi-temperature attachment: Diode laser heater, 300 to 1800 K
- ☑ Hi-pressure attachment: Diamond anvil cell, upto 70 GPa

 **HUBER**

**X-RAY DIFFRACTION EQUIPMENT**

HUBER Diffraktionstechnik GmbH & Co. KG  
Sommerstrasse 4  
D-83253 Rimsting / Chiemsee  
Germany

Tel: +49 (0)8051 68780  
Fax: +49 (0)8051 687810  
info@xhuber.com  
www.xhuber.com

## Chairman's Message - from John Squire

Once again CCP13 activity over the last twelve months has been at a high level and significant new software developments have been made. One of the criticisms of our software in the past has been that, although it is clearly robust and effective, it is sometimes difficult to use especially for newcomers. For this reason tremendous efforts have been made, particularly by Andrew He and Ganeshalingam Rajkumar, to generate updated and more user-friendly versions of such key programs as XCONV, XFIX, FTOREC and LSQINT. These programs have also been implemented in WINDOWS and have been put together into a new integrated package called ICE (the Integrated CCP13 Environment) which also includes a new image handling package called the CCP13 Image Viewer (See He *et al.*, this volume, for a description of ICE). At the moment Image Viewer has a restricted range of image handling routines, but these are gradually being enhanced so that in the end all the early image rotating, centering, scaling, adding or subtracting procedures that are needed, for example, to enhance signal to noise, to subtract camera backgrounds, and to properly orient the recorded diffraction images before further pattern modelling and data reduction actually take place, should be relatively easily achievable. Finally, with regard to data reduction, all of the classic CCP13 packages are gradually being implemented in JAVA so that they become platform-independent.

Data reduction is clearly only part of the CCP13 remit and several new modelling programs have now been included, or are about to be included, in the CCP13 portfolio. Of particular interest here, especially for those either not familiar with the nature or origin of helical diffraction patterns or who are themselves teaching others about helical diffraction, is that there is a new program called HELIX which is a very user-friendly program that simulates helical diffraction patterns. Using HELIX, the effects of adjustments to different helical parameters can be easily and quickly tested. It is hoped that HELIX will be a useful didactic tool for fibre diffraction, but it also has use as a research tool, since simple trial structures can be generated and tested against observed diffraction data from an unknown structure as a preliminary filter prior to going into full modelling. This brings us to the need to have available fully rigorous and well-documented modelling programs. CCP13 has now implemented three such programs. One is the program LALS (Okada, K., *et al.* & Arnott, S. (2003: *Comptl. Biol. & Chem.* 27, 265-285) which can model and refine molecular structures to atomic resolution against high-angle fibre diffraction data. The second is the program MOVIE, which is fully described in the paper by AL-Khayat *et al.* in this Volume. MOVIE can take a known molecular crystal structure, can model it as a collection of spheres or with full atomic coordinates, and, if the structure can be broken down into discrete sub-domains, the full molecular and sub-domain positions can be parameterised and a simulated-annealing approach used to optimise the molecular configuration and shape against observed low-angle fibre diffraction data (see AL-Khayat *et al.*, this volume, where the myosin head in muscle is used as an example). The third package, called CalcTrans, is a simple but versatile program that takes in object positions in cartesian coordinates or cylindrical polar coordinates and computes the cylindrically averaged Fourier transform.

Apart from software development, CCP13 has an important role in helping to form a coherent and active 'non-crystalline diffraction' (NCD) community, both in the UK and abroad, and both our annual Workshops and the production of this Journal help to achieve this. In addition we welcome and very much congratulate our US colleagues who have been successful in setting up the National Science Foundation-funded *FiberNet* organisation (see article by Gerald Stubbs in this Volume). We very much look forward to working with and contributing to *FiberNet* in the next few years. Since its inception, an important activity of CCP13 has been to support solution scattering studies. However, despite the inclusion of several solution scattering papers in *Fibre Diffraction Review* over the years, this approach has probably appeared to have a relatively low profile compared with fibre diffraction itself. The CCP13 Committee are very keen to be able to represent the important solution scattering component of the NCD community and efforts are currently being made to form close links with solution scatterers and their software and to supplement this software where it is needed. We are also interacting fully with such organisations as CanSAS.

The Annual CCP13/NCD Workshop in 2003 was a splendid affair held at Fitzwilliam College in Cambridge and very ably organised by Jane Crawshaw to whom our thanks are due. A brief report on this very successful Workshop is given elsewhere in this Volume of *Fibre Diffraction Review*. The Workshop this year, this time being held in Grenoble, France, the first ever CCP13/NCD Workshop not to be held in the UK, is being organised by Trevor Forsyth with the support of ILL and ESRF. This welcome development illustrates the growing interactions between CCP13 and the European 'central facilities'. For many years we have appreciated the support of the CLRC Daresbury Laboratory which was instrumental in getting both CCP13 and our software development off the ground. Now our central facility links not only continue at Daresbury but are also spreading to the ILL and the ESRF in France, and to ISIS at the Rutherford Laboratory along with the newly emerging DIAMOND synchrotron at the same site. There is enormous synergy between the aims of the NCD activities at these facility sites and the activities of CCP13 and in the future it is hoped that we can be more involved with the whole data analysis procedure so that good software is available at each beamline for immediate data reduction and on-line evaluation of new data as it is being recorded. As an indicator of this need, a new grant application to our sponsors BBSRC and EPSRC has just been submitted for renewal of our support from October 2004. As an important part of the package presented in the new grant application, all of the central facilities mentioned above have made financial commitments to CCP13 staff support in the next grant period, as has the University of Cardiff which will host the CCP13 Workshop in 2005.

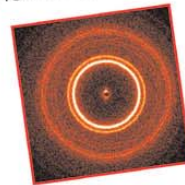
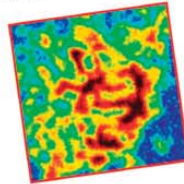
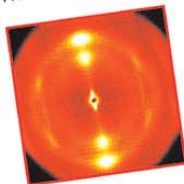
I look forward to seeing you all at the Grenoble Workshop in June, where, as well as excellent talks and posters, there will also be hands-on demonstrations of the CCP13 software together with an opportunity to visit the ILL and ESRF facilities. Why not bring your poster along to this meeting and try to win one of the prestigious cash Poster Prizes that are awarded each year.



## NANOSTAR – ENTER THE UNIVERSE OF NANOSTRUCTURE ANALYSIS

The NanoSTAR is the most versatile experimental platform for nanostructure analysis.

- Offers a wide field of applications for polymers, biological materials, fibres, metals, nanopowders and complex fluids, etc.
- Provides analysis of sizes, size distributions, shapes and orientation distributions in liquids, powders or bulk samples
- The efficient solution for scientists as well as researchers requiring fully automated measurements
- All-in-one instrument:
  - nanostructure analysis by means of Small Angle X-ray Scattering (SAXS)
  - nanostructure mapping by means of X-ray Nanography
  - molecular structure determination by Wide Angle X-ray Scattering (WAXS)



BRUKER ADVANCED X-RAY SOLUTIONS



Bruker AXS Ltd.: Tel. (+44) (0)1260 296-900 • Fax (+44) (0)1260 296-909 • E-Mail: [info@bruker-axs.de](mailto:info@bruker-axs.de) • [www.bruker-axs.de](http://www.bruker-axs.de)  
 Bruker AXS GmbH: Tel. (+49) (0)721 595-2888 • Fax (+49) (0)721 595-4587 • E-Mail: [info@bruker-axs.de](mailto:info@bruker-axs.de) • [www.bruker-axs.de](http://www.bruker-axs.de)  
 Bruker AXS, Inc.: Tel. (+1) 608 276-3000 • Fax (+1) 608 276-3006 • E-Mail: [info@bruker-axs.com](mailto:info@bruker-axs.com) • [www.bruker-axs.com](http://www.bruker-axs.com)

## A North American Fibre Diffraction Network

A number of fibre diffraction laboratories in the USA have joined together to form an American network that will be similar to CCP13 in many of its goals and activities, and will work closely with CCP13 for the development of fibre diffraction on both sides of the Atlantic. The network, formally known as Research Coordination Network: Fiber Diffraction from Biological Polymers and Assemblies, and informally as *FiberNet*, is supported by the US National Science Foundation.

The goal of the network is to develop biological fibre diffraction methods, particularly computational methods. This will be done through a program of software development, and through a series of retreats and workshops. The network software will be complementary to CCP13 software; together, they will eventually cover all aspects of fibre diffraction. The network emphasis on biological fibre diffraction comes from the fact that *FiberNet* is supported by the NSF Division of Molecular and Cellular Bioscience. However, fibre diffraction methods in general are usually common to biological and materials science applications, and the needs of materials scientists and others will be kept in mind, especially in software development. Of course, the network welcomes participation by all fibre diffractionists, and in the future plans to seek funding from both biologically and non-biologically oriented sources.

The experimental focus for the network will be the BioCAT X-ray beamline facility at the Advanced Photon Source synchrotron, Argonne National Laboratory. BioCAT (Biophysics Collaborative Access Team) is a national and international research resource for diffraction studies of partially ordered biological molecules, complexes of biomolecules, and cellular structures under conditions similar to those present in living cells. Many CCP13 members have collected data at the BioCAT facility. The beamline supports fibre diffraction, solution scattering, and X-ray absorption scattering, and although *FiberNet* is primarily concerned with fibre diffraction, it shares many interests with other scattering communities, and especially with small angle solution scattering. The BioCAT facilities provide a resource unique on the North American continent - worldwide, only SPring8 and ESRF operate similar facilities.

A major emphasis of the network will be cooperation between fibre diffractionists in the USA and others, particularly those in Britain. CCP13, although it is larger than *FiberNet* and more comprehensive in its scientific interests, has to some extent been a model for *FiberNet*. The director of *FiberNet* and the director of BioCAT are both co-opted members of the CCP13 Steering Committee; reciprocally (and what would a diffraction committee be without reciprocity?) the Chairman of the CCP13 Steering Committee will always be a member of the *FiberNet* Steering Committee.

The network will also be affiliated closely with the American Crystallographic Association's Fiber Diffraction Special Interest Group. The SIG is a much more loosely-organized group than CCP13, and its only activity is to organize sessions at the

Annual Meeting of the ACA. These sessions have, however, been of great value in the exchange of information among biological and synthetic fibre diffractionists in the USA. One obvious reason that the SIG has not taken more of a leading role in the co-ordination of fibre diffraction in the USA is that it has no funds of its own apart from occasional donations from industry sponsoring particular sessions; to some extent, the establishment of *FiberNet* will fill this gap. Over the years, several members of the *FiberNet* Steering Committee have served as chairs of the SIG, and like the CCP13 chairman, the SIG chair will always be a member of the *FiberNet* Steering Committee.

Like CCP13, *FiberNet* will hold annual meetings. These will be of three types, roughly rotating from year to year.

In years when the ACA SIG holds a session on biological fibre diffraction at the ACA Annual Meeting, the network will support speakers and student attendees at the session; it is hoped that this support will add new vigor to the SIG meetings.

The second type of meeting will be reminiscent of the old informal State Park meetings. Many CCP13 members will remember these meetings - the first of them, featuring Struther Arnott and Ken Holmes as keynote speakers, was held at Fall Creek Falls State Park in Tennessee in 1989, and organized by Gerald Stubbs. The second was at McCormick's Creek State Park in Indiana in 1993, organized by Rick Millane. The third, organized by Rick and Gerald, was at Jennie Wiley State Park in Kentucky (which, for those whose American geography is a bit rusty, is between Tennessee and Indiana) in 1997. These workshops were attended by about 20 to 40 participants, including speakers from the UK and Europe each time. In fact, the program for the third meeting included seven speakers from the UK and one from Italy. Some people's most vivid memory of these meetings may be Richard Denny's near-sinking of a pontoon boat at Jennie Wiley when a trailing rope caught on the bottom of the lake, but most of us also remember remarkable opportunities to exchange ideas in a relaxed atmosphere, and we are looking forward to renewing the series.

State parks are good places to exchange ideas, and with smaller and faster computers, they can even be good places to discuss and develop software. But they tend to be a bit weak in facilities for X-ray diffraction, so in some years, the meeting will be held at BioCAT. These meetings will be network retreats, like the State Park meetings, but they will feature the data collection capacity of BioCAT, and will include a strong element of experimental training. State Park and BioCAT workshops will emphasize methods rather than results; most fibre diffractionists attend other types of meeting where results dominate the presentations, but there are very few opportunities for fibre diffractionists to discuss methods. The ACA-SIG workshops may be on methods or results, depending on other themes at any given meeting.

*FiberNet* is administered by a Steering Committee, very similar in function to the CCP13 Steering Committee. At present, the members of the committee are Gerald Stubbs (Vanderbilt University, Nashville, TN, chairman), Rengaswami Chandrasekaran (Purdue University, West Lafayette, IN), Tom Irving (Illinois Institute of Technology, Chicago, IL), Dan Kirschner (Boston College, Chestnut Hill, MA), Jianpeng Ma (Baylor College of Medicine and Rice University, Houston, TX), Joseph Orgel (The Rosalind Franklin University of Medicine and Science, North Chicago, IL), and from CCP13, Trevor Forsyth (Keele and ILL), and John Squire (Imperial College London). The network has recently hired Wen Bian to develop software. Wen will be based at Vanderbilt, and will

coordinate his work with the CCP13 staff members. Wen is experienced in both software development and fibre diffraction, having worked with Chandrasekaran and Struther Arnott at Purdue University.

We are looking forward to a long and productive association between *FiberNet* and CCP13!

Gerald Stubbs - Vanderbilt University - January 2004

## US-RCN Research Assistant Profile - Wen Bian

### Dr Wen Bian

Wen Bian received his B.E. and M.A. degrees from Ocean University of China in 1994 and 1997, and his Ph.D. from Purdue University in 2001. At Purdue, he worked on the structures of industrially important polysaccharides and the relationship between structure and function in polysaccharides, using X-ray fibre diffraction analysis and computer modeling. His work at Purdue was primarily with Rengaswami Chandrasekaran, and also with Struther Arnott. While at Purdue, he developed a great interest in programming, so upon completion of his doctoral studies, he went on to complete an M.S. degree in computer science at Purdue.

Wen's software-related experience includes maintenance of in-house molecular modelling programs, development of various distributed applications, and data processing and visualization programs on Windows and UNIX platforms. He joined Gerald Stubbs's group at Vanderbilt University in January, 2004, where he will be the principal software developer for *FiberNet*, collaborating with the software developers for CCP13.



## Meeting Reports

### The 2003 CCP13/NCD Workshop in Cambridge

Fitzwilliam College provided an excellent and compact setting for the 2003 CCP13/NCD Annual Workshop, which, like its predecessors, proved to be a very enjoyable meeting. The College also hosted us very helpfully and well. All the local arrangements for the Workshop, which ran from July 2-4, had been sorted out by Jane Crawshaw who had forgotten nothing. Supported by the willing and expert help of the stalwarts of these Workshops on the registration desk, Alison Mutch and Sue Waller, and the expert photography and technical help of Stuart Eyres (see next page), everything ran smoothly and without hassle, and I for one am very indebted to them all.

The Workshop included the usual mix of presentations on synthetic polymers, biological fibres, solution scattering, liquid-crystalline structures and structural modelling, along with poster presentations and hands-on tutorials on existing and new software packages. Because this year was the 50th anniversary of the discovery of the structure of DNA by Watson and Crick using fibre diffraction data obtained by Rosalind Franklin in the laboratory of Maurice Wilkins, it seemed entirely appropriate to include in the Workshop a presentation on the early history of DNA fibre diffraction analysis. This talk was to have been given by Professor Struther Arnott FRS, who was part of the Wilkins team that actually confirmed the true DNA structure about 10 years after the initial discovery; a structure that was, in fact, significantly different in detail from the original Watson & Crick version. Unfortunately, in the end, Struther was unable to come, but we were delighted to be able to ask another pioneer in the Wilkins team, Dr. Don Marvin, to present his personal view of the early DNA story at King's College London - and fascinating it was too. I am very grateful to Don for stepping in at such short notice and for giving such an interesting presentation.

A major talk on the last day of the meeting was given by one of our leading fibre diffractionists, Professor Alan Windle FRS.

Along with Jane Crawshaw, Alan was also our 'host' in Cambridge. His talk opened up a new area for possible fibre diffraction studies, namely the analysis of carbon nanotubes. This also raised the interesting possibility of extending our range of useful radiations beyond X-rays and Neutrons to Electrons, since many carbon nanotube structures, and indeed other nano-structures, lend themselves to analysis by electron diffraction methods. Professor Don Caspar and his team had already raised this possibility in his presentation on amyloid structure at the 2002 Workshop at Keele University together with their subsequent publication in *Fibre Diffraction Review* (Diaz-Avalos *et al.*, FDR 2003, **11**, 79-86). Since the 'nano' area is one of such growing importance, both in the materials science and biological arenas, the presentation at the Cambridge Workshop by Alan Windle was a timely sampler of what might be done not just with carbon nanotubes but also with protein (or DNA) nanostructures.

As usual we had an excellent conference dinner on the second day of the Workshop and as usual it was my pleasure on this occasion to be able to award two significant cash prizes to those chosen by our independent judges to be the best two posters at the Workshop. This time the winners were Elisabeth Joebstl and Valeria Castelletto, whose extended 'prize-winning' abstracts appear elsewhere in this Volume of *Fibre Diffraction Review*. Since the standard of the science and the quality of presentation of posters is at such a high level these days, to be awarded a best poster prize is a significant achievement - and the cash prizes are well worth having! Our congratulations go to Elisabeth and to Valeria on their excellent achievements.

John Squire - Imperial College London - April 2004

**Don't forget the next CCP13/NCD workshop  
at Cardiff University  
in July 2005!**



Scenes from the 2003 Cambridge Workshop

## The non-crystalline Diffraction beamline for Diamond – An Update

N.J. Terrill<sup>1</sup>, A.F. Grant<sup>2</sup>, A.R. Marshall<sup>1</sup>, A.D. Smith<sup>2</sup>, K.J. Sawhney<sup>1</sup>,

[1] Diamond Light Source, Rutherford Appleton Laboratory, Chilton, Didcot, Oxfordshire, OX11 0QX

[2] CCLRC Daresbury Laboratory, Daresbury, Warrington, Cheshire, WA4 4AD, UK

Received and accepted 5th January 2004

### ABSTRACT

*Non-Crystalline Diffraction is an important method for studying the structural properties of non- or semi-crystalline states of matter. These include biological macro-molecules e.g. fibres or proteins and their complexes in solution, synthetic polymers, gels, liquid crystals, oils, paints, ceramics and environmental aggregates. The technique yields information on the shape and size of these molecular assemblies and is particularly sensitive to phase changes or conformational rearrangements on a length scale ranging from 10 to 10000 Å. Diamond is the new third generation synchrotron source that is currently being designed and constructed for the UK Science community. The 3GeV machine will begin operations in 2006 with commissioning of the first seven beamlines to follow. I22 is now in the detailed design phase after successfully passing through its concept design review. The science case has specified the beamline to operate at energies between 4-20keV utilising the low divergence beams from an undulator. The beamline is to include features for standard Small Angle Scattering and Fibre Diffraction together with a combined SAXS/WAXS capability. A modular Microfocus facility will also be incorporated.*

Diamond is the largest scientific facility to be built in the UK for nearly thirty years. The facility when operational in 2007 will produce highly focused high brightness beams that will enable scientists and engineers to probe deep into the basic structure of matter and materials, answering fundamental questions about everything from the most sophisticated structures in a cell to the origins of our planet. State-of-the-art beamlines will maximise the effectiveness of the source, ensuring that researchers from the UK and abroad have access to cutting-edge analytical techniques and services for the next twenty years or more. Such fundamental research is at the heart of the competitiveness of the UK economy.

There has been strong pressure to provide the non-crystalline Diffraction community with a world class facility at the earliest possible point in the project. I22, the identifier for the non-crystalline Diffraction beamline, is being designed to meet those broad ranging needs.

The UK has an active community that has been at the forefront of developments in this field for many years. Community interests, as identified in the responses to the announcement for this beamline and in earlier consultations, encompass the fields of medicine, biology and materials processing. Interests include; studies of supramolecular organisation in biological systems, the structure and function of muscle filaments, elastic proteins, bone nanostructures, corneal transparency, biological membranes, polymer processing, self-assembly of mesoscopic metal particles, colloids, ceramics, environmental nanoparticles, barrier materials, mineral colloids, liquid crystals and nanoscale devices. The work is supported by the BBSRC, EPSRC, MRC, NATO, NERC and the Wellcome trust. Non-Crystalline Diffraction is one of the truly synergistic interdisciplinary sectors within UK science and the wider international arena.

At present, the programme is supported by three beamlines at the SRS, as well as others at the ESRF including ID02, ID13 and DUBBLE. The ESRF does not have the capacity to take up the expected demand after the closure of the SRS or to provide the variety of environments that will be needed to advance our

knowledge of behaviour of the wide range of biological and materials systems that will be studied.

The non-crystalline Diffraction beamline will bridge the gap between optical and more conventional X-ray measurements. It will play an important role in developing our knowledge of macromolecular structure into function and into advancing the industrial development of biomaterials, biosensors, and lead to the manufacture of better designed polymers and a more efficient production technology. The beamline will represent a facility at the cutting edge of synchrotron technology that will provide a robust SAXS service for an international community. The design of the beamline also looks to the future challenges of SAXS where the objectives will be characterisation of larger and more transient structures.

**Insertion Device** - A consultation with the user community to gauge expected energy requirements is reproduced in Figure 1. The consultation clearly indicated that while there was excellent science to be performed at the extremes of the beamlines range, including Calcium edge, biomineralisation, bioceramics and food science at 4keV and high pressure studies above 16keV, the main focus of the work to be carried out on the non-crystalline Diffraction beamline will be between 10-12keV. This is also the experience of Beamline Principals at other third generation sources, including those from ID02 and DUBBLE at the ESRF and BIO-CAT on the APS.

A request was therefore made to ASTEC to design an insertion device with low divergence and high flux which delivered photons continuously over the energy range 4-20keV and gave good performance between 10-12keV. The requirements resulted in ASTEC supplying three options to consider (Figure 2).

Further analysis of the undulator performance suggests that a U25 in vacuum device gives the best overall performance. The 7<sup>th</sup> harmonic of the U25 device covers the primary range requested whereas to cover the same range with an ex-vacuum

# The non-crystalline Diffraction beamline for Diamond – An Update

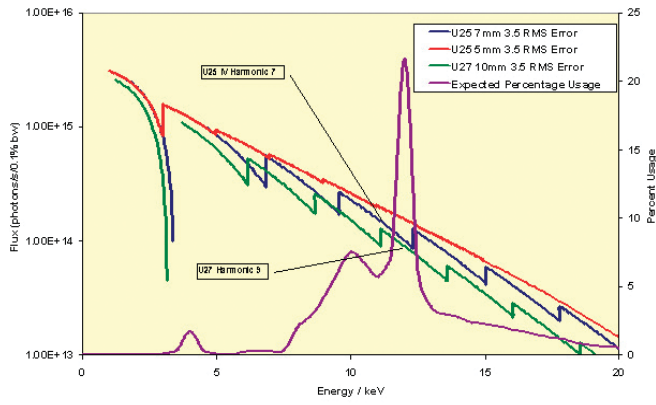


Figure 1. Undulator Options against Expected Energy Demand for I22

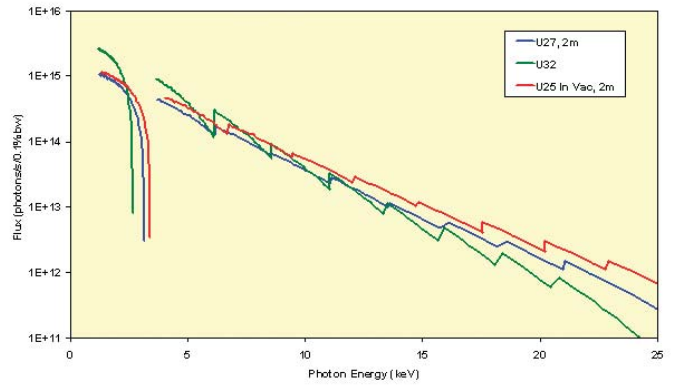


Figure 2. Undulator Options for I22

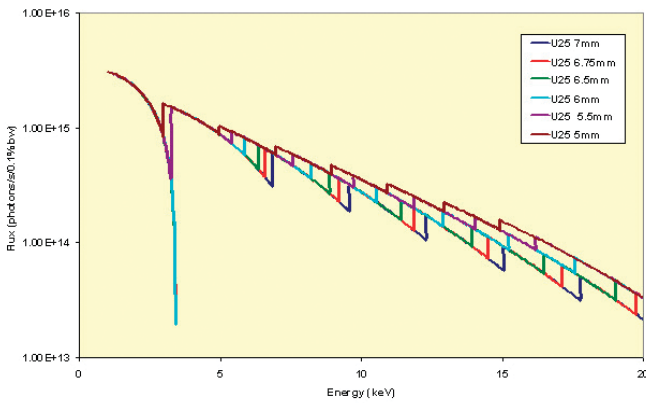


Figure 3. Effect of gap reduction on U25 IV Undulator.

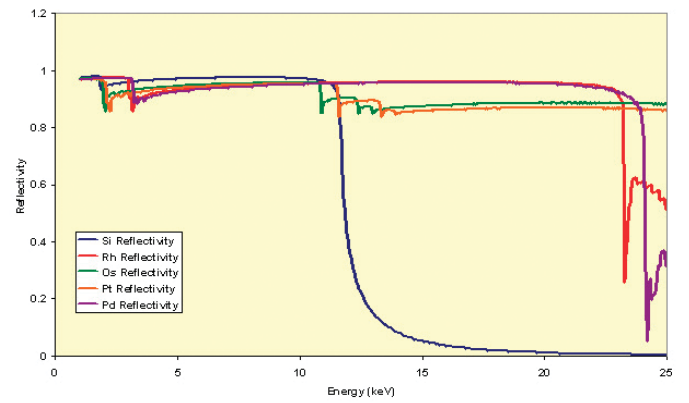


Figure 4. Reflectivity of different mirror coatings for a mirror inclined at 2.6mrad

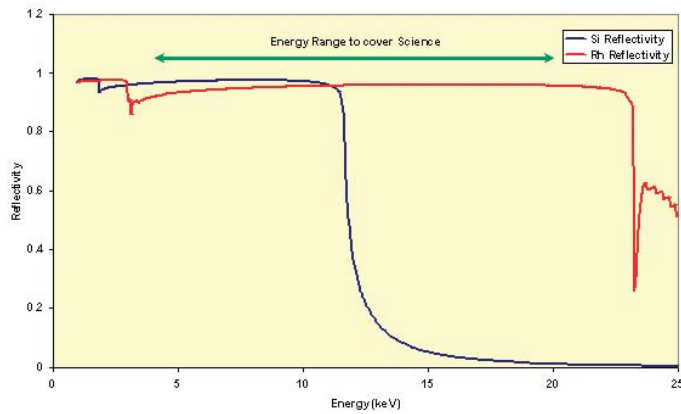


Figure 5. Reflectivity for a bare and Rh coated mirror (Rh layer 30nm thick) at grazing incidence angle 2.6mrad.

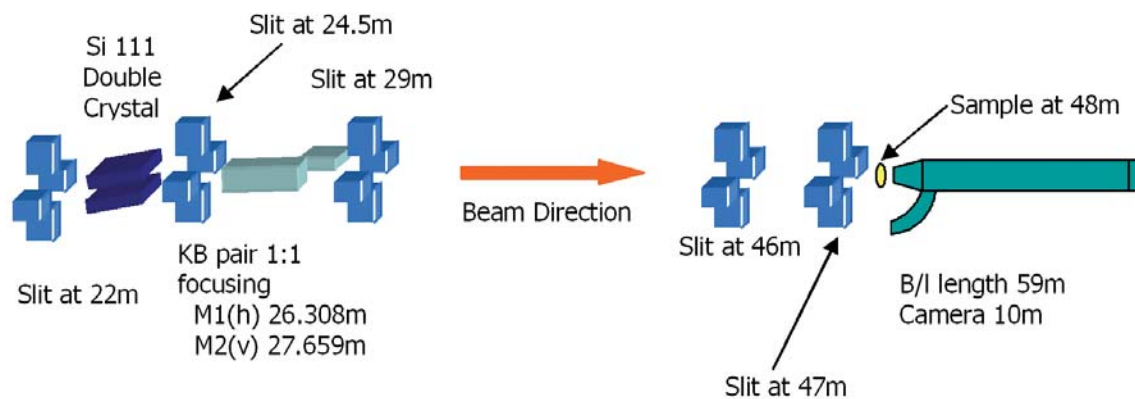


Figure 6. Outline layout of I22

U27 device use of the 9<sup>th</sup> harmonic is required. Real undulators have magnet phase errors associated with them (Figure 2). These degrade the performance output of the undulator and affect the higher harmonics more than the lower ones therefore working with lower harmonics is always preferable.

As the ring vacuum conditions it should be possible to reduce the gap of an in-vacuum device further, from 7mm to 5mm and possibly even narrower, thus giving additional performance gains (Figure 3).

**Outline Optics Scheme** - Flexibility is the key to the design of the optics as this beamline has to cater for a wide range of scientific challenges. For this reason interchangeable and adaptable components will be necessary.

**Monochromators** - The scientific case has identified anomalous small angle X-ray scattering (ASAXS) to be an important option. Such measurements call for good energy resolution, therefore a double crystal Si(111) monochromator (DCM) ( $\Delta E/E \approx 2 \times 10^{-4}$ ) will be included in the beamline design. There are other parts of the programme that call for less energy resolution but do call for a high flux on the sample. Macromolecular solution scattering measurements and many parts of the polymer case fall into this category. The science therefore calls for a multilayer-based monochromator to be considered where the bandpass is 1-2 orders of magnitude higher than a Si monochromator.

The monochromator will be the first optical element in the beamline located at approximately 23.5m. Having the DCM as the first optical element will allow simplification in design of all downstream elements. Mirrors and any microfocusing elements will not require cooling as most of the power will be removed from the beam by the 1<sup>st</sup> crystal of the monochromator. It is planned that the monochromator will be of a fixed exit design. This is to ensure that minimal movements of the beam occur at the sample when the wavelength is changed for anomalous (high angle non-crystalline /fibre) and microfocus work.

**Mirrors** - Primary focusing will be achieved with a Kirkpatrick-Baez (K-B) mirror pair; these are grazing incidence elliptical reflecting mirror pairs that have extreme surface precision. This combination has been chosen for two reasons; 1) the choice allows flexibility in the location of focus anywhere along the 10m SAXS camera and possibly in a pre-hutch for microfocus work, and 2) it allows decoupling of the horizontal and vertical focusing. This will enable experimentalists, if necessary, to split the focus between the sample (maximum photons on sample e.g. horizontally) and the detector (maximum resolution e.g. vertically).

The K-B mirror pair, located at approximately 26.3m (h) and 27.7m (v) will provide approximately 1:1 focusing into the experimental hutch at 54m. However, these positions will need validating in the detailed design in light of any further design work that may be required for a technical design review that is to take place in May 2004.

At these distances mirrors of length 1.2m (h) and 0.4m (v) respectively would comfortably collect the entire beam profile. Both mirrors will be set at 2.6mrad. The selection of coating is

between palladium (Pd) and rhodium (Rh) which could both be utilised over the whole energy range of the beamline. Other common coatings have edges in the range so can be discarded (Figure 4).

The mirrors could have one coating. If, however, the mirrors are striped, i.e. only part of their surface is coated longitudinally with, for example Rh, the variation in cut-off energy between the different mirror coatings could be used to prevent contamination of the beam from energy harmonics transmitted by the monochromator. For example, with a Si(111) monochromator, if a beam of 6keV is used, then there is likely to be contamination from the Si 333 reflection coming in at (6x3) keV i.e. 18keV. However if the bare Si was used in this situation then there would be no contamination from the harmonic as Si does not reflect at 2.6mrad above ~12keV. So for routine operation between 10-20keV one could use a rhodium coated Si mirror, but for operation below 10keV one could use an uncoated Si mirror (Figure 5).

The decision on which stripe to choose in addition to the uncoated stripe will be made after discussions with manufacturers - it may be that one material is easier to handle than the other (rhodium doesn't require a binding layer of chromium) or the use of one would result in a significant cost saving (palladium is expensive).

This information leads to the following outline layout for I22 (Figure 6).

Preliminary ray tracing with 1:1 focusing at 54m, halfway along the maximum SAXS camera length, shows that a beam approximately 310 x 75mm can be expected (Figure 7). An estimate of the effect of slope errors using a simple wave oscillation has been included in the calculation of the focus spot. A more realistic model would include a randomisation effect and not produce the "dumbbell" shape illustrated below but a smoother beam profile.

**Microfocusing Options** - X-ray microfocus is the provision of small intense X-ray beams, using a variety of optical elements that focus rather than merely collimate the beam. The main advantages are two-fold; firstly the technique can be used to illuminate very small samples whilst minimising the scattering from the surrounding substratum. Secondly, X-ray microfocus can allow textures to be distinguished within a material on the micron and sub micron length scale. There are a number of materials science and biological investigations where the use of microfocus technology is becoming crucial for maximising the information that can be obtained on the structure and behaviour of materials. For example examining the microtextural variation of bone nanocrystallites is important in understanding bone-ligament and bone cartilage interfaces. The textural variation measured in skin-core experiments imparts information about polymer alignment and crystallinity within a single fibre.

Two options for the microfocusing capability of this beamline are currently being pursued.

**Small K-B pair** - This is the option chosen by the microfocus XAFS beamline on Diamond and is one of the more widespread

# The non-crystalline Diffraction beamline for Diamond – An Update

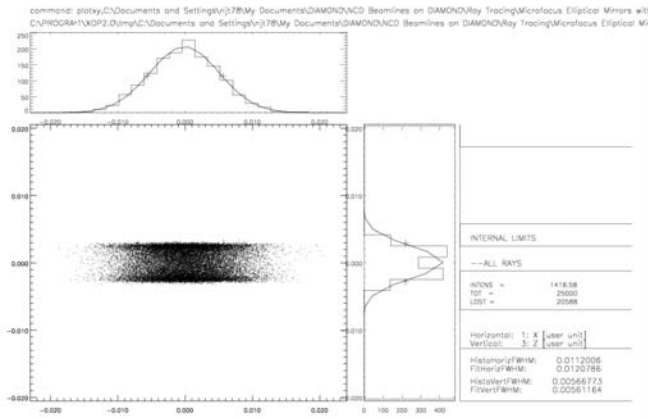


Figure 7. Shadow Output for Outline layout of I22

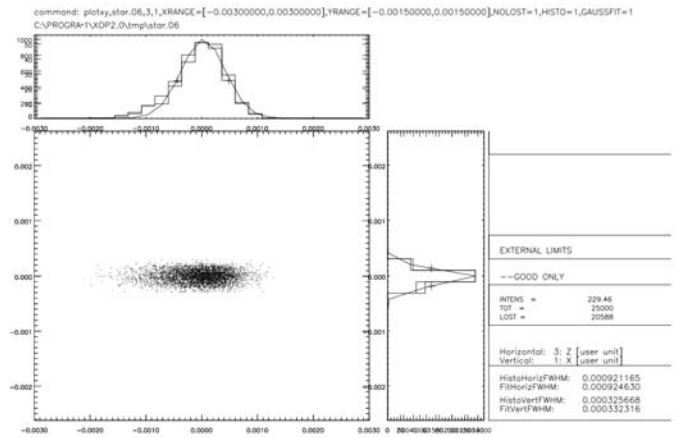


Figure 9. Shadow Output for microfocusing K-B pair for I22

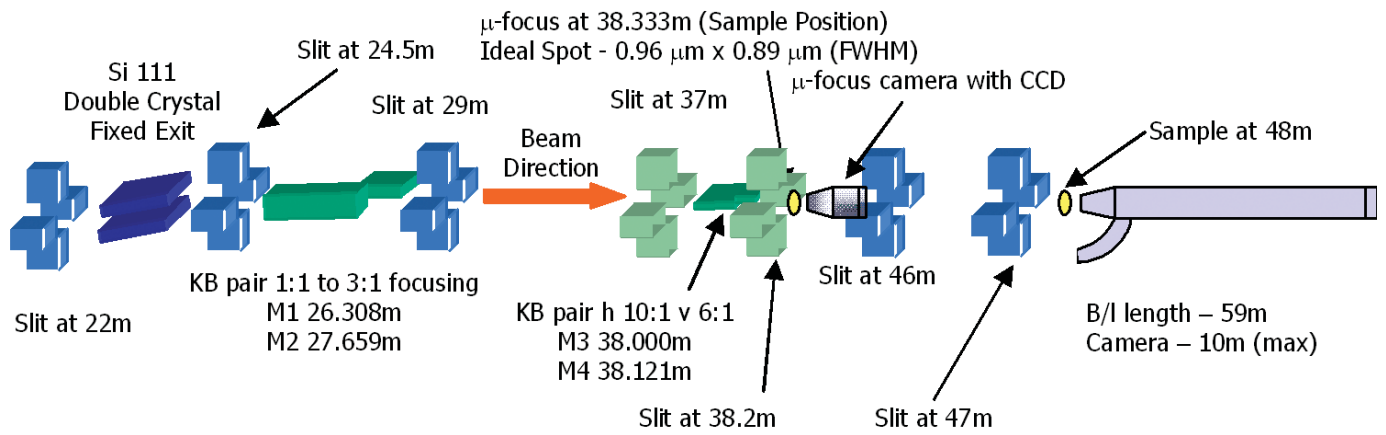


Figure 8. Outline layout for microfocusing K-B pair for I22

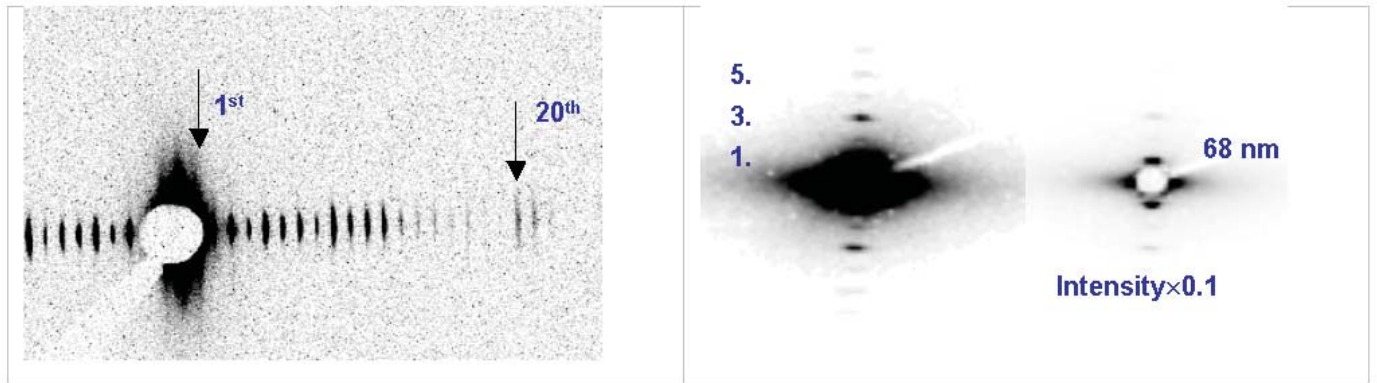


Figure 10. CRL output for collagen on ID18

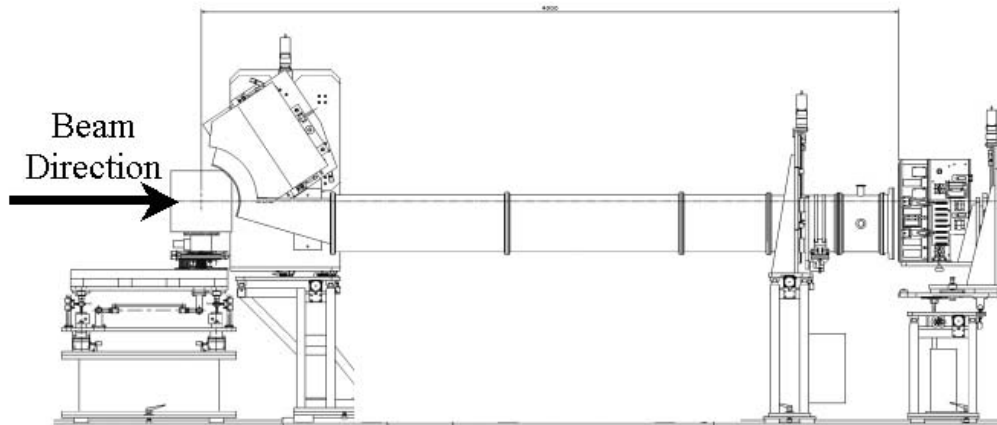


Figure 11. Possible End station layout for I22

choices now available. A number of the beamlines on the ESRF are adding this capability through their own design of small K-B mirror pair.

This option will require either a pre hutch or an extension upstream of the main experimental hutch. An outline of a possible configuration is given in Figure 8.

A preliminary ray tracing study (Figure 9) of this arrangement has been carried out using similar slope errors to those for the large K-B pair. This should give a worst case scenario for the focus. The spot size deliverable from this arrangement is of order  $9 \times 3 \mu\text{m}$ . Additional collimation would be required to deliver sub-micron beam sizes.

Further design work is ongoing to define the best arrangement for this optical option.

**Compound Refractive Lenses** - These are an attractive option if microfocusing is to be a complementary technique to the main function of the beamline. They are small, easy to align and relatively simple to maintain. There are encouraging results from the ESRF with a set of Aluminium lenses for SAXS experiments. The scattering patterns in Figure 10 show data obtained on ID18 for Collagen<sup>1</sup>, a common SAXS standard. They clearly show the first order axial peak at 68nm.

This option would require a platform to be built to accommodate lenses, sample stage and detector. For a set-up similar to ID18 this experimental table would be located at approximately 56-58m from the source at the end of the experimental hutch.

**End Station** - A modular design that closely resembles MPW 6.2 at the SRS and DUBBLE at the ESRF will be considered for the end station. These are both productive stations which cater for the wide range of SAXS disciplines. The outline drawing below is taken from MPW 6.2 (Figure 11). Although not identical, I22 will share a number of features:

- All sections to be mounted from alignment rail in floor of experimental hutch.
- SAXS camera made up from 0.25, 0.5 and 1m sections to accommodate multiple camera lengths from 1-10m. This type of SAXS camera is chosen in preference to the large evacuated vessel found on ID02 at the ESRF as it enables the use of RAPID without major modification, an essential component of the detector portfolio.
- SAXS camera to be evacuated to roughing vacuum and to utilise interchangeable window materials for the variety of experiments and energies contemplated.
- Independent Y, Z mounting for front and back of SAXS camera.
- Separate mount for SAXS detector including Y, Z, pitch, yaw and roll motions.
- WAXS detector to be mounted directly to the nose cone section of the SAXS camera and given some  $2\theta$  movement.
- Nose cone to pivot about notional sample position.
- Flexible Sample platform to accommodate Y, Z, limited pitch and roll, and a rotary table mounted about the Z axis. Demountable precision X, Y, Z platform to be included for small sample environments.

**Detector Options** - The scientific case calls for both 1-d and 2-d capability from the detection systems on I22. Although the options will be evaluated in detail later an indication of the requirements is given below.

**RAPID (for fast time resolved 2-d work)** - This detector has been highlighted as the primary option for fast time resolved 2-d SAXS studies. RAPID has been tested at the ESRF on the high brilliance beamline ID02 with positive feedback from the user community. As an example of the sort of experiments which this detector is capable, included below is a muscle stretching experiment carried out over 40ms (Figure 12)<sup>ii</sup>. Time courses of temperature, force and intensities of M3 and A1 reflections are displayed opposite. M3 and A1 are the results of 162 T-jumps. Force and temperature are representative traces. All traces were normalised to facilitate superposition.

It must be noted that RAPID is the only detector technology currently available to this community which allows on-line data collection with sub-millisecond time resolution.

**CCD (for Microfocus and Fibre Diffraction)** - The science case calls for the beamline to perform fibre diffraction experiments. These experiments are not possible with the detector outlined for the fast dynamic experiments as RAPID does not have the spatial resolution capabilities for high angle diffraction. The Microfocus function of the beamline will also require a high spatial resolution detector. Here the obvious choice is a CCD where the majority of the work will be concerned with mapping samples rather than in dynamics. If fast dynamics are required then, due to the modular design of the end station and the data acquisition electronics the beamline's RAPID system could be utilised with the accepted loss in spatial resolution.

**HOTSAXS/WAXS (for fast time resolved 1-d work)** - To perform fast, combined, 1-D SAXS/WAXS well requires an excellently matched set of detectors. Until recently no such options were available. Now both wire and glass microstrip heads are feasible and offer high count rate capabilities  $>5\text{MHz}$  global, excellent dynamic range (107 - 108) and very fast time framing  $<10\mu\text{s}$ . This is again far in excess of anything possible with the latest CCD technology. It is also possible with the photon counting option to utilise the same backup electronics as will service the RAPID 2-D system thus saving on hardware costs.

The HOTWAXS detector is the subject of an ongoing project within CCLRC, the prototyping having been very successful on beamline 8.2 on the SRS and a build to cost option should be available for I22. HOTSAXS is the subject of a development project sponsored by Diamond and the Non-Crystalline Diffraction beamline. Early indications are very promising that the station can be supplied with a world leading fast 1-d detector pair.

**Beamline layout** - Reproduced in Figure 13 is a layout option for the Non-Crystalline Diffraction beamline. It includes provision for a microfocus hutch before the primary experimental hutch. This option is dependent on choosing a K-B pair for microfocusing. The decision will be the subject of a detailed study prior to the Technical Design Review for the beamline in May 2004.

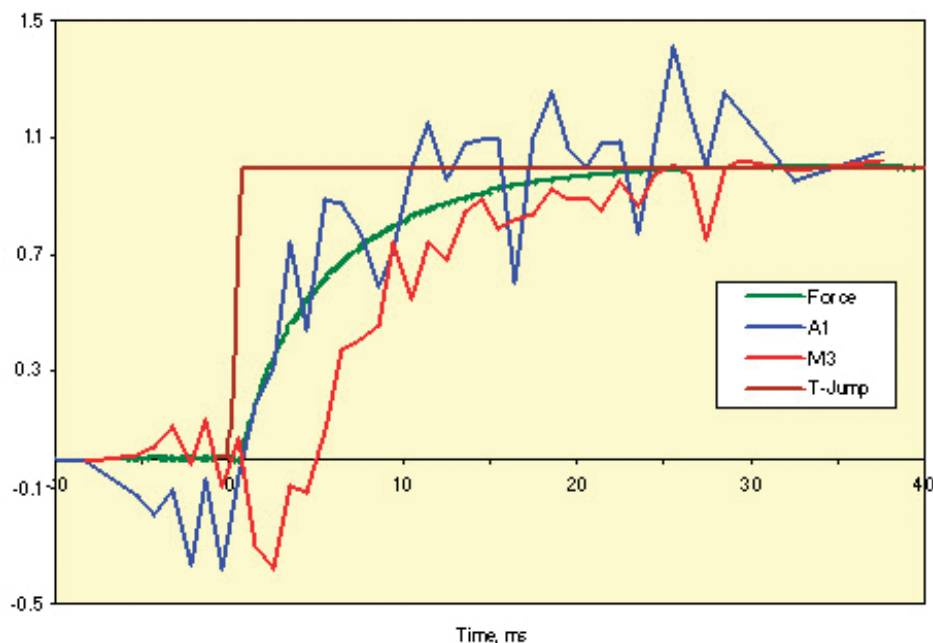


Figure 12. RAPID Results from ID02 experiments

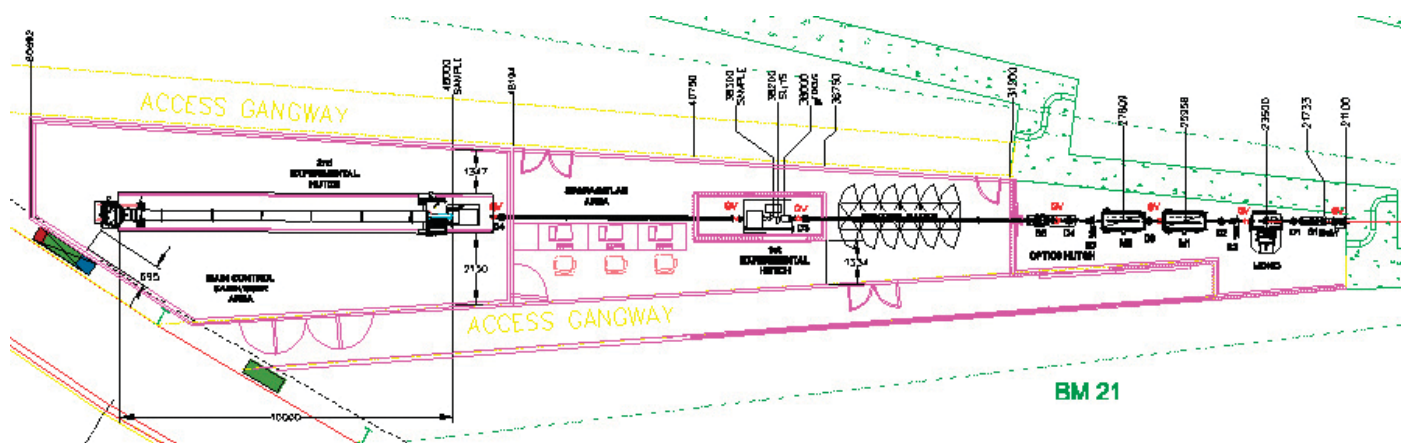


Figure 13. Overall Schematic Layout for I22

**Sample environment** - The beamline will be equipped with a range of integrated sample environments for simultaneous experiments including DSC, other furnaces/humidity chambers, stop flow cells, etc.

A purpose built platform will be provided for the manipulation of samples for microfocus work. Consideration will also be given to the demands of high throughput and facilities for automatic sample changing will be provided. An offline preparation facility will complete the beamline facilities.

**Other Facilities** - There are plans for a research complex at RAL to support Diamond; this is seen as an important opportunity to create a world-leading facility in the UK. It will be a research centre and not just a facility provider. Examples of the types of science that could take place in such a facility are in biology work on membrane proteins and large complexes. Examples in physical science could include be research on extreme conditions, environmental research and dynamic structural chemistry.

**Timescale** - It is hoped that the technical design for the beamline will be completed by the summer of 2004 with installation due to commence towards the end of 2005. Commissioning should commence during the autumn of 2006 for operation later in 2007.

<sup>i</sup>Tim Wess, Michael Drakopolous, ID18, 2003, Collagen sample collected with CRL system.

<sup>ii</sup>Experiment SC889, Michael Ferenczi\*, Sergey Bershtitsky#, Andrey Tsaturyan@ and Verl Siththanandan\*, ID02 at the ESRF in Grenoble from 9<sup>th</sup> to 12<sup>th</sup> April 2003. The work benefited from the help of Daresbury Staff who moved, installed, tested and maintained the RAPID detector (William I. Helsby, Anthony Gleeson, Mark Hillon and Nick Clague) and ESRF Staff who modified ID02 to accommodate RAPID and aligned and tested the station (Theyencheri Narayanan, Pierre Panine, Manfred Roesle, Jacques Gorini).

\*Biomedical Sciences Division, Imperial College, Sir Alexander Fleming Building, South Kensington, London SW7 2AZ; #Institute of Immunology and Physiology, Ural Branch, Russian Academy of Sciences, 91 Pervomajskaya, Yekaterinburg 620219 Russia; @Institute of Mechanics, Moscow University, 1 Mitchurinsky prosp., Moscow 119992 Russia.

## Facility Report on ISIS, with a brief Introduction to Neutron Scattering

S.M. King

Large Scale Structures Group, ISIS Facility, Rutherford Appleton Laboratory, Chilton, OX11 0QX, UK

Received 3rd December 2003; accepted in revised form 16th March 2004

### ABSTRACT

*The purpose of this report is to highlight to the CCP13 community the instrumentation and opportunities for neutron fibre and non-crystalline diffraction (including solution scattering) that currently exist at the ISIS Spallation Neutron Source, and some of the developments that are planned or already underway.*

### Introduction

Neutron scattering will be more familiar to some in the NCD community than it is to others. Consequently this report has been broken down into a number of subsections so that the reader can jump in wherever they feel comfortable.

Governments have made similar arrangements for their researchers. For further information simply contact the appropriate facility User Office. Details will be found on the relevant facility web pages.

#### How does ISIS work?

ISIS produces neutrons by bombarding a tungsten target with relativistic protons (travelling at 84% of the speed of light!) from a particle accelerator based around a linac and what is currently the most powerful *proton* synchrotron in the world [2]. The facility started operations just before Christmas in 1984. In order to lose energy, the excited tungsten nuclei "evaporate" sub-atomic particles, including neutrons. This process, called "spallation", is clearly very different to the only (useful) alternative method of producing neutron beams at present, nuclear fission. In turn, the way that instrumentation at the two types of source utilises the neutrons produced is subtly different. This will be expanded on later.

Though there is a preponderance of reactor-based neutron facilities over accelerator-based sources of approximately 8:1 at this time, growing environmental concerns, engineering limitations, and the age profile of the reactors will see this imbalance steadily reduce. In contrast, the future for accelerator sources is bright. The USA and Japan are presently constructing new facilities, both more powerful than ISIS, and ISIS itself is upgrading.

#### Time-of-flight

Anyone with experience of laboratory or synchrotron X-ray scattering will be used to the idea of working at a fixed wavelength (with a small bandpass). This is also exactly how a reactor-based neutron diffraction instrument works. A crystal monochromator or, more commonly in Small-Angle Neutron Scattering (SANS), a device called a "velocity selector", preselects a narrow wavelength band from the incident neutron distribution. As the name suggests, a velocity selector only allows neutrons with the required velocity to pass along it and onto the instrument. It works because although photons travel at the speed of light, neutrons have mass and therefore travel much more slowly! A velocity selector is, however, rather wasteful, because most of the neutrons being produced by the target/moderator assembly are being rejected by it. The

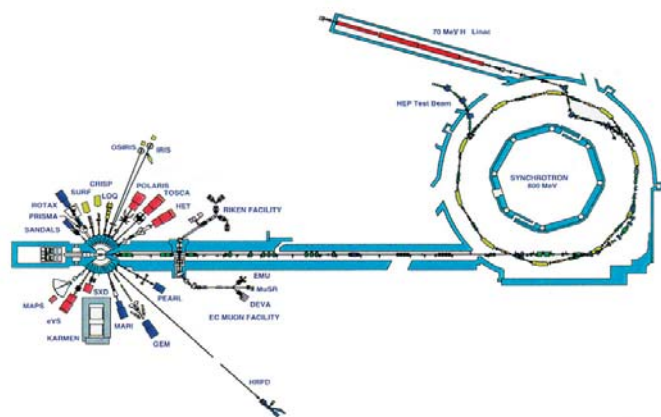


**Figure 1.** Schematic layout of the ISIS accelerator and neutron Target Station I. For scale, the synchrotron is 50 m in diameter. The KARMEN neutrino detector was removed in 2002/3. © ISIS.

#### What is ISIS?

ISIS is the name of the neutron beam research facility owned and operated by the UK Council for the Central Laboratory of the Research Councils (CCLRC) [1]. This is the same organisation that is responsible for the Daresbury Synchrotron Radiation Source and the major shareholder in the new Diamond Light Source project.

CCLRC exists to provide, maintain, and develop *large facilities* for the benefit of the UK research community, though it is always pleased to welcome international guests and partners. Use of its facilities is *free at the point of access* unless you plan to conduct commercial research. All of the major UK Research Councils have signed access agreements on behalf of the researchers that they sponsor, and a number of oversees

bandpass could be broadened to increase the flux at the sample, but only at the expense of degrading the wavelength and Q resolution of the instrument.

The ISIS particle accelerator produces and accelerates its protons in bunches. Consequently the neutrons are produced in pulses (at 50 Hz) and the beams have an intrinsic time structure that can be utilised. The Swiss SINQ spallation source, on the other hand, produces its protons continuously [3]. This is technologically less challenging, and allows the SINQ target to produce more neutrons per second, but because it is simply using an accelerator to emulate a reactor its instruments also need to use monochromators and velocity selectors.

On a pulsed source, as at ISIS, all it is necessary to do is to time the arrival of the neutrons to any given point; the faster (higher energy, shorter wavelength) neutrons will arrive before the slower (lower energy, longer wavelength) ones! This "time-of-flight" (tof) approach actually conveys a number of advantages over fixed-wavelength operation. Two are worth highlighting here:

### Fixed-geometry instrumentation

The Q-range of any fixed-wavelength instrument is determined by the incident wavelength, the sample-detector distance, and the radial distance subtended by the detector(s). The last two factors, of course, define the scattering angle.

Now consider a detector in "transmission geometry", as is often the case in SAXS or SANS. Photons or neutrons arriving close to the centre of the detector (the "straight-through" beam) will have been scattered to small Q values and vice versa. However, because the minimum and maximum radii of the detector are fixed, the corresponding Q-range is quite small. The only ways of changing the Q-range are: (i) by changing the wavelength (but with neutrons this may adversely change the incident flux), or (ii) by changing the scattering angle; either (a) by changing the sample-detector distance (if lengthened, photons or neutrons scattered through the same angle will appear on the detector at larger radial distances and vice versa), or (b), if possible, by moving the detector "off-axis" (which is like changing the minimum and maximum radial limits).

The subtlety of a time-of-flight instrument lies in the realisation that even though the scattering angle is still determined by the sample-detector distance and the radial limits of the detector, *different wavelength neutrons* (arriving at the detector at different times) scattered through the *same angle* will have *different Q-values*! Therefore each different incident wavelength contributes part of the overall scattering pattern, and the broader the incident wavelength range, the wider the Q-range of the instrument. Since this can all be achieved without moving the detector (if needs be), time-of-flight instruments are also known as "fixed-geometry" instruments.

It is the wide dynamic Q-range of the fixed-geometry instrument that is its defining characteristic. It obviates the need to repeat measurements, backgrounds, normalisations and calibrations at different sample-detector distances that must then be overlapped (usually with different Q-resolution), and is ideal for the study of samples where there are a range of length scales or, possibly, where the length scales are uncertain.

### Better Q-resolution

The Q-resolution of an instrument,  $\Delta Q/Q$ , the precision with which a particular "Q-point" can be determined, is largely (but not entirely) determined by the wavelength resolution,  $\Delta\lambda/\lambda$ . This latter quantity differs markedly between fixed-wavelength and fixed-geometry neutron instruments.

On a fixed-geometry instrument  $\Delta\lambda/\lambda$  is determined by the precision with which the neutron times-of-flight can be measured. Since these are typically a few milliseconds, timing is quite straightforward with modern electronics and a  $\Delta\lambda/\lambda \sim 5\%$  would not be uncommon. Conversely velocity selectors typically have a *Gaussian* bandpass of  $\sim 8 - 20\%$  FWHM. This already appears to make the fixed-geometry instrument look better, but to really compare like with like it is necessary to compare the standard deviation of a rectangular timing bin with the standard deviation of a Gaussian. It is then found that for a velocity selector [4]:

$$\text{effective rectangular } \Delta\lambda/\lambda = FWHM \times \sqrt{12}/\sqrt{8\ln(2)}$$

and so the wavelength resolution of the fixed-wavelength instrument is more like 11 - 30%, quite substantially worse!

### Why use neutrons?

Anyone who has never used neutrons might be forgiven for wondering what all the fuss is about. What neutrons are not is a panacea! They are not better than X-rays, nor are they any worse than X-rays. As with all experimental techniques some samples work better than others. But what neutrons do offer is an *alternative* view of a sample.

This comes about because whereas light and X-ray photons are scattered by the electrons surrounding atomic nuclei, neutrons are scattered by the atomic nuclei themselves. The consequence of this is summarised in Figure 2. That X-rays are scattered more strongly by heavier elements is, of course, widely known and no doubt familiar to the reader. Indeed, it forms the basis of the technique of isomorphous replacement in X-ray Crystallography. The problem comes when one wants to use X-rays to study samples composed of lighter elements (e.g. H, C, N, O). An even bigger problem presents itself if the

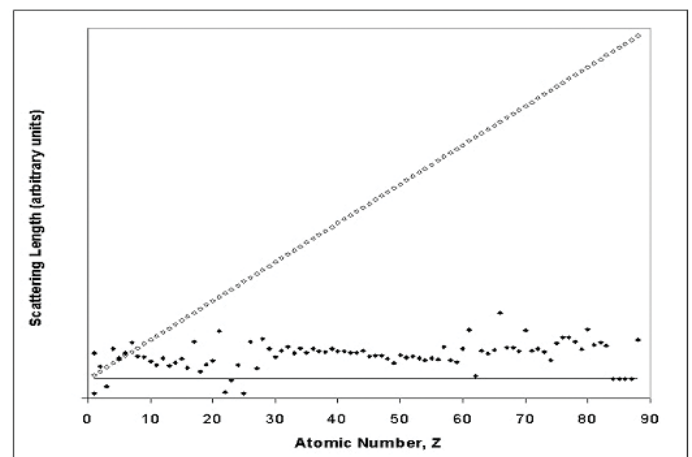


Figure 2. The relative variation of the atomic (open symbols) and nuclear (filled symbols) scattering lengths with atomic number. The continuous horizontal line marks zero scattering length.

experimental objective is to study multi-component samples (e.g. protein or polymer in solution) where all the components contain light elements. Then one component scatters much the same as any other and separating out their individual contributions is not straightforward because the "contrast" is poor.

From a first glance at Figure 2 it may not be obvious what neutrons have to offer. The answer is that with neutrons one can look at samples containing both light and heavy elements without the latter dominating the scattering. Better, the astute will have observed that elements  $^1\text{H}$  and  $^2\text{D}$  have nuclear scattering lengths of different sign! Why this is so (see, for example, [5]) is, though, much less important than the consequence; it means that by substituting D for H in a sample it is possible to selectively manipulate the contrast to highlight what is of interest. And, since a significant fraction of structural biology revolves around how water interacts with proteins, enzymes and nucleic acids, the potential benefits of neutron scattering to this area are enormous. On the other hand, readers who work with synthetic polymers might like to consider what could be accomplished by replacing their current organic solvent by its deuterated analogue, or by mixing normal (all-H) and deuterated versions of the monomers, and so on.

The downside is that neutrons interact much less strongly with matter than X-rays do, but even this presents an opportunity. It is possible to make neutron scattering measurements on thicker samples, or samples in metallic containers or inside quite complicated pieces of sample environment (cryostats, pressure cells, rheometers, and so on).

It goes without saying that neutrons can be produced with wavelengths that would enable the reader to probe the sorts of length scales that would be of interest to them, or that they currently probe with X-rays (a few nm to a few hundred nm). Typical "cold" neutron wavelengths range from  $\sim 0.1 - 2.5$  nm; compare this with  $\text{Cu}_{K\alpha}$  X-radiation at 0.154 nm, for example.

What will probably be less readily appreciated is the difference in the energy of the radiation. A 0.5 nm X-ray photon has an energy of  $\sim 2.5$  keV. The energy of a 0.5 nm neutron is by comparison just 3.2 meV, 780,000 times less! Samples that might only last a few seconds in a synchrotron beam would not suffer any radiation-induced damage in a neutron beam. As an aside, instruments that measure the neutron vibrational (i.e., like IR) spectrum of a sample also exist.

Finally, in SANS, absolute intensity measurements are routine. This means that the measured cross-section data (the numbers on the "Y-axis" of a "scattering curve") can be used to derive molecular weights, aggregation numbers, thermodynamic parameters, or to improve the confidence of any model-fit. In fact SANS data has been used to put SAXS data on an absolute scale!

### So what is the catch?

Well, there are two in fact. One is the cost and effort involved in using deuterium-labelled samples, though this is rarely enough to prohibit an experiment (and even then there may be alternative strategies).

The biggest single drawback with neutron scattering today is its relative lack of flux. Data collection times are typically minutes to hours, and not milliseconds to minutes as they are in X-ray scattering. But a great deal depends on the volume of, and contrast within, any given sample as some of the examples below will demonstrate.

Since neutrons cannot be focussed (at least not in the conventional sense) achieving a smaller beam footprint to study a small sample means collimating down and throwing away yet more flux. But do not get the wrong impression; beam diameters of a few millimetres are quite normal. And a small beam footprint can often be traded off against a thicker sample to improve statistics.

### Small- & wide-angle scattering

ISIS has one SANS instrument, called LOQ (Figure 3). It is a traditional three-pin-hole instrument and normally operates at 25 Hz, half of the ISIS frequency. This is to avoid a condition called "frame overlap" that affects all long tof beam lines, whereby short wavelength neutrons from pulse (n+1) can overtake the long wavelength neutrons from pulse (n)! The Soller bender (at short wavelengths) and the frame overlap

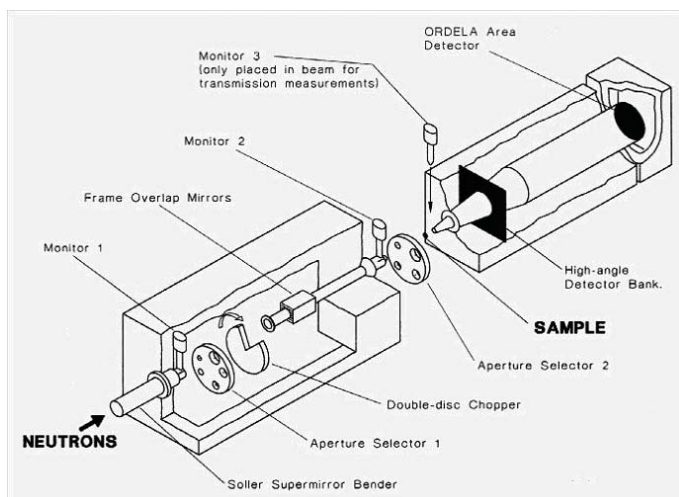


Figure 3. Schematic view of the LOQ small-angle scattering instrument. The sample position is 11 m from the cold moderator, the SANS detector is 4.1 m from the sample. © ISIS.

mirrors (at long wavelengths) in the primary collimation also help alleviate this condition. LOQ can operate at 50 Hz (and sometimes this is desirable, see Table 1), but only by taking a restricted wavelength range, control of which is achieved with the double-disc chopper.

As with X-rays, much of the primary and secondary collimation is evacuated (to stop the neutrons colliding with the much more massive air molecules).

LOQ has two, two-dimensional (or "area"), detectors. The SANS detector is a true multiwire  $^3\text{He}$  gas detector (128 x 128 wires on a square array with 5 mm spatial resolution) manufactured by ORDELA (USA) and approximately covering  $1^\circ \leq 2\theta \leq 11^\circ$ . The High-Angle detector 0.5 m from the sample was manufactured in-house. It is constructed from 4 abutted rectangular modules (neatly avoiding the meridian & equator!),

Chopper Frequency (Hz)	Wavelength Range (nm)	Q Range (nm <sup>-1</sup> )	Relative Count Rate	Remarks
25	0.22 - 1.00	0.06 - 15.0	1.0	Normal operation, uses all detectors
50	0.26 - 0.67	0.12 - 2.3	1.4	Higher flux, but reduced Q-range
50	0.63 - 1.00	0.06 - 0.7	0.2	Reduces Bragg edges from short- $\lambda$

**Table 1.** The most common configurations of LOQ. The numbers shown assume a chopper opening angle of 126°.

each of 12 x 29 ZnS scintillator pixels, 12 mm square. This detector has an angular coverage of approximately  $22^\circ \leq 2\theta \leq 70^\circ$ , but with the virtue of tof both detectors overlap in reciprocal-space between about  $1.5 \text{ nm}^{-1} \leq Q \leq 3.0 \text{ nm}^{-1}$ .

The instrument is furnished with a good selection of sample environment apparatus - a thermostatted sample changer, shear flow cells, a pressure cell and a 2T electromagnet - but can additionally draw on "ISIS standard" equipment like furnaces and cryostats if needed. For solution scattering experiments samples are contained in quartz/silica cuvettes of the type normally employed in UV spectrophotometry. A recent innovation is a simple fibre specimen holder (Figure 4). Many User Groups have also developed their own apparatus. For further information the reader is directed to the LOQ web pages [6].

On April 8 2003 the UK Government announced that ISIS would get a second Target Station (TS-II), the largest investment by the Government in a single science project

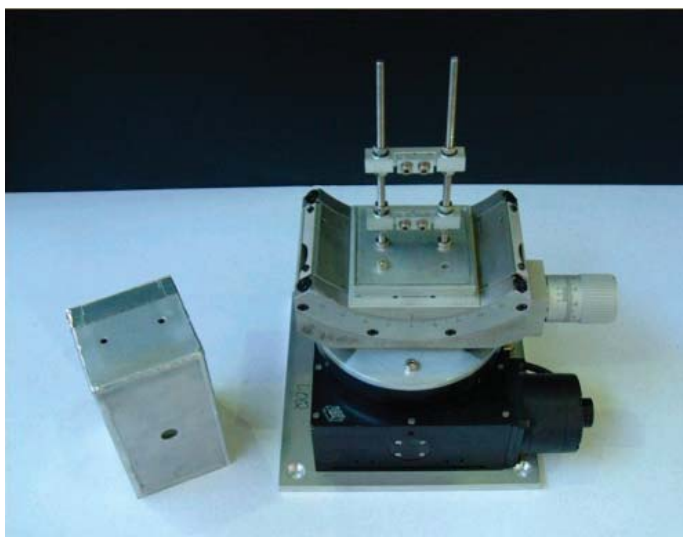


**Figure 4.** View of the LOQ fibre specimen holder. The ends of the sample are clamped between the two crosspieces. On the left is the cover that maintains humidity around the sample. The beam entry hole is visible on the front surface. A laser beam directed along the neutron flight path allows samples to be positioned accurately on the beamline. © ISIS.

(Figure 5) [7]. TS-II will operate at 10 Hz and is being specifically optimised towards the production of long wavelength neutrons. A new SANS instrument, currently designated SANS2b, features in the "day one" suite of instrumentation, and simulations indicate that the neutron flux at the sample should exceed that on LOQ by well over an order of magnitude.

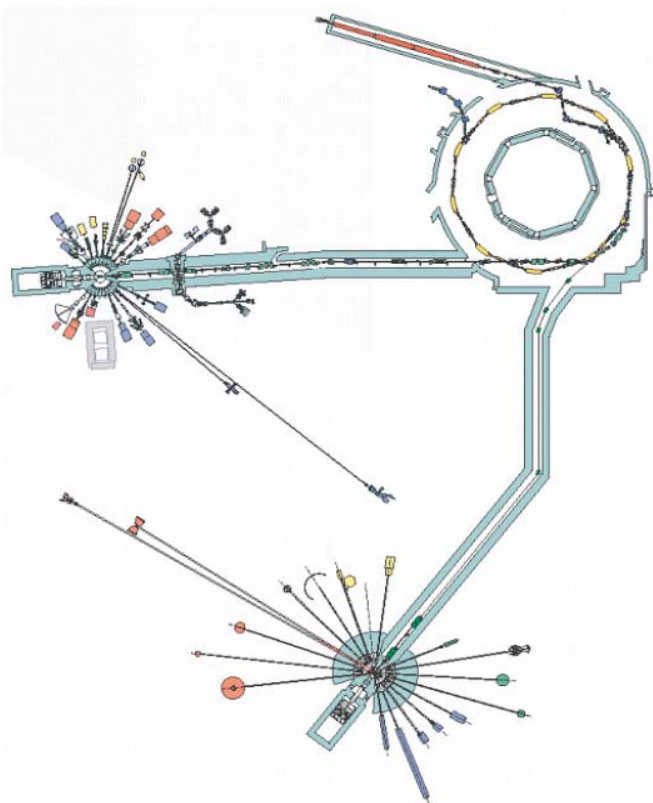


**Figure 5.** Schematic layout of the new Second Target Station in relation to the existing ISIS Facility. SANS2b is the long beam line in the lower-right quadrant. © ISIS.

SANS2b will be a much longer instrument than LOQ. This will allow a broader wavelength band to be utilised giving it, in turn, both a lower minimum-Q and a higher maximum-Q than is presently possible on LOQ. But the really unusual design feature of SANS2b is that it will use two, *moveable*, area detectors (each larger than the present LOQ ORDELA detector) side-by-side, with the ability to be offset vertically across their radius, in a huge "detector cave". This revolutionary design for a pulsed-source SANS instrument will offer unrivalled flexibility and dynamic range, and offer count rate improvements in the case of weakly scattering samples or experiments with more highly collimated beams, simply because there will be twice the detector area available to record the scattering pattern. SANS2b is expected to undergo commissioning towards the end of 2007. The provision of a *second* SANS instrument on TS-II, perhaps optimised for low-Q, is being discussed, as too is the future of LOQ.

This section on SANS instrumentation is concluded with some examples of recent work conducted on LOQ. The first, taken from the authors own work, shows the changes in the SANS pattern from synthetic rope fibres under strain (Figure 6) [8]. The second example is very possibly the most technically demanding experiment ever conducted on LOQ, involving *in-situ* real-time temperature-jump measurements (Figure 7) [9].

There are two other instruments at ISIS that warrant mention in this report:

### Single crystal (Laue) diffraction

SXD is a general purpose Laue diffractometer, but operating under the principles of tof [10]. It is also equipped with two-dimensional detectors, and together this allows it to simultaneously survey large volumes of reciprocal space in a

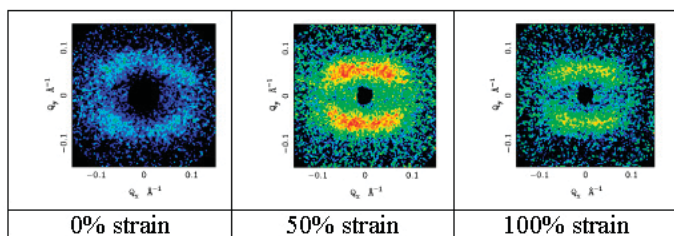


Figure 6. The scattering from nylon fibres hydrated with D2O (to the same intensity-colour scale) [8]. The sample size was approximately 30 (long) x 3 (wide) x 1 mm (thick) and was illuminated with a vertical 8 x 2 mm slit. Each pattern represents about a 40 minute exposure.

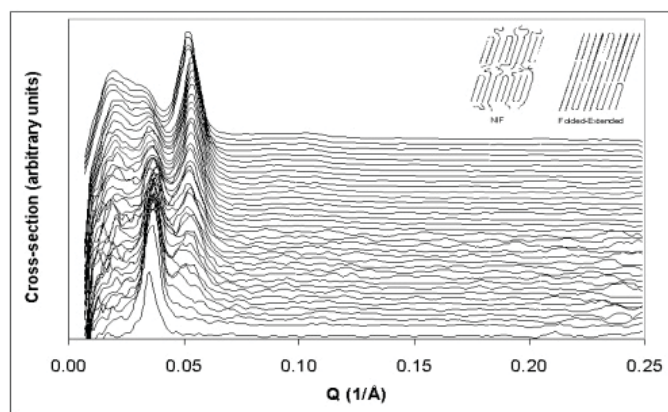


Figure 7. The SANS from the synthetic alkane  $C_{12}D_{25}C_{192}H_{384}CHDC_{11}D_{23}$  isothermally crystallised at  $110^{\circ}C$ , showing the transition from the non-integer folded to folded-extended configurations [9]. These data, displaced vertically for clarity, represent a contiguous time series of just over 20 minutes. The first 20 scattering curves are 10 second exposures! The sample was approximately 10 mm in diameter and 1 mm thick.

single measurement. So unlike a "conventional" Laue diffractometer it is not necessary to repeatedly rotate the sample or detectors to access all of the reflections.

The instrument underwent a major upgrade between 1999-2001 that brought the total number of detector banks up to 11 (SXD-II). The low-angle coverage has also been substantially improved (Figure 8).

The sample volumes required are typically around  $100 \text{ mm}^3$ , but ultimately depend on the unit cell size and the scattering characteristics.

A fibre diffraction program has yet to be established on SXD. Poor detector performance and poor angular coverage hampered early experiments, but both of these issues have now been addressed.

A "second-generation" instrument, LMX (the Large Molecule Crystallography diffractometer), has been proposed for TS-II and was added to the "Day Two" instrument short list by the TS-II Science Advisory Council in June 2003.

The LMX design calls for upwards of  $10^5$  detector pixels with higher efficiency than at present; partly to take advantage of a flux increase of perhaps as much as x40, and partly to offer substantially improved detector spatial resolution. Together

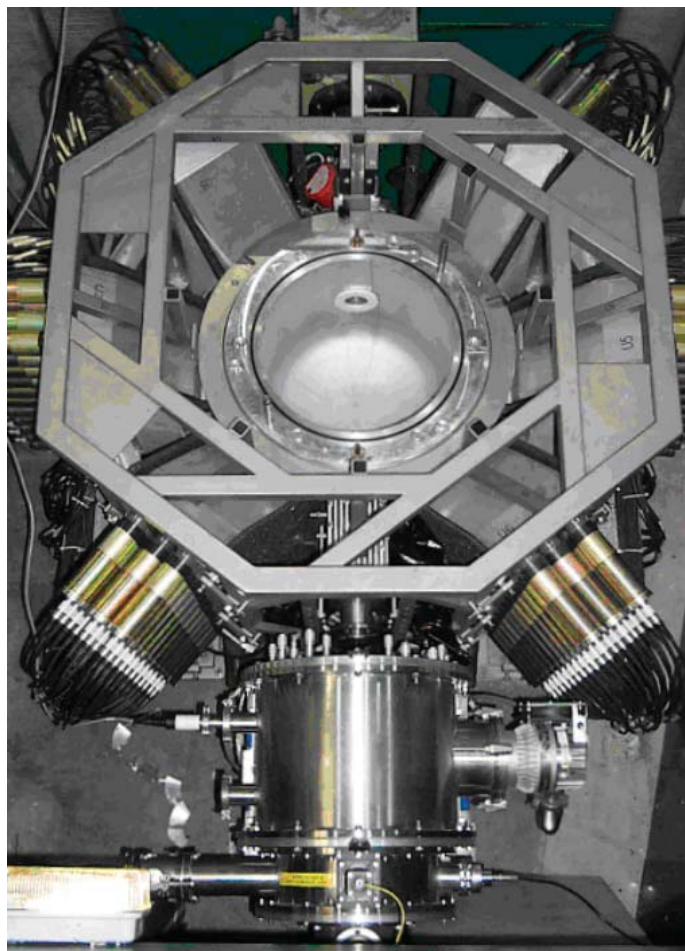


Figure 8. View of the SXD-II single crystal diffractometer sample position, showing the new jaws assembly at the bottom and some of the additional detector banks funded by the recent upgrade. In this view the incident neutron beam travels upward from the bottom centre. The sample and sample environment sit in the cylindrical well in the centre of the image. © ISIS.

these factors should make LMX highly complementary to instruments like D19 at the ILL for fibre diffraction studies, and provide a second instrument (alongside LADI at the ILL) for the study of single crystals with small unit cells.

#### Amorphous diffraction

GEM, the General Materials diffractometer, is the newest addition to the ISIS instrument suite (Figure 9). It has been especially designed for high-intensity, high-resolution, powder diffraction from disordered and crystalline samples [11]. Already GEM has demonstrated that it is capable of measuring refinable patterns in just a few seconds (in the case of favourable samples), or patterns from samples weighing just a couple of milligrams in around 10 hours.

One of the principal features of GEM is its enormous angular coverage; 6550 scintillator detector elements (of which over 98% are already installed) spanning  $1^{\circ} \leq 2\theta \leq 170^{\circ}$ .

The capabilities of GEM have recently been used to evaluate the conformational changes that may accompany the formation of mesophases prior to crystallisation in synthetic polymers (Figure 10).

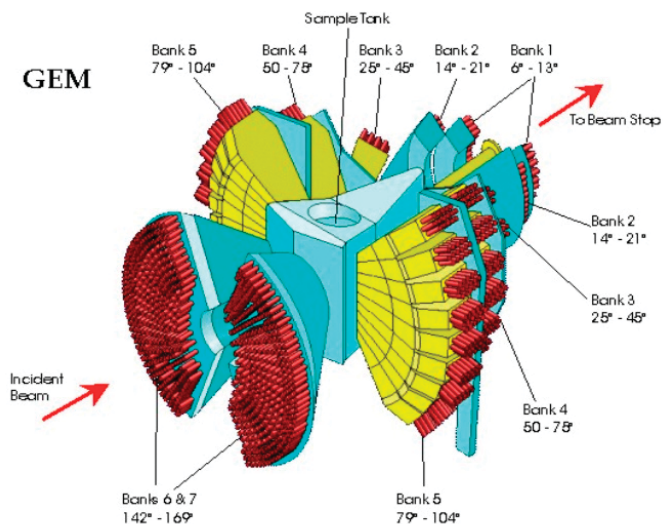


Figure 9. Schematic isometric view of the GEM powder diffractometer, including the layout of its detector banks. © ISIS.

### Summary and conclusions

December 2004 will herald the 20th Anniversary of the production of the first neutrons at ISIS. In the intervening years ISIS has matured into a vibrant User Facility whose instruments now support over 1500 researchers worldwide.

The TS-II Upgrade will ultimately double the size of the instrument suite and, in areas such as solution scattering, fibre diffraction, and small-molecule crystallography, also offer significant count rate gains with improvements in resolution and Q-ranges.

The complementary nature of neutrons and X-rays is now widely recognised, the benefits are appreciated, and the gap between sample exposure times is diminishing. Real-time experiments, if not at the sub-second timescale, are becoming a reality on modern neutron instrumentation.

Shortly before TS-II becomes operational the Diamond Light Source will have delivered beam to its instrumentation. Diamond is situated at the same site (the Rutherford Appleton Laboratory) as ISIS and there is a determination to ensure that maximum benefit is extracted from the co-location of these two important facilities.

Whether you are a neutron practitioner or an X-ray practitioner, the future is bright.

### Acknowledgements

I would like to thank Goran Ungar, X. Zeng (Sheffield University) and Steve Spells (Sheffield Hallam University) for allowing me to include Figure 7, and Jintana Siripitayanon and Geoffrey Mitchell (University of Reading) for allowing me to include Figure 10.

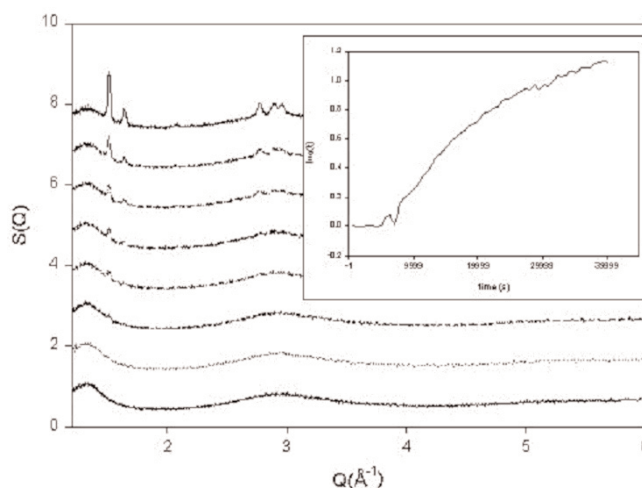


Figure 10. Wide-angle neutron scattering data from a sample of perdeuterated linear polyethylene quenched from the melt at 155°C to 129°C, as recorded on the GEM 25°-45° detector bank (Siripitayanon/Mitchell, 2003). The data was accumulated on a cycle time of 600 s. The curves represent data recorded at increasing time periods (since the sample was quenched) and follow the isothermal crystallisation process. The inset shows how the height of the first crystalline peak (110) at  $Q \sim 1.5 \text{ \AA}^{-1}$  changes with time. These data show that GEM can record high quality broad-Q scattering data up to  $Q \sim 50 \text{ \AA}^{-1}$  in the time period before the crystalline peaks can be observed.

### References

- [1] <http://www.clrc.ac.uk>
- [2] <http://www.isis.rl.ac.uk>
- [3] <http://sinq.web.psi.ch>
- [4] Heenan, R.K., Penfold, J., King, S.M. (1997) SANS at Pulsed Neutron Sources, *J. Appl. Cryst.*, **30**, 1140.
- [5] Lovesey, S.W. (1986) *Theory of Neutron Scattering from Condensed Matter*, Oxford University Press.
- [6] <http://www.isis.rl.ac.uk/LargeScale/LOQ/loq.htm>
- [7] <http://www.isis.rl.ac.uk/targetstation2/>
- [8] King, S.M., Bucknall, D.G., Heenan, R.K. (2004) SANS from Surfactant Treated Nylon Fibres, *ibid.*
- [9] Zeng, X.B., Ungar, G. (2003) Triple-Layer Superlattice in Deuterium-Labeled Binary Ultralong Alkanes, *Macromol.*, **36**, 4686. (additional work is still in progress).
- [10] <http://www.isis.rl.ac.uk/crystallography/sxd/>
- [11] [http://www.isis.rl.ac.uk/disordered/gem/gem\\_home.htm](http://www.isis.rl.ac.uk/disordered/gem/gem_home.htm)

### Further reading

King, S.M. (1999) Small-angle neutron scattering. Chapter 7 in *Modern Techniques in Polymer Characterisation*. Pethrick, R.A., Dawkins, J.V. (editors).

## Report on CCP13 Software Developments: Production of an Integrated CCP13 Environment (ICE) for Windows

Andrew He<sup>1</sup>, Ganeshalingam Rajkumar<sup>1</sup>, Trevor Forsyth<sup>2</sup> & John Squire<sup>1</sup>

[1] Biological Structure & Function Section, Biomedical Sciences Division, Imperial College London, London SW7 2AZ

[2] Institut Laue Langevin, 6 Rue Jules Horowitz, BP156 F-38042 Grenoble Cedex 9, France

Received 4th February 2004; accepted 10th February 2004

### ABSTRACT

*We report on recent developments in CCP13 software with particular emphasis on ICE, an integrated, internet-enabled, common desktop CCP13 environment. As an initial package, several heavily used data conversion and stripping programs have been integrated together in ICE with an easy to use Graphical User Interface (GUI) and enhanced functionality. ICE can dynamically group CCP13 programs together by using a program startup panel. At present the programs that have been integrated with ICE include CCP13 ImageViewer, XCONV, FTOREC, LSQINT, XFIX and the CCP13 Online Help Browser.*

### Introduction

One of the main goals of CCP13 is to develop software for non-crystalline diffraction. Over the last ten years CCP13 scientists have been developing and supporting a set of programs for stripping and analysing fibre diffraction patterns and other non-crystalline diffraction patterns and for systematic modelling of different kinds of structure. CCP13 software has become one of the important shared resources for the fibre diffraction, non-crystalline diffraction and solution scattering research community in the UK and world-wide. The aim of the CCP13 project has been to allow geographically distributed research groups to work together more effectively, sharing resources, data, knowledge and expertise in the community and to allow those multi-discipline groups to complete their tasks quickly and smoothly. Several recent developments as part of the CCP13 project have helped to promote these ideas, including providing an active CCP13 website and its mirror sites, providing updated and newly developed software for download, and providing the online version of *Fibre Diffraction Review*. Here we describe the recent development of the integrated CCP13 environment software known as *ICE*.

### Recent Developments for Fibre Diffraction

A major task for the CCP13 effort has concerned the extraction of useful intensity data from fibre diffraction patterns. The nature of the patterns from fibres can be quite diverse, ranging from those which exhibit Bragg sampling from polycrystalline specimens, to patterns where the intensity is continuously distributed along layer-lines, reflecting a complete lack of axial register across the sample. As a first attempt at providing an integrated software package, several heavily used data conversion and stripping programs have been put together into a user-friendly package with an easy to use Graphical User Interface (GUI) and enhanced functionality. This package is now called *ICE*. Users can still enjoy the freedom to start up and use each individual program independently by opening them either from the program menu or from the *ICE* common desktop environment.

*ICE* is an integrated, internet-enabled, common desktop CCP13 environment. It can dynamically group the CCP13 programs together by using a program start-up panel. In *ICE* version 1.0, six applications have been developed and integrated. They are: CCP13 *ImageViewer*, XCONV, FTOREC, LSQINT, XFIX and the CCP13 *Online Help* Browser. *ICE* also provides a CCP13 program editor so that users can use it to create batch files for applications like FTOREC and LSQINT in order to run them under the batch mode. Like any integrated commercial program editor, it supports functions such as copy, cut, paste, print, font and colour selection. The motivation to do this is that the user has to conduct a sequence of related computational tasks quite often and repeatedly. Such tasks flow from one application (e.g. XCONV) to a second application (e.g. XFIX) and so on. This is a 'work flow' problem and is very common in CCP13 processing, as described in Squire *et al.* (2003). For instance, to process a raw fibre diffraction pattern, the raw data can be viewed initially by *ImageViewer*. Then it is put through the file conversion program XCONV to convert it into BSL format and the BSL image may itself be displayed and manipulated by *ImageViewer*. The BSL image is then put into the analysis program XFIX which outputs parameters such as fibre tilt and rotation for input into FTOREC, where the pattern is corrected and remapped into reciprocal space. Then, the corrected data from FTOREC can be fitted in LSQINT either as continuous intensities or as Bragg peaks after suitable background removal. Intensities output from LSQINT can then be used in modelling processes. The philosophy behind the development of *ICE* is to make possible a much improved pattern of 'work flow' through these CCP13 programs. *ICE* is an XML-enabled environment. XML can play a key role as a data definition language in the 'work flow' problem when transferring data from one application to another. To make implementation of a sequence of related computational tasks both quick and reliable, it is possible to use the integrated program editor to support the syntax and grammar checks for creating batch files and work flow files. Using 'drag and drop' to view images and texts has become a standard feature in the *ICE*-enabled applications.

*ICE* consists of a menu bar, a tool bar, a program startup panel and a CCP13 program text editor as presented in Figure 1.

Both *ImageViewer* and *Online Help* are newly developed CCP13 applications. CCP13 *ImageViewer* intends to provide comprehensive visualisation and image data manipulation capability. It will be used to preview different types of images before running XCONV and will be able, for example, to rotate the images in a series through a defined angle to align them parallel to a common axis, to scale them to a common size, and to put them on a common centre, so that several images can be added to increase the signal to noise. CCP13 *Online Help* provides specific online help and support to the CCP13 users, powered by the newly developed internet-enabled CCP13 web browser which makes automatic online updates of the *ICE* software and documents possible. The tool bar of *ICE* includes

XFIX is designed to help ascertain some important parameters of a fibre diffraction pattern. Information such as the pattern centre, detector orientation and fibre tilt can be estimated and refined and putative unit cells can be plotted over the pattern. In addition, more general functions are available such as the capability to plot and fit integrated slices or scans through the pattern. The program can also be used to remove the background of fibre diffraction patterns. XFIX has been newly designed and developed for Windows. This has improved the application's stability, expandability, modularity and performance. It has replaced the original loose-coupled communication between XFIX and the background FIX application with one application that combines both BSL image

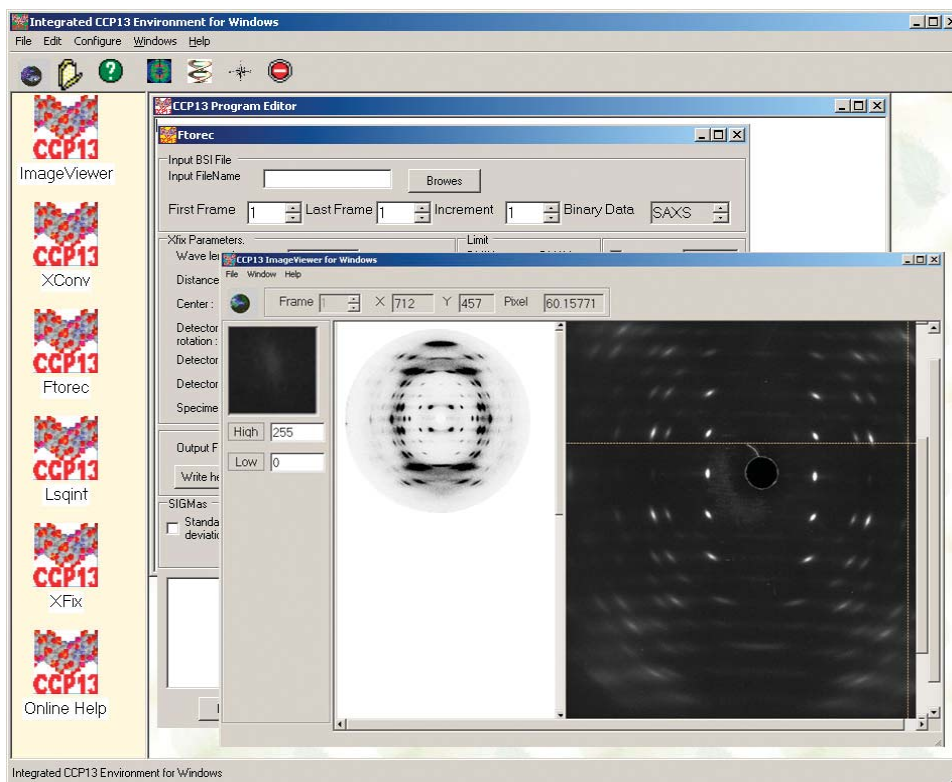


Figure 1. The Integrated CCP13 Environment (ICE) for Windows, showing opened FTOREC and ImageViewer windows.

speed image buttons so that users can start a Microsoft file explorer, access the CCP13 *Online Help*, CCP13 website and *Fibre Diffraction Review* website directly by using the CCP13 web browser. The reason for including Microsoft File Explorer is that 'Drag and Drop' functionality is supported by most of the *ICE*-enabled applications such as XFIX and *ImageViewer*. For example, you can drag a JPG image file from Microsoft File Explorer and then drop it onto CCP13 *ImageViewer* to be displayed. Furthermore, most of the *ICE* integrated applications support hint-tip style text sensitive help when your mouse is over a command button. XCONV, FTOREC, LSQINT and XFIX have been ported from UNIX to Windows with enhanced functionalities.

XCONV is a program that can input data files from a variety of data sources and can convert them to BSL/TIFF formats. BSL format is at present the standard format for most of the CCP13 processing software. XCONV has been newly developed under Microsoft Windows with enhanced support for a wide range of image file formats from a variety of detectors and will be continuously updated as new detectors and image formats are used. The newly supported image formats include Mar345, BRUKER and ILL\_SANS. Please refer to the *Online Help* document for details.

display and data-processing functions together. Plotting and fitting integrated slices or scans through the pattern was supported by the original version of XFIX by using third party graphical image display software PGPLOT. The current version of XFIX has replaced this by introducing our own CCP13 image display modules with enhanced visualisation capability and extendibility. Background subtraction and refinement in XFIX was always a time-consuming process. The computational speed has now greatly improved. The new version of the XFIX drawing objects function is quite easy to use as well. Furthermore XFIX can now handle any size of image. Since FTOREC is integrated with XFIX, it automatically passes the parameters that need to go to FTOREC. The postscript format output in the original XFIX has been replaced with JPG and BMP image formats.

FTOREC is designed to take all or part of a diffraction image and to transform this portion of the image into reciprocal space, given knowledge of the specimen to film distance, orientation of the image, wavelength and tilt of the specimen determined in XFIX. FTOREC has been re-developed under the Microsoft .Net platform as a user-friendly GUI application. It can run under *ICE* as a standalone application and it has also been integrated into a part of XFIX as well. LSQINT provides an

automatic method for the integration of intensities for fibre diffraction data. It has been newly developed and supports three modes: the non-GUI DOS command line mode, the batch Windows mode, and the Windows GUI mode.

## Future Developments

Feedback from users has suggested that there is still plenty of room for further improvements to the *ICE* software and that we should also develop and integrate more CCP13 applications into *ICE*. In fact, instrumentation and experimentation developments are already pushing for improvements in existing CCP13 programs. For example, where high spatial precision is needed in X-ray diffraction patterns, A3 size image plates are being used with a pixel size of about 100 $\mu$ m. This generates enormously large files. The lack of standardisation of file formats and the increasing number of new detectors and raw image data formats are also pushing for continuously updating inter-conversion programs such as XCONV. There are also increasing demands for visualising and pre-viewing the raw images in the new data formats.

LSQINT can handle patterns which are largely crystalline in nature, or patterns which have intensity continuously distributed along layer-lines, with sampling only occurring parallel to the c-axis. More than one lattice can be fitted in a single pattern. The approach used is to generate spot profiles and then to fit these profiles to the observed pixel values. The current version of LSQINT for Windows is a GUI-based application supported by the LSQINT DOS application in the background. Running the LSQINT program is a time-consuming process. Planned improvements will include shorter processing times, improved data visualisation and display and a more user-friendly GUI, as well as removal of the restrictions on the dimensional size of an input image.

The subtraction of appropriate backgrounds plays an important role in extracting high quality data from fibre diffraction patterns. In LSQINT and XFIX, several background subtraction methods are available. For example, a global background can be fitted simultaneously with the spot profiles; a notional roving aperture and filter can be used to define a background; or a background plane can be fitted in a region of the pattern along with the spot profiles. The on-going tasks include the development of better background subtraction modules, the design and development of new background subtraction algorithms, the further reduction in background subtraction and refinement processing time, and the implementation of these modules in both XFIX and LSQINT.

On the other hand, the existing CCP13 software, now proved and accepted as being effective and robust, needs to be made as simple to handle as possible for new users. Many users are currently trying out the CCP13 software for their own applications. This is both testing the software under varied real world conditions and also, in some cases, leading to requests for the software to be modified or enhanced for user specific needs. There remains a major task of improving user interfacing; specifically in the writing of up-to-the minute, comprehensive and comprehensible manuals for the various software packages, including self-help tutorials.

## Conclusions

Traditionally, CCP13 software has been developed and supported under various UNIX platforms, and UNIX Workstations have been the main computational resources for fibre diffraction researchers. However, this situation is changing. Upgrading and maintaining UNIX workstations is more expensive than for PCs, and, because of the growth in computer speed, disk capacity and memory, modern PC workstations running under Linux or Microsoft Windows can be very powerful machines in their own right. During the past decade, Linux has had a large impact on the traditional UNIX platforms, and major UNIX machine providers such as Sun, IBM and HP have run to support Linux as well. There have been very useful developments in the implementation of CCP13 packages on Linux which can reside either on Intel-powered relatively inexpensive PCs or on traditional UNIX workstations. However, Linux may not be available free of charge in the near future as SCO is demanding Linux license payments. The potential impact of this on academic users is not clear. On the other hand, the Microsoft Windows operating system and software development toolkit have now become almost free for academic use under Microsoft campus agreements. This enables us to develop and to maintain high standard user-friendly graphical user interface (GUI) and visualisation applications across Windows platforms. CCP13 programs need to support visualisation, frequent user and program interaction, and time-consuming tasks as well. Nowadays, most of the CCP13 users have a PC, but they have lacked a set of CCP13 programs running under Windows. Following the successful porting of CCP13 programs into DOS, several of the most widely used CCP13 applications have now been developed under the Microsoft Windows environment to support the majority users of PCs. For example, *ICE* is a software package intending to make CCP13 software as readily, extensively and productively used as possible. It will meet demanding tasks such as those of both high computational performance and graphic visualisation capacity and, at the same time, it is hoped that it will reduce the "energy barrier" for new users as well as providing additional useful functionality. One of the on-going tasks for the forthcoming months is to deliver *ICE* for Linux. Both Linux and Windows have large user bases in our community. It is important to deliver solutions for both operating systems.

## Acknowledgements

We acknowledge the grant support from the BBSRC and EPSRC (#25/B15281) which makes these CCP13 developments possible. The CCP13 programs XCONV, XFIX, LSQINT and FTOREC were originally developed and updated by CCP13 scientists Drs. R. Denny and M. Shotton under various UNIX platforms, in collaboration with Dr. Geoff Mant (Daresbury Laboratory) and Prof. J. Squire (Imperial College London).

## References

- [1] Squire, J.M., AL-Khayat, H.A., Arnott, A., Crawshaw, J., Denny, R., Diakun, G., Dover, S.D., Forsyth, V.T., He, A., Knupp, C., Mant, G., Rajkumar, G., Rodman, M.J., Shotton, M. & Windle, A.H. (2003) New CCP13 software and the strategy behind further developments: Stripping and modelling of fibre diffraction data. *Fibre Diffraction Review*, **11**, 7-19.

## Development of CORFUNC

Matthew Rodman

CLRC Daresbury Laboratory, Keckwick Lane, Warrington WA4 4AD.

Received and accepted 17th March 2004

The Corfunc programme [1] is an application in the CCP13 suite designed to perform correlation function analysis on one-dimensional SAXS and SANS data in order to yield physical parameters of the specimen in terms of an ideal lamellar morphology. The correlation function calculated by the programme is essentially a Fourier transform of the input data. In order to achieve this overall aim, the task is split into three logical parts:

1. *Extrapolation*: prior to performing the transform, the data curve must be modelled to remove the restriction of finite  $q$ , and finite intensity values. The programs 'tailjoin' and 'tailfit' fulfil this role: with tailjoin being responsible for the shape of the curve as  $q$  tends to zero, and tailfit modelling the curve as it tends to infinity.

2. *Fourier transform*: the program 'transform' performs a Fourier transform on the extrapolated data, yielding the one-dimensional correlation function,  $\Gamma_1$ . (It can also re-transform the result back into a smoothed copy of the extrapolated data).

3. *Interpretation of  $\Gamma_1$* : the program 'extract' interprets the features of  $\Gamma_1$ , based on an ideal lamellar morphology.

The Corfunc program has been written in modular form in order for individual elements of it to be edited without disrupting the application as a whole. (Indeed, many parts of it may be edited without necessitating a full re-compile, or even swapped-out at run-time for a module with an identical programmatic interface, but with a dissimilar purpose.)

As far as the end user is concerned the compartmentalisation of Corfunc is irrelevant. In order to remove the user from unnecessary exposure to the internal workings of the application, a Java GUI (Graphical User Interface) is provided. The programming language Java was chosen as this affords a compile once, run everywhere strategy (at least for the interface: the underlying command-line programs still require compilation for each end-user platform).

It is the modular nature of Corfunc we shall be exploiting in order to augment its functionality to encompass the study of adsorbed layers in colloidal dispersions. In this addition to Corfunc's scope we are primarily interested in harnessing its curve-fitting ability, if not, necessarily, developing its existing direction: we then only need to provide an alternative 'transform' module in order to expand the program's potential to incorporate new uses in the area of colloidal dispersions.

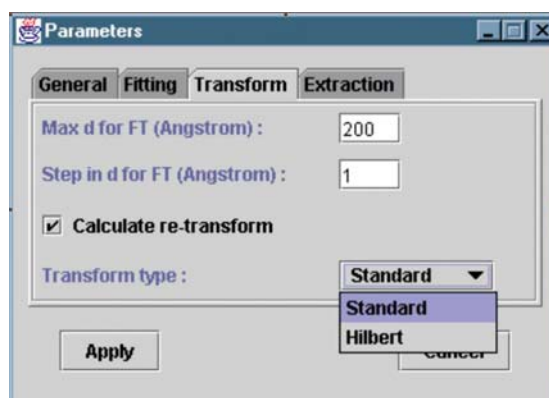


Figure 1. The edited transform parameters pane showing the new Hilbert option.

The particular area we are interested in concerns the manipulation of small-angle scattering data to yield information about the radial distribution of adsorbed layers of polymer or surfactant molecules. Using a Hilbert transform based on a method discussed in King, *et al.*, [2] we can directly substitute the existing transform module and then plot the results via Corfunc's in-built display procedures, without having to edit the way Corfunc deals with transform output files.

An important caveat to bear in mind with this new development is that existing users may be unsure how to respond with the new 'Hilbert' option that appears in the interface. In order to lessen the risk that an injudicious selection of transform may cause, Corfunc's online help files have been edited to include a description of the purpose and relevance of the new functionality.

## References

- [1] T. M. W. Nye, *SAXS Correlation Function Analysis: Notes on the Software at Daresbury*. <http://www.ccp13.ac.uk/software/program/corfunc.html>
- [2] S. M. King, P.C. Griffiths, and T. Cosgrove. Using SANS to study adsorbed layers in colloidal dispersions, in "Applications of Neutron Scattering to Soft Condensed Matter", ed. B.J. Gabrys, Gordon & Breach Science Publishers, Amsterdam, 2000.

## Reviews

### Normal-mode-based Refinement of an F-actin Model Against Fibre Diffraction Data

Yinghao Wu<sup>3</sup> & Jianpeng Ma<sup>1,2,3</sup>

[1] Graduate Program of Structural and Computational Biology and Molecular Biophysics

[2] Verna and Marrs McLean Department of Biochemistry and Molecular Biology, Baylor College of Medicine, One Baylor Plaza, Houston, TX 77030

[3] Department of Bioengineering, Rice University, Houston, TX 77005

Received 17th February 2004; accepted in revised form 16th March 2004

#### ABSTRACT

*This review briefly summarizes the recent development in fibre diffraction refinement of flexible filamentous systems using long-range normal modes as adjustable parameters. Among all the long-range modes, the low-frequency bending modes were found to contribute the most to the improvement of the refinement. The use of several low-frequency modes in the refinement decreased significantly both  $R$ - and  $R_{free}$ -factors, demonstrating the advantage of this procedure in achieving a good refinement without the risk of over-fitting. Moreover, the study provided strong evidence that substantial errors in conventional refinements are due to long-range deformations, especially the bending, of the filaments. These intrinsic deformations must be properly accounted for in order to improve the refinement efficiency.*

Fibre diffraction is widely employed for studying structures of biologically important filamentous systems (Stubbs, 1999) ranging from simple polypeptides to cytoskeletal filaments and filamentous viruses. In fibre diffraction experiments, the fibre specimens are aligned axially, but not azimuthally, and diffraction patterns are cylindrically averaged, which leads to the characteristic layer lines. Because of this averaging, the number of independent diffractions of fibres is significantly smaller than that from crystals. One usually does not have sufficient data to refine the Cartesian coordinates of each atom in the fibres. This feature imposes a severe challenge in choosing proper refinement parameters (Wang and Stubbs, 1993).

In the conventional fibre diffraction refinement procedures, fibres are assumed to be perfect straight helices. In reality, however, fibres are flexible and undergo all sorts of static and dynamic disordering that contribute to the modulation of diffraction patterns. Such disordering should be taken into account in refinement in order to obtain more accurate models.

In recent studies (Ming *et al.* 2003a; Ming *et al.* 2003b), collective long-range deformations of a filament, such as bending, twisting and stretching, were effectively modeled by long-range normal modes of the filament. Following that, a small set of low-frequency modes was used as adjustable parameters to refine the model of  $F$ -actin (Wu and Ma 2004), a system known to be highly flexible and dynamic (Egelman 2001; Egelman *et al.* 1982; Egelman and Orlova 1995; Galkin *et al.* 2002; Huxley *et al.* 1994; Kojima *et al.* 1994; Orlova *et al.* 2001; Wakabayashi *et al.* 1994). As an approximation, deformations were assumed to occur within the periodic repeat, the helical unit cell, of the  $F$ -actin filaments. The straight rigid filament model used in conventional refinement procedures was thereby substituted by wave-like conformations described by normal modes.

With the new refinement procedure, it was demonstrated that the long-range deformations of the filaments, especially the bending, are the dominant sources of refinement errors. By taking into account such deformations in the refinement, with only 7–9 low-frequency normal modes as adjustable parameters, it was possible to lower both  $R$ - and  $R_{free}$ -factors by ~2%. Therefore, the long-range filament deformations of fibres indeed need to be properly accounted for in order to improve the refinement.

#### Structural Models of $F$ -actin

The various states of the monomeric G-actin subunit have been visualized by X-ray crystallography (Kabsch *et al.* 1990; McLaughlin *et al.* 1993; Otterbein *et al.* 2001; Robinson *et al.* 1999; Schutt *et al.* 1993). The polymeric  $F$ -actin filaments have several models. The standard Holmes model (Holmes *et al.* 1990) was established by combining fibre diffraction data and the X-ray structure of G-actin subunit (Kabsch *et al.* 1990). In this model,  $F$ -actin filaments have two right-handed long-pitch helical strands with a rise of 27.5 Å and a rotation angle of -166.15° per monomer. There are 13 subunits in the minimum repeat of the double-stranded helix (the 13-subunit repeat) with a length of 37.5 nm. A second model (Tirion *et al.* 1995) was refined on the basis of the standard Holmes model, with the deformations of the G-actin subunits modeled by normal modes. Although a reduced number of refinement parameters were used by employing normal modes calculated on a single G-actin sub-unit, no effects of long-range filament deformations were considered. Another model of  $F$ -actin (Lorenz *et al.* 1993) was obtained using directed mutation algorithm. However, too many parameters were used in the refinement, which has a potential problem of over-fitting (Tirion *et al.* 1995). A new model was provided by Kenneth C. Holmes (unpublished results, personal communication). In this model, each subunit was refined as five rigid bodies, the four G-actin domains and a heptapeptide phalloidin. The  $R$ -factor of

this model is 8.7% and it was used as the starting model for the new normal-mode-based refinement (Wu and Ma, 2004).

### Normal-mode-based Refinement Procedure

In the new refinement procedure, in order to study the effects of long-range deformations on refinement, the four-domains of G-actin were treated as rigid-bodies. Various assemblies of G-actin subunits were used as helical unit cells in the refinement against fibre diffraction data (Holmes *et al.* 1990). Within each unit cell, no helical symmetry was considered so that there was only one asymmetric unit in each unit cell and all atoms were treated as unique. The approximate assumption was that *F*-actin filaments deform in the unit of the helical unit cells. This assumption would result in additional layer lines generated in the calculations.

The low-frequency normal modes of the helical unit cells were determined using  $C\alpha$ -based normal mode analysis, the anisotropic network model (ANM) (Atilgan *et al.* 2001) and the substructure synthesis method (SSM) (Ming *et al.* 2003b). The eigenvectors of normal modes describe the  $C\alpha$ -based trajectories of molecular deformations. The coordinates for all atoms in the unit cell along the deformational trajectories were generated by superimposing the four domains of G-actin subunit, as rigid-bodies, onto the  $C\alpha$ -trajectories along the eigenvectors of normal modes. This assumption of the domains as rigid bodies is reasonable, given that only the low-frequency modes were chosen to describe the long-range collective deformations of the filament in the refinement. Additionally, inter-domain constrains suggested by Holmes in his recent work (unpublished results, personal communication) are also applied (Wu and Ma 2004) to maintain constant distances between two neighboring  $C\alpha$ -atoms located at the boundary of different domains.

### Refinement Using Individual Low-frequency Modes of A 13-subunit Repeat

The minimum 13-subunit repeat of *F*-actin was first used as a helical unit cell for the refinement. The low-frequency normal modes of the repeat were calculated (Atilgan *et al.* 2001) and

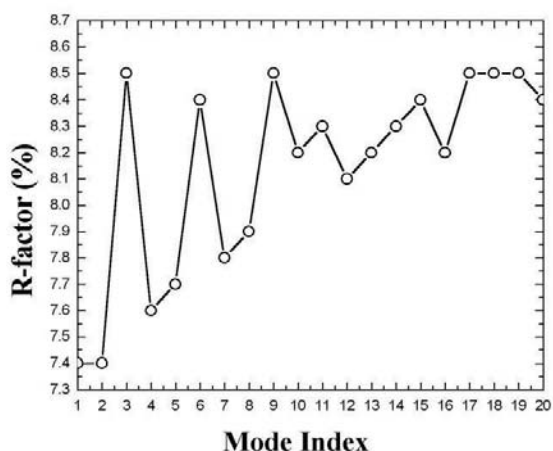


Figure 1. Refinement results using each of the first 20 lowest-frequency modes with 13-subunits as a helical unit cell. The ceiling of the figure is the value of *R*-factor (8.7%) of the starting model of the normal-mode-based refinement (Wu and Ma, 2004).

individually employed as adjustable parameters to refine the model. Results in Figure 1 clearly showed that the refinement was improved to various degrees for all the first 20 lowest-frequency modes plotted (the ceiling of the figure is the *R*-factor of the starting model, 8.7%). The smallest *R*-factor (7.4%) was achieved by each of the two very lowest-frequency modes (the 1<sup>st</sup> and 2<sup>nd</sup> vibrational modes after excluding the first six zero modes) that are two perpendicular bending modes. In the first 11 lowest-frequency modes, all modes are various types of bending modes, with the exception of the 3<sup>rd</sup> and 6<sup>th</sup> modes (twisting) and the 9<sup>th</sup> mode (stretching). All these bending modes reduced the *R*-factor to a larger degree (0.4~1.3%) than non-bending ones (0.2~0.3%). The decrease of *R*-factor caused by the bending modes becomes progressively smaller as the frequency (or modal index) increases. These results clearly suggest that bending modes of *F*-actin filament, especially the very low-frequency ones, have large impacts on the structure refinement.

### Refinement Using Individual Low-frequency Bending Modes of Longer Repeats

To investigate the effects of deformations with longer-wavelength, the refinements were further carried out using helical unit cells of longer than 13-subunits. For longer *F*-actin repeats, the low-frequency normal modes were generated by

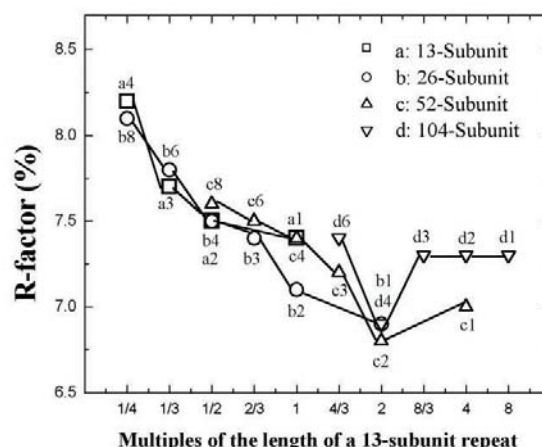


Figure 2. Refinement results using individual bending modes with different lengths of repeating units as helical unit cells. For illustrative purpose, the figure was drawn to align the modes according to their wavelengths. The intervals of the X-axis were expressed as multiples of a single 13-subunit repeat. To make the points in figure spread evenly, all intervals were arranged along the X-axis evenly (rather than based on the numerical values of the actual multiples). The modes were marked according to their half wavelengths by approximately assuming the shapes of waves are trigonometric, *i.e.* those of standing waves. The numerical numbers following the letters at each point were inverted to the types of bending waves in terms of their wavelengths. For example, the 1<sup>st</sup> type of bending mode of the 13-subunit repeat had a multiple of 1 and was labeled as a1 and the 2<sup>nd</sup> type of bending mode had a multiple of 1/2 and was labeled as a2, and so on. All the modes for longer repeating units were aligned correspondingly. For clarity, only one of the two degenerate modes was used in each type of wave.

SSM (Ming *et al.* 2003b) based on the modes calculated for a 13-subunit repeat (Ming *et al.* 2003a).

Fig.2 shows the results of refinement by individual bending modes at different lengths of repeats. The X-axis was calibrated to the multiples of the length of a 13-subunit repeat. The curves were aligned according to their approximate half wavelengths that were approximately defined by comparing the shape with that of a standing wave (for the shapes of the first four types of bending modes for standing waves and free vibrations with equal wavelengths, see Fig.3 in reference (Wu and Ma, 2004)). It was noted that there was a specific point at which all the curves converged to a minimum of  $R$ -factor. The wavelength of that point corresponds to modes with a half wavelength of the length of a 26-subunit repeat (the 1<sup>st</sup> type of bending mode of a 26-subunit repeat, the 2<sup>nd</sup> type of bending mode of a 52-subunit repeat, and the 4<sup>th</sup> type of bending mode of a 104-subunit repeat).

### Refinement Using Multiple Modes

The effects of multiple modes on the refinement were also examined because an increased number of degrees of freedom, represented by multiple modes, were expected to better describe the deformations of the filament.

As shown in Fig.3, the use of multiple low-frequency modes indeed further decreased the  $R$ -factor. For example, the inclusion of 9 lowest-frequency modes of a 13-subunit repeat in the refinement resulted in an  $R$ -factor of 7.0%. More importantly, the  $R_{free}$ -factor was decreased to a similar degree (see Table 1 in reference Wu and Ma, 2004), indicating a real improvement of the refinement. The trends of changes in  $R$ -factor were similar for larger helical unit cells (26-subunit and 52-subunit repeats). The lowest value of  $R$ -factor was 6.3% for the 52-subunits using 7~9 lowest-frequency modes.

### The Refined Structures

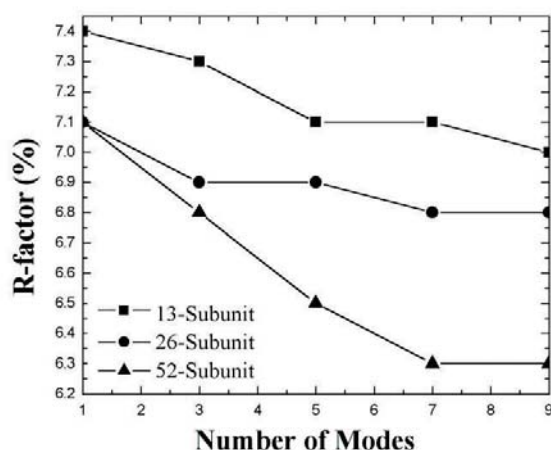


Figure 3. Refinement results using multiple low-frequency normal modes as adjustable parameters with various lengths of repeats as helical unit cells.

The long-range normal-mode refinement procedure improves the fit between the model and the diffraction data mainly by a more realistic modelling of the long-range deformations. Local structural adjustments in individual subunits and domains are relatively small (see Fig.5 in reference Wu and Ma, 2004). This is illustrated in Fig.4 in which the G-actin subunit in the standard Holmes model is superimposed with the G-actin structure refined using a 52-subunit as a helical unit cell by employing 7~9 lowest-frequency modes (with  $R$ -factor of 6.3%). The refined G-actin structure is very similar to the new Holmes model that was used as a starting model of this study, with an average root-mean-square (rms) deviation of 0.1~0.2 Å.

### Summary

This review briefly summarizes the results of a recent study (Wu and Ma, 2004) on the refinement of the  $F$ -actin model against fibre diffraction data using long-range normal modes as adjustable parameters to account for the collective filament deformations. In the refinement, each of the four domains of a G-actin subunit was treated as rigid-body in order to separate the contributions of long-range deformations from those of local structural deformations. Among all the low-frequency long-range modes, bending modes were found to contribute the most to the improvement of the refinement. Moreover, the largest decrease of both  $R$ - and  $R_{free}$ - factors was achieved by using multiple low-frequency modes. The results clearly demonstrated the advantage of normal-modes-based refinement in using a small number of adjustable parameters to achieve a good fitting efficiency, which helps avoid the risk of the over-fitting problem. More importantly, the results provided strong evidence that, for fibre diffraction refinement of flexible systems, substantial errors arise from the ignorance of long-range deformations, especially bending, of the filaments. Therefore, the effects of these deformations must be included in the refinement for flexible systems.

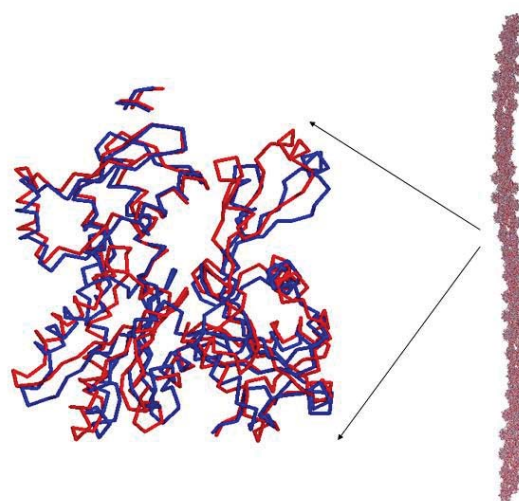


Figure 4. The superposition of the G-actin subunit in the standard Holmes model (blue) with the G-actin structure refined using a 52-subunit as a helical unit cell by employing 7~9 lowest-frequency normal modes (red). The refined G-actin structure is very similar to the new Holmes model that was used as a starting model of this study, with an average rms deviation of 0.1~0.2 Å. The starting model is omitted in the figure for illustration clarity.

In the current normal-mode-based refinement procedure (Wu and Ma, 2004), the contributions from slightly higher-frequency modes with wavelengths similar to the physical sizes of the domains were eliminated due to the use of rigid body for each of the four domains of the G-actin subunit. It is expected to further improve the refinement once such a restriction is lifted to allow local structures to adjust within each individual domain. Another important aspect of the new refinement procedure is that there is only one asymmetric unit in each unit cell in which all atoms were regarded unique and participated in the calculations. This treatment will be especially useful in the later stage of fibre diffraction refinement, when it is possible to determine long-range normal modes from a model refined using conventional methods. However, it needs to be emphasized that, as the size of unit cell used in normal-mode-based refinement increases, the computational cost quickly increases, which may affect the application of the method to systems with very large unit cells. Future development should be devoted to resolve this issue.

## Acknowledgements

The authors gratefully acknowledge Professor Kenneth C. Holmes for providing the experimental diffraction data and the unpublished *F*-actin model. J.M. thanks the support from the American Heart Association (AHA-TX0160107Y), the Robert A. Welch Foundation (Q-1512), the National Institutes of Health (R01-GM067801), and the National Science Foundation Career Award (MCB-0237796). J.M. is also a recipient of the Award for Distinguished Young Scholars Abroad from National Natural Science Foundation of China.

## References

- [1] Atilgan AR, Durell SR, Jernigan RL, Demirel MC, Keskin O, Bahar I. (2001) Anisotropy of fluctuation dynamics of proteins with an elastic network model. *Biophys J*, **80**(1), 505-515.
- [2] Egelman EH. (2001) Actin allostery again? *Nat Struct Biol*, **8**(9), 735-736.
- [3] Egelman EH, Francis N, DeRosier DJ. (1982) *F*-actin is a helix with a random variable twist. *Nature*, **298**, 131-135.
- [4] Egelman EH, Orlova A. (1995) New insights into actin filament dynamics. *Curr Opin Struct Biol*, **5**(2), 172-180.
- [5] Galkin VE, VanLoock MS, Orlova A, Egelman EH. (2002) A new internal mode in *F*-actin helps explain the remarkable evolutionary conservation of actin's sequence and structure. *Curr Biol*, **12**(7), 570-575.
- [6] Holmes KC, Popp D, Gebhard W, Kabsch W. (1990) Atomic model of the actin filament. *Nature*, **347**(6288), 44-49.
- [7] Huxley HE, Stewart A, Sosa H, Irving T. (1994) X-ray diffraction measurements of the extensibility of actin and myosin filaments in contracting muscle. *Biophys J*, **67**, 2411-2421.
- [8] Kabsch W, Mannherz HG, Suck D, Pai EF, Holmes KC. (1990) Atomic structure of the actin:DNase I complex. *Nature*, **347**(6288), 37-44.
- [9] Kojima H, Ishijima A, Yanagida T. (1994) Direct measurement of stiffness of single actin filaments with and without tropomyosin by in vitro nanomanipulation. *Proc Natl Acad Sci USA*, **91**(26), 12962-12966.
- [10] Lorenz M, Popp D, Holmes KC. (1993) Refinement of the *F*-actin model against X-ray fibre diffraction data by the use of a directed mutation algorithm. *J Mol Biol*, **234**(3), 826-836.
- [11] McLaughlin PJ, Gooch JT, Mannherz HG, Weeds AG. (1993) Structure of gelsolin segment 1-actin complex and the mechanism of filament severing. *Nature*, **364**(6439), 685-692.
- [12] Ming D, Kong Y, Wu Y, Ma J. (2003a) Simulation of *F*-actin Filaments of Several Microns. *Biophys J*, **85**, 27-35.
- [13] Ming D, Kong Y, Wu Y, Ma J. (2003b) Substructure Synthesis Method for Simulating Large Molecular Complexes. *Proc. Nalt. Acad. Sci. USA*, **100**, 104-109.
- [14] Orlova A, Galkin VE, VanLoock MS, Kim E, Shvetsov A, Reisler E, Egelman EH. (2001) Probing the structure of *F*-actin: cross-links constrain atomic models and modify actin dynamics. *J Mol Biol*, **312**(1), 95-106.
- [15] Otterbein LR, Graceffa P, Dominguez R. (2001) The crystal structure of uncomplexed actin in the ADP state. *Science*, **293**(5530), 708-711.
- [16] Robinson RC, Mejillano M, Le VP, Burtnick LD, Yin HL, Choe S. (1999) Domain movement in gelsolin: a calcium-activated switch. *Science*, **286**(5446), 1939-1942.
- [17] Schutt CE, Myslik JC, Rozycki MD, Goonesekere NC, Lindberg U. (1993) The structure of crystalline profilin-beta-actin. *Nature*, **365**(6449), 810-816.
- [18] Stubbs G. (1999) Development in Fibre Diffraction. *Curr. Opin. Struct. Biol.*, **9**, 615-619.
- [19] Tirion MM, ben-Avraham D, Lorenz M, Holmes KC. (1995) Normal modes as refinement parameters for the *F*-actin model. *Biophys J*, **68**(1), 5-12.
- [20] Wakabayashi K, Sugimoto Y, Tanaka H, Ueno Y, Takezawa Y, Amemiya Y. (1994) X-ray diffraction evidence for the extensibility of actin and myosin filaments during muscle contraction. *Biophys J*, **67**, 2422-2435.
- [21] Wang H, Stubbs G. (1993) Molecular dynamics in refinement against fibre diffraction data. *Acta Crystallogr A*, **49**, 504-513.
- [22] Wu Y, Ma J. (2004) Refinement of *F*-actin Model Against Fibre Diffraction Data by Long-range Normal Modes. *Biophys. J.*, **86**, 116-124.

## The Structure of Amyloid

O. Sumner Makin<sup>1</sup> & Louise C. Serpell<sup>2</sup>

[1] Cambridge Institute for Medical Research (CIMR), Wellcome Trust/MRC Building, Addenbrooke's Hospital, Hills Road, Cambridge CB2 2XY, UK

[2] Department of Biochemistry, School of Life Sciences, University of Sussex, Falmer, East Sussex, BN1 9QG, UK

Received 19th December 2003; accepted in revised form 16th March 2004

### ABSTRACT

*The local or systemic deposition of insoluble amyloid fibrils is characteristic of the pathogenesis of the heterogeneous group of diseases known as the amyloidoses. Normally soluble, innocuous proteins undergo a change in conformation and self assemble into insoluble, potentially toxic, amyloid fibrils. Electron microscopy shows amyloid fibrils to be straight, unbranching structures, 70 to 120 Å in diameter and of indeterminate length. The potential for amyloidogenesis may be a near universal property of protein. Knowledge of the structure of these fibrils is a crucial element in the development of an understanding of their stability and assembly. With this information, the rational design of drugs to prevent amyloidogenesis and promote disassembly might be enabled. Furthermore, it may grant some insight into the generality of protein folding. Single crystal X-ray crystallography and solution NMR are not possible due to the fibrillar inability to crystallise and to intrinsic insolubility. X-ray and recently electron fibre diffraction have proved to be of great value in the elucidation of the structure of amyloid. This review discusses the advances made and how fibre diffraction is used in conjunction with other structural techniques.*

### INTRODUCTION

Alzheimer's disease is the leading cause of dementia; it affects nearly half the population over eighty-five and costs the US economy some 100 billion dollars per annum (Alzheimer's Association, 2002). Abnormal amyloid-like aggregates are involved in the pathogenesis of this and an increasing list of other diseases, including the transmissible spongiform encephalopathies (e.g. Mad Cow disease) and type 2 diabetes (Rochet & Lansbury, 2000; Kelly, 1996). In these diseases, known collectively as the Amyloidoses, insoluble amyloid fibrils are self-assembled from normally soluble protein and deposited extracellularly. There is no apparent commonality between precursor proteins in amino acid sequence, molecular weight or morphology. Furthermore, many proteins not implicated in conformational disease have also been shown to form amyloid *in vitro*, leading to the hypothesis that the potential for amyloidogenesis may be a near universal feature of protein (Dobson, 2001).

Amyloidosis cases have been described for well over 300 years, whilst Rudolph Virchow first classified Amyloid in 1854 (Cohen, 1986; Sipe & Cohen, 2000). Yet it is only within the past 20 years that the specific makeup and structure of amyloid has begun to be understood. Amyloid is now characterised by specific staining, the X-ray diffraction pattern and its appearance under the electron microscope. An apple green birefringence pattern is observed after staining with Congo red dye and viewing between crossed polarisers under a light microscope (Khurana *et al.*, 2001). The X-ray diffraction pattern is described as cross- $\beta$ , consisting of two major reflections, a sharp meridional at 4.7Å and a more diffuse equatorial at between 10 and 11 Å (Figure 1b). Electron micrographs reveal fibres with a similar ultrastructural morphology - being straight, unbranching, 70 to 120 Å in diameter and of indeterminate length (see Figure 3a).

Knowledge of the structure of the mature amyloid fibril is a necessary step in the rational development of drugs to prevent the formation and promote the disassembly of the fibrils. To this end, a great variety of structural techniques have been employed. Unfortunately, structural exegesis by means of X-ray crystallography is not possible since amyloid does not generally crystallise. Similarly, solution nuclear magnetic resonance (NMR) is thwarted due to the insolubility of amyloid. Successful techniques include electron microscopy, light scattering, solid state NMR, Fourier transform infrared spectroscopy (FTIR), circular dichroism (CD), selective mutation experiments, atomic force microscopy (AFM), small angle neutron scattering (SANS) and X-ray fibre diffraction. The utility of fibre diffraction might be established by means of comparison with the other techniques.

### Following fibrillogenesis

The process of self-assembly is examined in kinetic studies using CD, AFM and light scattering. CD provides insight into the changes in the secondary structure and the environment and orientation of aromatic side chains, which accompany amyloidogenesis (Ganesh & Jayakumar, 2003). High-resolution data gathered using AFM has illuminated the mechanism and kinetics of the assembly (Goldsbury *et al.*, 1999), whilst light scattering allows one to establish the accompanying changes in particle size (Murphy, 1997). These studies have demonstrated that amyloidogenesis is a process of nucleation and growth, with nucleation being the rate determining step. In FTIR, certain vibrational bands have been assigned to particular conformations of  $\beta$ -sheets by empirical studies of model peptides and normal mode computations (Janek *et al.*, 1999). Fibre diffraction is used to study the mature amyloid fibril. It is therefore complementary to electron microscopy, FTIR and solid state NMR.

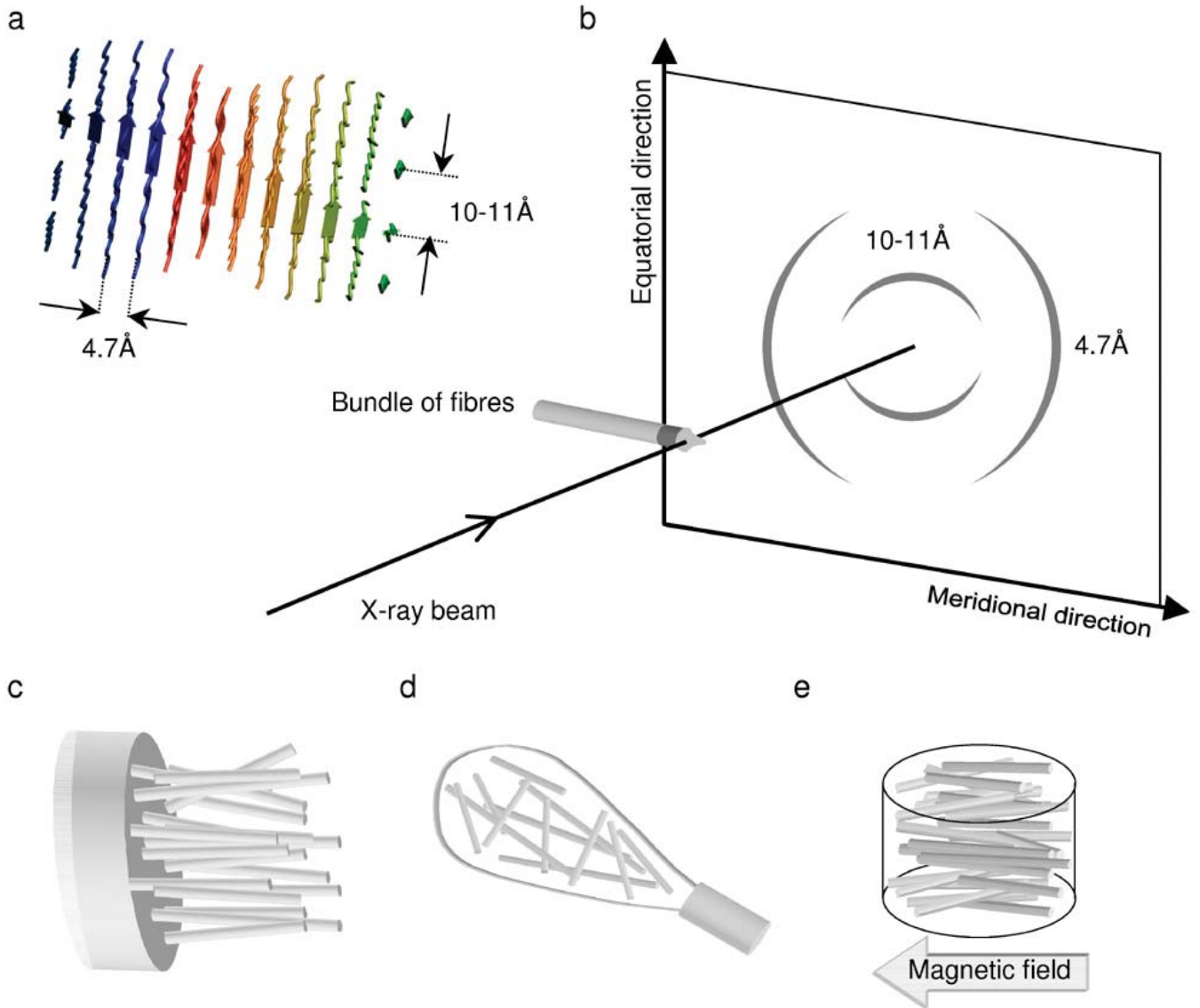


Figure 1. Upper panel: illustration of amyloid fibre diffraction showing the position and orientation of the  $\beta$ -strands and the resulting diffractogram. Lower panel: three different possible fibre orientations are shown, from left to right, stretch frame, mat and magnetically aligned.

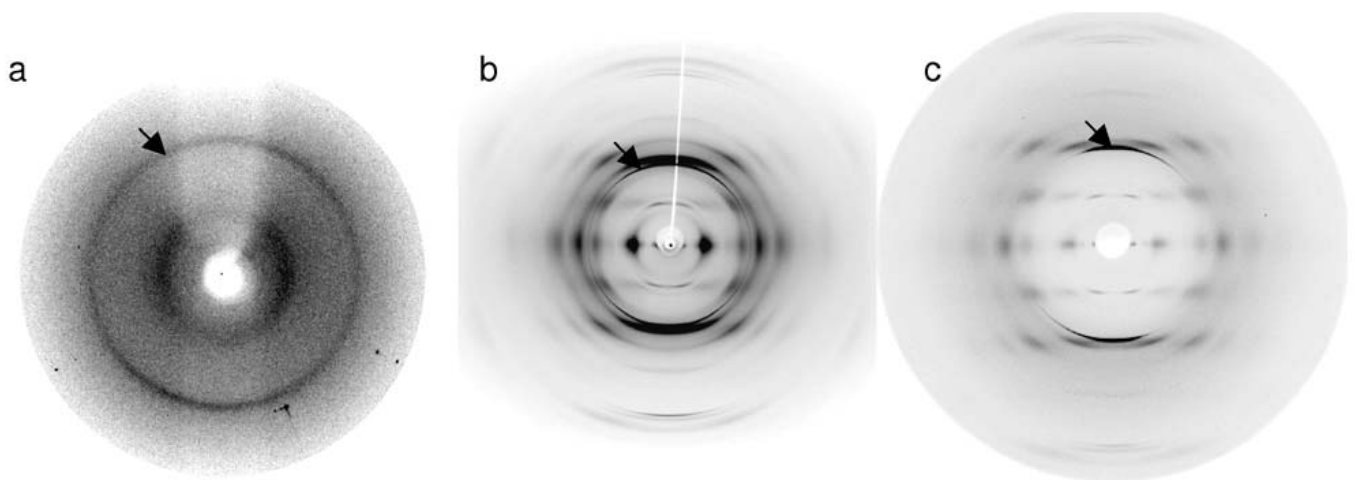
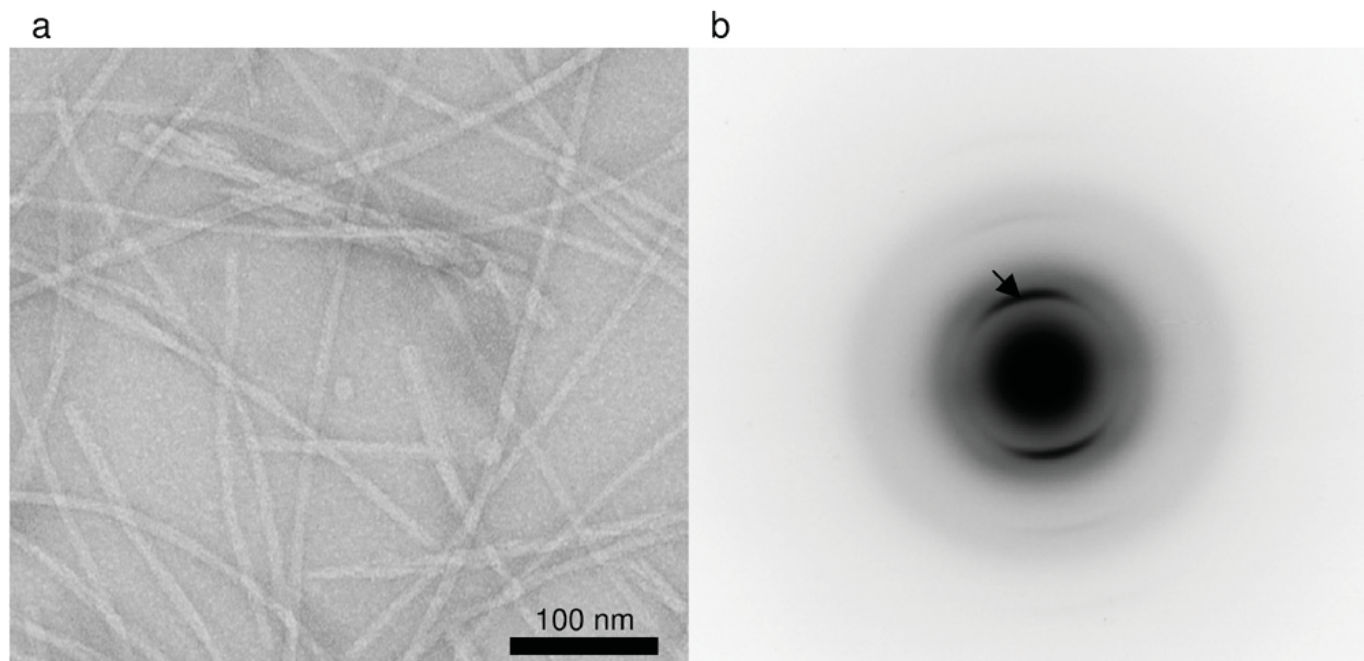


Figure 2. Comparison of diffraction patterns from amyloid fibrils formed from unaligned  $A\beta(1-42)$  on the left, with stretch-frame aligned fibrils of  $A\beta(11-25)$  in the centre and magnetically aligned  $A\beta(11-25)$  in the right-hand panel (Sikorski *et al.*, 2003).



**Figure 3. Electron microscopy and electron diffraction from amyloid fibrils formed from full-length islet amyloid polypeptide (IAPP), showing the long straight amyloid fibrils and the cross- $\beta$  position of the 4.7Å meridional reflection from electron diffraction (Makin and Serpell, in press).**

## SANS and SAX

Small angle neutron scattering (Yong *et al.*, 2002; Yonezawa *et al.*, 2002; Lu *et al.*, 2003) has been used for the study of fibril assembly and the mature fibril. Its use is somewhat constrained by the requirement for a neutron source and much of the information can be gathered by alternative means. SANS of A $\beta$  (10-35), used in conjunction with NMR and negative stain EM (Burkoth *et al.*, 2000), is an example of using various techniques to build up sufficient to construct a plausible model. Molecular dynamics simulation could then be employed to extend the structural assignment (Lakdawala *et al.* 2002). In the same manner, small angle X-ray equatorial diffraction has had the potential to determine the number and arrangement of protofilaments. Simple theoretical models were compared with equatorial traces from fibre diffraction patterns. On the meridian, small angle reflections indicate the long-range repeating unit along the hydrogen bonding direction, which may be consistent with helical twisting (Fraser *et al.*, 1991; 1992a; 1992b). Amyloidogenesis can be followed using time-resolved small angle X-ray diffraction to monitor the dimensions of the sample's constituents (Botelho *et al.*, 2003; Yonezawa *et al.*, 2002).

## Solid state NMR and amyloid

Solid state NMR (ssNMR) is used to determine the distance between  $^{13}\text{C}$  labels less than 6Å apart (Tycko, 2001). These measurements are then found to be consistent with either a parallel or antiparallel arrangement, since the peptide structure may be modelled given distance measurements between labelled residues. This is less information than might be expected from a well-aligned X-ray sample. Results may be misleading if the  $\beta$ -strands are simply out of register rather than antiparallel or a mixture of parallel and antiparallel. Distances of over 6 Å are unable to be measured. Consequently, there is a

range of reported results. Some have not been consistent with those from FTIR (Antzutkin *et al.*, 2000), explained by noting that the FTIR experiments used models significantly less complex than  $\beta$ -amyloid peptides. Balbach *et al.* (2000) analysed A $\beta$ (16-22) using multiple quantum NMR and rotational echo double resonance, whilst Lansbury *et al.* (1995) examined A $\beta$ (34-42) using rotational resonance, in both cases results were consistent with an antiparallel model. In contrast, A $\beta$  (1-42) and A $\beta$  (10-35) have been shown to have a parallel arrangement using multiple quantum NMR and dipolar recoupling in windowless sequence measurements (Antzutkin *et al.*, 2000; Benzinger *et al.* 2000), though it is unclear how the forty residue chain is folded such that the fibre diameter matches that observed in electron micrographs, since an extended strand of 40 residues would span ~140 Å (Sikorski *et al.*, 2003). Unfortunately, the fibre diffractogram (Figure 2a) (Sikorski *et al.*, 2003) is unable to provide further insight, but it is suggested that the data are consistent with intersheet  $\beta$ -hairpins.

## The macromolecular structure of amyloid from electron microscopy and atomic force microscopy

AFM is clearly useful due to the measurements being taken in real time in near physiological conditions (Goldsbury *et al.*, 1999; Wang *et al.*, 2003; Stolz *et al.*, 2000). Resolutions down to 10 Å have been achieved, with the mechanical damage due to dragging a tip across the sample being reduced by the use of tapping modes. Unfortunately, this is insufficient to reveal the arrangement of  $\beta$ -strands even though a helical twist might be evident.

Negative stain, platinum shadowing and cryo electron microscopy (EM) have been employed to visualise the fibrils. Fibrils assembled from the same peptide may have different

morphologies (Goldsbury *et al.*, 1997), which may or may not be dependent on the conditions. It has been possible to directly visualise the  $\beta$ -strands making up the fibrils formed from A $\beta$ (11-25) (Serpell & Smith, 2000). Thin cross-sections of fibrils have been analysed using single particle methods to determine the number and arrangement of protofilaments (Serpell *et al.* 2000), these results can be compared to those extracted from small angle X-ray and neutron scattering. Scanning tunnelling microscopy (Wang *et al.*, 2003; Shivji *et al.*, 1995; Baxa *et al.*, 2003) has had some use determining the mass per unit length of fibres to confirm or eliminate possible models. Finally, reconstruction using single particle methods of images of SH3 amyloid (Jiménez *et al.*, 1999) has allowed a three-dimensional model to be built within the electron density. Hence EM has provided information commensurate with the models developed from fibre diffraction. Whilst these techniques may be described as high resolution, fibre diffraction is more so and helps untangle the disagreements between methods based on the modelling of idealised peptides.

### The cross- $\beta$ diffraction pattern

X-ray diffraction from amyloid reveals the characteristic cross- $\beta$  pattern, comprised of two spots (Figure 1b). A sharp reflection on the meridian is observed at a resolution of 4.7 Å. This corresponds to the distance between the  $\beta$ -strands that comprise a  $\beta$ -sheet. The other, more diffuse spot is found on the equator between 10 and 11 Å, which can be explained as the distance between stacked  $\beta$ -sheets (Figure 1a,b). There is variation in the distance between  $\beta$ -sheets according to the size of the side chains. Geddes *et al.* described the cross- $\beta$  pattern in egg stalk of the green lacewing fly *Chrysopa flava* (Geddes *et al.* 1968) and the same pattern was noted for amyloid fibrils formed from Bence Jones protein (Eanes & Glenner, 1968). In many amyloid diffraction patterns a layer line at 9.4 Å is observed (Sikorski *et al.*, 2003) (see Figure 2b and c). The presence of a 9.4 Å (=2 x 4.7 Å) spacing suggests that the strands must be in an antiparallel arrangement. Unfortunately, the absence of a 9.4 Å spot (*eg.* Figure 2a) does not necessarily imply that the strands are parallel to one another since a systematic absence may suppress the reflection.

It is thought that individual peptides fold to form  $\beta$ -strands, which are orthogonal to the fibre. Long protofilaments are formed from  $\beta$ -sheets stacked face-to-face (Pauling & Corey, 1951), running parallel to the fibre axis. Diffraction from *ex vivo* transthyretin fibrils implies a model in which several  $\beta$ -sheets turn about a central axis (Blake & Serpell, 1996) (Figure 1). Finally the fibre itself is comprised of protofilaments, which may be twisted about one another in a helical manner.

Synthetic peptides are generally used to form fibrils owing to their greater availability and purity, compared to those extracted from tissue. Truncated peptides have also been used to grow fibrils which are straighter and more ordered, whilst maintaining morphological and chemical similarity to fibrils grown from the full length peptide (Jarvis *et al.*, 1993; Nguyen *et al.*, 1995; Serpell, 2000).

### Methods of alignment for preparing amyloid fibre diffraction specimens

Fibril alignment is important since a higher degree of orientation will result in more information being extractable from the resulting diffractogram (Figure 2a versus 2b and c). The main methods of alignment are a stretch frame, glass capillary magnetic alignment and diffraction from a film or mat (Figure 1c,d,e). The nature of the sample often determines the preferred method. If the sample contains many long fibrils, then the high viscosity will make it far more amenable to stretch frame alignment (Sunde *et al.*, 1997). In the case of small crystallites, magnetic alignment may be favoured (Inouye *et al.*, 1993; Malinchik *et al.*, 1998; Sikorski *et al.*, 2003). Here the sample is dried between the poles of a permanent 2 Tesla magnet. This large magnetic flux density orients the fibres so that they are parallel to the field lines. Alignment is due to anisotropy in diamagnetic susceptibility due to bond resonance in certain side groups (Glucksman *et al.*, 1986; Worcester, 1978; Pauling, 1979), which was first exploited by Kirschner (Inouye *et al.*, 1993) to examine fibrils formed from fragments of the Alzheimer's A $\beta$  peptide and has since been used for other peptides (Inouye and Kirschner, 1998, Sikorski *et al.*, 2003). A mat of fibrils can be used as to provide an additional texture for extra information. The substrate can be glass, Parafilm or Teflon (Fandrich & Dobson, 2002; Perutz *et al.*, 1994). This method has been used for AA amyloid fibrils (Turnell *et al.*, 1986), and poly-Q (Perutz *et al.*, 1994; Perutz *et al.*, 2002). Alternatively, a cryo-loop normally used for freezing single crystals can be dipped into the fibrillar solution and allowed to dry, resulting in a thin, flat film (Serpell and Makin, unpublished data). This avoids the requirement for the film to be carefully lifted off the substrate, which may be difficult if the fibres are short and therefore non-viscous.

### The contribution of electron diffraction to amyloid structure

Until recently, electron diffraction (ED) has been of limited benefit often only confirming the cross- $\beta$  structure, with only the 4.7 Å reflection and little else being visible (Berriman *et al.*, 2003; Perutz *et al.*, 1994) (Figure 3b). High-resolution information, which is already faint due to the intensity being spread about reciprocal space, is further reduced by the  $k$ -squared term in the Mott formula for calculating electron structure factors. Furthermore, the beam saturates the film concealing low-resolution spots. In the case of nanocrystals (Diaz-Avalos *et al.*, 2003a; 2003b), electron diffraction has proved invaluable. Single crystals can be selected for examination owing to the electron beam having a far smaller diameter than is the case with X-rays. The diffraction spots can also be widened to produce an image of the sample area being diffracted; thus allowing direct confirmation of the relationship between spot location and fibre orientation. Radiation damage is a problem; one may observe the spots fading as the beam and sample interact. There is therefore a trade-off between long exposures, which ensure weak spots are observable and a higher signal to noise ratio is achieved and short exposures, which fulfil the necessity to keep the specimen intact. Unfortunately, the measurement of structure factors in electron diffractograms is unreliable, owing to electrons interacting with

matter in a far stronger manner than X-rays, leading to multiple scattering, which is difficult to account for. The micrograph film would also need to be well calibrated to ensure the expected relationship between exposure and image intensity. These lead to electron diffraction being a potentially useful technique whilst one is aware of the potential issues. ED has proved to be useful in the study of the structure of fibrils of  $\alpha$ -synuclein (Serpell *et al.*, 2000a), nanocrystals (Makin *et al.*, unpublished), IAPP (Makin & Serpell, 2004) and other amyloid (Ferguson *et al.*, 2003). One expects the development of ED in relation to amyloid to be useful in future.

### X-ray fibre diffraction and amyloid models

X-ray fibre diffraction has demonstrated that amyloid fibrils have a common core structure, which is a series of continuous beta sheets running parallel to the fibre axis (Sunde *et al.*, 1997; Blake & Serpell, 1996). In the case of transthyretin amyloid, indexing of meridional reflections revealed a helical repeat distance of 115.5Å, commensurate with twisted  $\beta$ -sheets known to be energetically favourable (Chothia, 1973). From this work, a model was presented for the core structure of the generic amyloid fibril (Blake & Serpell, 1996, Sunde *et al.*, 1997). X-ray diffraction patterns from amyloid fibrils formed from A $\beta$ (1-40) were interpreted as arising from three to five tubular protofilaments, each composed of pairs of  $\beta$ -sheets (Malinchik *et al.*, 1998). A similar structure was concluded from amyloid fibrils formed from a range of shorter fragments of A $\beta$  (Inouye *et al.*, 1993). Further detailed discussion of these models is included in Serpell, 2000.

More recently, Sikorski *et al.* (2003) presented a detailed model of A $\beta$ (11-25) from data taken using a magnetically aligned sample. Three different diffractions patterns were obtained from orthogonal directions around the crystalline specimen suggesting a preferred orientation of the fibrils. In the fibrillar structure, A $\beta$ (11-25) forms extended  $\beta$ -strands that stack into  $\beta$ -ribbons that then slip relative to each another by the length of two amino-acid units (0.70 nm). X-ray diffraction patterns simulated using Cerius2 (Accelrys, San Diego, CA, USA) were compared with empirical data and shown to be very similar (additional details may be found in Sikorski *et al.*, 2003). Very recently, the structure of A $\beta$ (11-25) amyloid fibrils has been examined using ssNMR (Petkova *et al.*, 2004). Interestingly, it was shown that A $\beta$ (11-25) was able to form two slightly different packing arrangements at different pH. This seems to suggest that A $\beta$ (11-25) peptides have the ability to pack differently depending on environment and presumably are able to slide across one another. The fibre diffraction sample examined by us (Sikorski *et al.*, 2003) is a crystalline sample, so it may be that the environment favoured the particular packing arrangement described. The structure of A $\beta$  (31-35) has also been obtained (Bond *et al.*, 2003), though in this case powder diffraction provided much of the required information.

There has been discussion about the amount of native structure remaining - how much of the original protein unfolds before forming amyloid. Inouye *et al.* (1998) suggest a transthyretin amyloid model in which the monomer structure is retained with the  $\beta$ -sheets simply lining up in an appropriate manner, thus contradicting the unfolding suggested in Blake & Serpell's earlier model. However, in order to satisfy the cross- $\beta$  pattern, it is essential that the  $\beta$ -strands are perpendicular to the fibre

axis. In the case of the yeast prion, Ure2p it is disputed as to whether the fibres are amyloid at all (Baxa *et al.*, 2003; Bousset *et al.*, 2003), since it appears that the native structure of Ure2p (predominantly  $\alpha$ -helical) may be retained within the fibres. The fibres have the characteristic birefringence pattern and appearance under the electron microscope. Other alternative structures for amyloid have been proposed. Lazo and Downing (1998) suggest an  $\alpha$ -helical model in which protofilaments are formed from  $\beta$ -strands forming a tetrahedral shape. Perutz *et al.* (2002) have studied fibres formed from polyglutamine and concluded that amyloid fibrils are water filled nanotubes. These models are schematically similar in having  $\beta$ -strands wrapped around a core in antiparallel and parallel configurations respectively. Nevertheless, further evidence will be required if the received understanding, of the structure consisting of stacked  $\beta$ -sheets, is to be displaced, since the  $\beta$ -helical models do not appear to satisfy the cross- $\beta$  diffraction pattern (Sikorski, unpublished).

### CONCLUSION

X-ray fibre diffraction has always been an important part of the structural analysis of amyloid. Indeed, the cross- $\beta$  pattern is an intrinsic characteristic of amyloid. It has provided information unavailable by other means, on both large and small length scales. Fibre diffraction using X-rays, neutrons and electrons is now an indispensable component of the armoury of structural techniques. The papers reviewed herein have demonstrated that increased efficacy is achieved by means of a cocktail of such techniques, particularly with regard to electron microscopy. Knowledge of amyloid structure and assembly are important in our understanding of the amyloidoses. Additionally, the implications of amyloid self-assembly to the production of fibres in nano-biotechnology have yet to be understood (Scheibel *et al.*, 2003). These ensure that the application of fibre diffraction to the elucidation of amyloid structure is likely to increase in importance.

### Acknowledgements

LCS is a Wellcome Trust Research Career Development fellow, OSM is supported by an MRC studentship and the research is supported by Wellcome Trust and BBSRC funding. The authors would like to thank Dr T Stromer for helpful discussions and reading the manuscript.

### References

- [1] Alzheimer's Association (2002) Alzheimer's Disease: The Costs to U.S. Businesses in 2002 <http://www.alz.org/Media/newsreleases/archived/2002/062602ADCosts.pdf>
- [2] Antzutkin, O., Balbach, J.J., Leapman, R.D., Rizzo, N.W., Reed, J. & Tycko, R. (2000) Multiple quantum solid state NMR indicates a parallel, not anti-parallel organisation of  $\beta$ -amyloid fibrils. *Proc. Nat. Acad. Sci. USA*, **97**, 13045-13050.
- [3] Balbach, J.J., Ishii, Y., Antzutkin, O.N., Leapman, R.D., Rizzo, N.W., Dyda, F., Reed, J. and Tycko, R. (2000) Amyloid fibril formation by A $\beta$ 16-22, a seven residue fragment of the Alzheimer's  $\beta$ -amyloid peptide, and structural characterisation by *solid state NMR Biochemistry*, **39**, 13748-13759.

- [4] Baxa U., Taylor, K.L., Wall, J.S., Simon, M.N., Cheng, N., Wickner, R.B. & Steven, A.C. (2003) Architecture of Ure2p Prion Filaments. *J. Biol. Chem.*, **278**, 43717-43727.
- [5] Benzinger, T.L.S., Gregory, D.M., Burkoth, T.S., Miller-Auer, H., Lynn, D.G., Botto, R.E. and Meredith, S.C. (2000) Two-Dimensional Structure of  $\beta$ -Amyloid (10-35) Fibrils *Biochemistry*, **39**, 3491-3499.
- [6] Berriman, J., Serpell, L.C., Oberg, K.A., Fink, A.L., Goedert, M., Crowther, R.A. (2003). Tau filaments from human brain and from in vitro assembly of recombinant protein show cross-beta structure. *Proc. Natl. Acad. Sci. USA*, **100**, 9034-9038.
- [7] Blake, C. & Serpell, L. (1996) Synchrotron X-ray studies suggest that the core of the transthyretin amyloid fibril is a continuous  $\beta$ -sheet helix. *Structure*, **4**, 989-998.
- [8] Bond, J.P., Deverin, S.P., Inouye, H., El-Agnaf, O.M.A., Teeter, M.M. & Kirschner, D.A. (2003) Assemblies of Alzheimer's peptides A $\beta$  25-35 and A $\beta$  31-35: Reverse turn conformation and side chain interactions revealed by X-ray diffraction. *J. Struct. Biol.*, **141**, 156-170.
- [9] Botelho, M.G., Gralle, M., Oliveira, C.L., Torriani, I. & Ferreira S.T. (2003) Folding and stability of the extracellular domain of the human amyloid precursor protein. *J. Biol. Chem.*, **278**, 34259-34267.
- [10] Bousset, L., Thomson, N.H., Radford, S.E. & Melki, R. (2002) The yeast prion Ure2p retains its native  $\alpha$ -helical conformation upon assembly into protein fibrils in vitro. *EMBO J.*, **21**, 2903-2911.
- [11] Burkoth, T. S., Benzinger, T.L.S., Urban, V., Morgan, D.M., Gregory, D.M., Thiagarajan, P., Botto, R.E., Meredith, S.C. & Lynn, D.G. (2000) Structure of the  $\beta$ -Amyloid (10-35) Fibril. *J. Am. Chem. Soc.*, **122**, 7883-7889.
- [12] Chothia, C. (1973) Conformations of twisted  $\beta$ -sheets in proteins. *J. Mol. Biol.*, **75**, 295-302.
- [13] Cohen, A.S. (1986) General introduction and a brief history of the amyloid fibril, in Marrink, J. & Van Rijswijk, M. H. (Eds.), *Amyloidosis*, pp. 3-19, Nijhoff, Dordrecht
- [14] Diaz-Avalos R., Long, C., Fontano, E., Balbirnie, M., Grothe, R., Eisenberg, D. & Caspar, D.L.D. (2003) Cross-beta structure of an amyloid-forming peptide studied by electron nano-crystallography. *Fibre Diffraction Review*, **11**, 79-86.
- [15] Diaz-Avalos R., Long C., Fontano E., Balbirnie M., Grothe R., Eisenberg D. & Caspar D.L. (2003) Cross-beta Order and Diversity in Nanocrystals of an Amyloid-forming Peptide. *J. Mol. Biol.*, **330**, 1165-1175.
- [16] Dobson, C. (2001) The structural basis of protein folding and its links with human disease *Phil. Trans. R. Soc. Lond. B*, **366**, 133-145.
- [17] Eanes E.D. & Glenner G.G. (1968) X-ray diffraction studies on Amyloid Filaments. *J. Histochem. Cytochem.*, **16**, 673-677.
- [18] Fandrich, M. & Dobson, C.M. (2002) The behaviour of polyamino acids reveals an inverse side chain effect in amyloid structure formation. *EMBO J.*, **21**, 5682-5690.
- [19] Ferguson, N., Berriman, J., Petrovich, M., Sharpe, T.D., Finch, J.T. & Fersht, A.R. (2003) Rapid amyloid fiber formation from the fast-folding WW domain FBP28. *Proc. Natl. Acad. Sci. USA*, **100**, 9814-9819.
- [20] Fraser, P.E., Duffy, L.K., O'Malley, M.B., Nguyen, J., Inouye, H. & Kirschner, D. A. (1991) Morphology and antibody recognition of synthetic  $\beta$ -amyloid peptides *J. Neurosci. Res.*, **28**, 474-485.
- [21] Fraser, P.E., Nguyen, J.T., Chin, D.T. & Kirschner, D.A. (1992a) Effects of Sulfate ions on Alzheimer  $\beta$ /A4 peptide assemblies: implications for Amyloid fibril-proteoglycan interactions *J. Neurochem.*, **59**, 1531-1540.
- [22] Fraser, P.E., Nguyen, J.T., Surewicz, W.K., Selkoe, D.J., Podlinsky, M.B. & Kirschner, D.A. (1992b) Fibril formation by primate analogues of Alzheimer amyloid  $\beta$ -protein. *Biochemistry*, **31**, 10716-10723.
- [23] Ganesh, S. & Jayakumar R. (2003) Structural transitions involved in a novel amyloid-like beta-sheet assemblage of tripeptide derivatives. *Biopolymers*, **70**, 336-345.
- [24] Geddes, A.J., Parker, K.D., Atkins, E.D.T. & Beighton, E. (1968) "Cross-beta" conformation in proteins. *J. Mol. Biol.*, **32**, 342-358.
- [25] Glucksman, M.J., Hay, R.D. & Makowski, L. (1986) X-ray diffraction from magnetically oriented solutions of macromolecular assemblies. *Science*, **231**, 1273-1276.
- [26] Goldsbury, C.S., Cooper, G.J., Goldie, K.N., Muller, S.A., Saafi, E.L., Gruijters, W.T., Misur, M.P., Engel, A., Aebi, U. & Kistler, J. (1997) Polymorphic fibrillar assembly of human amylin. *J. Struct Biol.*, **119**, 17-27.
- [27] Goldsbury, C., Kistler, J., Aebi, U., Arvinte, T. & Cooper, G.J. (1999) Watching amyloid fibrils grow by time-lapse atomic force microscopy. *J. Mol. Biol.*, **285**, 33-39.
- [28] Inouye, H. & Kirschner, D.A. (1997) X-ray diffraction analysis of scrapie prion intermediate and folded structures in a peptide containing two putative  $\alpha$ -helices *J. Mol. Biol.*, **268**, 375-389.
- [29] Inouye, H., Fraser, P.E. & Kirschner, D.A. (1993) Structure of  $\beta$ -crystallite assemblies formed by Alzheimer  $\beta$ -amyloid protein analogues: analysis by x-ray diffraction. *Biophys. J.*, **64**, 502-519.
- [30] Inouye, H., Domingues, F.S., Damas, A.M., Saraiva, M.J., Lundgren, E., Sandgren, O. & Kirschner, D.A. (1998) Analysis of X-ray diffraction patterns from amyloid of biopsied vitreous humor and kidney of transthyretin (TTR) Met30 familial amyloidotic polyneuropathy (FAP) patients: axially arrayed TTR monomers constitute the protofilament. *Amyloid*, **5**, 163-174.
- [31] Janek, K., Behlke, J., Zipper, J., Fabian, H., Georgalis, Y., Beyermann, M., Bienert, M. & Krause, E. (1999) Water-soluble beta-sheet models which self-assemble into fibrillar structures. *Biochemistry*, **38**, 8246-8252.
- [32] Jarvis, J.A., Craik, D.J. & Wilce, M.C. (1993) X-ray diffraction studies of fibrils formed from peptide fragments of transthyretin. *Biochem. Biophys. Res. Commun.*, **192**, 991-998.
- [33] Jiménez, J.L., Guijarro, J.I., Orlova, E., Zurdo, J., Dobson, C.M., Sunde, M. & Saibil, H.R. (1999) Cryo-electron microscopy structure of an SH3 amyloid fibril and model of the molecular packing. *EMBO J.*, **18**, 815-821.
- [34] Kelly, J.W. (1996) Alternative conformations of amyloidogenic proteins govern their behaviour. *Curr. Opin. Struct. Biol.*, **6**, 11-17.
- [35] Khurana, R., Uversky, V.N., Nielsen, L. & Fink, A.L.. (2001) Is Congo red an amyloid-specific dye? *J. Biol. Chem.*, **276**, 22715-22721.
- [36] Lakdawala, A.S., Morgan, D.M., Liotta, D.C., Lynn, D.G. & Snyder, J.P. (2002) Dynamics and fluidity of amyloid fibrils: a model of fibrous protein aggregates. *J. Am. Chem. Soc.*, **124**, 15150-15151.

- [37] Lansbury Jr., P.T., Costa, P.R., Griffiths, J.M., Simon, E.J., Auger, M., Halverson, K.J., Kocisko, D.A., Hendsch, Z.S., Ashburn, T.T., Spencer, R.G., et al. (1995) Structural model for the  $\beta$ -amyloid fibril bases on interstrand alignment of an antiparallel-sheet comprising a C-terminal peptide. *Nat. Struct. Biol.*, **11**, 990-998.
- [38] Lazo, N.D. & Downing, D.T. (1998) Amyloid fibrils may be assembled from beta-helical protofibrils. *Biochemistry*, **37**, 1731-1735.
- [39] Lu, K., Jacob, J., Thiyagarajan, P., Conticello, V.P. & Lynn, D.G. (2003) Exploiting amyloid fibril lamination for nanotube self-assembly. *J. Am. Chem. Soc.*, **125**, 6391-6393.
- [40] Makin, O.S., Serpell, L.C. (2004) Structural characterisation of islet amyloid polypeptide fibrils. *J. Mol. Biol.*, **335**, 1279-1288
- [41] Malinchik, S.B., Inoue, H., Szumowski, K.E. & Kirchner D.A. (1998) Structural analysis of Alzheimer's  $\beta$ (1-40) Amyloid: protofilament assembly of tubular fibrils. *Biophys. J.*, **74**, 537-545.
- [42] Murphy, R.M. (1997) Static and dynamic light scattering of biological macromolecules: what can we learn? *Curr. Opin. Biotechnol.*, **8**, 25-30.
- [43] Nguyen, J.T., Inouye, H., Baldwin, M.A., Fletterick R.J., Cohen F.E., Prusiner, S.B. & Kirschner, D.A. (1995) X-ray diffraction of scrapie prion rods and PrP peptides. *J. Mol. Biol.*, **252**, 412-422.
- [44] Pauling, L. (1979) Diamagnetic Anisotropy of the Peptide Group. *Proc. Natl. Acad. Sci. USA*, **76**, 2293-2294.
- [45] Pauling, L. & Corey, R. B. (1951) The pleated sheet, a new layer configuration of polypeptide chains. *Proc. Natl. Acad. Sci. USA*, **37**, 251-256.
- [46] Perutz, M.F., Johnson, T., Suzuki, M. & Finch, J.T. (1994) Glutamine repeats as polar zippers: their possible role in inherited neurodegenerative diseases. *Proc. Natl. Acad. Sci. USA*, **91**, 5355-5358.
- [47] Perutz, M.F., Finch, J.T., Berriman, J. & Lesk, A. (2002) Amyloid fibers are water-filled nanotubes. *Proc. Natl. Acad. Sci. USA*, **99**, 5591-5595.
- [48] Petkova, A. T., Buntkowsky, G., Dyda, F., Leapman, R. D., Yau, W. M. & Tycko, R. (2004). Solid state NMR reveals a pH-dependent antiparallel beta-sheet registry in fibrils formed by a beta-amyloid peptide. *J. Mol. Biol.*, **335**, 247-260.
- [49] Rochet, J.C. & Lansbury, P.T. (2000) Amyloid fibrillogenesis: themes and variations. *Curr. Opin. Struct. Biol.*, **10**, 60-68.
- [50] Serpell, L.C. (2000) Alzheimer's amyloid fibrils: structure and assembly. *Biochim. Biophys. Acta.*, **1502**, 16-30.
- [51] Serpell, L.C. & Smith J.M. (2002) Direct visualisation of the  $\beta$ -sheet structure of synthetic Alzheimer's amyloid. *J. Mol. Biol.*, **299**, 225-231.
- [52] Serpell, L.C., Berriman, J., Jakes, R., Goedert, M. & Crowther, R.A. (2000a) Fiber diffraction of synthetic alpha-synuclein filaments shows amyloid-like cross-beta conformation. *Proc. Natl. Acad. Sci. USA*, **97**, 4897-4902.
- [53] Serpell, L., Sunde, M., Benson M.D., Tennent G.A., Pepys, M.B. & Fraser P.E. (2000b) The protofilament substructure of Amyloid fibrils. *J. Mol. Biol.*, **300**, 1033-1039.
- [54] Scheibel, T., Parthasarathy, R., Sawicki, G., Lin, X.M., Jaeger, H. & Lindquist, S.L. (2003) Conducting nanowires built by controlled self-assembly of amyloid fibers and selective metal deposition. *Proc. Natl. Acad. Sci. USA*, **100**, 4527-4532.
- [55] Sikorski, P., Atkins, E.D., Serpell, L.C. (2003) Structure and texture of fibrous crystals formed by Alzheimer's abeta(11-25) peptide fragment. *Structure*, **11**, 915-926.
- [56] Sipe, J.D., Cohen, A.S. (2000) Review: history of the amyloid fibril. *J. Struct. Biol.*, **130**, 88-98.
- [57] Shivji, A.P., Brown, F., Davies, M.C., Jennings, K.H., Roberts, C.J., Tendler, S.J., Wilkinson, M.J. & Williams, P.M. (1995) Scanning tunnelling microscopy studies of beta-amyloid fibril structure and assembly. *FEBS Lett.*, **28**, 25-28.
- [58] Stolz, M., Stoffler, D., Aebi, U. & Goldsbury, C. (2000) Monitoring biomolecular interactions by time-lapse atomic force microscopy. *J. Struct. Biol.*, **131**, 171-180.
- [59] Sunde, M., Serpell, L.C., Bartlem, M., Fraser, P.E., Pepys, M.B. and Blake, C.C.F. (1997) The common core structure of amyloid fibrils by synchrotron X-ray radiation. *J. Mol. Biol.*, **273**, 729-739.
- [60] Turnell, W., Sarra, R., Baum, J.O., Caspi, D., Baltz, M.L. & Pepys, M.B. (1986) X-ray scattering and diffraction by wet gels of AA amyloid fibrils. *Mol. Biol. Med.*, **3**, 409-424.
- [61] Tycko R. (2001) Solid-state nuclear magnetic resonance techniques for structural studies of amyloid fibrils. *Methods in Enzymol.*, **339**, 390-413.
- [62] Wang, Z., Zhou, C., Wang, C., Wan, L., Fang, X. and Bai, C. (2003) AFM and STM study of beta-amyloid aggregation on graphite. *Ultramicroscopy*, **97**, 73-79.
- [63] Worcester D. L. (1978) Structural Origins of Diamagnetic Anisotropy in Proteins. *Proc. Natl. Acad. Sci. USA*, **75**, 5475-5477.
- [64] Yonezawa, Y., Tanaka, S., Kubota, T., Wakabayashi, K., Yutani, K. & Fujiwara, S. (2002) An Insight into the pathway of the amyloid fibril formation of hen egg white lysozyme obtained from a small-angle X-ray and neutron scattering study. *J. Mol. Biol.*, **323**, 237-251.
- [65] Yong, W., Lomakin, A., Kirkitadze, M.D., Teplow, D.B., Chen, S.H. & Benedek, G.B. (2002) Structure determination of micelle-like intermediates in amyloid beta-protein fibril assembly by using small angle neutron scattering. *Proc. Natl. Acad. Sci. USA*, **99**, 150-154.

## Original Articles

### Combined microdrop generation and microdiffraction for biopolymer hydration experiments

C. Riekkel, M. Burghammer, D. Flot and M. Rössle

European Synchrotron Radiation Facility, B.P. 220, F-38043 Grenoble Cedex, France

Received 5th January 2004; accepted in revised form 16th March 2004

#### ABSTRACT

*The article discusses instrumentation developed at the ESRF ID13 beamline for the study of rapid biopolymer hydration reactions. An introduction into currently available optics and sample environments is provided and the use of a 0.7  $\mu\text{m}$  beam is demonstrated for SAXS/WAXS patterns recorded from a starch granule. An inkjet system is described, which allows hydration of biopolymers locally with about 50  $\mu\text{m}$  diameter water droplets. The application of this system to  $\beta$ -chitin hydration is described and an outlook on future possibilities, including rapid droplet mixing reactions, is given.*

#### Introduction

The microstructural properties of biopolymers depend often on their water content and it is therefore important to control the hydration level in X-ray scattering experiments. The high flux density of synchrotron radiation (SR) microbeam experiments [1] is particularly challenging for in-situ experiments on hydrated biopolymers due to the risk of secondary radiation damage as for protein crystals [2]. Thus the crystallinity in hydrated potato starch granules was found to disappear at room temperature for X-ray doses above 5 photons  $\text{nm}^{-3}$ , which limited data collection times in SR-microdiffraction experiments to a few seconds per pattern [3]. An experimental challenge is therefore to conceive techniques, which allow investigating the local hydration kinetics of a biopolymeric sample - such as a starch granule - by SR-microdiffraction. We are currently exploring inkjet-systems [4] for such applications at the ESRF microfocuss beamline (ID13).

Microdrops (or droplets) of water or other liquids can be generated by various inkjet-systems [4]. The minimum droplet size can reach the  $\mu\text{m}$ -scale. Water droplets of 30-50  $\mu\text{m}$  diameters can be easily produced by drop-on-demand systems [4]. For such systems, droplets are not heated during ejection and can carry proteins or even biological objects without damage. A useful property of water droplets is the domination of the surface energy ( $E_{\text{sur}}$ ) with respect to kinetic energy ( $E_{\text{kin}}$ ) for droplet diameters of about 100  $\mu\text{m}$  or smaller: (Fig.1.A)

$$E_{\text{kin}}/E_{\text{sur}} = (1/6 \rho/\sigma)v^2 r \quad (1)$$

with the parameters: r: radius, v: velocity,  $\rho$ : density,  $\sigma$ : surface tension. For droplets with  $r=25 \mu\text{m}$ ,  $\rho=1 \text{ g/cm}^3$ ,  $\sigma=0.073 \text{ N/m}$  and  $v=2.5 \text{ m/sec}$  a value of  $E_{\text{kin}}/E_{\text{sur}} \approx 0.36$  is calculated. This implies that the droplets will not splash when hitting a target. The surface properties of the fibre will not play a role in this impact phase [5]. The high position definition of droplets is shown in Fig.1.B where a single droplet was dispensed on a 12 $\mu\text{m}$  diameter Kevlar fibre. The hydrophobic fibre surface

results in this case in a high contact angle and the water droplet will disappear upon evaporation. For more hydrophilic surfaces spreading of the droplet will occur depending on the contact angle [5]. In addition volume hydration as observed for  $\beta$ -chitin is possible [6], which could be used for locally hydrating a fibre.

The aim of the present report is to give an update on the current ID13 beamline instrumentation, the technical aspects of microdrop experiments and future experimental possibilities. As a practical case, the hydration of the polysaccharide  $\beta$ -chitin will be discussed.

#### Experimental methods

Synchrotron radiation set-ups used at the ID13 beamline are located in two experimental hutches: EH-1/EH-2 [7]. EH-1 houses a microgoniometer, which is used for microcrystallography and fibre diffraction [8]. The minimum beam size is currently 5  $\mu\text{m}$  for a 0.2 mrad divergence based on a condensing ellipsoidal mirror and a defining aperture. EH-2 houses a scanning small-angle/wide-angle X-ray scattering (SAXS/WAXS) set-up [7, 9]. A beam size of 5  $\mu\text{m}$  for a 0.2 mrad divergence is obtained by a combination of Kirkpatrick-Baez (KB) mirror [7, 10] and defining/guard apertures. The typically available SAXS-resolution is shown in Fig.2.A for a pair of dry rats tail collagen fibres held at right angles. A high demagnification KB-mirror system [11] has been recently commissioned for sub- $\mu\text{m}$  beam applications. The free space available between the optics and the sample is  $\approx 16\text{mm}$ , which provides more space for sample environments as compared to glass capillary optics [1] and allows to introduce guard apertures for optimizing SAXS signals [9]. A beam size of 0.7 $\mu\text{m}$  for a divergence of  $\approx 0.3\text{mrad}$  has been reached with this set-up. The SAXS-resolution currently available is shown in Fig. 2.B for a collagen fibre. This set-up will provide new opportunities for soft condensed matter and biopolymer experiments. Thus Fig. 3 shows a scan across an about 70  $\mu\text{m}$  diameter hydrated potato starch granule with 5  $\mu\text{m}$  step increment and 100 ms exposure time using a MAR CCD detector (see below). The grain was kept in water filled

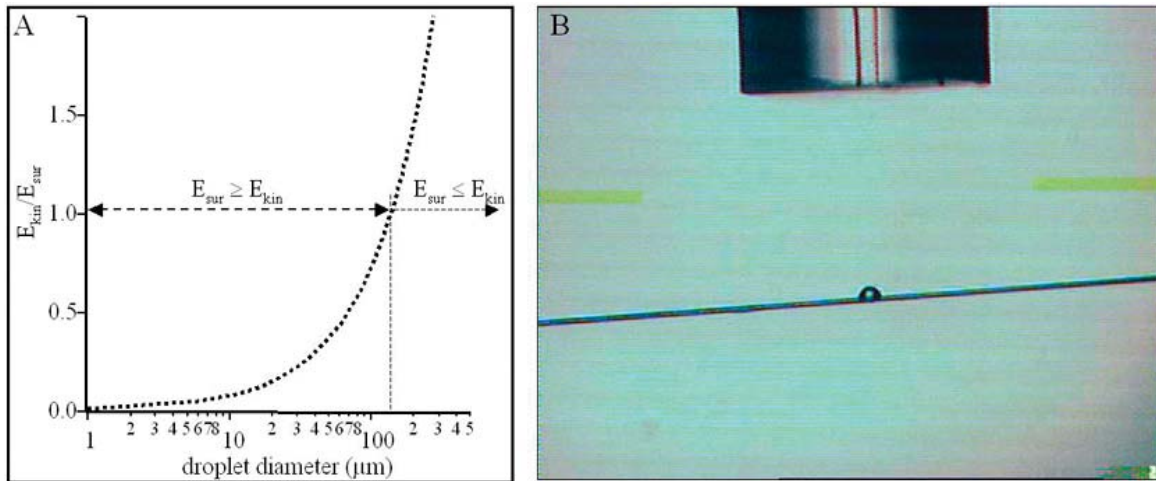


Figure 1. A: variation of ratio of surface energy ( $E_{sur}$ ) and kinetic energy ( $E_{kin}$ ) as a function of the size of a spherical water droplet; B: a 50  $\mu\text{m}$  diameter water droplet has been ejected from the glass capillary head of the dispensing system and has remained attached to the surface of a 12  $\mu\text{m}$  diameter Kevlar fibre.

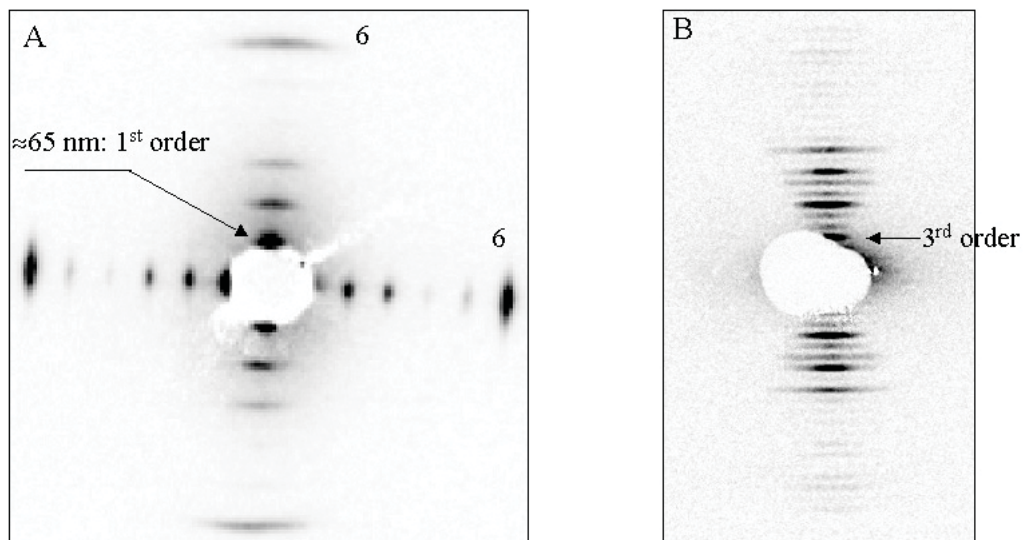


Figure 2. A: SAXS pattern of a cross of dry rats tail collagen fibres recorded with 5  $\mu\text{m}$  beam; B: SAXS pattern of same collagen fibre recorded with a 0.7  $\mu\text{m}$  beam.

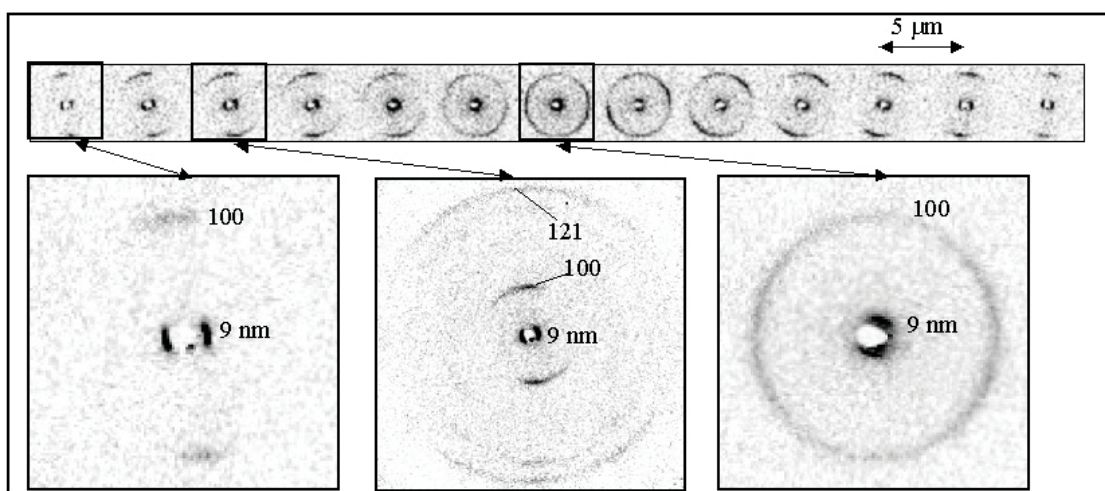


Figure 3. SAXS/WAXS patterns recorded with a 0.7  $\mu\text{m}$  beam for a step-scan with 5  $\mu\text{m}$  increment across a hydrated potato starch granule. The upper display range of the patterns in the sequence is limited to the 100 reflection. Selected patterns are shown in more detail.

borosilicate capillary. The patterns correspond to the starch B structure [12]. The combined SAXS/WAXS experiment shows for the first time for a single granule the coexistence of the meridional ( $d \approx 9$  nm) and the equatorial ( $100: d = 1.5_5$  nm) reflections [13-15]. The meridional reflection is due to the lamellar morphology of the semicrystalline material [16, 17] while the equatorial reflection is due to the incorporation of water into the lattice sites of the starch structure [12, 18, 19].

Experiments on biopolymers in EH-2 are usually performed with a monochromatic beam of  $\lambda = 0.097$  nm, which is close to the optimum flux of an in-vacuum undulator with 18 mm period [7, 10]. Diffraction patterns reported below have been recorded using a MAR-CCD (2Kx2K; 16 bit readout). By binning to 512x512 pixels the readout time per frame can be reduced to 3.5 sec. The set-up is shown schematically in Fig. 4.

The microdrop generator is based on a glass capillary mounted concentrically in a piezoelectric actuator. (Microdrop, Norderstedt, Germany). This system has been used until now at the microgoniometer [8] but is in principle portable. The droplet diameter is defined by the capillary exit to about 50  $\mu$ m. A droplet frequency of a few Hz allows the maintenance of a constant liquid supply at the sample position. The control unit of the system is triggered by a TTL signal from a VME frequency generator board. Software control is possible through a SPEC interface (Certified Scientific Software). The droplet can be visualized by stroboscopic illumination triggered by the microdrop electronics. (Fig. 4)

## Applications and perspectives

### $\beta$ -Chitin

The monoclinic  $\beta$ -chitin structure is composed of  $\beta$ -chitin microfibrils, packed parallel into flat ribbons, which form sheets by hydrogen-bonding (Fig.5.A) [20, 21]. Water can be intercalated between these sheets to form a monohydrate and a dihydrate phases, which can be reversibly transformed [22]. The intercalation increases basically only the size of the b-axis.

The  $\beta$ -chitin material used came from *Birsteinia* tubes, which are the habitat of the deep-sea worm *Pogonophora* (Fig. 5.B,C). Flat ribbons of parallel chitin microfibrils, which are embedded in a protein matrix, form the tube wall. Dry tube fragments were mounted on glass tips, glued to standard crystallography sample holders and transferred to the microgoniometer. A 100 ms diffraction pattern shows a weak fibre texture (Fig. 5.D) in agreement with the fibrillar morphology (Fig. 5.C).

For the hydration reaction water droplets of 50  $\mu$ m diameter (=65 pl) were dispensed with a frequency of 10 droplets per second. Short exposure time (100 msec) and changing the probing position of the 5  $\mu$ m beam by 8  $\mu$ m steps in a systematic way, allowed reduction of secondary radiation damage. A time sequence of 1D-diffraction patterns is shown in Fig. 6 [6]. The reflection positions show that the anhydrous phase is transformed into the dihydrate phase via an intermediary diffuse monohydrate phase. In contrast to the steady state analysis [23], the kinetic data suggest that the monohydrate phase is a highly disordered nucleation phase for the dihydrate phase. One should also note that the total water

consumption is only about 100 nl, which is very useful when working with precious (e.g. protein containing) solutions.

## Perspectives

Faster processes could be investigated provided that the onset of hydration can be better defined. Thus for a droplet with 2 m/sec speed the flight time from the microdrop capillary exit to the -say- 200  $\mu$ m distant sample surface is only 0.1 msec. By synchronizing the droplet ejection with the data acquisition system one could therefore reach ms- or sub-ms time-scales. Instead of solid/liquid reactions one could also investigate liquid/liquid reactions involving conformational changes in solution (e.g. proteins) or nucleation/precipitation reactions. Fast conformational changes have been investigated on the ms-scale with microfluidic devices using a lamellar flow geometry [24-26] while crossed-droplet experiments would correspond to turbulent mixing processes. For such applications the triggering pulse from the microdrop electronics has to be synchronized with the data acquisition system in order to stroboscopically observe droplets at a selected position after ejection from the capillary nozzle (Fig. 7). This is possible for the ID13 *Frelon* CCD-camera (current parameters: 2Kx2K pixels, 14 bit readout, readout frequency: 10 Hz), which has an image intensifier stage based on a *Proxitronic* microchannel plate (MCP) (Fig. 4). The MCP can be operated in a triggered gated mode with 100 ns minimum gating time [28]. Mixing liquids by continuous stream methods are further possibilities, which have not been explored until now [4].

## Acknowledgements

The authors wish to thank H. Chanzy, CERMAV-Grenoble who kindly provided the  $\beta$ -chitin material. I. Snigireva (ESRF) recorded the SEM pictures. H. Gonzalez, L. Lardiere, J. Meyer and C. Ponchut provided technical support.

## References

- [1] Riekkel, C. (2000) New avenues in X-ray microbeam experiments. *Rep. Prog. Phys.*, **63**, 233-262.
- [2] Teng, T. and Moffat, K. (2000) Primary radiation damage of protein crystals by intense synchrotron X-ray beam. *J. Synchrotron Rad.*, **7**, 313-317.
- [3] Buléon, A., Pontoire, B., Riekkel, C., Chanzy, H., Helbert, W. and Vuong, R. (1997) Crystalline Ultrastructure of starch granules revealed by synchrotron radiation microdiffraction mapping. *Macromolecules*, **30**, 3952-3954.
- [4] Lee, E.R. (2003) in *Microdrop Generation*. Nano- and Microscience, Engineering, Technology, and Medicine Series, S.E. Lyshevski, Editor, Boca Raton: CRC Press.
- [5] Maier, C., a.d. Wiesche, S., and Hofer, E.P. (2000) Impact of Microdrops on Solid Surfaces for DNA-Synthesis. in *2000 International Conference on Modeling and Simulation of Microsystems*. Nano Science & Technology Institute, **3**, 586-589.
- [6] Rössle, M., Flot, D., Engel, J., Riekkel, C. and Chanzy, H. (2003) Fast intra-crystalline hydration of  $\beta$ -chitin revealed by a combined microdrop generation and on-line synchrotron radiation microdiffraction. *Biomacromolecules*, **4**, 981-986.
- [7] Riekkel, C. (2002) Current limits of X-ray microdiffraction in soft condensed matter experiments. *Fibre Diffraction Review*, **10**, 11-18.

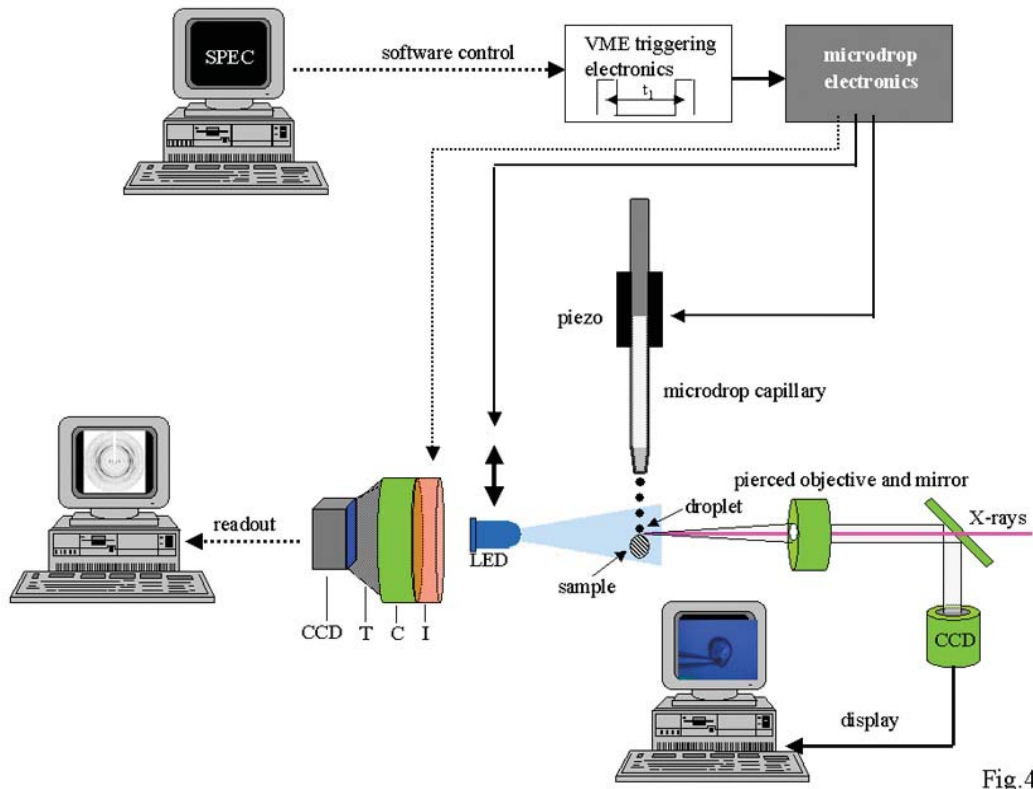


Fig.4

Figure 4. Schematic design of data acquisition system used for microdrop experiments. The microdrop electronics is controlled through a VME board by a UNIX workstation with SPEC software. The triggering signal from the microdrop electronics triggers the microdrop-piezo and the LED for stroboscopic illumination. The detector is composed of a converter screen (C), a fibre-optics taper (T) and a CCD. For special applications, an image intensifier stage with converter screen (I) is coupled with a CCD. The trigger signal from the microdrop electronics triggers the intensifier stroboscopically. The sample observation system corresponds to the microgoniometer [8].

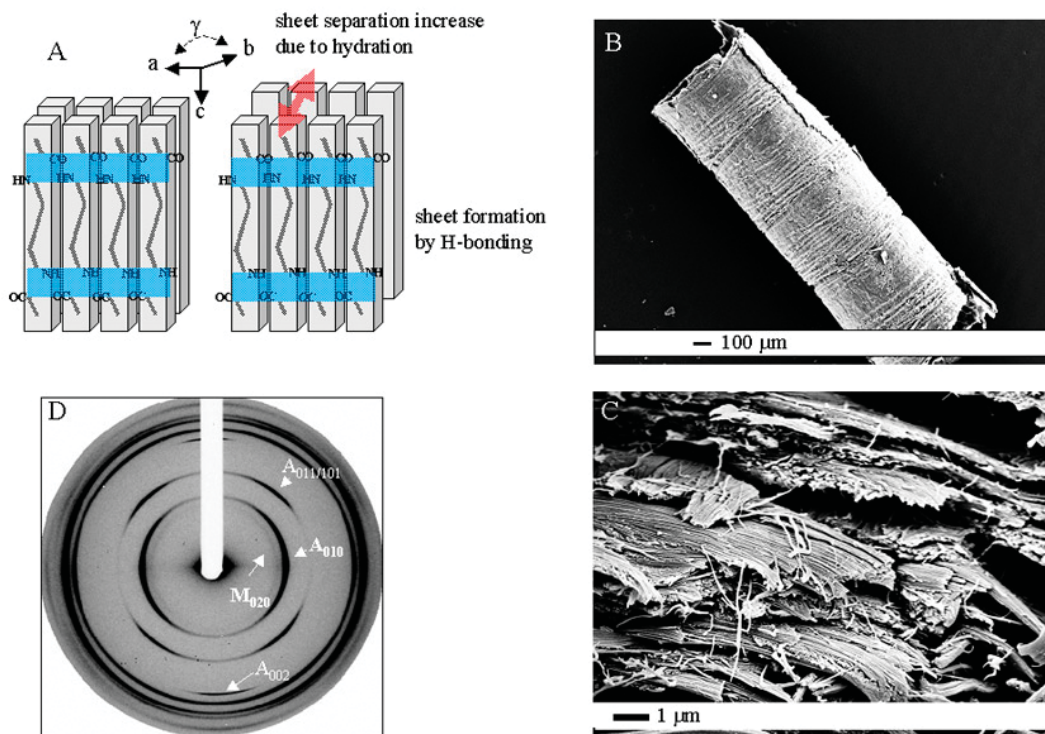


Figure 5. A: schematic structure of monoclinic  $\beta$ -chitin: P21:  $a=0.485$ ,  $b=0.926$ ,  $c=1.038$ ,  $\gamma=97.50$  [20]. The polymeric chains are depicted as slabs, which form sheets through hydrogen-bonding interactions. Hydration increases the  $b$ -axis via the sheet-separation; B: scanning electron microscopy image (SEM) of dry *Birsteinia* tube; C: higher resolution SEM image of the tube wall; D: diffraction pattern from the tube wall recorded in 100 ms using a  $5 \mu\text{m}$  beam. The pattern shows principally reflections of anhydrous  $\beta$ -chitin (A) and a weak fraction of monohydrate phase (M).

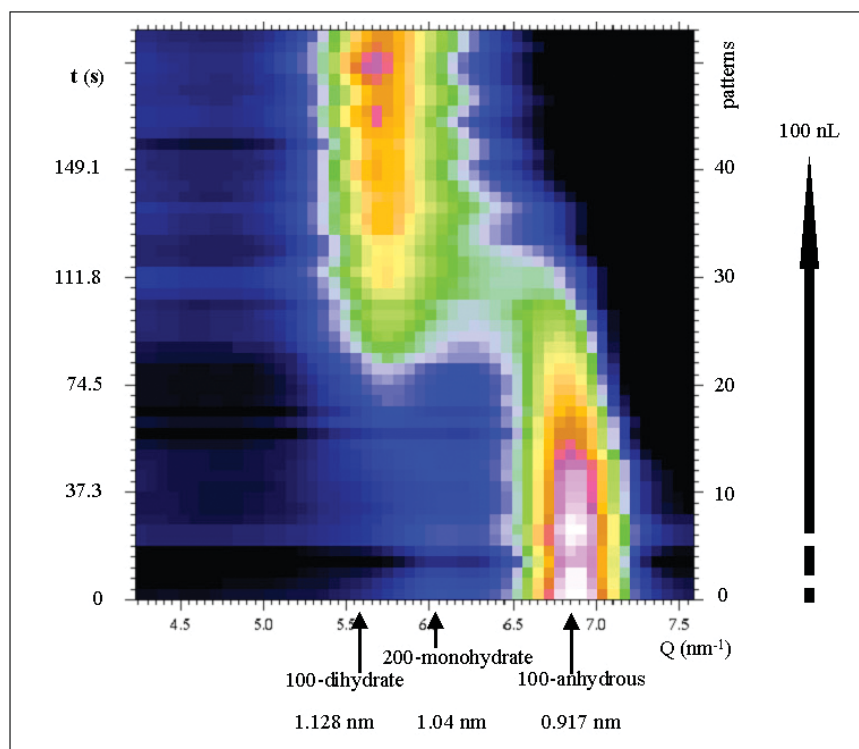


Figure 6. Variation of 1D-diffraction patterns during  $\beta$ -chitin hydration. The reported reflection positions of  $0k0$  reflections corresponding to the layer-separation of  $\beta$ -chitin [20, 22], monohydrate[20] and dihydrate[27] phases have been indicated (adapted from Rössle *et al.*, [6]).

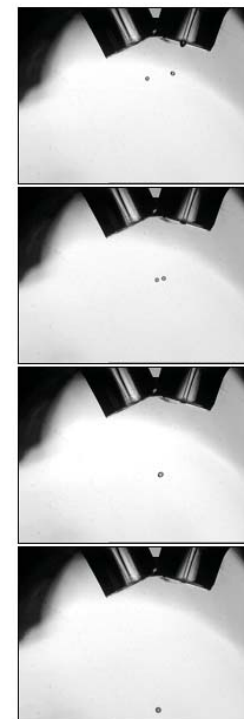


Figure 7. Crossed droplet experiment based on two microdrop capillary heads. The stroboscopic images show the ejection of two droplets and their fusion into a single droplet.

[8] Riekkel, C. (2003) Recent developments in microdiffraction on protein crystals. *J. Synchr. Rad.*, **11**, 4-6.  
 [9] Riekkel, C., Burghammer, M. and Müller, M. (2000) Microbeam small-angle scattering experiments and their combination with microdiffraction. *J. Appl. Cryst.*, **33**, 421-423.  
 [10] Riekkel, C. and Vincze, L. (2003) Status and perspectives of capillary optics at a third-generation synchrotron radiation source. *X-ray spectrometry*, **32**, 208-214.  
 [11] Hignette, O., Rostaing, G., Cloetens, P., Rommeveaux, A., Ludwig, W. and Freund, A. (2001) Submicron focusing of hard X-rays with reflecting surfaces at the ESRF. in *SPIE Conference Proceedings 4499*. I. McNulty, Editor, San Diego, 105-116.  
 [12] Sarko, A. and Wu, H.C.H. (1978) The crystal structure of A,B and C polymorphs of amylose and starch. *Starch/Staerke*, **30**, 73-78.  
 [13] Buléon, A., Colonna, P., Planchot, V. and Ball, S. (1998) Starch granules: structure and biosynthesis. *Int. J. Biol. Macrom.*, **23**, 85-112.  
 [14] Waigh, T.A., Donald, A.M., Heidelbach, F., Riekkel, C. and Gidley, M.J. (1999) Analysis of the native structure of starch granules with small-angle X-ray microfocus scattering. *Biopolymers*, **49**, 91-105.  
 [15] Waigh, T.A., Hopkinson, I., Donald, A.M., Butler, M., Heidelbach, F. and Riekkel, C. (1997) Analysis of the native structure of starch granules with X-ray microfocus diffraction. *Macromolecules*, **30**, 3813-3812.  
 [16] Oostergetel, G.T., and van Bruggen, E.F.J. (1989) On the Origin of a Low Angle Spacing in Starch. *Starch/Staerke*, **41**, 331-335.  
 [17] Jenkins, P.J., Cameron, R.E. and Donald, A.M. (1993) A universal feature in the study of starch granules from different botanical sources. *Starch/Staerke*, **45**, 417-420.

[18] Buléon, A., Bizot, H., Delage, M.M., and Multon, J.L. (1982) Evolution of crystallinity and specific gravity of potato starch versus ad- and desorption. *Starch/Staerke*, **34**, 361-366.  
 [19] Imberty, A., Buléon, A., Trans, V., and Pérez, S. (1991) Recent advances in knowledge of starch structure. *Starch/Staerke*, **43**, 375-384.  
 [20] Blackwell, J. (1969) Structure of  $\beta$ -chitin or parallel chain systems of poly- $\beta$ -(1-4)-N-acetyl-D-glucosamine. *Biopolymers*, **7**, 281-298.  
 [21] Gardner, H.H. and Blackwell, J. (1975) Refinement of the structure of  $\beta$ -chitin. *Biopolymers*, **14**, 1581-1595.  
 [22] Saito, Y., Okano, T., Gail, F., Chanzy, H. and Puteaux, J.L. (2000) Structural data on intra-crystalline swelling of  $\beta$ -chitin. *Int. J. of Biol. Macrom.*, **28**, 81-88.  
 [23] Saito, Y., Kumagai, H., Wada, M. and Kuga, S. (2002) Thermally reversible hydration of  $\beta$ -chitin. *Bio-macromolecules*, **3**, 407-410.  
 [24] Pollack, L., Tate, M.W., Darnton, N.C., Knight, J.B., Gruner, S.M., Eaton, W.A. and Austin, R.H. (1999) Compactness of the denatured state of a fast-folding protein measured by submillisecond small-angle x-ray scattering. *Proc. Natl. Acad. Sci. USA*, **96**, 10115-10117.  
 [25] Pollack, L., Tate, M.W., Finnefrock, A.C., Kalidas, C., Trotter, S., Darnton, N.C., Lurio, L., Austin, R.H., Batt, C.A., Gruner, S.M. and Mochrie, S.G.J. (2001) Time resolved collapse of a folding protein observed with small angle X-ray scattering. *PRL*, **86**, 4962-4965.  
 [26] Knight, J.B., Vishwanath, A., Brody, J.P. and Austin, R.H. (1998) Hydrodynamic focusing on a silicon chip: Mixing Nanoliters in Microseconds. *PRL*, **80**, 3863-3866.  
 [27] Saito, Y., Okano, T., Gaill, J.L. and Chanzy, H. (1998) in *Advances in Chitin Science*, A. Domard, G.A.F. Roberts, and K.M. Varum, Editors Jacques Andre Publ.: Lyon, 507.  
 [28] web page: [www.proxitronic.de](http://www.proxitronic.de).

## SANS from Surfactant-Treated Nylon Fibres

S.M. King<sup>1</sup>, D.G. Bucknall<sup>2</sup>, and R.K. Heenan<sup>1</sup>

[1] Large Scale Structures Group, ISIS Facility, Rutherford Appleton Laboratory, Chilton, OX11 0QX, UK

[2] Department of Materials, University of Oxford, Parks Road, Oxford, OX1 3PH, UK

Received 9th December 2003; accepted in revised form 16th March 2004

### ABSTRACT

*We report preliminary results from a Small Angle Neutron Scattering (SANS) study of nylon rope fibres treated with environmental contaminants of the type that the fibres may experience in everyday use.*

### Introduction

Modern high performance ropes are no longer made from siseal or hemp but from synthetic polymers such as nylon-6 (e.g. Perlon®, Ultramid B®, Zytel PA®, and Akulon®), nylon-6/6, polyesters, polypropylene, high-modulus polyethylene (e.g. Dyneema® or Spectra®), aramids (e.g. Twaron® or Kevlar®), and more recently even liquid crystalline polymers (e.g. Vectran®).

Another major difference is in the construction of the rope. Natural fibre ropes have traditionally been hawserlaid (or plaited), but modern synthetic fibre ropes have a kernmantel construction in which a core bundle (the "kern") of coiled yarns is encased in a woven outer sheath (the "mantle"), free to slip against the core (Figure 1).

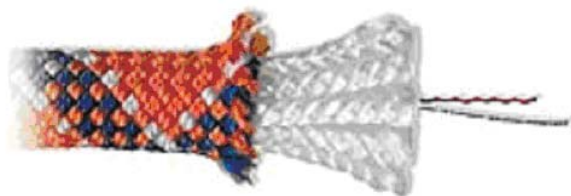


**Figure 1.** The internal construction of a modern synthetic rope. © Edelrid GmbH. For scale the diameter of the sheath is about 10mm. On the right are marker and tracer threads. In this rope the sheath houses 14 strands, each coiled from 3 yarns. Each yarn contains many single fibre filaments.

The actual type of fibre and the degree of coiling and arrangement (plaited together or not) of the core yarns determines the energy absorption capability of the rope (through the degree of extension under load) and thus to a large extent determines the mechanical properties as well. Ropes that extend more are called "dynamic" or "climbing" ropes, and those that extend less are called "static", "caving" or "abseil" ropes. These two types of rope are used in very different situations. Indeed, if a person were to shock load a static rope (e.g. as might happen in a fall) it would very likely prove fatal.

In kernmantel ropes the load handling capability is also partitioned between the core and the sheath. Some manufacturers also offer combination ropes in which the core

and sheath are different polymer fibres. This allows the performance of the rope to be matched to particular applications.

Whilst the condition of the sheath is clearly easy to establish, the same is not true of the core fibres. Contemporary methods of rope testing are reliant on destructive mechanical tests (and it has been said that the interpretation of some of the data often leave a great deal to be desired).

### Background

One of the major problems with synthetic fibre ropes is the degree to which environmental factors affect the chemical stability of the fibres. Nylons, for example, are degraded by UV radiation (e.g. sunlight), and are chemically attacked by acids (such as might leak from a miner's or cavers lead-acid battery). The mechanical test data even indicate that water affects the physical properties of the fibres (Figure 2). Soiled ropes present

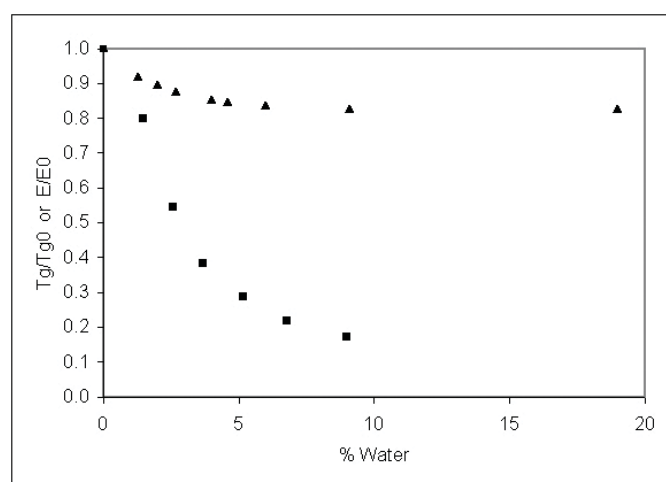


**Figure 2.** The relative variation of the glass transition temperature  $T_g$  (▲) and Young's modulus  $E$  (■) of nylon-6 with the degree of hydration. Data taken from References [1], [2] & [3].

another worry, that of how best to clean them. Even though the fibres are essentially the same as those used in textile manufacture, there is conflicting evidence about the wisdom of

using commercial detergent formulations and fabric conditioners on synthetic fibre ropes.

Tests conducted in a study by Smith [4] indicate that treatment with concentrated fabric conditioner reduced the strength (breaking load) of new rope in dynamic tests. Frank [5] showed that certain ropes treated with dilute conditioner (as per the manufacturer's recommendations) were actually stronger than the same rope without conditioning, after ageing and wear. Frank proposed that the likely mechanism at work explaining these results was that the fibre lubricants present in new rope are lost with age, allowing the fibres to cut one another. The addition of fabric conditioner then replaces some of the lubricants, but excess quantities effectively leave the rope fibres wet, with a corresponding loss in strength (as depicted in Figure 2).

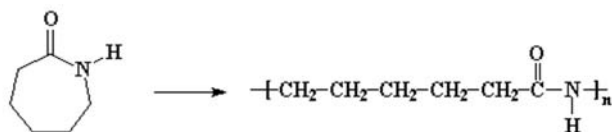
With this mechanism in mind, a further argument for treatment with fabric conditioner would be its effect on the "Hookean spring constant" of the rope. Since the spring constant would be determined by both the properties of the nylon fibre and the weave, it is likely that conditioner will offset premature stiffening due to the loss of internal lubricants.

Given that ropes actually have a significant part to play in modern life (and life styles) - for example, the now infamous Millennium Dome in London was "roofed" by a team of Rope Access Technicians, and each year hundreds of thousands of people worldwide trust their lives to the integrity of their ropes whilst climbing and potholing - there is clearly a need for a more rigorous scientific understanding of some of these phenomena.

There might also be considerable interest from rope manufacturers and users alike if a non- or less-destructive rope-testing regimen could be devised.

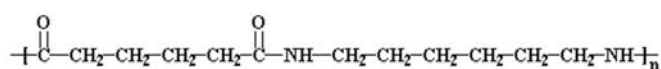
## Nylons

Nylon-6 is made by a ring opening polymerisation of  $\epsilon$ -caprolactam (1-aza-2-cycloheptanone):



The polymer is therefore also known as polycaprolactam, polyamide-6 (PA-6) or poly[imino(1-oxo-1,6-hexanediy)]].

Note that this is a very different polymer to nylon-6/6 (PA-66), patented by Dupont in the 1940's and often made in school chemistry lessons, which has become synonymous with the colloquial term *nylon*. PA-66, made by condensation polymerisation of adipic acid (hexanedioic acid) and hexamethylene diamine (1,6-hexanediamine), is:



A comparison of some physical properties of nylon-6 and nylon-6/6 are given in Table 1.

Property	Nylon 6	Nylon 6/6
Density (g/cm <sup>3</sup> )	1.12 - 1.14	1.09 - 1.14
T <sub>glass</sub> (°C)	47 - 57	35 - 78
T <sub>softening</sub> (°C)	200	243
T <sub>melting</sub> (°C)	210 - 223	255 - 280
Yield stress (MPa)	40 - 90	60 - 98
Yield strain (%)	16 - 7	18 - 4.5
Elongation (%)	260 - 70	250 - 46
Tensile modulus (MPa)	1300 - 3500	1700 - 3300
Water absorption (%)	10	8.5

**Table 1. Some physical properties of nylon-6 and nylon-6/6. Where a range is given for mechanical data, the former figure refers to 50% Relative Humidity and the latter to the dry state. Data are predominantly taken from the Polymer Data Handbook, Reference [6].**

Fibres are formed from the polymer in a two-step process involving melt-spinning and drawing. It is the drawing (though a 100  $\mu\text{m}$  orifice at perhaps 100  $\text{ms}^{-1}$ ) that imparts molecular orientation and modifies the crystallinity of the fibres [7].

The crystallographic structure and morphology of nylon-6 have been extensively studied. No fewer than *four* monoclinic crystal phases (denoted  $\alpha$ ,  $\alpha'$ ,  $\beta$ , and  $\gamma$ ) have been reported [8, 9, 10, 11]. The  $\alpha'$ -phase is a high-temperature phase, the existence of which has been taken as evidence of a Brill transition in nylon-6. There is also evidence of a fifth, triclinic, phase (denoted  $\lambda$ ) but this has so far only been observed in nylon-6 oligomers [12, 13]. In the thermodynamically stable  $\alpha$  phase and in the  $\beta$  phase, hydrogen bonds form between neighbouring, all-trans ("ribbon-like"), *antiparallel* chains. The chains are directed along the *c*-axis and the hydrogen bonds parallel to the *a*-axis. This gives rise to flat sheets in the *ac*-plane. In the  $\alpha$ -phase adjacent sheets are separated by a repeat distance of  $\Delta b = 1.724$  nm and interdigitated ("sheared") parallel to the *a*-axis by  $\Delta c \leq 0.21$  nm (perhaps around 0.14 nm). In the  $\gamma$ -phase sheets of hydrogen-bonded chains are also present but with several notable differences. The secondary amide groups are twisted out of the *ac*-plane by  $66^\circ$  (giving the  $\gamma$ -phase a "twisted-helical" conformation) and this allows hydrogen bonding to take place between neighbouring *parallel* chains. The separation of the sheets is slightly smaller,  $\Delta b = 1.688$  nm, and the direction of the chains also reverses in alternating sheets.

The significance of these structures to the present contribution is that nylon-6 fibre production has a tendency to promote the formation of the kinetically favoured  $\gamma$ -phase over the  $\alpha$ -phase, but because melting and recrystallisation can convert  $\gamma \rightarrow \alpha$  both are usually present in the final fibre (the ratio depending on the actual processing conditions).

In contrast, nylon-6/6 has *three* triclinic crystal phases (denoted  $\alpha_1$ ,  $\alpha_2$ , and  $\beta$ ) but no  $\gamma$  phase. There is however a high-temperature form of the  $\alpha_1$  phase which is monoclinic. The  $\beta$  phase is only formed during high-temperature annealing in a vacuum. The structures of the  $\alpha$  and  $\beta$  phases are analogous to those in nylon-6, but because the nylon-6/6 unit cell is centrosymmetric there is no concept of parallel and antiparallel chains, the two arrangements are equivalent.

The above is, however, not a complete description of the fibre structure because the lamellar sheets are not of infinite length. Each fibre actually consists of finite sections of crystalline lamellae (the "sheets" discussed earlier) joined by equivalently finite sections of amorphous polymer to form what is termed a "lamellar stack" (Figure 3). Nylons are thus *semi-crystalline* polymers. The crystallinity of a lamellar stack is 70 - 80%, but the overall crystallinity of a fibre is perhaps only 45 - 50%.

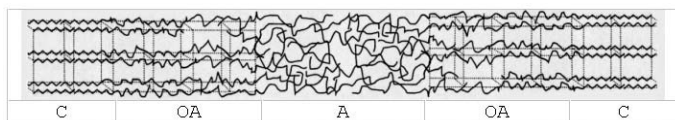


**Figure 3. Idealised schematic representation of the arrangement and different types of polymer chain conformations in a lamellar stack. Key: C = crystalline, OA = oriented amorphous, A = amorphous. Adapted reprint from Reference [17]. Copyright (2002), with permission from Elsevier.**

The amorphous polymer (along with a small contribution from thermal diffuse scattering from the ordered polymer) gives rise to an amorphous halo in the scattering pattern, the position and width of which varies with the degree of orientation in the fibre and changes in the density of the amorphous regions. In an unoriented nylon-6 fibre sample this halo occurs at a  $d \sim 0.42$  nm ( $Q \sim 14.96$  nm<sup>-1</sup>) [15, 18]. In an oriented fibre it has been shown that the amorphous polymer also has preferential orientation [15, 19], some chains align parallel to the chain axis, others align perpendicular to the chain axis. The former are more " $\alpha$ -like", the latter are more " $\gamma$ -like".

A useful overview of the structural characterisation of nylon-6 has recently been given by Rieger [20]. The hierarchy of the fibre structure is summarised in Figure 4.

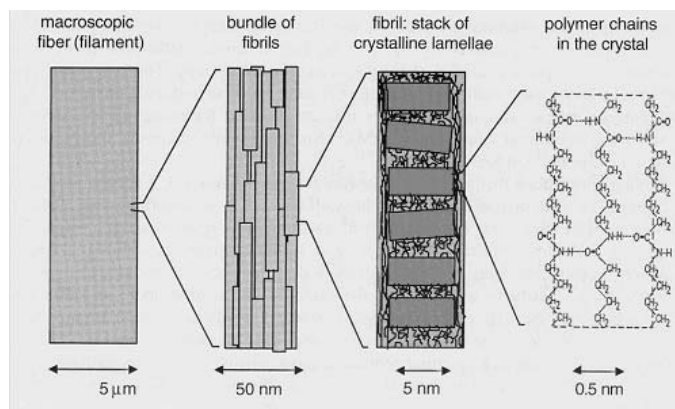


**Figure 4. The hierarchical structure of a nylon-6 fibre. The locations of the inter-lamellar and inter-fibrillar amorphous polymer are clearly visible. Reprinted from Reference [20]. Copyright (2002), with permission from Elsevier.**

## Previous Work

It is the very presence of the regions of amorphous (non-crystalline) polymer in the fibre that actually mediate many of the physical and mechanical properties conferred on the fibre by the crystalline polymer. Of particular interest in this work is the fact that the solvation of nylon fibres proceeds by diffusion of solvent molecules into the amorphous regions. From here a proportion of these solvent molecules probably also diffuse between the lamellae in the crystalline regions. It is this incorporation of solvent that gives rise to the sort of reversible effects depicted in Figure 2, as intercatenary hydrogen bonds are replaced by interactions with water molecules [3]. On average, one water molecule is associated with every amide (-CONH-) linkage in the amorphous regions [21].

There is a significant body of work on the mechanisms and molecular consequences of the hydration of nylon-6 by Murthy and co-workers [21, 22, 23, 24, 25] and others [26] using techniques such as SAXS, WAXS, SANS, INS, IR/Raman and <sup>2</sup>D-NMR. Murthy [25] also compared solvation by water with that by ethylene glycol (a "stronger" solvent known to affect the properties of nylons).

The NMR data show two types of "bound" water and a more mobile form. This is interpreted as evidence of partitioning between the lamellar stacks and the inter-fibrillar domains. One, perhaps surprising, observation is that it appears as much as two-thirds of the amorphous chains lie outside of the lamellar stacks. There is also evidence that water and other small solvent molecules can diffuse directly through the fold surfaces of the crystalline lamellae.

When fibres of different draw ratio (degree of orientation) are compared it is found that the amount of water in the inter-fibrillar domains remains quite constant, whereas that in the inter-lamellar regions decreases. This suggests that the amount of amorphous polymer in the inter-fibrillar regions remains unchanged during the drawing process and, in turn, suggests that the increases in crystallinity are due to amorphous chains in the inter-lamellar region being incorporated into the lamellae.

In contrast, the available literature concerning the effects of the adsorption of surfactants by nylon is, to all intents and purposes, non-existent (though there are some examples relating to the adsorption of dyes and proteins/DNA). However, this may in part be for reasons of commercial confidentiality.

## Why Neutron Fibre Diffraction?

Though X-ray fibre diffraction is of course a well-established, high-flux, high-resolution technique, it is not actually very well suited to the aims of the present study. For example:

- since the amount of adsorption of surfactants onto/into the fibres will not be particularly high it is not sufficient to examine a handful of treated fibres with a  $\mu$ m-sized beam, an element of bulk averaging is required;
- even synchrotron X-ray beams struggle to pass through a polymer sample more than 1 mm thick, or contained in a cuvette filled with solvent;
- ionic surfactants contain high-Z counterions which will dominate the underlying scattering from the polymer;
- non-ionic surfactants, being composed of atoms of similar Z to the polymer, will exhibit little electron density difference ("contrast").

Neutron beams on the other hand are typically collimated to several mm in size (a natural consequence of the larger source) and are highly-penetrating (in a brief test that we conducted it proved possible to measure a SANS pattern from a *whole* 8 mm diameter nylon kernmantel rope). In addition, by exploiting <sup>2</sup>D for <sup>1</sup>H substitution it is possible to selectively manipulate the contrast, or to effectively remove the contribution to the scattering of some components. The drawback with neutron fibre diffraction is the relative lack of flux that puts data collection times on current sources into the range of minutes to

hours and therefore rules out the sort of *in-situ* kinetic studies (e.g. cold drawing, simultaneous DSC) that are possible with X-rays.

Perhaps because of this there are very few examples of *neutron* diffraction from synthetic polymer fibres. The work on nylon-6 (cited above) and Tencel® (a cellulosic fibre) [27] are thus significant in this regard. Neutron diffraction from *biological* fibres (e.g. DNA) is much more widely established because of its ability to locate coordinated water.

## Instrumentation

Small- and wide-angle neutron diffraction data were simultaneously collected on the LOQ instrument at the ISIS Spallation Neutron Source, Chilton, Oxfordshire, UK [28]. This is a fixed-geometry, "white beam", instrument that utilises time-of-flight techniques on neutrons with wavelengths between 0.2 and 1 nm to provide a continuous and simultaneous  $Q$ -range of 0.06 - 14 nm<sup>-1</sup> (where  $Q$  is the modulus of the scattering vector) [29]. LOQ has two 2D position-sensitive detectors that overlap in  $Q$ -space. The incident beam was collimated to a circular cross-section of 8 mm diameter or a rectangular slit 8mm (H) x 2mm (W).

Each raw scattering dataset was corrected for the sample transmission and background scattering, detector efficiency and linearity, and converted to scattering cross-section data ( $\partial\Sigma/\partial\Omega$  versus  $Q$ ) using the instrument-specific software [30]. The reduced data are placed on an absolute scale using a well-characterized solid blend of hydrogenous and perdeuterated polystyrene as a calibrant [31].

## Experimental

Yarns approximately 3 cm in length were extracted from the core of a metre length of Edelrid Superstatic® static kernmantel rope. The rope had previously been soaked in pure water for 10 days (to remove the sizing used in manufacture) and then dried at room temperature whilst hanging under their own weight for a further 8 days. Samples of these yarns were then soaked in:

- deuterium oxide, **D<sub>2</sub>O**, (as a control);
- a 20 wt% solution of sodium deuterioxide, **NaOD**, in D<sub>2</sub>O;
- 11 wt% and 33 wt% solutions of perdeuterated sulphuric acid, **D<sub>2</sub>SO<sub>4</sub>**, in D<sub>2</sub>O;
- a 13 cmc solution of the *anionic* surfactant perdeuterated sodium dodecyl (or lauryl) sulphate, **dSDS** (CH<sub>3</sub>(CH<sub>2</sub>)<sub>11</sub>SO<sub>4</sub><sup>-</sup>Na<sup>+</sup>), in D<sub>2</sub>O;
- a 13 cmc solution of the *cationic* surfactant perdeuterated hexadecyl (or cetyl) trimethyl-ammonium bromide, **dC<sub>16</sub>TAB** (CH<sub>3</sub>(CH<sub>2</sub>)<sub>15</sub>N<sup>+</sup>(CH<sub>3</sub>)<sub>3</sub>Br<sup>-</sup>), in D<sub>2</sub>O;
- a 13 cmc solution of the *non-ionic* surfactant perdeuterated hexaethyleneglycol mono-dodecyl ether (or 6 lauryl ether), **dC<sub>12</sub>E<sub>6</sub>** (CH<sub>3</sub>(CH<sub>2</sub>)<sub>11</sub>(OCH<sub>2</sub>CH<sub>2</sub>)<sub>6</sub>OH), in D<sub>2</sub>O.

where *cmc* refers to the critical micelle concentration. The deuterium oxide, sodium deuterioxide, sulphuric acid and dSDS were obtained from Aldrich Chemical Co. Ltd. The dC<sub>16</sub>TAB and dC<sub>12</sub>E<sub>6</sub> were gifts from Dr I. Tucker of Unilever Research. The rationale behind the selection of chemical treatment was as follows. The alkali solution is of equivalent strength to the

electrolyte found in a Ni-Fe cell (battery), whilst the stronger of the two acid solutions is of equivalent strength to the electrolyte found in a Pb-acid cell. Both types of cell are used by miners, cavers and potholers. In addition it is well known that polyamides undergo acid-catalysed hydrolysis of the amide linkage. Hence samples treated with the two different strength acid solutions were expected to show different degrees of degradation. This would in turn allow the sensitivity of the study to be evaluated. Finally, cationic and non-ionic surfactants are the major constituents (typically 10 - 20%) of commercial washing powders and fabric conditioners. Anionic surfactants are sometimes also present.

Some measurements were also made with samples soaked in "*null scattering water*" (a mixture 8.7 wt% D<sub>2</sub>O : 91.3 wt% H<sub>2</sub>O that has a neutron scattering length density,  $\rho$ , of zero and thus does not scatter neutrons) and "*contrast match water*" (a mixture 21.8 wt% D<sub>2</sub>O : 78.2 wt% H<sub>2</sub>O that has a neutron scattering length density equal to the average of that for crystalline, 0.91x10<sup>10</sup> cm<sup>-2</sup>, and amorphous, 0.80x10<sup>10</sup> cm<sup>-2</sup>, nylon-6 [22]; that is  $\rho = 0.85x10^{10}$  cm<sup>-2</sup>). To a very good approximation the scattering length densities of nylon-6 and nylon-6/6 are the same.

Two types of sample mounting were used. In our earlier experiments the yarns were placed in 1 mm path length quartz cuvettes. Initially two-part cuvettes of the "dish-and-cover slip" variety were used. These allowed something of the macroscopic alignment of the fibres to be maintained in the beam, but unfortunately made it difficult to keep the fibres fully hydrated over the period of data collection (~2 hrs) as the cells were not leak-tight. Consequently a second set of measurements as made with the yarns tamped into conventional rectangular (but un-necked) cuvettes that were then filled with the relevant solution and sealed with PTFE plumber's tape. This "small-angle scattering" approach is not by any means an optimum arrangement, is certainly unconventional (in the X-ray sense), and could not be expected to yield discrete Bragg peaks because of the orientational averaging. It is nonetheless perfectly valid. The scattering from cuvettes only filled with the different solutions as also recorded and subtracted from the fibre scattering. This also removed the inherent instrumental background scattering.

Later experiments utilised a "fibre holder" made in-house (Figure 5). Mounted on a goniometer cradle on top of a rotation stage, this not only ensured that the macroscopic alignment of the yarns was standardised but, if desired, the moveable clamps permitted an extensional strain to be applied. To maintain relative humidity a small dish of D<sub>2</sub>O was placed under the yarn before the holder was encased by a box cover with aluminium foil beam entry/exit windows.

## Results and Discussion

Representative (except for the case of 33 wt% D<sub>2</sub>SO<sub>4</sub>) radially averaged (0° - 360°) scattering data are shown in Figure 6. Several features are apparent. At very low- $Q$  there is quite intense scattering that decays rapidly (from ~ 100 cm<sup>-1</sup> at  $Q = 0.06$  nm<sup>-1</sup> in the case of the D<sub>2</sub>O data shown) with increasing  $Q$ . This scattering has a power law dependence of  $\sim Q^{-3.9}$ , suggesting that it arises from surface scattering from the fibrils.

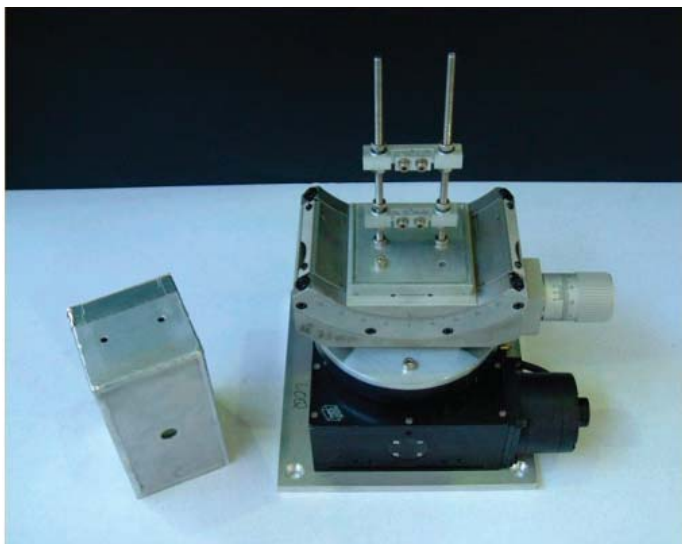


Figure 5. The fibre holder employed in later SANS experiments. The ends of the yarn are clamped between the two cross-pieces. On the left is the cover that maintains humidity around the sample. The beam entry hole is visible on the front surface. A laser beam directed along the neutron flight path allowed the sample to be positioned accurately on the beam line.

Superimposed on this power law decay is a broad diffraction peak centred on  $Q \sim 0.76 \text{ nm}^{-1}$ ; a repeat distance of  $\sim 8.3 \text{ nm}$ . This has been identified as the Long Period,  $L$ , arising from the separation of the crystalline and amorphous regions in the lamellar stacks [21, 26]. The crystalline lamellae are  $\text{D}_2\text{O}$ -deficient in the hydrated fibres, whereas the amorphous regions are  $\text{D}_2\text{O}$ -rich. There is thus a regularly repeating pattern of low and high neutron scattering length density in each stack. When this contrast difference is negligible, as in dry fibres or fibres hydrated in "null" or "contrast match" water, the Bragg peak all but disappears. The width of the peak clearly reflects a broad distribution of repeat distances within the lamellar stacks. Thus the crystalline and amorphous regions are not all of the same length, and neither are the stacks (fibrils).

Finally, at higher  $Q$  values, there is a much weaker and very broad peak apparently centred on  $Q \sim 8.5 \text{ nm}^{-1}$ . This could, at least in part, be evidence of the [020] reflection from the monoclinic unit cell of nylon-6. The higher order crystalline reflections are beyond the detection limit of the LOQ instrument being between  $14 < Q (\text{nm}^{-1}) < 17$  [14, 15, 16].

To extract the Long Period data for the different samples a  $Q^{-3.9}$  power law background was first subtracted from the data to reduce the skewing of the peak. The resulting data are then fitted to a Cauchy function using the CCP13 *XFIT* program [32]

Treated with:	L (nm)	$\Delta Q$ ( $\text{nm}^{-1}$ )	Treated with:	L (nm)	$\Delta Q$ ( $\text{nm}^{-1}$ )
Month 1			Month 41		
D2O	8.61	0.71	-	-	-
dSdS	8.73	0.67	dSdS	7.76	0.74
dC16TAB	8.98	0.85	-	-	-
dC12E6	8.38	0.68	dC12E6	8.17	0.54
NaOD	8.06	0.65	NaOD	7.80	0.81
11%D2S04	8.61	0.66	11%D2S04	9.00	0.53
33%D2S04	21.7	0.42	-	-	-

Table 2: Summary of the structural data derived from peak fitting analysis. Key:  $L$  = Long Period,  $\Delta Q$  = peak width.

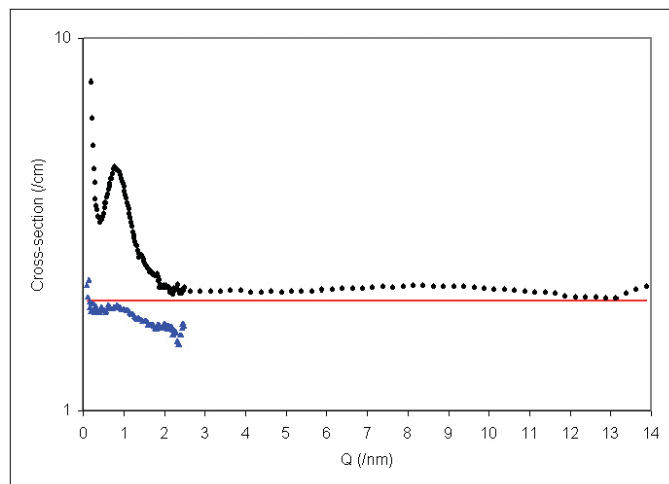


Figure 6. The small- and wide-angle scattering from static fibres hydrated with  $\text{D}_2\text{O}$  ( $\blacklozenge$ ). The  $Q$ -resolution of the two detector banks is different and this gives rise to the change in spacing between data points. An arbitrary baseline has also been added in order to emphasise the feature at high- $Q$ . Also shown for comparison (cross-section x 2) is the small-angle scattering from the same fibres hydrated with "contrast match water" ( $\blacktriangle$ ).

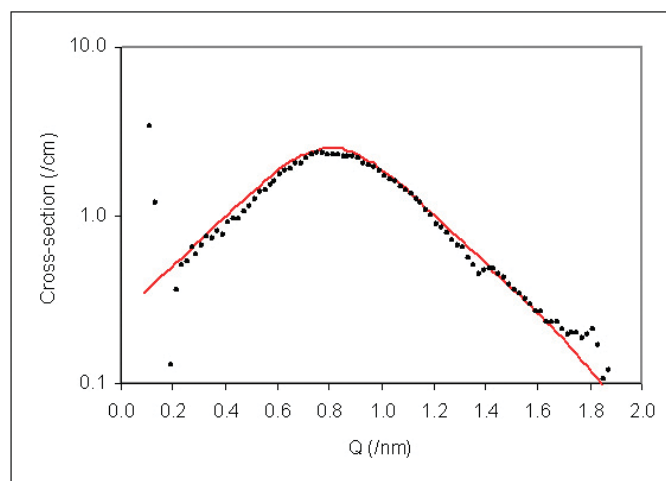
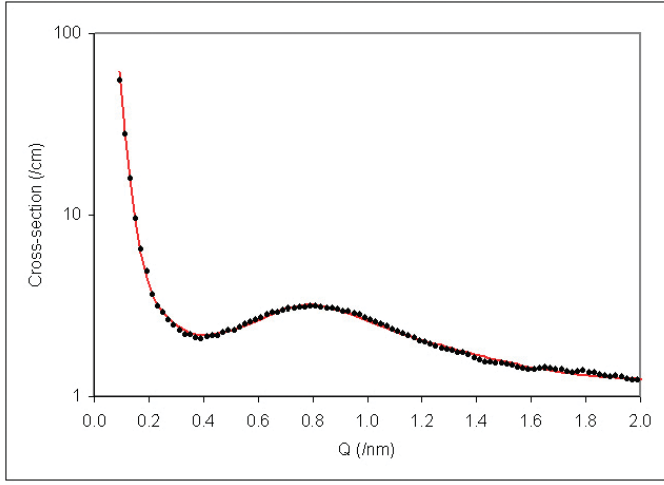


Figure 7. The small-angle scattering from static fibres hydrated with  $\text{D}_2\text{O}$  after subtraction of the underlying surface scattering ( $\blacklozenge$ ), together with a Cauchy peak fit.

(Figure 7).

The Bragg peaks in the data from the dry fibres, and those hydrated with "null water" and  $\text{H}_2\text{O}$ , were too weak to be fitted with any reliability. The Long Period data are given in Table 2.

The drawback with this type of peak fitting analysis is that the information it can provide is necessarily limited. A more rigorous approach would be to fit as much of the scattering as possible to a representative model. The one-dimensional "paracrystal" model of Kotlarchyk & Ritzau [33] is one such description. When coupled with a  $Q^{-4}$  background function this gives a good description of the scattering from the fibres, see Figure 8.



**Figure 8.** The small-angle scattering from static fibres exposed to 11 wt%  $D_2SO_4$  (◆) together with a paracrystal model-fit assuming an "idealised" lamellar structure (see text).

Two variants of the paracrystal model were tested against the scattering data. In the first, the separation and thickness of the lamellar regions were assumed to be constant; i.e. the model was one of an "idealised" lamellar structure. In the second variant, the separation and thickness of the lamellae were both allowed to randomly vary within a Gaussian distribution of length scales (but the scattering length density profiles were still sharp-sided; no allowance was made for "transition regions" between the crystalline lamellae and amorphous polymer). During the fitting the scattering length densities of the crystalline polymer and bulk medium were fixed at their known values; i.e. it was assumed that solvent could only penetrate the amorphous regions.

The former model proved more sensitive to the repeat distance and number of lamellae, but not to the thickness of the lamellae. The latter model was more sensitive to the thickness of the lamellae and solvent penetration into the amorphous regions, but not to the number of lamellae.

A comparison of the information derived from such fits is shown in Table 3. The fits were performed using the *FISH* model-fitting program written by one of the present authors [34].

	$D_2O$	11% $D_2SO_4$
	"idealised"	
Number of lamellae	5-6	4-5
Thickness, T (nm)	2.99	3.04
$\sigma_T / T$	0.05	0.05
Long Period, L (nm)	6.78	6.73
$\sigma_L / L$	0.35	0.35
	"Gaussian"	
Number of lamellae	<20	<10
Thickness, T (nm)	2.68	2.85
$\sigma_T$ (nm)	1.09	0.97
Long Period, L (nm)	5.99	5.98
$\sigma_L$ (nm)	2.19	2.24
$\phi_{polymer}$	0.29	0.24

**Table 3.** Comparison of the structural data derived from example paracrystal model fits to the scattering from static fibres.  $\phi_{polymer}$  is the composition of the amorphous region derived from the scattering length density term included in the "Gaussian" model.

The scattering from fibres exposed to the 33 wt%  $D_2SO_4$  solution is rather different (Figure 9). It is more intense, and the Long Period has increased by such a large extent that the diffraction peak is now a shoulder on the low- $Q$  decay. There is also a complete absence of structure at higher  $Q$  values. This should not, perhaps, be too surprising since the fibres in this sample had been rather seriously degraded. It is nonetheless reassuring to see that such changes are reflected in the scattering. Initially the scattering decays as  $Q^{-1.1}$  to  $Q^{-1.5}$  then, after the shoulder, as  $Q^{-2.2}$  to  $Q^{-2.6}$ . This is completely different behaviour to that exhibited by the other samples, even those treated with 11 wt%  $D_2SO_4$ . Another method of analysing

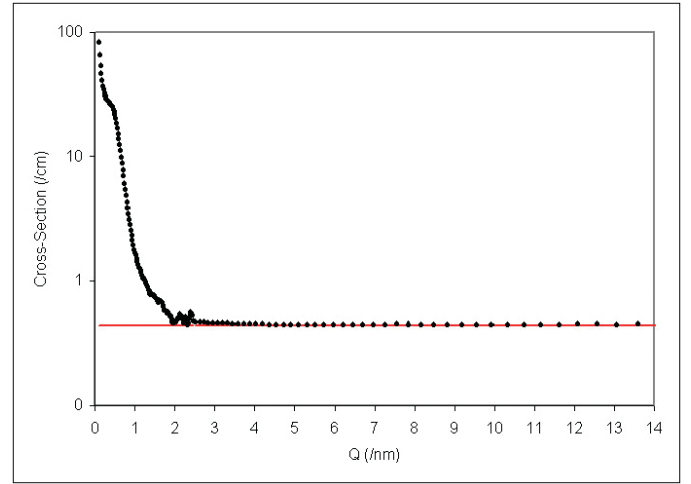


**Figure 9.** The small- and wide-angle scattering from static fibres exposed to 33 wt%  $D_2SO_4$  (◆). An arbitrary baseline has also been added. The apparent features around  $Q \sim 2 \text{ nm}^{-1}$  are at the limit of the low-angle detector and are not statistically significant.

scattering patterns from a system with a regular spacing is to calculate the one-dimensional correlation function,  $\Gamma_1(z)$  [35], from which a wide variety of structural characteristics can be inferred.  $\Gamma_1(z)$  is given by the expression:

$$\Gamma_1(z) = \int_0^\infty \frac{d\Sigma}{d\Omega}(Q) Q^2 \cos(Qz) dQ / \int_0^\infty \frac{d\Sigma}{d\Omega}(Q) Q^2 dQ$$

Note that the denominator in the above is identical with the so-called Invariant Integral,  $Q^*$ . This contains information about the composition of, and scattering length density difference between, the different phases. Given the length scales being investigated in this work, and the fact that the underlying surface scattering has been subtracted, the lamellar stacks can be treated as being just two-phase; crystalline polymer ("c") and hydrated amorphous polymer ("a"). Thus [36]

$$\begin{aligned} Q^* &= 2\pi^2 (\rho_c - \rho_a^{eff}) \phi_{stacks} \omega_c (1 - \omega_c) \\ &= 2\pi^2 (\rho_c - \rho_a^{eff}) \phi_c (1 - \omega_c) \end{aligned}$$

where  $\rho$  is the scattering length density,  $\omega_c$  is termed the local crystallinity, and  $\phi_c$  is the *volume* or *bulk* crystallinity. These last two parameters are derived from analysis of the relevant correlation functions. We note in passing that Crawshaw *et al* [27] have used a three-phase variant of the above expression to consider the system TENCEL fibres / air-filled voids / water. The effective scattering length of the hydrated amorphous

polymer can be used to estimate the volume fraction of solvent,  $\phi_{sol}$ , present since

$$\rho_a^{eff} = (1 - \phi_{sol})\rho_a + \phi_{sol}\rho_{sol}$$

Correlation functions were generated using the CCP13 *CORFUNC* program after Guinier or Vonk (low- $Q$ ) and sigmoidal (high- $Q$ ) extrapolations respectively. The latter is essentially a Porod function modified to allow for a finite width ( $\sqrt{F}$ ) at the boundary between the crystalline and amorphous regions [37].

$$\frac{d\Sigma}{d\Omega}(Q \rightarrow 0) = A \exp(-BQ^2) \quad \text{Guinier}$$

$$\frac{d\Sigma}{d\Omega}(Q \rightarrow 0) = C - DQ^2 \quad \text{Vonc}$$

$$\frac{d\Sigma}{d\Omega}(Q \rightarrow \infty) = \frac{E}{Q^4} \exp(-FQ^2) + G \quad \text{Sigmoid}$$

Here  $A$  and  $E$  are scalars related to the number concentration of fibrils,  $B$  is related to the size of the fibrils, and  $G$  is the residual (principally incoherent) background. The calculated  $\Gamma_1(z)$  functions are shown in Figure 10.

It is immediately apparent that the microstructure of the nylon fibres appears unaffected by treatment with any of the surfactant solutions. But the same cannot be said of those fibres treated with acid or alkali. Some of the parameters derived from these correlation functions are given in Tables 4 and 5. Reassuringly, there is good agreement with the model-fit data in Table 3.

Treated with:	$L$ (nm)	$l_c$ (nm)	$l_a$ (nm)	$O_s$ (nm <sup>-1</sup> )	Asym
D2O	6.50	1.31	5.18	0.316	1.03
dSDS	6.50	1.32	5.17	0.308	1.00
+41months	5.90	1.52	4.37	0.327	0.96
dC16TAB	5.80	1.26	4.53	0.314	0.91
dC12E6	6.30	1.31	4.98	0.319	1.00
+41months	6.50	1.45	5.04	0.332	1.08
NaOD	5.80	1.24	4.55	0.311	0.90
+41months	6.40	1.06	5.33	0.368	1.18
11% D2SO4	6.40	1.81	4.58	0.282	0.90
+41months	7.40	1.16	6.24	0.324	1.20
33% D2SO4	11.4	2.56	8.83	0.166	0.95

**Table 4.** Summary of the structural data derived from correlation function analysis. Key:  $L$  = Long Period,  $l_c$  = average thickness of crystalline region,  $l_a$  = average thickness of amorphous region,  $O_s$  = specific inner surface, Asym =  $(O_s/2) \times L$  = asymmetry of distribution of nearest-neighbour spacings [38].

It should be noted that the correlation function for a system of crystallinity  $\omega_c$  is identical with that for a system of crystallinity  $(1 - \omega_c)$  because the two cases are mathematically equivalent (by virtue of Babinet's Theorem). Since the *CORFUNC* program has no *a priori* way of knowing whether  $\omega_c < 0.5$  or  $\omega_c > 0.5$  in a given system it is necessary to interpret its output in the light of any other known information. In the present case it was judged that the program had correctly assigned  $l_c$ ,  $\phi_c$ , and  $\omega_c$  to the right (i.e. crystalline) phase. The basis for this judgement is that  $l_c$  is close to the dimension of the monoclinic

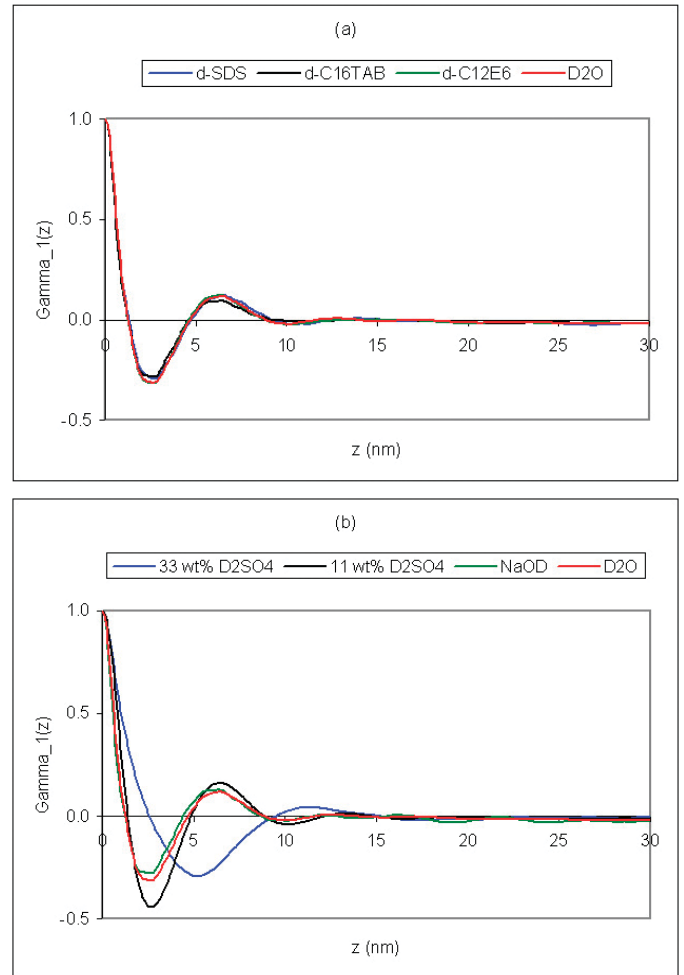


**Figure 10.** The correlation functions calculated from the 1D small-angle scattering data such as that shown in Figures 6, 8 and 9. (a) D<sub>2</sub>O and surfactant solutions. (b) Acid and alkali solutions.

Treated with:	$\phi_c$	$\omega_c$	$\phi_{sol}$	$10^{-21} Q^*$ (cm <sup>-4</sup> )	$10^{-29} E$ (cm <sup>-5</sup> )
D2O	0.207	0.202	0.690	4.492	0.241
dSDS	0.204	0.203	0.618	3.549	0.164
+41months	0.249	0.258	0.252	0.604	0.029
dC16TAB	0.198	0.217	0.717	4.582	0.226
dC12E6	0.209	0.207	>1	12.29	0.208
+41months	0.241	0.224	0.189	0.324	0.014
NaOD	0.194	0.215	0.342	0.963	0.056
+41months	0.196	0.166	0.269	0.616	0.053
11% D2SO4	0.257	0.284	0.533	2.953	0.195
+41months	0.188	0.157	0.522	2.430	0.109
33% D2SO4	0.213	0.224	n/a	n/a	0.208

**Table 5.** Summary of the physical data derived from correlation function and invariant analysis. Key:  $\phi_c$  = volume crystallinity,  $\omega_c$  = local crystallinity,  $\phi_{sol}$  = volume fraction of solvent in amorphous regions,  $Q^*$  = measured invariant integral ( $-1.5 < Q$  (nm<sup>-1</sup>)  $< 1.5$ ),  $E$  = Porod constant.

unit cell ( $c \sim 1.72$  nm), and  $\phi_c$  and  $\omega_c$  are more in keeping with expected crystallinities.

Inspection of the 2D small-angle diffraction patterns reveals them to be anisotropic, see Figure 11.

When the integrated intensity in the Bragg peak is plotted against azimuthal angle a distinct four-peak pattern emerges, evidence of biaxial alignment in the fibres (Figure 12).

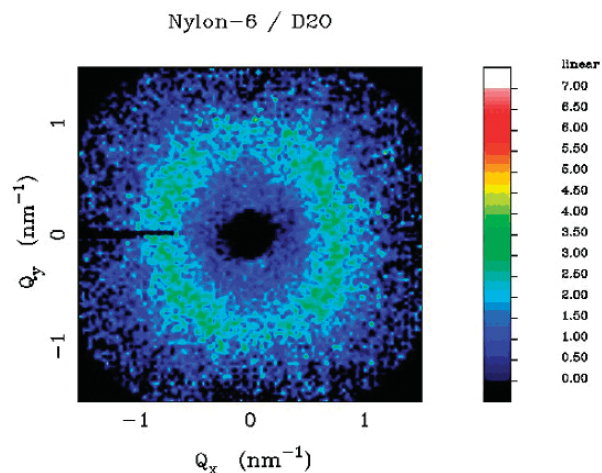


**Figure 11.** The 2D small-angle scattering from static fibres hydrated with  $D_2O$ . The data have had a  $Q^{-3.9}$  power law background subtracted. The feature cutting across the left side of the pattern at  $Q_y = 0$  is an artefact of the way the image was processed. The slight tilt of the pattern is a consequence of poor sample mounting.

This alignment would have been imparted during the manufacturing process. Significantly the scattering patterns for fibres treated with NaOD and 33 wt%  $D_2SO_4$  do not show this feature.

It is quite clear that exposure of the fibres to water, the surfactant solutions, and even dilute acid, has negligible effect on this inherent alignment. In contrast, concentrated acid and alkali have a marked effect; the four-point pattern becomes a two-point pattern. The significant differences in overall scattering between fibres treated with water and 33 wt%  $D_2SO_4$  have already been remarked on, but curiously there are no obvious and equivalent differences in the scattering from fibres treated with NaOD.

## Summary and Conclusions

Small-Angle Neutron Scattering has been used to probe for changes in the microstructure of nylon fibres following exposure to concentrated surfactant, acid and alkali solutions.

The data are capable of differentiating between untreated and treated fibres.

In respect of exposure to surfactant solutions, there do not appear to be any untoward *chemical* consequences, though the cationic surfactant appears to be more effective at keeping the amorphous regions hydrated than either the anionic or non-ionic surfactants. This is in qualitative agreement with the observations of Frank [5].

It remains to be seen if there are any *mechanical* consequences. These might arise, for example, from surfactant crystallites that have penetrated into the core yarns "sawing" through the fibres, or by "connecting" adjacent fibres and thereby reducing the fibre redundancy that contributes to the load handling capability. Further work to address some of these outstanding issues is already in progress.

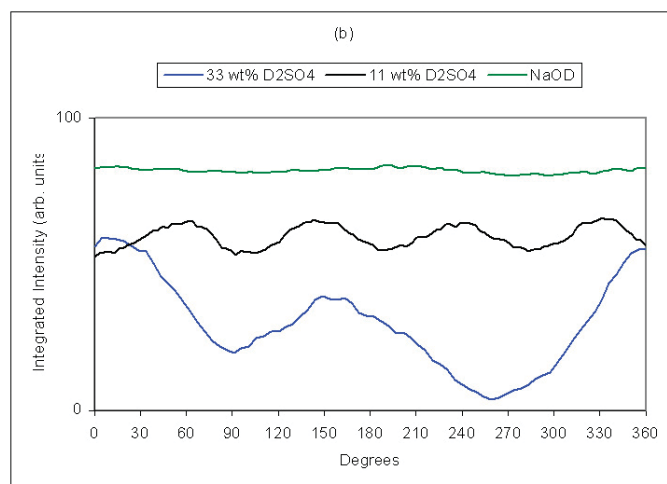
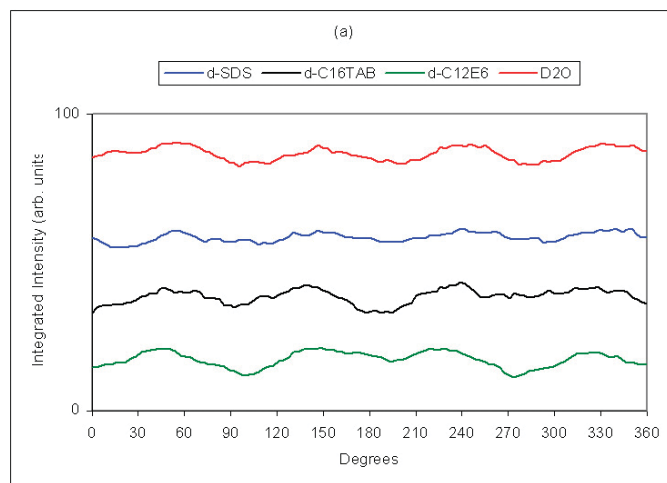


**Figure 12.** The (exponentially smoothed) integrated intensity in the Bragg peak. (a) Static fibres hydrated with  $D_2O$  and surfactant solutions. (b) Static fibres hydrated with acid and alkali solutions. With the exception of the  $D_2O$  curve in (a), the curves have been displaced vertically to aid clarity. The artefact in Figure 11 has been removed from these data.

One striking observation is just how robust the fibres are to acid hydrolysis. The degree of microstructural perturbation after 41 months in 1/3-strength car battery acid is really quite small, though more concentrated acid solutions degrade the fibres rather rapidly.

Additional diffraction measurements, and mechanical tests on the same samples, are already underway and will be reported in the near future.

## Acknowledgements

An oral contribution ("Hanging by a Thread") based on the subject matter of this paper was delivered at the 10<sup>th</sup> Annual CCP13 Fibre Diffraction and Non-Crystalline Diffraction Workshop in Stirling, Scotland, 13-15 June 2001.

The routine to convert LOQ reduced data files in ASCII format into BSL was written by J. Günter Grossmann at the Daresbury Synchrotron Radiation Source. It is now incorporated into the XCONV program in the CCP13 program suite.

The chemical structure diagrams are taken from the Macrogalleria at [www.psrc.usm.edu/macrog/index.htm](http://www.psrc.usm.edu/macrog/index.htm).

## References

- [1] Kaimin, I.F., Apinis, A.P., Galvanovskii, A.Ya. (1975) *Vysokomol. Soedin.*, **A17**, 41.
- [2] Inoue, K., Hoshino, S. (1976) *J. Polym. Sci., Polym. Phys. Ed.*, **14**, 1513.
- [3] Reimschuessel, H.K. (1978) Relationships on the effect of water on glass transition temperature and Young's modulus of nylon 6. *J. Polym. Sci., Polym. Chem. Ed.*, **16**, 1229-1236.
- [4] Smith, B. (1988) Effects of Rope Aging. *NSS News, Journal of the National Speleological Society of America*.
- [5] Frank, J.A. (1989) Fabric Softener and Rescue Rope. *Nylon Highway*.
- [6] Mark, J.E. (1999) *Polymer Data Handbook*. Oxford University Press.
- [7] Samon, J.M., Schultz, J.M., Hsiao, B.S. (2002) Structure development in the early stages of crystallisation during melt spinning. *Polymer*, **43**, 1873-1875.
- [8] Holmes, D.R., Bunn, C.W., Smith, D.J. (1955) *J. Polym. Sci.*, **17**, 159.
- [9] Arimoto, H., Ishibashi, M., Hirai, M., Chantani, Y. (1965) *J. Polym. Sci. Part A*, **3**, 317.
- [10] Salem, D., Weigmann, H., Polym. (1989) *Comm.*, **30**, 336.
- [11] Murthy, N.S., Curran, S.A., Aharoni, S.M., Minor, H. (1991) Premelting crystalline relaxations and phase transitions in nylon 6 and 6/6. *Macromol.*, **24**, 3215-3220.
- [12] Cooper, S.J., Atkins, E.D.T., Hill, M.J. (1998) Temperature-induced changes in lamellar crystals of monodisperse nylon 6 and nylon 6/6 oligoamides. *Macromol.*, **31**, 8947-8956.
- [13] Sikorski, P., Jones, N.A., Atkins, E.D.T., Hill, M.A. (2001) Measurement of the intersheet shear along the chain axis in nylon 6. *Macromol.*, **34**, 1673-1676.
- [14] Ramesh, C., Bhoje Gowd, E. (2001) High-temperature X-ray diffraction studies on the crystalline transitions in the a- and g- forms of nylon-6. *Macromol.*, **34**, 3308-3313.
- [15] Murthy, N.S., Minor, H., Bednarczyk, C., Krimm, S. (1993) Structure of the amorphous phase in oriented polymers. *Macromol.*, **26**, 1712-1721.
- [16] Zhang, Q.-X., Fu, P.-P., Zhang, H.-F., Mo, Z.-S. (2002) Microstructure analysis of nylon 66 by WAXD and SAXS. *Chem. Res. Chinese Uni.*, **18**, 358-363.
- [17] Wu, J., Schultz, J.M. (2002) Calculation of mesophase percentage of polymer fibres from 2D wide-angle X-ray scattering patterns. *Polymer*, **43**, 6695-6700.
- [18] Roldan, L.G., Kaufman, H.S. (1963) *J. Polym. Sci., Polym. Lett.*, **1**, 603.
- [19] Matyi, R.J., Crist, B. (1978) Small-angle X-ray scattering by nylon-6. *J. Polym. Sci., Polym. Phys. Ed.*, **16**, 1329-1354.
- [20] Rieger, J. (2002) Use of scattering methods in chemical industry - SAXS and SANS from fibers and films. Chapter 21, *Neutrons, X-rays and Light: Scattering Methods Applied to Soft Condensed Matter*, Lindner, P., Zemb, Th. (editors), North-Holland.
- [21] Murthy, N.S., Stamm, M., Sibilia, J.P., Krimm, S. (1989) Structural changes accompanying hydration in nylon-6. *Macromol.*, **22**, 1261-1267.
- [22] Murthy, N.S., Orts, W.J. (1994) Hydration in semicrystalline polymers: small-angle neutron scattering studies of the effect of drawing in nylon-6 fibres. *J. Polym. Sci. Part B*, **32**, 2695-2703.
- [23] Papanek, P., Fischer, J.E., Murthy, N.S. (2002) Low-frequency amide modes in different hydrogen-bonded forms of nylon-6 studied by inelastic neutron scattering and density-functional calculations. *Macromol.*, **35**, 4715-4182.
- [24] Hutchinson, J.L., Murthy, N.S., Samulski, E.T. (1996) Deuterium nmr studies of water in oriented nylon-6 fibres. *Macromol.*, **29**, 5551-5557.
- [25] Murthy, N.S., Akkapeddi, M.K., Orts, W.J. (1998) Analysis of lamellar structure in semicrystalline polymers by studying the absorption of water and ethylene glycol in nylons using small-angle neutron scattering. *Macromol.*, **31**, 142-152.
- [26] Plestil, J., Baldrian, J., Ostanevich, Yu.M., Bezzabotnov, V.Y. (1991) Small-angle neutron and X-ray scattering study of swollen nylon-6. *J. Polym. Sci. Part B*, **29**, 509-514.
- [27] Crawshaw, J., Vickers, M.E., Briggs, N.P., Heenan, R.K., Cameron, R.E. (2000) The hydration of TENCEL cellulose fibres studied using contrast variation in small angle neutron scattering. *Polymer*, **41**, 1873-1881.
- [28] [www.isis.rl.ac.uk](http://www.isis.rl.ac.uk)
- [29] [www.isis.rl.ac.uk/LargeScale/LOQ/LOQ.htm](http://www.isis.rl.ac.uk/LargeScale/LOQ/LOQ.htm)
- [30] King, S.M., Heenan, R.K. Using COLETTE. RAL Report RAL-95-005, Rutherford Appleton Laboratory (1995).
- [31] Wignall, G.D., Bates, F.S. *J. Appl. Cryst.*, **20**, 28-40 (1987).
- [32] [www.ccp13.ac.uk](http://www.ccp13.ac.uk)
- [33] Kotlarchyk, M., Ritzau, S.M. (1991) Paracrystal model of the high-temperature lamellar phase of a ternary microemulsion system. *J. Appl. Cryst.*, **24**, 753-758.
- [34] Heenan, R.K. (1989) "FISH" Data Analysis Program. RAL Report RAL-89-129, Rutherford Appleton Laboratory. Also see: [www.isis.rl.ac.uk/LargeScale/LOQ/FISH/FISH\\_intro.htm](http://www.isis.rl.ac.uk/LargeScale/LOQ/FISH/FISH_intro.htm)
- [35] Strobl, G.R., Schneider, M. (1980) Direct evaluation of the electron density correlation function of partially crystalline polymers. *J. Polym. Sci., Polym. Phys. Ed.*, **18**, 1343-1359.
- [36] Li, L., Koch, M.H., de Jeu, W.H. (2003) Crystalline structure and morphology in nylon-12: A small- and wide-angle X-ray scattering study. *Macromol.*, **36**, 1626-1632.
- [37] Koberstein, J., Stein, R.J. J. (1983) *Polym. Sci., Polym. Phys. Ed.*, **21**, 2181-2200.
- [38] Strobl, G.R., Schneider, M.J., Voigt-Martin, I.G. (1980) Model of partial crystallisation and melting derived from small-angle X-ray scattering and electron microscopic studies on low-density polyethylene. *J. Polym. Sci., Polym. Phys. Ed.*, **18**, 1361-1381.

## Modelling Oriented Macromolecular Assemblies from Low-angle X-ray Fibre Diffraction Data with the Program MOVIE: Insect Flight Muscle as an Example

Hind A. AL-Khayat<sup>1</sup>, Liam Hudson<sup>1</sup>, Michael K. Reedy<sup>2</sup>, Thomas C. Irving<sup>3</sup>  
and John M. Squire<sup>1</sup>

[1] Biological Structure & Function Section, Biomedical Sciences Division, Faculty of Medicine, Imperial College London, London SW7 2AZ, UK

[2] Dept of Cell Biology, Duke University, Durham, NC 27710, USA

[3].BioCAT, Dept. Biological, Chemical and Physical Sciences, Illinois Institute of Technology, Chicago, IL 60616, USA

Received and 3rd March 2004; accepted in revised form 2nd April 2004

### ABSTRACT

Many extended biological structures such as actin and myosin filaments, intermediate filaments, microtubules, flagella and so on can form oriented fibrous assemblies which are either naturally occurring, as in muscle or hair, or can be induced to form synthetic fibres. Such structures can yield very rich fibre diffraction patterns. Part of the remit of CCP13 in Fibre Diffraction and Solution Scattering is to strip such diffraction patterns to produce reliable intensity values for the diffraction peaks. However, since such diffraction patterns usually arise from structures with cylindrical symmetry around the preferred long axis, implying that even well-sampled fibre patterns inevitably contain many overlapping diffraction peaks, they cannot be phased in the same way as for protein crystallography and it is necessary to devise modelling strategies to interpret the diffraction patterns. For high-angle diffraction data from highly organised molecular structures (e.g. DNA or cellulose) the program LALS can be used effectively. In the case of low-angle X-ray fibre diffraction patterns we have generated the program MOVIE to take known protein crystal structures and use these in simulated annealing configurational searches to optimise the fit between the observed and calculated diffraction data. Here we describe the rationale behind MOVIE and the steps involved in applying MOVIE to a typical case, namely the analysis of the low-angle X-ray fibre diffraction data from relaxed insect flight muscle recorded on the BioCat beamline at the Argonne APS.

### Introduction to Muscle and the Strategy behind MOVIE

Muscle cells (fibres) contain two parallel sets of protein filaments made of myosin and actin respectively (Figure 1(a)). During stretch or shortening, the overlapping myosin and actin filaments each keep virtually constant length as they slide past each other. They change their overlap as the muscle changes length. To perform the sliding motion, myosin heads (crossbridges) projecting out from the myosin filament surface cyclically bind to, bend on, then release, adjacent actin filaments as if they were walking along the actin. The bind-and-bend phase of each cycle is called a powerstroke. The end of the powerstroke, in which myosin heads have already bent and are strongly bound to actin, is called the rigor-like conformation. This conformation has previously been visualised both by electron microscopy and by modelling X-ray diffraction data (e.g. Rayment *et al.*, 1993b; Harford *et al.*, 1996). However, the orientation of the unbound heads in myosin's relaxed initial state or in the first attachment to actin have not been known in detail until recently. Comparing the

positions of the heads in the two states can help to deduce the structural transitions involved in the powerstroke mechanism following muscle activation.

The structure of the myosin head (myosin subfragment 1 or S1) has been determined by protein crystallography (Figure 1(b)). Myosin S1 heads are enzymes (ATPases) which bind and split the energy-giving molecule ATP (adenosine triphosphate) to give the products ADP (adenosine diphosphate) and inorganic phosphate (Pi). The myosin head state that initially attaches to actin in the pre-powerstroke state is M.ADP.Pi, giving AM.ADP.Pi when attached to actin. Force production and movement occur when Pi and then ADP are released from the heads to leave the AM (rigor-like) state. Addition of ATP to AM causes the release of the heads from actin and the resulting M.ATP state rapidly dissociates to M.ADP.Pi once again, leaving the head ready for a further cycle of attachment and movement on actin. The first myosin head shape to be solved by protein crystallography was in the absence of nucleotide, as in the 'rigor' state (Rayment *et al.*, 1993a). Since that time attempts have been made to mimic the head shape in the pre-powerstroke state in protein crystals,

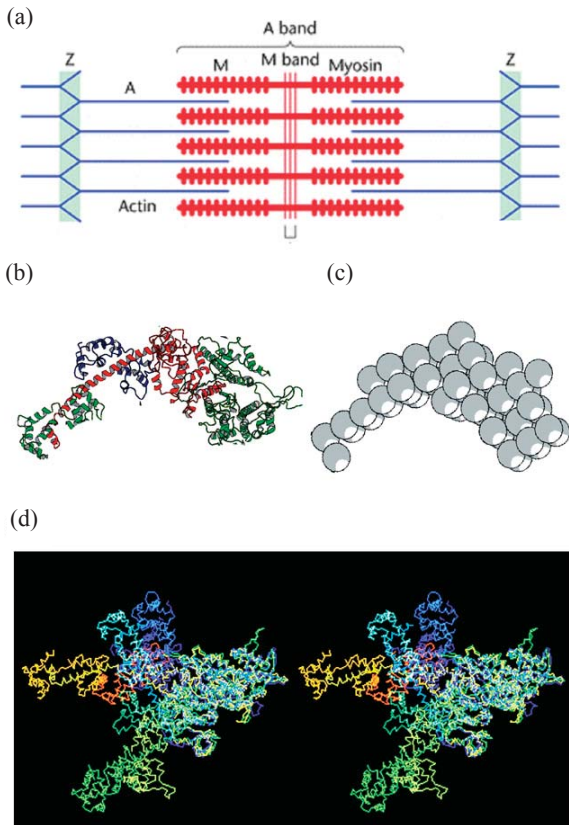


Figure 1. (a) The structure of a striated muscle sarcomere, which extends from Z-band (Z) to Z-band, showing the overlapping actin and myosin filaments and the projections on the myosin filaments in the muscle A-band. (b) The myosin head structure (Rayment *et al.*, 1993a) as downloaded from the PDB database and illustrating the myosin heavy chain (green and red on the right (the catalytic domain) and red on the left (the neck region)). The neck region or lever arm also has the two light chains; the regulatory light chain (green on the left) and essential light chain (blue). The long  $\alpha$ -helical part of the heavy chain in red in the core of the light chains region provides the link between the catalytic domain and the rest of the myosin filament which joins at the bottom left hand part of the red helix. The actin-binding face of the myosin head is top right and slightly facing up and out of the page. (c) Representation of (b) in terms of a 59 sphere model. The volume of these spheres, each of radius 8.61 Å, was chosen to express the overall mass of the myosin head, assuming constant protein density within all spheres. (d) Stereo-images of various crystal structures of the myosin head with different nucleotides bound. All are superimposed at the motor catalytic domain on the right, so that the differences between models are expressed by the different positions of the neck regions or lever-arms on the left. Green and pointing slightly towards the viewer is the Rayment *et al.* (1993a,b) chicken skeletal myosin with no nucleotide (i.e. rigor-like); dark blue is the Dominguez *et al.* (1998) chicken smooth muscle myosin in ADP·AlF<sub>4</sub> form; pale blue is our *Lethocerus* model; orange is the Houdusse *et al.* (2000) scallop myosin in Mg·ADP·VO<sub>4</sub> form. The view has the actin filament axis vertical and to the right, with the M-band at the top and Z-band at the bottom.

yielding success with smooth muscle myosin and bound ADP·AlF<sub>4</sub> in the work of Dominguez *et al.* (1998) and with scallop muscle myosin and bound ADP·VO<sub>4</sub> in the work of Houdusse *et al.* (2000). These and other crystallographic studies of myosin have shown that the ATP-binding part of the head, known as the catalytic or motor domain, is relatively constant in shape, at least at low resolution, but that the rest of the head forms a relatively narrow and straight neck region which can change its angle relative to the motor domain

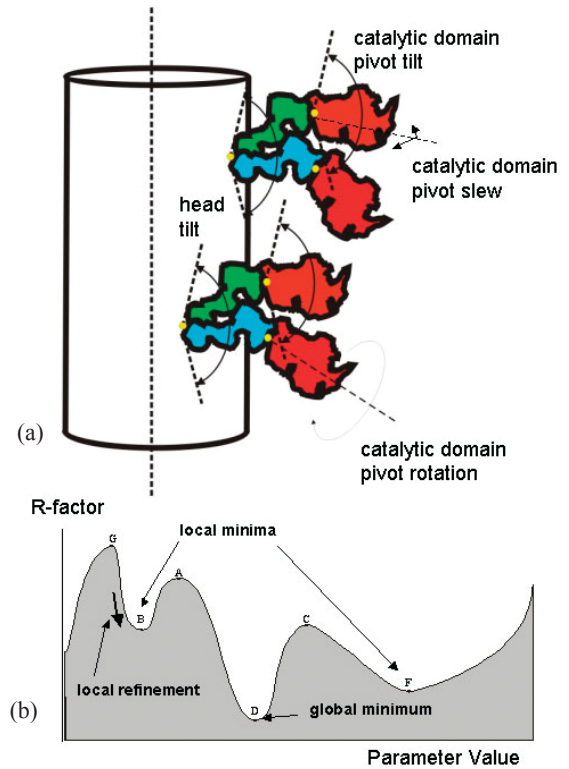


Figure 2. (a) Illustration of pairs of myosin heads on helical tracks on the surface of a roughly cylindrical myosin filament backbone, with the hinge points at the filament surface and between the motor domain and neck region illustrated (yellow circles), together with some of the kinds of parameters which can describe the head shape and position. (b) Illustration of the variation of the R-factor in hypothetical parameter space showing local minima at B and F and a global minimum at D.

depending on the attached nucleotide. Several different head shapes are illustrated in Figure 1(d).

Myosin molecules comprise two of the S1 heads discussed above, each about 16 nm long, on the end of a rod-shaped tail about 150 nm long. The myosin tails or rods pack together to form the shaft of the myosin filaments with the myosin heads in quasi-helical arrays on the filament surface (Figure 2(a)). In resting muscles the heads are often relatively well-ordered on the filament backbones and they give rise to strong diffraction features in low-angle X-ray diffraction patterns (Figure 3). The process of head movement and attachment to actin filaments during muscle contraction clearly disrupts this starting structure and gives rise to new diffraction features. In this paper we are primarily concerned with illustrating the use of the program MOVIE by discussing how to model the myosin filaments in resting insect flight muscle. The problem is that, although we know the geometry and symmetry of the lattice of heads that occurs on the myosin filament surface (and this is different for different muscle types), we do not know the head shape in this state (the heads are probably predominantly in the M·ADP·Pi biochemical state; Hibberd and Trentham, 1986; Xu *et al.*, 1999) and we do not know the arrangement of the two heads of each pair on the filament surface. This is where the program MOVIE comes into play.

## What MOVIE does

The problem is as follows, remembering that we are dealing with diffraction features at relatively low resolution. We can define the position of each of the myosin heads in a pair (Figure

2(a)), using the far end of the neck or lever arm away from the motor domain as an origin, in terms of their radius ( $R$ ) from the filament axis, and in terms of various angles such as the head slew ( $\alpha$ ) around an axis through the head origin and parallel to the filament long axis, the head tilt ( $\beta$ ) in a direction parallel to the filament axis, and the head rotation ( $\theta$ ) about the myosin head's own long axis. In addition, since we do not know the head shape, we can suppose that, with the neck position defined by the angles  $\alpha$ ,  $\beta$  and  $\theta$ , the motor domain can rotate relative to the neck region around three further mutually perpendicular axes (motor pivot tilt  $\alpha_p$ , motor pivot slew  $\beta_p$ , and motor pivot rotation  $\theta_p$ ). In addition, the two heads in one pair cannot have identical origins on the filament surface, so they need to be offset by two further parameters (their separation  $H_s$  and the tilt of the line joining the origins  $H_t$ ). In the case of insect flight muscle, which is highly ordered in 3-dimensions, the orientation ( $\phi$ ) of the whole myosin filament about its own long axis within the muscle unit cell is also an important factor. These parameters are explained in detail in AL-Khayat *et al.* (2003).

The insect flight muscle myosin filament is a relatively simple example of its kind since the myosin head array appears to be purely helical. The filaments have 4-fold rotational symmetry, meaning that there are the heads of four myosin molecules equally spaced in a ring around the myosin filament. Such a ring is known as a 'crown'. Successive crowns along the filament are separated axially by 14.5 nm and by a rotation of  $33.75^\circ$ , giving the filament a true axial repeat after  $8 \times 14.5$  nm (116 nm). It is therefore enough in the MOVIE program to define the positions of each head in the pair belonging to one molecule and then to assume that all the other heads are related to these first heads purely by applying the helical symmetry of the filament. This means that the diffraction pattern from the filament can be computed using Fourier transforms involving Bessel functions as described elsewhere (Harford and Squire, 1997; Squire, 2000; AL-Khayat *et al.*, 2003).

From the discussion of appropriate parameters above, the insect problem reduces to optimising the value of 13 parameters, assuming that both heads have the same shape ( $\alpha$ ,  $\beta$  and  $\theta$  for each of two heads,  $\alpha_p$ ,  $\beta_p$ ,  $\theta_p$  defining the common head shape, and  $R$ ,  $H_s$ ,  $H_t$ ,  $\phi$ ). What we would ideally like to do is to represent the myosin head by its atomic coordinates as in a PDB file and then run a global search routine where every parameter is stepped through a small increment, the diffraction pattern for each parameter combination is checked against the observed pattern and a 'goodness of fit factor,  $R$ , is calculated (like the crystallographic  $R$ -factor). However, in attempting to do this one soon comes up against a chronic shortage of computing power. The various head parameter angles will range either from  $-90^\circ$  to  $+90^\circ$  or from  $-180^\circ$  to  $+180^\circ$  and we would wish to sample these in steps of say  $1^\circ$  or  $2^\circ$  (i.e. 90 to 360 steps for each angle). Other angles such as  $H_t$  and  $\phi$  might have smaller ranges, say  $\pm 45^\circ$  in steps of  $2^\circ$  for  $H_t$  (45 combinations) and say  $0^\circ$  to  $12^\circ$  for  $\phi$  in steps of  $1^\circ$  (13 values). Distances such as  $R$  and  $H_s$  might have a limited sensible range (say 7 to 10 nm for  $R$  and 2 to 5 nm for  $H_s$ ) and one would want to step these in increments of, say, 0.1 or 0.2 nm (about 15 to 30 steps for each). Even taking the larger step sizes, the number of parameter combinations is at least  $(90)^9 \times (15)^2 \times 45 \times 13 = 5.099 \times 10^{22}$ . Let us suppose (optimistically) that each parameter

computation and comparison with the observed diffraction data, resulting in a value for the goodness of fit factor  $R$ , takes 1 ms. This then means that the whole search will take of the order of  $10^{12}$  years! Even a computer farm and a great deal of parallel computing will not help very much. However, a number of strategies may be invoked to speed things up. First of all one can try to make each individual calculation faster. This can be done by representing the low-resolution shape of the myosin head by a relatively small number of spheres rather than by all the atomic coordinates. We have found that a model involving 59 spheres each of radius 8.61 Å (Figure 1(c)) can adequately represent the myosin head at the resolution we are considering (say 6 nm). In fact the computed diffraction patterns from the sphere model and the PDB model (Figure 1(b)) agree with a correlation coefficient of 0.995 to 6.5 nm resolution. This simplification speeds up the calculation considerably. In fact, for a single MOVIE calculation for only one parameter set takes 1.052 seconds with the full PDB file and 0.054 seconds with the sphere model, and so the search with the sphere model is about 20 times faster than with using the full PDB file. Next we can think of less systematic but faster ways of searching through parameter space to home in on the best parameter set. In fact there are various established approaches to this, such as the Downhill Simplex refinement (Nelder and Mead 1965; Brent, 1973). However, one can imagine being in a local minimum in  $R$  space (points B or F in Figure 2(d)) and being taken to the bottom of that minimum by the Downhill Simplex procedure, but then being trapped there, even though the true minimum is elsewhere (point D). A good way to avoid this problem is to use the process of simulated annealing (Kirkpatrick *et al.*, 1983; Kirkpatrick, 1984). This has the effect of allowing the parameters to effectively 'jump around' in parameter space, thus avoiding local minima traps, with the range of the jumping defined by the 'temperature' at which the simulation is running. In successive cycles this 'temperature' can be reduced until a stable set of parameters is obtained. Subsequent local refinement by a Downhill Simplex run will then, it is hoped, take the parameters to the bottom of the global minimum well (D in Figure 2(d)). As described below, application of such a simulated annealing approach to the muscle problem using the program MOVIE has already yielded excellent results (Hudson *et al.*, 1997; Squire *et al.*, 1998; AL-Khayat *et al.*, 2003).

## Getting good intensity data using LSQINT

The diffraction pattern in Figure 3 was stripped and analysed as illustrated in Figure 4, where Figure 4(a) is the quadrant-folded version of Figure 3. Analysis of this pattern presented a number of problems. Firstly the pattern contains mixed contributions from actin filaments as well as myosin filaments. Because the helical symmetry and repeats in both filaments are known, we knew that layer-lines with spacings common to both filaments (2320 Å) would have contributions from myosin and actin on the same layer-line (e.g. the 6<sup>th</sup> order of 2320 Å at 38.7 nm). It was, therefore, necessary to separate out the few layer-lines coming solely from myosin and to use these in our analysis. Secondly, because we did not need either the equator or the meridian to do the analysis, we could mask off those regions of the diffraction pattern as in Figure 4(b). Finally, in trying to use LSQINT, it was noted that, for example, the 6<sup>th</sup> layer-line at a 38.7 nm spacing, which has strong contributions from the actin filaments, had different peak shapes from the layer-lines arising solely from the myosin filaments. However, Figure 4(c) shows

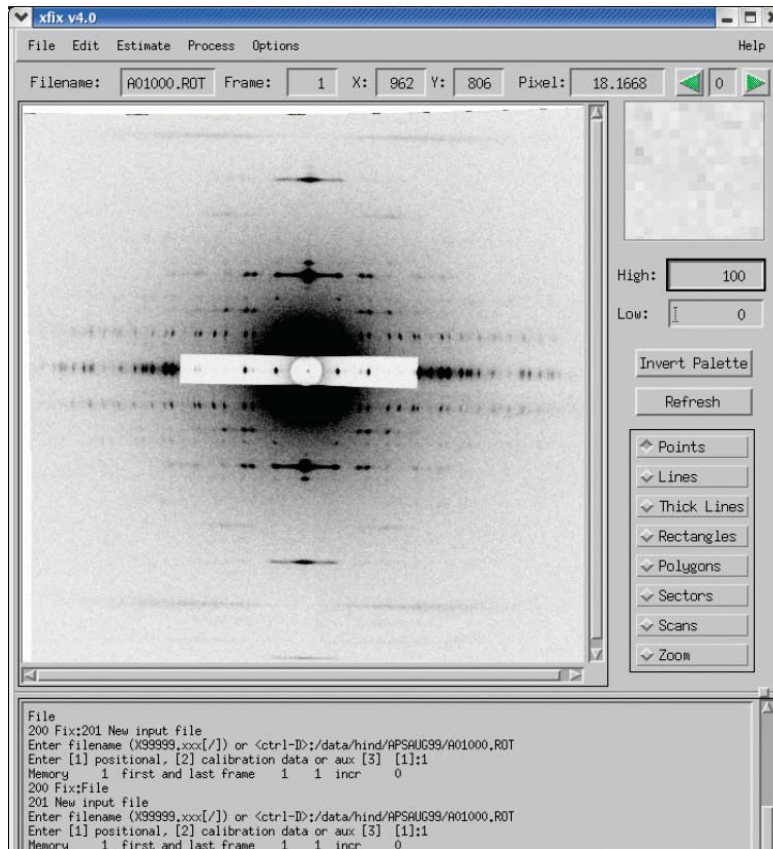


Figure 3. A low-angle X-ray diffraction pattern from relaxed flight muscle fibres [dorsal longitudinal muscles (DLM)] from the giant waterbug (*Lethocerus indicus*) recorded using X-rays of  $\lambda = 1.033 \text{ \AA}$  on the BioCAT beamline 18-ID at the APS using the small angle camera described by Irving T.C. *et al.*, (2000) at a 1960 mm specimen-detector distance and a CCD detector (Reedy, M.K. *et al.*, 2000). A strip of Al sheet metal about 0.4 mm thick was positioned over the CCD along the equator, attenuating the strongest equatorial spots to about 0.01 and thereby avoiding a readout artefact in the CCD images. 100 ms exposures using 90% beam attenuation routinely gave good patterns from fibre bundles 250-350  $\mu\text{m}$  in diameter. About ten patterns approaching this quality were obtained, but none quite matched its orientation and spot-sharpness, so this pattern was used for definitive final analysis. Here the pattern is shown contained in the window of the CCP13 XFIX program.

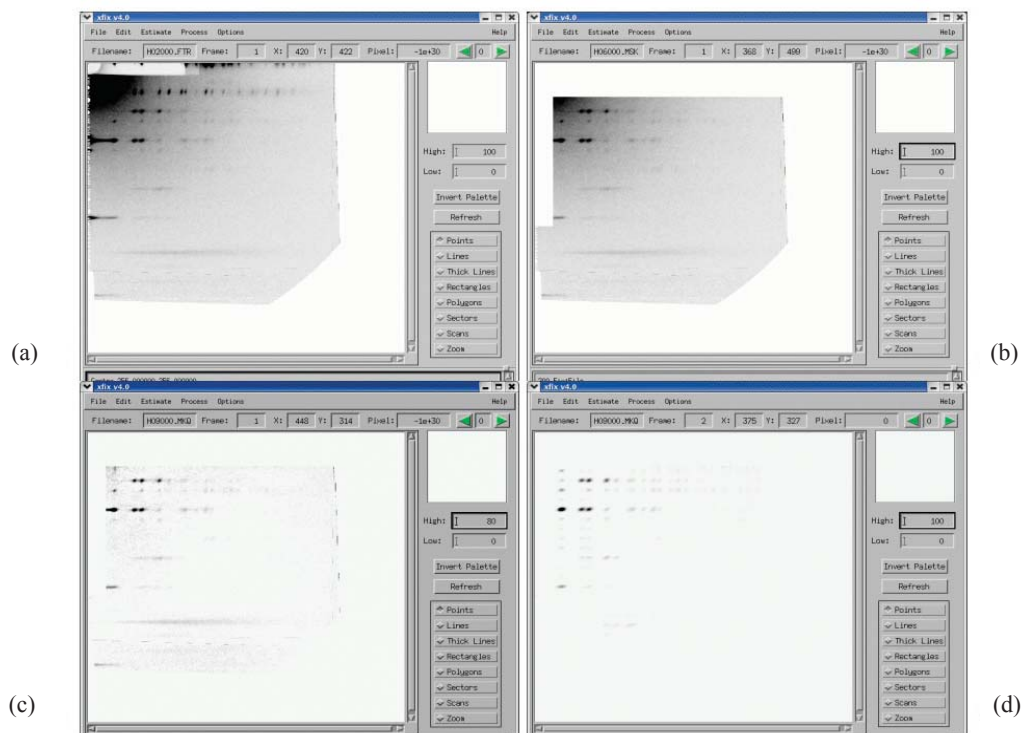


Figure 4. (a) Average of four quadrants of Figure 3 after converting into reciprocal space in FTOREC, (b) same as in (a) but with a mask on the equator, the 38.7 nm layer line and the meridian, (c) LSQINT output of fitting the pattern shown in (b) after subtracting the fitted background, (d) fitted intensity peaks in (c) produced by LSQINT and as used in the modelling studies of this paper. All these patterns are shown contained in the window of the CCP13 XFIX program.

the pattern in Figure 4(b) after fitting and subtracting a suitable background, and Figure 4(d) shows the LSQINT fit to the remaining Bragg peaks. The original pattern had over 468 Bragg reflections, of which over 65 were strong and exclusively from the myosin filaments to a resolution of  $1/65 \text{ \AA}^{-1}$ . These 65 intensities were then modelled as described above using the known myosin head shape represented as spheres, a hinge between the motor (catalytic) domain and the light chain-binding (neck) region (lever arm), and a simulated annealing model search procedure.

## Running the MOVIE program

MOVIE is a program originally written by J. M. Squire in Fortran 77 (it was originally called MUSCLE3D). It was converted to the C language and the simulated annealing parameter search procedure was added by L. Hudson (Hudson, 1996). It was later modified by H. A. AL-Khayat. It runs on a UNIX shell using LINUX or ALPHA workstations.

The program is centred around a command line interface which works by the user inputting keywords and numerical values/character strings to set up the starting conditions. The keywords may be split into three distinct types: Single commands: these keywords can either be ENABLED or DISABLED. They always default to DISABLED (Figure 5a, with all default model parameters set to zero) and can be ENABLED when selected (e.g. myosin, actin, simplex, anneal, view etc). Simple commands: these keywords are always followed by another single parameter which can either be an integer, floating point or a character string (e.g. cell 523.44, mrepeat 1167.41, filaments 1, numreps 3, mcrowns 8). Complex commands: these keywords have a range of sub-keywords associated with them. Each sub-keyword is in effect a simple command mentioned above, each with its own number or character string associated with it (e.g. mslew head 1 start -65.03 scale 2.0). All these commands can be in lower or upper case. MOVIE has about 120 keywords and a complete list of all the commands plus their descriptions can be obtained by pressing the 'RETURN' key while within MOVIE.

Under normal usage, it is easier to create a template file which contains a list of commands and model parameter values. This file can be parsed via the 'load' keyword. An example template file is shown in Figure 5(b) for running a simulated annealing search. The processing then starts with the command 'run'. By default, the program always outputs its results to the terminal screen (Figure 6), this can be re-directed to a named file via the keyword 'outputfile'. This enables the user to view the output file when the user is not necessarily sitting at the terminal. All commands inputted to the program are recorded along with any error messages in a log file called 'Movie.log'. This file can be analysed if a process does not produce the expected results.

A typical template file created to be used in MOVIE for a simplex search run for local minimisation and refinement is shown in Figure 7(a).

MOVIE has three output forms for the viewing mode: (i) a PDB atomic coordinates format, (ii) a sphere representation, (iii) DCAD, format which can be viewed with a WINDOWS software package called DESIGNCAD3D, and finally (iv) a 3D electron density map.

A typical template file to be used in creating an output PDB file for the coordinates of a model is shown in Figure 7(b). The second form of output from MOVIE, in which model parameters are output in cartesian coordinates for the positions of the centres and radii of spheres, we can use AVS for displaying the model in 3D space. The template file used in creating an output ascii file for the cartesian coordinates of a sphere representation of the model is shown in Figure 8(a). For the output file of this to be read in AVS, an AVS field file of the form shown in Figure 8(b) is also required.

The result of the PDB viewing mode is shown in Figure 9(a) displayed in RASMOL, showing one crown in end-on view (left) and slightly tilted side view (right) for the best model. The PDB file can also be viewed using any other crystallographic software, including FRODO, GRASP, O and PDBVIEWER. Figure 9(b) is the same as in Figure 9(a) but in the sphere representation viewed in AVS of the end-on view (left) and slightly tilted side view (right). It clearly shows the close similarity between the two forms of representation of the model and gives strength to the use of the sphere representation in the modelling procedure in MOVIE. Figure 9(c) shows an end-on view of the best insect myosin filament model for eight crowns, also displayed as AVS. This nicely shows the overall arrangement of the outer heads with their motor domains projecting outwards and with the inner heads forming a ring round the backbone.

Another viewing mode is to show the model as a 3D electron density map so that we can easily compare it with myosin filament models from EM analysis. To do this, MOVIE can be run in the 'reflection mode' where it computes the Fourier transform of a model along with the phases in CCP13 or CCP4 type format. The CCP13 format output file can be loaded into LSQINT to simulate the diffraction pattern and then displayed with XFIX, making it easy to visually compare the calculated diffraction pattern with the observed pattern shown in figure 4(d). The CCP4 format output file can be used to create a 3D density map. A typical template file used in MOVIE to create an output ascii reflection file for the h, k, l, intensity values of the best model is shown in Figure 10(a). The resolution limit can be set and, for this particular example, it was put at  $15 \text{ \AA}$  resolution. The output file is then fed into a command file (Figure 10(b)) that runs various CCP4 programs to create the final 3D density map. The resolution of the reconstruction can be selected and for this particular example it was set at  $200 \text{ \AA}$  to  $20 \text{ \AA}$ . This map file is in CCP4 format. It can either be directly displayed in PYMOL or CHIMERA. However, if AVS is used to display the map file, then a field file is required by AVS to display the 3D density map produced by the command file of Figure 10(b). This field file is shown in Figure 10(c). The result is shown in Figure 11 where the best insect myosin filament model is visualised both in the sphere representation (Figure 11a) and as a 3D density map (Figure 11b:left).

## Results for Insect Flight Muscle Myosin Filaments using the CCP13 and MOVIE programs

Application of MOVIE to the insect myosin filament diffraction data using the methods described above resulted in a best model with a 'goodness of fit' R-factor of 9.7% (AL-Khayat *et al.*, 2003). Interestingly, the best head conformation angles around

```

Terminal
MOVIE > status

Current Status

Modelling Method -
Global Parameter Search : DISABLED Down Hill Simplex Method : DISABLED
Powell's Method : DISABLED View Model : DISABLED
View Intensities : DISABLED Combined Refinement : DISABLED
Simulated Annealing : DISABLED Fourier Difference : DISABLED
Output Reflections : DISABLED Obs Output Reflections : DISABLED
Down Hill Replex Method : DISABLED Stochastic Torus Method : DISABLED

Similarity Measure -
Least Squares R-factor : DISABLED Similarity Weighting : DISABLED
Correlation Function : DISABLED Crystallographic R-factor: DISABLED
Scoring Method : DISABLED Manually Scale Data : DISABLED

Model Components -
Myosin Coordinates : DISABLED C_Protein Coordinates : DISABLED
Titin Coordinates : DISABLED Backbone Coordinates : DISABLED
Actin Coordinates : DISABLED Troponyosin Coordinates : DISABLED

Miscellaneous BOOL's -
OneShot Iteration : DISABLED Generate Bogus Data : DISABLED
BrookeHaven S1 : DISABLED No Perturbations : DISABLED

Search Range -

General Parameters -
No Of Molecular Strands : 0
Unit Cell Size : +0.0000A
Score Deviations : 0
Combine Weighting : 0.0
Number Of Filaments : 0
Resolution Cutoff : 0.0
Total Repeat Of Model : +0.0000A
Intensity Filename :
Data Output Filename :

MOVIE > run
    
```

(a)

```

Template_sim_anneal.ini (modified)
This is a template file for use with Movie
Contained here is a set of commands
to initialize Movie properly for simulated annealing search

Hind AL-Khayat 14th July 2003

Myosin Parameters

myosin
noperts
besnum 20
myheads 2
MPCROWN 8
STRANDES 4
MREPEAT 1167.41
MRMASTER 14.29
MSPHERE 8.607
mpivpoint 21
CELL 523.44
NUMREPS 2
totrepeat 1167.41
replevel 10.66666667
FILAMENTS 1
cutoff 65.0
HEADFILE /usr/users/hind/programs/Movie/Head_Data/Myosin_14.29A_Rot_Trans.asc
IFILE /usr/users/hind/APSAUG99/h09blsqse1_msk.dat
mslew head 1 start -65.8027708024 scale 5.0
mtilt head 1 start 24.0833472556 scale 5.0
mrotation head 1 start 4.1338040059 scale 5.0
mslew head 2 start 37.7505657482 scale 5.0
mtilt head 2 start 30.8411207739 scale 5.0
mrotation head 2 start 44.1261372208 scale 5.0
mheadsep start 5.5099967394 scale 5.0
mheadang start -5.1702109525 scale 5.0
mradisc start 60.3245221391 scale 5.0
LATTICEROT START 292.3800154568 scale 5.0
mpivtilt start 0.5255349971 scale 5.0
mpivslw start 0.0329833660 scale 5.0
mpivrot start 5.0 scale 5.0
TEMPERATURE 0.3
TEMPDROP 0.9
ITERATIONS 3000
anneal leastsq weighted
OUTPUTFILE data_sim_anneal.dat
status
    
```

(b)

Figure 5. (a) Screen shot when initially running Movie with the default parameters, being zero for all model parameters and (b) a typical template file to run with MOVIE when using simulated annealing for global search.

```

Terminal
MOVIE > status

Current Status

Modelling Method -
Global Parameter Search : DISABLED Down Hill Simplex Method : DISABLED
Powell's Method : DISABLED View Model : DISABLED
View Intensities : DISABLED Combined Refinement : DISABLED
Simulated Annealing : ENABLED Fourier Difference : DISABLED
Output Reflections : DISABLED Obs Output Reflections : DISABLED
Down Hill Replex Method : DISABLED Stochastic Torus Method : DISABLED

Similarity Measure -
Least Squares R-factor : ENABLED Similarity Weighting : ENABLED
Correlation Function : DISABLED Crystallographic R-factor: DISABLED
Scoring Method : DISABLED Manually Scale Data : DISABLED

Model Components -
Myosin Coordinates : ENABLED C_Protein Coordinates : DISABLED
Titin Coordinates : DISABLED Backbone Coordinates : DISABLED
Actin Coordinates : DISABLED Troponyosin Coordinates : DISABLED

Miscellaneous BOOL's -
OneShot Iteration : ENABLED Generate Bogus Data : DISABLED
BrookeHaven S1 : DISABLED No Perturbations : ENABLED

Search Range -
Myosin Positional Parameters:
Rot Lat - +292.3800 to +292.3800 Step +0.0000 Scale +5.0000
Radius - +60.3245 to +60.3245 Step +0.0000 Scale +5.0000
Head Sep - +5.5100 to +5.5100 Step +0.0000 Scale +5.0000
Head Angle - -5.1702 to -5.1702 Step +0.0000 Scale +5.0000
Pivot Tilt - +0.5255 to +0.5255 Step +0.0000 Scale +5.0000
Pivot Slew - +0.0330 to +0.0330 Step +0.0000 Scale +5.0000
Pivot Rot - +5.0000 to +5.0000 Step +0.0000 Scale +5.0000

Head 1: Slew - -65.8028 to -65.8028 Step +0.0000 Scale +5.0000
Tilt - +24.0833 to +24.0833 Step +0.0000 Scale +5.0000
Rot - +4.1338 to +4.1338 Step +0.0000 Scale +5.0000
Head 2: Slew - -37.7506 to -37.7506 Step +0.0000 Scale +5.0000
Tilt - +30.8411 to +30.8411 Step +0.0000 Scale +5.0000
Rot - +44.1261 to +44.1261 Step +0.0000 Scale +5.0000
    
```

(a)

```

Terminal
Paxial - +0.0000 to +0.0000 Step +0.0000 Scale +0.0000
Pazimuthal - +0.0000 to +0.0000 Step +0.0000 Scale +0.0000
Level 4: PRad - +0.0000 to +0.0000 Step +0.0000 Scale +0.0000
Paxial - +0.0000 to +0.0000 Step +0.0000 Scale +0.0000
Pazimuthal - +0.0000 to +0.0000 Step +0.0000 Scale +0.0000
Level 5: PRad - +0.0000 to +0.0000 Step +0.0000 Scale +0.0000
Paxial - +0.0000 to +0.0000 Step +0.0000 Scale +0.0000
Pazimuthal - +0.0000 to +0.0000 Step +0.0000 Scale +0.0000
Level 6: PRad - +0.0000 to +0.0000 Step +0.0000 Scale +0.0000
Paxial - +0.0000 to +0.0000 Step +0.0000 Scale +0.0000
Pazimuthal - +0.0000 to +0.0000 Step +0.0000 Scale +0.0000
Level 7: PRad - +0.0000 to +0.0000 Step +0.0000 Scale +0.0000
Paxial - +0.0000 to +0.0000 Step +0.0000 Scale +0.0000
Pazimuthal - +0.0000 to +0.0000 Step +0.0000 Scale +0.0000
Level 8: PRad - +0.0000 to +0.0000 Step +0.0000 Scale +0.0000
Paxial - +0.0000 to +0.0000 Step +0.0000 Scale +0.0000
Pazimuthal - +0.0000 to +0.0000 Step +0.0000 Scale +0.0000

Myosin:
Myosin Repeat : +1167.4100A
Myosin Crowns per Repeat : 8
S1 Head Raster Size : 14.29A
S1 Head Sphere Size : 8.61A
S1 Head Filename : /usr/users/hind/programs/Movie/Head_Data/Myosin_14.29A_Rot_Trans.asc
Pivotal Sphere Number : 21
Number Of Myosin Heads : 2
Number of Turns In Repeat : 10.67

General Parameters -
No Of Molecular Strands : 4
Unit Cell Size : +523.4400A
Score Deviations : 0
Combine Weighting : 0.0
Number Of Filaments : 1
Resolution Cutoff : 65.0
Number of Jn Functions : 20
Total Repeat Of Model : +1167.4100A
Intensity Filename : /usr/users/hind/APSAUG99/h09blsqse1_msk.dat
Data Output Filename : data_sim_anneal.dat
Temperature Factor : 0.300
Annealing Schedule : 3000
Temperature Drop Factor : +0.9000

MOVIE >
    
```

(b)

Figure 6. (a) Screen shot of the beginning and (b) the end of the output when using the template file in Figure 5(b).

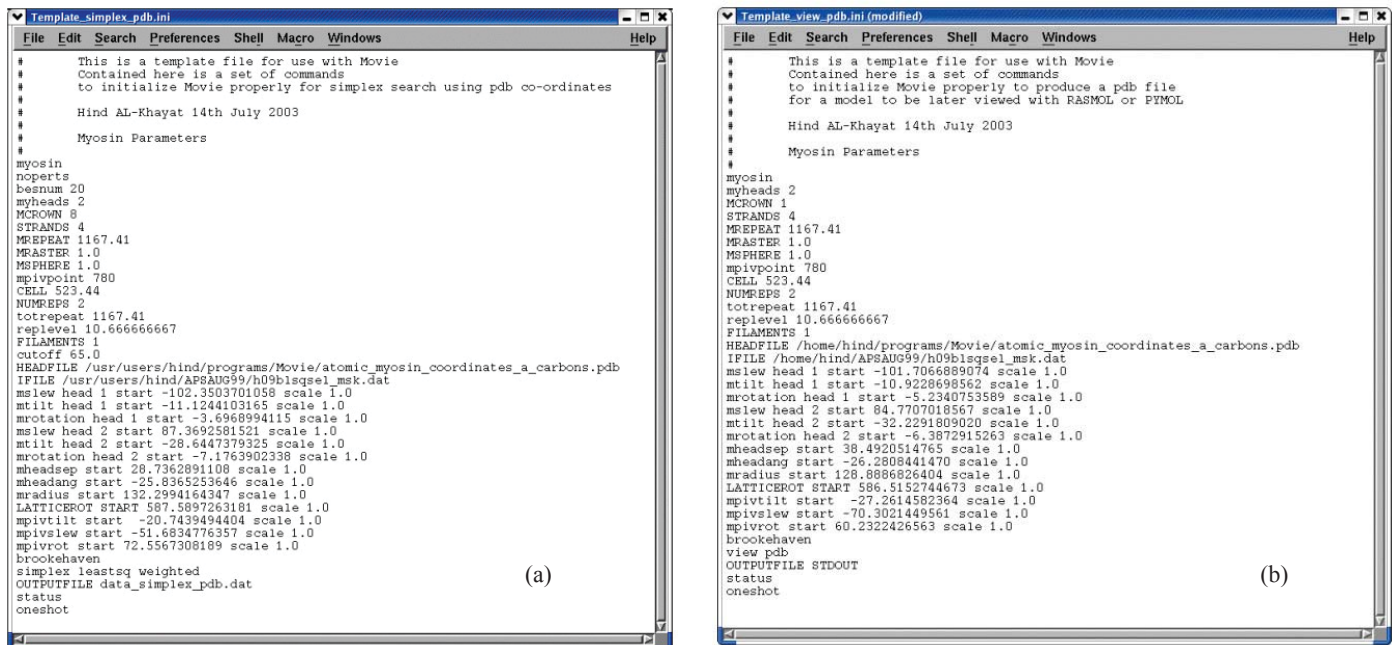


Figure 7. (a) Template file created to be used in MOVIE for a SIMPLEX search run for local minimisation and refinement. (b) Template file to be used in creating an output PDB file for the coordinates of a model.

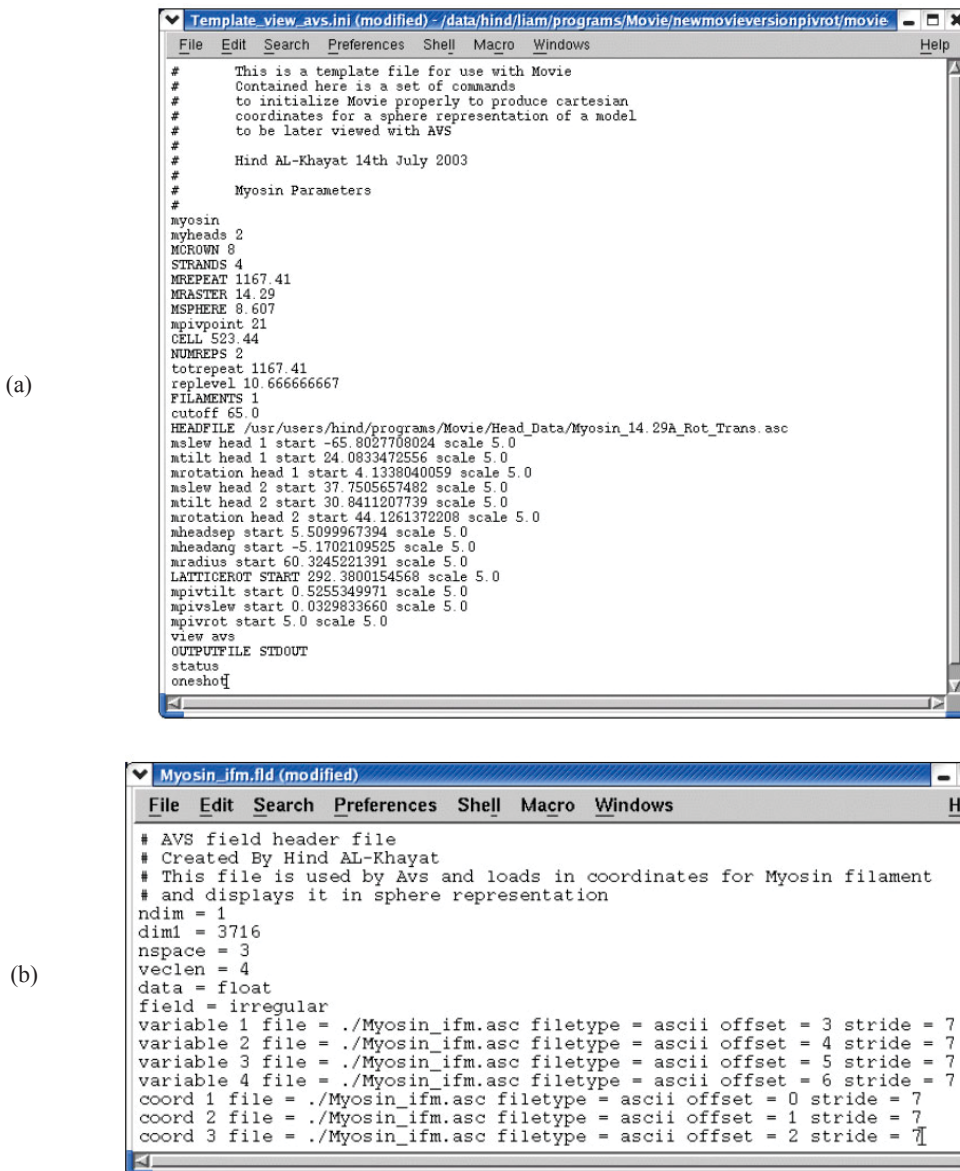


Figure 8. (a) Another form of output from MOVIE, outputting model parameter in cartesian coordinates for the positions of the centres of spheres and the radii of each, used in AVS for display, Template file to be used in creating an output ascii file for the cartesian coordinates of a sphere representation of the model. (b) field file required by AVS to display the sphere representation of a model produced in (a).

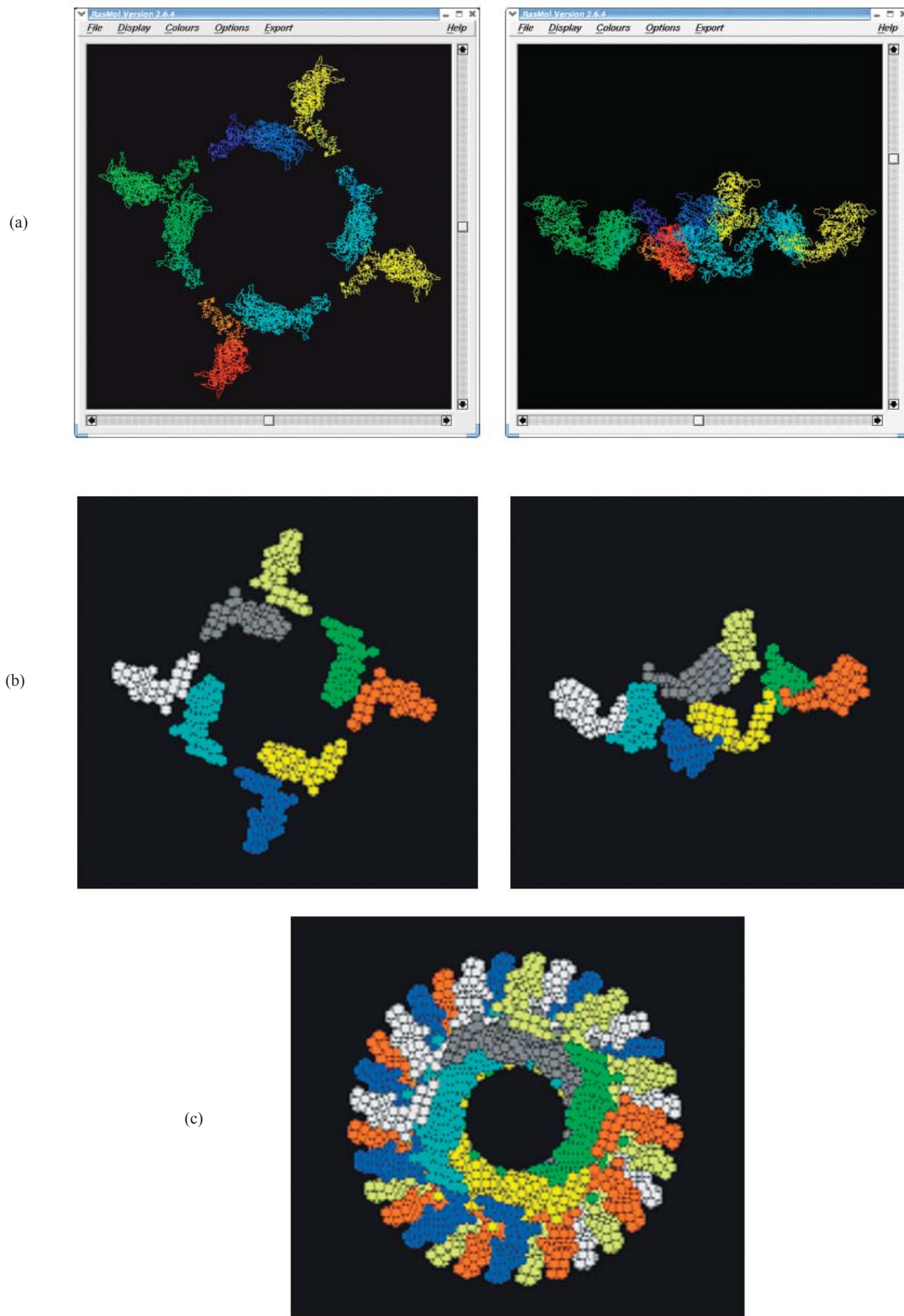


Figure 9. (a) MOVIE output as PDB coordinates and displayed in RASMOL, showing one crown in end-on view (left) and slightly tilted side view (right) for the best model. (b) same as in (a) but in the sphere representation, end-on view (left) and slightly tilted side view (right), for the best model displayed in AVS. (c) end-on view of the best model for eight crowns, also displayed in AVS.

(a)

```

Template.reflection.pdb.ini - /data/hind/liam/programs/Movie/newmoviever
File Edit Search Preferences Shell Macro Windows Help
#
# This is a template file for use with Movie
# Contained here is a set of commands
# to initialize Movie properly to produce a reflection file
# calculated using the pdb coordinates
# for a model to be later viewed with AVS or PYMOL
#
# Hind AL-Khayat 14th July 2003
#
# Myosin Parameters
#
myosin
myheads 2
MORROW 1
STRANDS 4
MREPEAT 1167.41
MRMASTER 1.0
MSPHERE 1.0
mpivpoint 780
CELL 523.44
NUMREPS 2
totrepeat 1167.41
replevel 10 66666667
FILAMEENTS 1
HEADFILE /home/hind/programs/Movie/atomic_myosin_coordinates_a_carbons.pdb
IFILE /home/hind/APSAU099/h09b1sgsel_msk.dat
mslew head 1 start -101.7066889074 scale 1.0
mtilt head 1 start -10.929389862 scale 1.0
mrotation head 1 start -5.2340753589 scale 1.0
mslew head 2 start 84.7707018567 scale 1.0
mtilt head 2 start -32.2291809030 scale 1.0
mrotation head 2 start -6.3872915263 scale 1.0
mheadsep start 38.4920514765 scale 1.0
mheadang start -26.2808441470 scale 1.0
mradius start 128.8886826404 scale 1.0
LATTICEROT START 596.5152744673 scale 1.0
mpivotlt start -27.2614582364 scale 1.0
mpivlev start -70.3021449551 scale 1.0
mpivotrt start 60.2322426563 scale 1.0
brookhaven
bosqdata
resbosqdata 15.0
reflection
OUTPUTFILE ifm_rfs.dat
status
oneshot

```

(b)

```

insect_ifm_ccp4.com
File Edit Search Preferences Shell Macro Windows Help
#
# This is a command file to run three CCP4 programs
# that reads in the reflection file created by Movie
# and creates a map file for the 3D electron density map.
#
# Hind AL-Khayat 10th February 2004
#
#
# Convert reflection file to mtz format using "f2mtz"
#
f2mtz hklin ifm_rfs.dat hklout ifm_rfs.mtz << eof
TITLE modelled data MTZ
CELL 523.44 523.44 1167.41 90 90 120
SYMMETRY P1
LABOUR H K L FP PHIC
CTYPE H H H F P
END
eof
#
# Convert mtz file to map file using "fft"
#
fft hklin ifm_rfs.mtz mapout ifm_rfs.map << eof
TITLE FFT model
LABIN F1=FP PHI=PHIC
AXIS X Y Z
RESOLUTION 200 25
GRID 72 72 160
SCALE F1 3000000
eof
#
# use "extend" to produce the final map file for
# full-length myosin filament
#
extend mapin ifm_rfs.map mapout ifm_rfs_ext.map << eof
XYZLIM -37 37 -37 37 0 349
eof
#

```

(c)

```

insect_ifm_ccp4.fld (modified)
File Edit Search Preferences Shell Macro Windows Help
#
# AVS field header file
# This file is used by Avs and loads the 3D map file created
# by insect_ifm_ccp4.com
#
#
ndim = 3
dim1 = 114
dim2 = 66
dim3 = 350
nspc = 3
veclen = 1
data = float
field = uniform
variable 1 file = ifm_rfs_ext.map.asc filetype=ascii skip = 1

```

Figure 10. (a) Template file to be used in MOVIE to creating an output ascii reflection file for the h, k, l, intensity values of the best model. (b) command file that reads in the output file of (a) from MOVIE and uses various CCP4 programs to create a 3D density map. (c) field file required by AVS to display the 3D density map produced in (b).

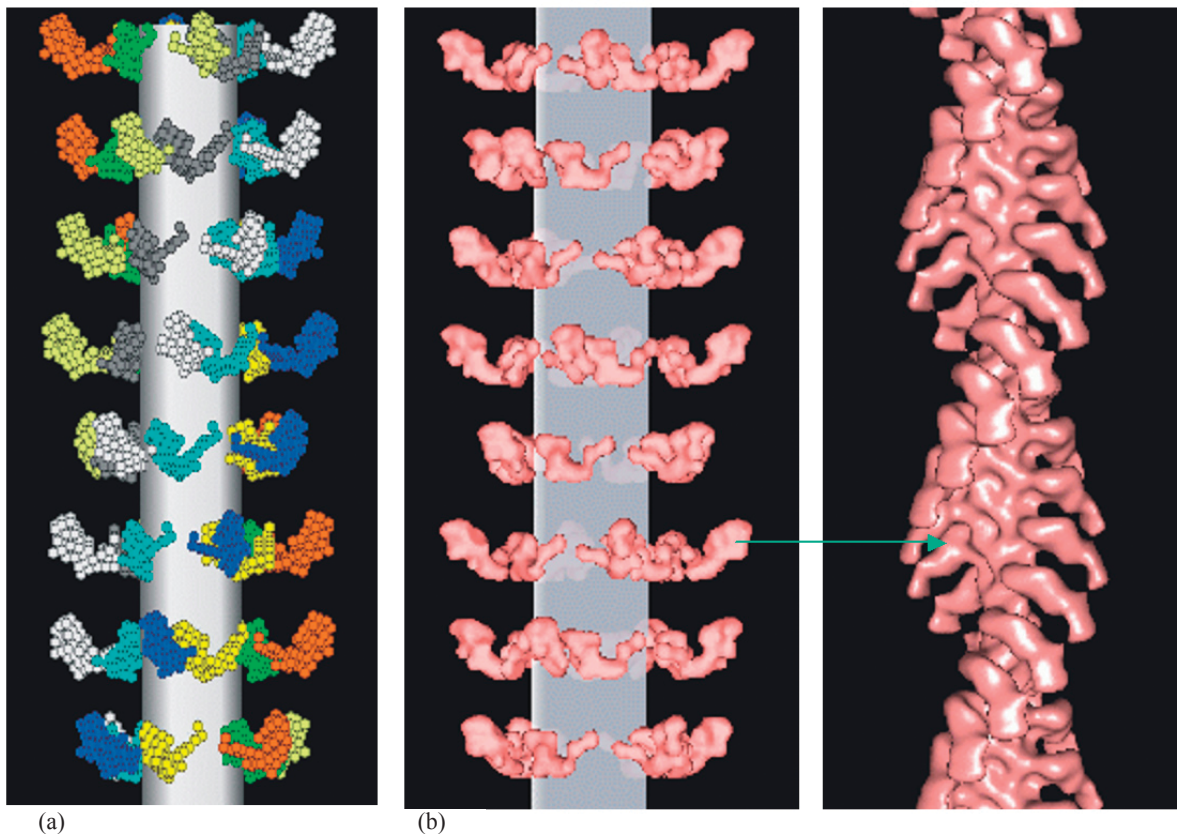


Figure 11. (a) The best model for IFM displayed as sphere representation, displayed in AVS. (b) left: as a 3-D density map using the PDB coordinates and reconstructed to 20 Å resolution, displayed in AVS; right: an actin filament labelled with S1 is shown to visualise the movement required by the myosin head in going from a relaxed myosin filament to finally attach to actin in the rigor confirmation, displayed in PYMOL.

the hinge gave a head shape that was close to that typical of relaxed M·ADP·Pi heads; a head shape never before demonstrated in intact muscle. The best packing constrained the 8 heads per crown within a compact crown shelf projecting perpendicular to the filament axis (Figure 11a, b:left). The two heads of each myosin molecule had non-equivalent positions, one head projecting outward while the other curves round the thick filament circumference to nose against the proximal neck of the projecting head of the neighbouring molecule (Figure 9a,b). The relaxed projecting head, oriented almost as needed for actin attachment, will attach, then release Pi followed by ADP, as the lever arm with a purely axial change in tilt drives ~100 Å of actin filament sliding on the way to the nucleotide-free limit of its working stroke (Figure 11b:right). ATP binding causes post-powerstroke myosin to release actin and relax again. Energy from splitting ATP fuels the next powerstroke. The four inward-pointing heads each touch an adjacent projecting head at a critical point, a contact that may simply inhibit the ability of both myosin heads to cleave high-energy ATP molecules. The final crown arrangement therefore appears well-designed to support the cycle of contraction of asynchronous fibrillar flight muscles used in flight by insects along with its well-known stretch-activation response. However, this is not the place to discuss such results in detail. This is done elsewhere (AL-Khayat *et al.*, 2003).

Our result shows that low-angle X-ray diffraction data is rich enough to give an atomic structure of the myosin head from intact relaxed muscle if used along with the powerful CCP13 stripping software and modelling by the simulated annealing search procedure using proteins of known molecular structures using MOVIE.

### Potential of low-angle X-ray diffraction

The potential exists using this approach to fully 'solve' the whole of the resting *Lethocerus* flight muscle unit cell to 65 Å resolution or better. There is also data to higher resolution, both axially and radially, but the sampling might not be as good as in the low-angle pattern. However, this should be sufficient to enable us to model the full IFM unit cell, using all of the 468 independent observed reflections. The modelling should include all the unit cell protein components, including actin filaments, troponin and tropomyosin as well as the thick filament. Our results serve to illustrate that a great deal can be achieved with low-angle X-ray diffraction data given that it has been properly stripped (e.g. by the appropriate CCP13 software) and has been carefully modelled with proteins of known molecular structure and the appropriate modelling software (e.g. MOVIE). This analysis and previous modelling studies on actin filament structure using related methods (AL-Khayat *et al.*, 1995) confirm that highly accurate modelling with positional sensitivities of a few Å can be achieved from low-angle X-ray diffraction data.

In order to model the myosin pattern even better than has been done in the present study, we need to add more parameters for myosin. This includes allowing the two heads within a molecular pair to have different shapes as well non-equivalent positions. This will require the addition of three more parameters for the pivot slew, pivot tilt and pivot rotation of the second head and will be part of future efforts. Other minor protein components of the thick filament might also affect the

myosin intensities. It will be very interesting to study the contributions of these proteins to the low-angle diffraction pattern pattern, although it is assumed to be small, as was found in modelling the myosin filament structure of relaxed bony fish (Hudson *et al.*, 1997).

### Conclusion

In summary, by rigorously stripping the low-angle X-ray diffraction pattern from relaxed insect flight muscle using CCP13 software and modelling the myosin filament structure using the program MOVIE we have been able to identify for the first time in intact muscle a myosin head shape clearly different from the nucleotide-free, rigor, state. This clearly illustrates the enormous power of the method. Our data add new and precise support for the active myosin head cycle first inferred from thin-section EM of relaxed and rigor IFM (Reedy *et al.*, 1965), finally showing resting cross-bridges truly at ~90°, with their actin-binding sites suitably oriented toward actin. The catalytic motor domain positions with respect to actin appear to be almost the same in both the relaxed and active or rigor states, as though the projecting relaxed heads are poised to enable very rapid attachment to correctly oriented target sites on an adjacent actin filament. Once the catalytic domain has attached, the head can sequentially release hydrolysis products Pi and ADP as it moves towards the nucleotide-free (rigor) state. This requires only an axial swing of the neck region (lever arm) through about 90° around the pivot point (making the whole head including the catalytic domain appear to rotate to the conventionally quoted 45° rigor angle) and giving an axial step of about 100 Å. An ATP-induced detachment and resetting of the head to the M·ADP·Pi state, followed by repositioning the head near to the original relaxed configuration will automatically set up another potential contractile cycle in the oscillating muscle. The resting myosin head configuration within the crown also provides a possible explanation for the uniquely developed stretch-activation response in insect flight muscle.

### Acknowledgements

We thank Bruce Baumann for assistance in collecting fibre X-ray diffraction patterns from IFM at the Argonne/ APS/ BioCAT beamline. We acknowledge specific support for this work to JMS from a UK BBSRC project grant (# 28/S10891). MKR was supported by NIH AR-14317. CCP13 software was developed as part of UK BBSRC/ EPSRC funded projects (e.g. # 28/B10368 & 28/B15281). Use of the Advanced Photon Source was supported by the U.S. Department of Energy, Basic Energy Sciences, Office of Energy Research, under Contract No. W-31-109-ENG-38. BioCAT is a U.S. National Institutes of Health-supported Research Centre RR08630.

### References

- [1] AL-Khayat, H.A., Yagi, N. & Squire, J.M. (1995) Structural changes in actin-tropomyosin during muscle regulation: Computer modelling low-angle X-ray diffraction data, *J. Molec. Biol.*, **252**, 611-632
- [2] AL-Khayat, H.A., Hudson, L., Reedy, M.K., Irving, T.C. & Squire, J.M. (2003) Myosin head configuration in relaxed

- insect flight muscle: X-ray modelled resting cross-bridges in a pre-powerstroke state are poised for actin binding, *Biophys. J.*, **85**, 1063-1079
- [3] Brent, R. P. (1973) *Algorithms for minimisation without derivatives* (Chap. 5) (Englewood Cliffs, NJ, Prentice-Hall).
- [4] Dominguez, R., Freyzon, Y., Trybus, K. M. & Cohen, C. (1998) Crystal structure of a vertebrate smooth muscle myosin motor domain and its complex with the essential light chain: visualization of the pre- power stroke state, *Cell*, **94**, 559-571
- [5] Harford, J. & Squire, J. M. (1997) Time-resolved diffraction studies of muscle using synchrotron radiation, *Rep. Prog. Phys.*, **60**, 1723-1787
- [6] Harford, J.J., Denny, R.C., Morris, E., Mendelson, R. & Squire, J.M. (1996) 3-D reconstruction from fibre X-ray diffraction patterns: Myosin-decorated actin filaments. *Fibre Diffraction Review*, **5**, 27-29.
- [7] Hibberd, M. G. & Trentham, D. R. (1986) Relationships between chemical and mechanical events during muscular contraction, *Ann. Rev. Biophys. & Biophys. Chem.*, **15**, 119-161
- [8] Houdusse, A., Szent-Gyorgyi, A. G. & Cohen, C. (2000) Three conformational states of scallop myosin S1, *Proc. Natl. Acad. Sci. U.S.A.*, **97**, 11238-11243
- [9] Hudson, L. (1996) *Ultrastructure of the A band unit cell in relaxed muscle*, Ph.D. thesis, University of London, London
- [10] Hudson, L., Harford, J. J., Denny, R. C. & Squire, J. M. (1997) Myosin head configuration in relaxed fish muscle: resting state myosin heads must swing axially by up to 150 Å or turn upside down to reach rigor, *J. Molec. Biol.*, **273**, 440-455
- [11] Irving, T. C., Fischetti, R., Rosenbaum, G. & Bunker, G. B. (2000) Fibre Diffraction Using the BioCAT Undulator Beamline at the Advanced Photon Source, *Nuclear Instruments and Methods (A)*, **448**, 250-254
- [12] Kirkpatrick, S., Gelatt, C. & Vecchi, M. (1983) Simulated annealing methods, *Science*, **220**, 671-680
- [13] Kirkpatrick, S. (1984) Simulated annealing methods, *J. Stat. Phys.*, **34**, 975-986
- [14] Nelder, J. & Mead, R. (1965) The simplex method for function minimisation, *Computer J.*, **7**, 308-313
- [15] Press, W. H., Teukolsky, S., Vetterling, T. and Flannery, B. (1992) *Numerical Recipes in C*, 2d edn (Cambridge, UK, Cambridge Univ. Press)
- [16] Rayment, I., Holden, H. M., Whittaker, M., Yohn, C. B., Lorenz, M., Holmes, K. C. & Milligan, R.A. (1993b) Structure of the actin-myosin complex and its implications for muscle contraction, *Science*, **261**, 58-65
- [17] Rayment, I., Rypniewsky, W. R., Schmidt-Bäse, K., Smith, R., Tomchick, D. R., Benning, M. M., Winkelmann, D. A., Wesenbergand, G. & Holden, H.M. (1993a) Three-dimensional structure of myosin subfragment-1: a molecular motor, *Science*, **261**, 50-58
- [18] Reedy, M. K., Holmes, K. C. & Tregear, R. T. (1965) Induced Changes in Orientation of the Cross-bridges of Glycerinated Insect Flight Muscle, *Nature*, **207**, 1276-1280
- [19] Reedy, M. K., Squire, J. M., Baumann, B. A., Stewart, A. & Irving, T. C. (2000) X-ray Fibre Diffraction of the Indirect Flight Muscle of *Lethocerus indicus*, In *Advanced Photon Source User Activity: Report 2000* (Argonne, IL, Argonne National Laboratory).
- [20] Squire, J. M. (2000) Fibre and Muscle Diffraction, In *Structure and Dynamics of Biomolecules*, E. Fanchon, E. Geissler, L.-L. Hodeau, J.-R. Regnard, and P. Timmins, eds. (Oxford, UK, Oxford Univ. Press), 272-301
- [21] Squire, J. M., Cantino, M., Chew, M., Denny, R., Harford, J., Hudson, L. and Luther, P. (1998) Myosin rod-packing schemes in vertebrate muscle thick filaments, *J. Struct. Biol.*, **122**, 128-138
- [22] Xu, S., Gu, J. Rhodes, T., Belknap, B., Rosenbaum, G., Offer, G., White H. & Yu., L.C. (1999) The M.ADP.P(i) state is required for helical order in the thick filaments of skeletal muscle, *Biophys. J.*, **77**, 2665-2676

## Expanded Poster-Prize Abstracts

### SAXS study of the influence of added clay particles on a block copolymer gel

V. Castelletto & I. W. Hamley

Department of Chemistry, University of Leeds, Leeds, LS2 9JT, UK

Received 28th October 2003; accepted in revised form 16th March 2004

#### 1. Introduction

Inorganic filler particles are added to soft materials such as polymers to improve their mechanical properties, and also to alter properties such as colour, flame resistance or permeability. Clay particles are plate-like mineral moieties, based on silicates or aluminosilicates [1]. They are widely used in those applications due to their ease of availability and processing and low cost. A recent focus has been on polymer-clay nanocomposites, in which the polymer chains are intercalated between clay layers [2].

In the present study, we investigate the effect of added clay particles on the structural and rheological properties of a hexagonal (H) mesophase formed by a triblock copolymer surfactant. An account of this work has been published recently [3]. However, some details of the calculation of the lamellar elasticity from the structure factor were incorrect, as discussed herein. The clay particles used are the synthetic hectorite, Laponite RDS. The triblock employed here is one of the widely used Pluronic family of poly(oxyethylene)-poly(oxypropylene)-poly(oxyethylene) (EPE) polymer surfactants - P123 ( $E_{20}P_{70}E_{20}$ ). We are not aware of previous studies of the structure or rheology of Laponite RDS suspensions. Laponite RDS differs from the more widely used Laponite RD due to the presence of a peptizing agent. The influence of shear on the orientation of PEO chains and Laponite RDS particles has been studied by SANS on mixtures of these two components in aqueous solution [4]. There has been also limited prior work on mixed Laponite/surfactant solutions. The adsorption of non-ionic surfactants ( $C_{12}E_5$  and  $C_{12}E_8$ , C=methyl) onto Laponite RD particles has been investigated by adsorption isotherm and small-angle neutron scattering measurements (SANS) [5]. In a subsequent study, the location of Laponite particles in the swollen lamellar (L) or sponge phase of aqueous solutions of  $C_{12}E_5$  and  $C_{12}E_4$  was probed by SANS [6].

#### 2. Experimental Section

**2.1. Materials.** The synthetic clay used was Laponite RDS, obtained as a gift from Rockwood Additives Ltd. Laponite RDS particles are stable at pH 9.5, so our solutions are prepared under these alkaline conditions [7-11]. Block copolymer surfactant Pluronic P123 was obtained as a gift from Uniqema. The molecular weight of this triblock copolymer is 5750 g mol<sup>-1</sup> [12]. The phase diagram of P123 in water has been reported [13].

**2.2. Preparation of Mixtures.** The clay dispersions were prepared by slowly adding Laponite RDS powder to ultrapure water (Milli-Q-Plus) with constant stirring for at least 15 min. The pH of the dispersions was maintained at 9.5 by adding analytical grade NaOH. Mixtures were prepared by adding aqueous gels containing Pluronic surfactant to Laponite solutions of different concentrations, such that the final mass fraction of P123 defined as  $w_S = m(\text{P123}) / [m(\text{P123}) + m(\text{Laponite} + \text{water})]$  was  $w_S = 0.5$  (50wt%), where  $m$  denotes mass. The mass fractions of Laponite are defined as  $w_L = m(\text{Laponite}) / [m(\text{Laponite}) + m(\text{water})]$  [6].

**2.3. Small angle X-ray Scattering (SAXS).** SAXS experiments were performed at the Synchrotron Radiation Source (SRS) at Daresbury Laboratory, Warrington, UK. Samples were studied either at rest or after oscillatory shear. Static experiments were performed on beamlines 8.2 and 2.1, while shear flow experiments were undertaken on beamline 16.1. All three stations are configured with an X-ray wavelength  $\lambda = 1.5 \text{ \AA}$ . On station 8.2 the scattered intensity was recorded using a quadrant SAXS detector that measures intensity in the radial direction, while on both beamline 2.1 and station 16.1, the scattered intensity was recorded on a multiwire gas-filled area detector. A scattering pattern from a specimen of wet collagen (rat-tail tendon) was used for calibration of the  $q$  scale ( $q = |\mathbf{q}| = (4\pi \sin\theta) / \lambda$ , where the scattering angle is  $2\theta$ ) of the scattering profile.

For the static measurements the samples were mounted in sealed 1 mm thick brass cells, with an inner spacer ring to hold liquids, sealed between mica windows, and connected to a water bath for temperature control. Oscillatory shear was applied to the samples using a Rheometrics RSA II soft solids system with shear sandwich geometry. A detailed description of the rheometer is provided elsewhere [14,15]. It enables simultaneous acquisition of SAXS and rheology data. The shear sandwich cell comprises three rectangular plates, perpendicular to the X-ray beam, which is incident along  $\nabla v$ , so that the  $(\mathbf{q}_v, \mathbf{q}_e)$  plane is accessed in SAXS experiments.

#### 3. Results and Discussion

Laponite particles have previously been shown to be plate-like. The SAXS data for 2 wt % Laponite RDS in aqueous solution at pH 10 was fitted to the form factor corresponding to a disk-like particle with thickness  $\Gamma$  and radius  $R$  [16] (Figure 1). The fitting provided  $2R = (35.3 \pm 0.3) \text{ nm}$  and  $\Gamma = (2.1 \pm 0.1) \text{ nm}$ . The

values  $2R = 30$  nm,  $\Gamma = 1$  nm and  $2R = 25$  nm,  $\Gamma = 0.9$  nm were reported, for Laponite RD, by Mourchid [7] and Kroon [17] respectively. Compared to the previous results for Laponite RD, the diameter and thickness reported here for Laponite RDS are both increased due presumably to the adsorbed anions.

The structure of gels containing 0-9 wt % added Laponite RDS at pH 10 was determined by SAXS, in the temperature range from 25 to 75 °C. The main feature of the SAXS patterns for gels of P123 in the absence of Laponite, is a series of Bragg reflections located in the positional ratio 1:  $\sqrt{3}$ :  $\sqrt{4}$ :  $\sqrt{7}$ :  $\sqrt{9}$ , as expected for a hexagonal lattice. These results are consistent with the previously reported phase diagram of P123 in water [13].

The SAXS intensity as a function of the temperature was then recorded for P123 gels with 3-7 wt% Laponite RDS. A discontinuity in the position of a higher order reflection, and in the intensity of the first order reflection is apparent at high temperature. We measured the position of the scattering peaks from each SAXS profile, and the results are contained in Figure 2, which shows the position of the scattering peaks as a function of temperature.

Figure 2 shows that at low temperature the gels are characterized by three to five reflections with a positional ratio 1:  $\sqrt{3}$ :  $\sqrt{4}$ :  $\sqrt{7}$ :  $\sqrt{9}$  corresponding to the first five orders of reflection from a H structure [18]. In contrast, at high temperature only two or three reflections were measured with a positional ratio 1:2:3 within the experimental error, which are indexed to the 100, 200 and 300 reflections respectively of a L phase [18]. For intermediate temperatures, and for samples containing between 3 and 7 wt % added Laponite, a set of reflections in the positional ratio 1:  $\sqrt{3}$ :  $\sqrt{4}$ :  $\sqrt{7}$  is also present, suggesting that both H and L orders co-exist in the system (Figure 2). A transition from H to L structures is not observed for a 50 wt % gel of the copolymer alone between 25 and 75 °C [13]. Therefore, the results shown in Figure 2 suggest that the addition of Laponite RDS to the system induces an H to L phase transition at high temperature.

To confirm a structural transition, SAXS patterns were obtained from samples aligned using large-amplitude oscillatory shear (frequency  $\omega = 100$  rad s<sup>-1</sup> and strain amplitude  $A = 70\%$ ). Figure 3 shows the two-dimensional SAXS patterns obtained at rest following shear, for a gel with 9 wt % Laponite RDS, at 30°C (Figure 3a) and 60°C (Figure 3b). In both cases, two pairs of equatorial reflections are observed. At 30°C, these are in the positional ratio 1:  $\sqrt{3}$  and at 60°C they are in the ratio 1: 2. The former is consistent with a shear-aligned H phase in which the cylinder axis is parallel to the direction of flow, while the latter results indicate that oscillatory shear orients the layers in the L phase perpendicular to the ( $\mathbf{q}_v$ ,  $\mathbf{q}_e$ ) plane, with the lamellae normal parallel to the neutral axis.

From the location of the SAXS peaks it is possible to determine the domain spacing in the H and L phases as a function of temperature. In particular, the average distance between cylinders in the H phase,  $d = 2\pi/q^*$  ( $q^*$  = position of the first scattering peak), is calculated in the same way as the interlayer distance  $d$  in the L phase. Figure 2 shows that  $q^*$  decreases (i.e.  $d$  increases) with temperature, and there are no discontinuities across the phase transition boundary. The fact that  $q^*$  changes

continuously across the transition (Figure 2) indicates that the transition between H and L structures is epitaxial.

It is possible to undertake a qualitative analysis of the order of the anisotropic particles dispersed in the L phase. Two relevant distances can be distinguished: the centre-to-centre particle separation,  $D_{2D}$ , and the intermembrane separation distance,  $D$ . The two-dimensional particle-particle separation, for particles located on average in the mid-plane between the surfactant lamellae separated by a water thickness  $D$ , is given by

$$D_{2D} = \sqrt{\frac{2V_L(C_L + \rho_L)}{3DC_L}}$$

( $V_L$  : volume of a Laponite disk,  $C_L$ : mass of dried Laponite divided by the mass of water and  $\rho_L = 2.53$  is the density of Laponite with respect to water). Using the parameters from the form factor fit to the SAXS profile from a Laponite disk (Figure 1),  $V_L = \pi R^2 H = 1923.3$  nm<sup>3</sup>. The intermembrane separation distance  $D = d(1-\phi)$  is expressed as a function of the hydrophobic layer thickness, where the  $d$  values are taken from  $q^*$ , and

$$\phi = \frac{w_s \rho_L (1 + C_L)}{d_s \rho_L + \rho_L w_s (1 - d_s) + C_L (\rho_s + w_s (\rho_L - \rho_s))}$$

is the volume fraction of polymer in the P123/Laponite/water system ( $w_s = 0.5$ : mass fraction of surfactant in the sample and  $\rho_s = 1.05$  is the density of P123 relative to water) [12].

Figure 4 shows the evolution of  $D_{2D}$  and the fraction  $D_{2D}/D$  as a function of temperature, for different concentrations of Laponite RDS, within the L phase. As expected, the average distance between the clay disks decreases with increasing Laponite concentration (Figure 4a) as does the ratio  $D_{2D}/D$  (Figure 4b). Figures 4b-d show that the centre-to-centre distance is always higher than the intermembrane distance, ensuring enough space for the disks to freely spread between the lamellae.

These calculations on the separation of Laponite particles within and between layers confirm that there is ample space for them to be intercalated between lamellae. It is thus proposed that the H-to-L transition is driven by the increase in packing entropy of the disks in the L phase, compared to the H phase. Assuming that the particles are preferentially located in the aqueous region, the volume available to the particles is smaller in the H phase since the packing fraction of surfactant is higher. The concentration dependence of the transition arises because the excluded volume available to the particles (more of which is "explored" by the Brownian motion of particles at high temperature) decreases with increasing particle concentration.

To obtain an insight into the effect of the Laponite on the elasticity of the layers in the L phase, we used the model of Caillé [19] to fit the shape of the SAXS reflections. For aligned one-dimensional systems the scattered intensity should exhibit an asymptotic power-law behaviour  $S(q) \sim |q - q_{0,m}|^{-2+\eta_m}$ , where  $\eta_m$  is the  $m$ th- order Caillé parameter and  $q_{0,m}$  is the position of the  $m$ th- order scattering peak [19,20]. This was the expression

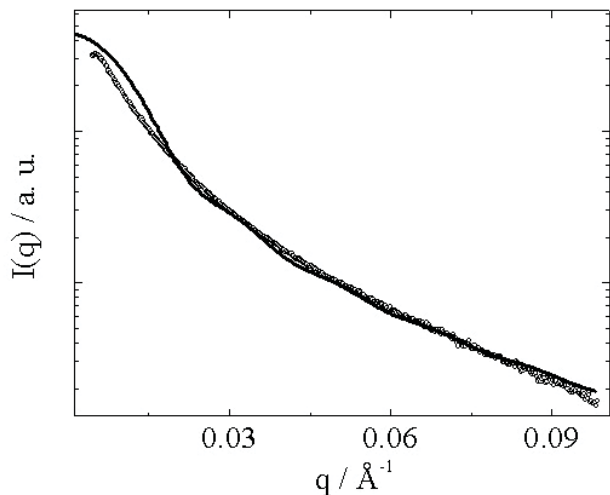


Figure 1. SAXS profile measured for a 2 wt % laponite RDS aqueous solution (O) and the calculated form factor for an isolated disk-shaped particle (—). In the model, the particle diameter and thickness are  $2R = 350 \text{ \AA}$  and  $\Gamma = 20 \text{ \AA}$  respectively.

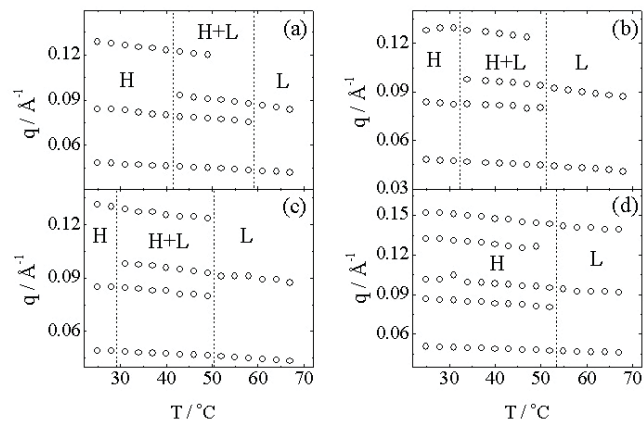


Figure 2. Temperature dependence of the Bragg peak positions for 50 wt% P123 with (a) 3, (b) 4.5, (c) 7 and (d) 9 wt% Laponite RDS. The traced lines divide the regions of hexagonal (H), lamellar (L) and H/L phase co-existence.

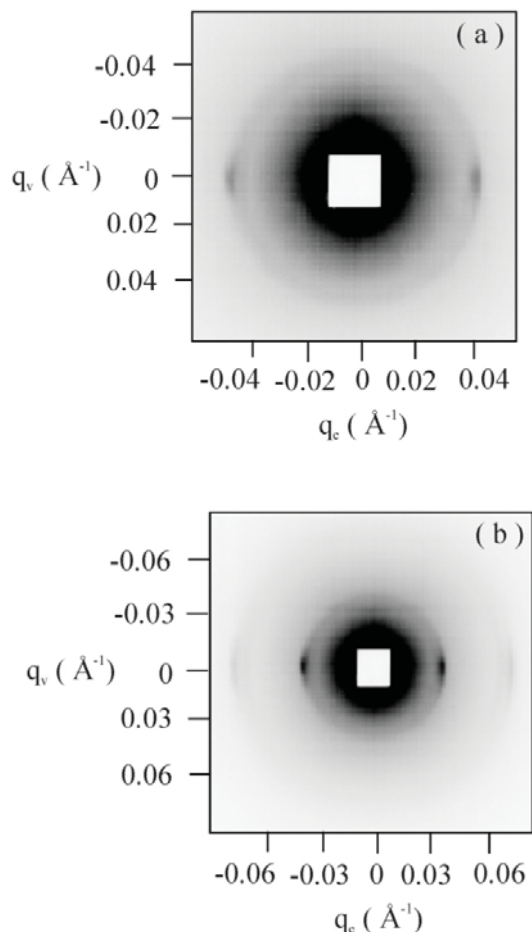


Figure 3. SAXS pattern in the  $(q_v, q_c)$  plane obtained at (a)  $30^\circ\text{C}$  (the second order peak is not shown in the figure because the contrast scale used does not allow first and second order reflections to be shown simultaneously) and (b)  $60^\circ\text{C}$  for a gel containing 9 wt% added Laponite RDS, at rest after oscillatory shear in the shear sandwich at a frequency  $\omega = 100 \text{ s}^{-1}$ , and strain amplitude  $A = 70\%$ .

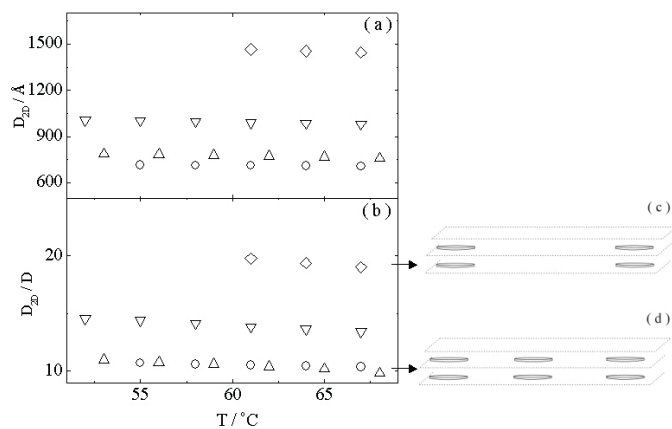
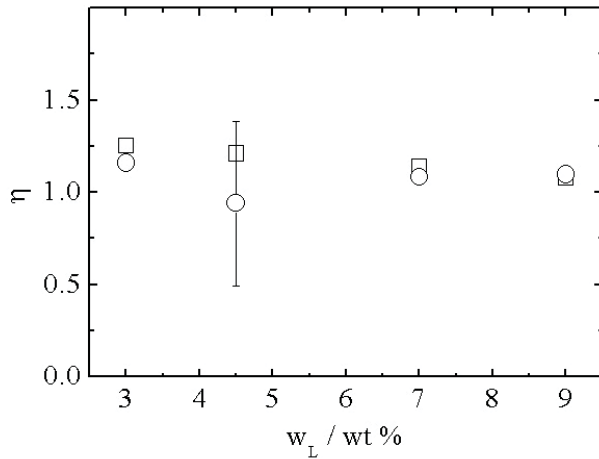


Figure 4. Dependence of (a)  $D_{2D}$  and (b)  $D_{2D}/D$  on temperature for a 50 wt % P123 gel with ( $\diamond$ ) 3, ( $\nabla$ ) 4.5, ( $\Delta$ ) 7 and (O) 9 wt% added Laponite RDS. Shown alongside are sketches indicating the size and spacing of disks compared to the lamellar spacing, for (c) 3 wt % added Laponite at  $75^\circ\text{C}$  and (d) 9 wt % added Laponite at  $67^\circ\text{C}$ .



**Figure 5.** Dependence of the Caillé parameter on concentration of added Laponite. (O) Caillé parameter extracted from fitting peaks in the SAXS profiles, (∇) calculated according to the Helfrich model. The standard deviation of the fitted Caillé parameter is shown for 4.5 wt % added Laponite.

used previously by us [3]. However, for unoriented samples, as investigated here, we need to take a powder average. This leads to  $S(q) \sim |q - q_{o,m}|^{-1+\eta_m}$  [21, 22].

An averaged value of the Caillé parameter,  $\bar{\eta}$ , was obtained using the set of  $\eta_m$  values for a particular SAXS profile, i.e. calculating the average of

$$\eta = \frac{\eta_m}{m^2} = \frac{q_o^2 k_B T}{8\pi \sqrt{KB}}$$

Here  $K$  and  $B$  are elastic and compression moduli for lamellae respectively [19,20]. The dependence of  $\bar{\eta}$  on concentration of added Laponite (at a constant temperature  $T = 61^\circ\text{C}$ ) is illustrated in Figure 5, together with the Caillé parameter calculated based on the theory of Helfrich developed for the L phase of nonionic surfactants [23]. In this model [20]

$$\eta = \frac{4}{3} \left(1 - \frac{\delta}{d}\right)^2$$

Figure 5 shows that the experimental  $\eta$  is very close that predicted by the Helfrich model, indicating the entropic interactions between fluctuating lamellae govern the elasticity of the lamellar substrates. This suggests, in contrast to the conclusions reached in our previous work [3], that the poly(oxyethylene) chains extending into the water layer might not interact with Laponite. It is also evident, in good agreement with our previous study [3], that both  $\bar{\eta}$  and the Caillé parameter predicted by the Helfrich model are essentially independent of Laponite content in the sample.

#### 4. Summary

A transition between a H phase formed from rod-like micelles and a L phase has been observed in a mixture of a concentrated block copolymer in water upon addition of synthetic clay, Laponite RDS. The block copolymer studied was a poly(oxyethylene)-poly(oxypropylene)-poly(oxyethylene) triblock, Pluronic P123, which is a non-ionic surfactant. This work complements prior work on the influence of added Laponite on the L and sponge phases of low molar mass nonionic surfactants [6].

The transition from H phase in a 50 wt% block copolymer solution to a L phase on addition of Laponite, at sufficiently high temperature, is tentatively ascribed to a difference in packing entropy of the disk-like particles in the two phases. There is a "packing frustration" for disks in the H phase due to a reduced excluded volume.

The form factor of the Laponite particles confirmed them to be disk-like, with a diameter  $2R = 35$  nm, and thickness  $\Gamma = 2$  nm. Using these dimensions, together with the density and amount of added laponite and the calculated thickness of the water layer between block copolymer lamellae, enabled the average separation between Laponite particles to be calculated in the L phase. It was thus shown that there was ample space to accommodate them within the water layer. The spacing between particles decreased with increasing Laponite content, as expected.

The structure factor in the vicinity of the Bragg peaks in the L phase was analysed using the Caillé model, from which an average Caillé exponent was determined from fits to all orders of reflection. This was found to be essentially independent of Laponite content, showing that the "stiffness" of the lamellae does not depend on the amount of added Laponite.

#### Acknowledgements.

We thank Prof. Wim de Jeu (AMOLF, Netherlands) for discussion concerning structure factors of smectic phases.

#### References

- [1] Hamley, I. W. (2000) *Introduction to Soft Matter*, John Wiley: Chichester.
- [2] Giannelis, E. P., Krishnamoorti, R., Manias, E. (1999) *Adv. Pol. Sci.*, **138**, 108.
- [3] Castelletto, V., Ansari, I. A., Hamley, I. (2003) *Macromolecules*, **36**, 1694.
- [4] Schmidt, G., Nakatani, A. I., Butler, P. D., Han, C. C. (2002) *Macromolecules*, **35**, 4725.
- [5] Grillo, I., Levitz, P., Zemb, T. (1999) *Eur. Phys. J. B*, **10**, 29.
- [6] Grillo, I., Levitz, P., Zemb, T. (2001) *Eur. Phys. J. E*, **5**, 377.

- [7] Mourchid, A., Delville, A., Lambard, J., Lecolier, E., Levitz, P. (1995) *Langmuir*, **11**, 1942.
- [8] Mourchid, A., Lecolier, E., van Damme, H., Levitz, P. (1998) *Langmuir*, **14**, 4718.
- [9] Levitz, P., Lecolier, E., Mourchid, A., Deville, A., Lyonard, S. (2000) *Europhys. Lett.*, **49**, 672.
- [10] Knaebel, A., Bellour, M., Munch, J.-P., Viasnoff, V. (2000) *Europhys. Lett.*, **52**, 73.
- [11] Cousin, F., Cabuil, V., Levitz, P. (2002) *Langmuir*, **18**, 1466.
- [12] Holmqvist, P., Alexandridis, P., Lindman, B. (1998) *J. Phys. Chem. B*, **102**, 1149.
- [13] Wanka, G., Hoffmann, H., Ulbricht, W. (1994) *Macromolecules*, **27**, 4145.
- [14] Pople, J. A., Hamley, I. W., Fairclough, J. P. A., Ryan, A. J., Komanschek, B. U., Gleeson, A. J., Yu, G.-E., Booth, C. (1997) *Macromolecules*, **30**, 5721.
- [15] Hamley, I. W., Pople, J. A., Gleeson, A. J., Komanschek, B. U., Towns-Andrews, E. (1998) *J. Appl. Cryst.*, **31**, 881.
- [16] Guinier, A., Fournet, G. (1955) *Small angle scattering of x-rays*, Wiley: New York.
- [17] Kroon, M., Wegdam, G. H., Sprik, R. (1996) *Phys. Rev. E*, **54**, 6541.
- [18] *International Tables for X-ray Crystallography*, Kynoch Press: Birmingham, 1959, Vol. II.
- [19] Caillé, M. A. C. R. (1972) *Acad. Sci. Paris*, **274**, 891.
- [20] Safinya, C. R., Roux, D., Smith, G. S., Sinha, S. K., Dimon, P., Clark, N. A., Bellocq, A. M. (1986) *Phys. Rev. Lett.*, **57**, 2718.
- [21] Roux, D., Safinya, C. R. (1988) *J. de Phys.*, **49**, 307.
- [22] Kaganer, V. M., Ostrovskii, B. I., de Jeu, W. H. (1991) *Phys. Rev. A*, **44**, 8158.
- [23] Helfrich, W. *Zeit. Natur. A.* (1978) *Phys. Sci.*, **33**, 305.

## Astringency - A Molecular Model for Polyphenol/Protein binding

Elisabeth Jöbstl<sup>3,1</sup>, John O'Connell<sup>2</sup>, J. Patrick A. Fairclough<sup>3</sup> and Michael P. Williamson<sup>1</sup>

[1] The Department of Molecular Biology and Biotechnology, University of Sheffield, S10 2UH, UK

[2] Unilever Research, Colworth House, Sharnbrook, Bedford MK44 1LQ, UK

[3] The Department of Chemistry, University of Sheffield, S3 7HF, UK

Received and accepted 15th December 2003

### Introduction

Astringency is recognized as a feeling of dryness, constriction and puckering of the palate, which takes a significant time to develop. It is caused by the intake of food, like grapes, dates or beverages, like tea, coffee, red wine or beer. All those beverages or food have in common that they contain plant polyphenols. Polyphenols are secondary metabolites, widely distributed in the plant kingdom and playing an important role in their defence mechanism [1]. It is commonly accepted that the astringent response is the result of polyphenols precipitating salivary proline-rich proteins (PRPs), which are part of the mucous surface layer of the mouth. The consequence is a loss of lubrication, which is generally perceived as an astringent sensation. In order to understand the mechanism of the astringent response, attention needs to be drawn to the complexation between plant polyphenols and salivary PRPs [2]. Since this is a complex process, a variety of techniques were applied to investigate different aspects of the binding process.

In this study  $\beta$ -casein was used as a model protein for PRPs and (-)-epigallocatechin gallate (EGCG) was chosen as a representative for polyphenols. Transmission electron microscopy and analytical ultracentrifugation demonstrate the polydispersity and the size distribution of the system, and analytical ultracentrifugation shows that as the proportion of EGCG is increased, the larger particles increase in both number and size. Small-angle X-ray scattering and dynamic laser light scattering show that there is an initial compaction of the protein as it coils around the polyphenol, and that aggregation sets in as the concentration of EGCG is increased, leading finally to precipitation. As a result of this investigation and supported by previous studies [3, 4] a binding model consisting of three steps for the interaction between salivary proline-rich proteins and polyphenols was developed.

### Experimental Procedure

As PRPs are difficult to purify to homogeneity,  $\beta$ -casein, which is readily available, was chosen as a model protein due to its conformational similarities with PRPs.  $\beta$ -casein is a protein of the mammalian milk and possesses 35 prolines evenly distributed throughout the amino acid sequence. In its original state it is an amphiphilic molecule due to five phosphoserine groups concentrated on the N-terminal [5, 6]. However, by enzymatic dephosphorylation the tendency to form micelles is suppressed.

(-)-epigallocatechin gallate (EGCG) is a typical constituent of many foodstuffs and beverages and was therefore chosen as

ligand for the polyphenol/protein interaction. It belongs to the group of condensed proanthocyanidins and possesses three aromatic rings, which act as potential binding sites [7].

The solvent used was H<sub>2</sub>O:DMSO (95:5 by volume) and all experiments were conducted at a pH of  $7.0 \pm 0.2$ . The concentration of EGCG was generally 10 mmol l<sup>-1</sup>, and it was mixed with  $\beta$ -casein at different ratios.

*Transmission electron microscopy (TEM)* -  $\beta$ -casein ( $4.2 \times 10^{-6}$  mol l<sup>-1</sup>, 0.1 mg ml<sup>-1</sup>) was mixed with EGCG in a molecular ratio of 1:1 and immediately after mixing fixed on a carbon grid and stained with uranyl formate. The sample grids were then examined using a Philips CM100 transmission electron microscope at an accelerating voltage of 100 kV.

*Analytical Ultracentrifugation (AUC)* - Measurements were conducted using an Optima XL-I analytical ultracentrifuge (Beckman Scientific Inc., Palo Alto, USA) at the National Centre for Macromolecular Hydrodynamics at the University of Nottingham with a  $\beta$ -casein concentration of  $4.2 \times 10^{-5}$  mol l<sup>-1</sup> (1.0 mg ml<sup>-1</sup>). The experiments were performed applying the sedimentation velocity method and a run speed of 50,000 rpm. The data were recorded as concentration versus radial position ( $r$ ) and sedimentation coefficients were determined using the time derivative software (DCDT+) developed by Dr. J. Philo (Biotechnology & Software Consulting, Thousands Oaks, USA) [8, 9].

*Small angle X-ray scattering (SAXS)* -  $\beta$ -casein, at a concentration of  $4.2 \times 10^{-4}$  mol l<sup>-1</sup> (10.0 mg ml<sup>-1</sup>) was mixed at different ratios with EGCG. The measurements were carried out on beamline 2.1 at the SRS Daresbury laboratory. The sample time was limited to 60 s because the protein was subject to radiation damage. The samples were measured at two camera lengths: 2.25 and 8.0 m, and subsequently the data were merged in order to fit the scattering curves using the program GIFT [10].

*Dynamic laser light scattering (DLS)* -  $\beta$ -casein was filtered using a Minisart sterile filter with a pore size of 0.2  $\mu$ m. The concentration was determined by UV spectrophotometry as  $1.8 \times 10^{-4}$  mol l<sup>-1</sup> (4.2 mg ml<sup>-1</sup>). The measurements were performed using a BI-200SM Goniometer version 2.0 from Brookhaven Instruments Corporation with Brookhaven Instruments Particle Sizing Software ver. 3.42 and measurements were conducted at an angle of 90°. A lognormal fitting procedure was applied to fit the time correlation function to a single particle size.

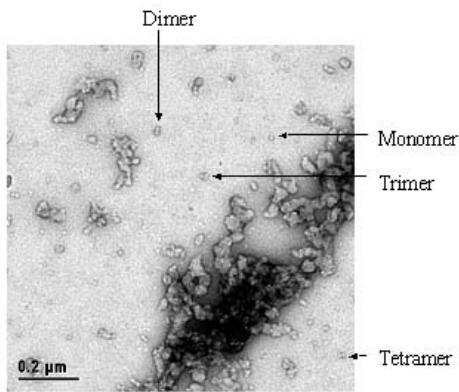


Figure 1. TEM micrographs of  $\beta$ -casein mixed with EGCG in the ratio 1:1 shows the polydisperse nature of the  $\beta$ -casein/EGCG mixtures. Monomers, dimer, trimers and higher aggregates can be seen.

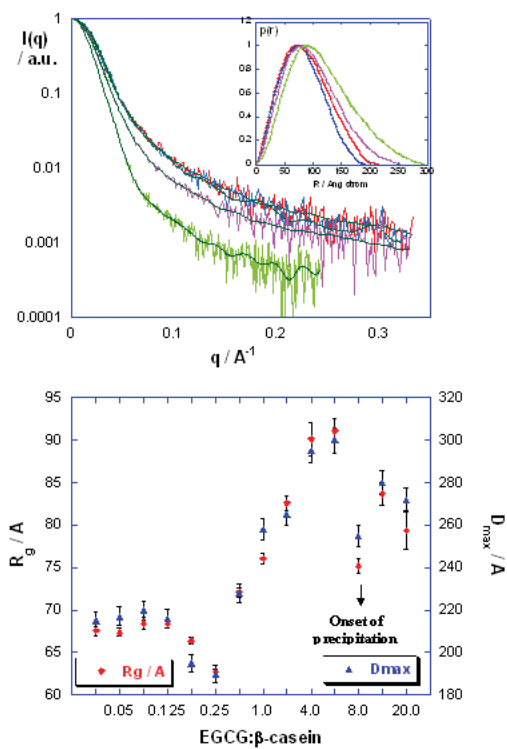


Figure 3. The normalized scattering curves and the corresponding pair distance distribution functions  $p(R)$  (inset) for  $\beta$ -casein mixed at different ratios with EGCG are shown. Red:  $\beta$ -casein, blue: EGCG: $\beta$ -casein 0.25:1, purple: EGCG: $\beta$ -casein 1:1, EGCG: $\beta$ -casein 4:1. (Top).  $R_g$  and  $D_{max}$  exhibit a minimum value at a ratio EGCG: $\beta$ -casein 0.25:1, due to increased coiling up of the protein around the polyphenols. As the EGCG concentration is increased, it starts to cross-link different proteins, which finally lead to precipitation. (Bottom)

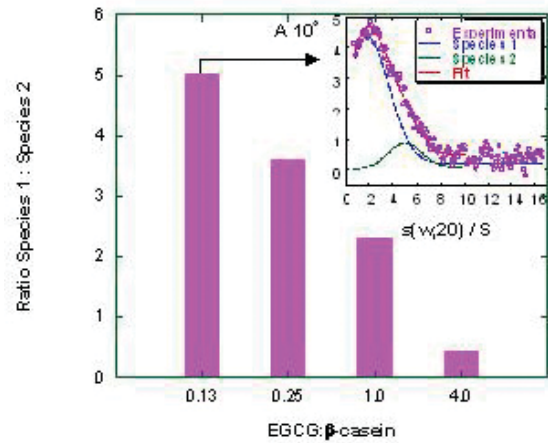


Figure 2. Analytical ultracentrifugation measurements show that the ratio of species 1 ( $s \sim 2$  S) to species 2 ( $s \sim 5$  S) decreases significantly as the concentration of EGCG: $\beta$ -casein is increased from 0.125:1 to 4:1. This is attributed to the progressive aggregation of protein molecules caused by the addition of EGCG. Inserted are the experimental data from the mixture EGCG: $\beta$ -casein 0.125:1 and their best fit. The curve can be fitted to two species, one exhibiting a sedimentation coefficient around 1.85 S and the larger species around 5.1S. Furthermore a very large aggregated species is present which however, migrates very rapidly to the bottom of the centrifuge tube and therefore cannot be measured.

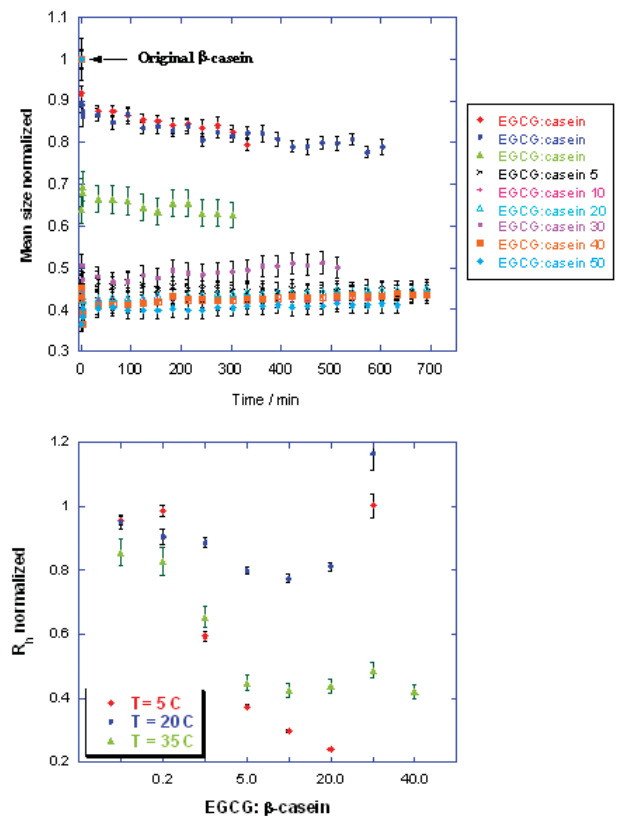
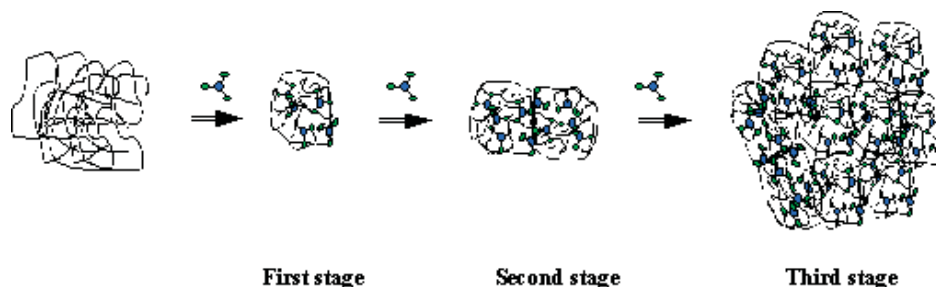


Figure 4. Dynamic laser light scattering (DLS) data show that the compaction of the  $\beta$ -casein molecule occurs within the first minute after mixing with EGCG, and thereafter there is little change in the particle size distribution. (Top) Dependence of particle size measured by DLS on EGCG: $\beta$ -casein ratio, at three different temperatures.  $\beta$ -casein mixed at different ratios with EGCG shows initially a reduction in the hydrodynamic radius ( $R_h$ ), which as the EGCG ratio is increased, rises due to complexation and aggregation. (Bottom)



**Figure 5.** The proposed molecular binding model for the interaction of salivary proline-rich proteins with polyphenols. In the initial stage the proteins compact, attributed to tight and multiple binding to the multidentate polyphenols. At the second stage a dimer of polyphenol coated protein is formed, rendering the complex insoluble. At the third stage, further complexation leads to large complexes and precipitation of the protein.

## Results

Transmission electron micrographs (Fig. 1) show the polydisperse nature of the  $\beta$ -casein - EGCG mixtures. Monomers, dimers, trimers and higher aggregates can be distinguished, whereby the monomers can be identified as spherically shaped.

In order to fit the analytical ultracentrifugation data adequately, it is necessary to include at least 2 species. It is of course likely that more than 2 species are present and it is assumed that each species in fact represents a distribution of particle sizes or shapes. The two species obtained from the fit have sedimentation coefficients of approximately 2 S and 5 S respectively. The ratio of species 1/species 2 when increasing the EGCG concentration shows a dramatic decrease indicating that at higher EGCG: $\beta$ -casein ratios the number of the larger aggregates increases at the expense of monomers and smaller aggregates (Fig. 2).

Fig. 3A shows the normalized scattering curves and the corresponding pair distance distribution functions  $p(R)$ , which yield the value of the maximum molecular dimension  $D_{\max}$ . Fitting of the scattering curves gives a value for the radius of gyration  $R_g$  of the  $\beta$ -casein molecules and from Fig. 3B it can be seen that at an EGCG: $\beta$ -casein ratio of 0.25:1,  $R_g$  as well as  $D_{\max}$  decrease caused by the compaction of the protein molecules. The minimum in particle size is followed by an increase, due to aggregation. As soon as the complexes become insoluble and precipitation occurs the data start to become unreliable. The  $p(R)$ -function gives an indication of the particle shape. The compact  $\beta$ -casein at low EGCG concentrations gives rise to a symmetric  $p(R)$ -function, illustrating that the protein adopts a rather spherical conformation compared to the elongated original structure [11]. Similar conclusions are reached by analysis of Kratky plots (data not shown).

Astringency is a sensation that develops over the course of approximately 30 seconds, and then is gradually lost, due to continual salivary flowing washing away complexes of PRPs [12, 13]. Dynamic laser light scattering (DLS) was therefore applied to measure the hydrodynamic radius ( $R_h$ ) of the proteins shortly after mixing with polyphenols. The DLS results (Fig. 4A) show that the compaction of the  $\beta$ -casein molecules occurs within the first minute after mixing and the

hydrodynamic radius ( $R_h$ ) then stays constant for hours. Fig 4 B shows that  $R_h$  passes through a minimum at a ratio EGCG: $\beta$ -casein  $\sim 10:1$ . This ratio, where the protein adopts the minimum size, is significantly higher compared to that observed in the SAXS data (0.25:1). This may be on the one hand explained by the way the different techniques average over polydisperse distributions. On the other hand it is likely that much of the difference is due to the fact that there are no  $\beta$ -casein aggregates present at the start of the DLS experiments, since DLS measurements require careful filtering of the solutions prior to measurements in order to remove dust particles, which would influence the scattering data greatly. It is therefore suggested that the presence of casein aggregates induces particle aggregation at lower EGCG: $\beta$ -casein ratios; in other words, EGCG-coated monomers appear to bind preferentially to casein aggregates.

## Discussion

This study aims to develop a molecular model for the interactions between salivary basic proline-rich proteins and dietary polyphenols, which are most likely responsible for the astringent sensation caused by polyphenol-rich foods and beverages. As a conclusion from the experimental results a binding model in three steps is suggested (Fig. 5). The association of polyphenols with proteins is principally a surface phenomenon. Polyphenols are multidentate ligands, whereby each phenolic ring is a potential binding site [14]. Therefore they are able to bind at more than one point on the protein stand. Multiple non-covalent bonds, mainly hydrophobic interactions complemented by hydrogen bonding, are responsible for the interactions of polyphenols with proteins [15].

At the first stage and at low EGCG concentration the polyphenol associates onto the protein surface and generally several polyphenol molecules bind simultaneously and tightly to the same protein. This causes the protein, which originally exists in a loose randomly coiled conformation, to 'wrap' around the polyphenols hence experiencing a compaction of its structure. At the second stage EGCG starts to cross-link different proteins leading to the recruitment of a second polyphenol-coated protein, which renders the complex insoluble, forming a colloidal solution. At the third and final stage, further cross-linking causes the aggregates to grow, finally leading to precipitation [3, 16].

## References

- [1] Haslam, E. (1988) *Journal of Chemical Ecology* **14**, 1789-1805.
- [2] Haslam, E., Williamson, M. P., Baxter, N. J. & Charlton, A. J. (1999) *Recent Advances in Phytochemistry* **33**, 289-318.
- [3] Charlton, A. J., Baxter, N. J., Khan, M. L., Moir, A. J. G., Haslam, E., Davies, A. P. & Williamson, M. P. (2002) *Journal of Agricultural and Food Chemistry* **50**, 1593-1601.
- [4] Charlton, A. J., Haslam, E. & Williamson, M. P. (2002) *Journal of the American Chemical Society* **124**, 9899-905.
- [5] Farrell, H. M., Jr., Qi, P. X., Wickham, E. D. & Unruh, J. J. (2002) *Journal of Protein Chemistry* **21**, 307-321.
- [6] Farrell, H. M., Jr. (1973) *Journal of Dairy Science* **56**, 1195-206.
- [7] Haslam, E. (1987) *Linchan Huaxue Yu Gongye* **7**, 1-16.
- [8] Philo, J. S. (1997) *Biophysical Journal* **72**, 435-444.
- [9] Philo, J. S. (2000) *Analytical Biochemistry* **279**, 151-163.
- [10] Glatter, O. (1995) *NATO ASI Series, Series C: Mathematical and Physical Sciences* **451**, 107-80.
- [11] Glatter, O. & Kratky, O. Editors (1982) *Small Angle X-ray Scattering*, Academic Press, London.
- [12] Breslin, P. A. S., Gilmore, M. M., Beauchamp, G. K. & Green, B. G. (1993) *Chemical Senses* **18**, 405-17.
- [13] Valentova, H., Skrovankova, S., Panovska, Z. & Pokorny, J. (2002) *Food Chemistry* **78**, 29-37.
- [14] Siebert, K. J., Troukhanova, N. V. & Lynn, P. Y. (1996) *Journal of Agricultural and Food Chemistry* **44**, 80-5.
- [15] Haslam, E. (1998) *Practical Polyphenolics: from Structure to Molecular Recognition and Physiological Action*.
- [16] Charlton, A. J., Baxter, N. J., Haslam, E. & Williamson, M. P. (1999) in *Polyphenols in Food*, (Ed. R. Amadò, H. Andersson, S. Bardócz and F. Serra), Office for Official Publications of the European Communities, Luxembourg, 179-185.

## 12th Annual Workshop Abstracts

### MYOSIN HEAD CONFIGURATION IN RELAXED INSECT FLIGHT MUSCLE: X-RAY MODELLED RESTING CROSS-BRIDGES IN A PRE-POWERSTROKE STATE ARE POISED FOR ACTIN BINDING

Hind A. AL-Khayat<sup>1</sup>, Liam Hudson<sup>1</sup>, Michael K. Reedy<sup>2</sup>, Thomas C. Irving<sup>3</sup> and John M. Squire<sup>1\*</sup>

[1] Biological Structure & Function Section, Biomedical Sciences Division, Faculty of Medicine, Imperial College London, Exhibition Road, London SW7 2AZ, UK

[2] Dept of Cell Biology, Duke University, Durham, NC 27710, USA

[3] BioCAT, Dept. Biological, Chemical and Physical Sciences, Illinois Institute of Technology, Chicago, IL 60616, USA

Low-angle X-ray diffraction patterns from relaxed insect flight muscle recorded on the BioCat beamline at the Argonne APS have been modelled to 6.5 nm resolution (R-factor 9.7%, 65 reflections) using the known myosin head atomic coordinates, a hinge between the motor (catalytic) domain and the light chain-binding (neck) region (lever arm), together with a simulated annealing procedure. The best head conformation angles around the hinge gave a head shape that was close to that typical of relaxed M·ADP·Pi heads; a head shape never before demonstrated in intact muscle. The best packing constrained the 8 heads per crown within a compact crown shelf projecting at ~90° to the filament axis. The two heads of each myosin molecule assume non-equivalent positions, one head projecting outward while the other curves round the thick filament surface to nose against the proximal neck of the projecting head of the neighbouring molecule. The projecting heads immediately suggest a possible cross-bridge cycle. The relaxed projecting head, oriented almost as needed for actin attachment, will attach, then release Pi followed by ADP, as the lever arm with a purely axial change in tilt drives ~10 nm of actin filament sliding on the way to the nucleotide-free limit of its working stroke. The overall arrangement appears well-designed to support precision cycling for the myogenic oscillatory mode of contraction with its enhanced stretch-activation response used in flight by insects equipped with asynchronous fibrillar flight muscles.

### Order-order transitions in block copolymer solutions: epitaxy, mechanisms, and kinetics

T. P. Lodge, J. Bang, M. J. Park, and T. Chastek

Departments of Chemistry and Chemical Engineering & Materials Science

Block copolymer solutions exhibit a rich variety of thermotropic and lyotropic order-order transitions. Many of these transitions are epitaxial, although quite complicated in

detail. The use of shear-orientation in combination with SAXS is crucial in understanding the transition mechanisms, as will be illustrated for the transformation of close-packed to body-centred lattices of spherical micelles. A combination of SANS and SAXS has been used to quantify the temperature dependence of the micellar characteristics, and thus to establish exactly how changes in solvent selectivity determine the choice between close-packed and body-centered packings. Finally, transition kinetics can be followed by a variety of techniques, but the use of polarized optical microscopy is particularly helpful in characterization nucleation density and individual grain growth rates, as will be demonstrated for the formation of the gyroid phase.

### Astringency - A Molecular Approach

Elisabeth Joebstl, Michael Williamson, Patrick Fairclough

Dainton Building, Brook Hill, University of Sheffield, S3 7HF Sheffield

Astringency is generally described as a feeling of dryness, puckering or roughness in the mouth and is associated with a number of beverages, including tea, coffee, beer and red wine. All those beverages contain tannins which are water-soluble, polyphenolic compounds with molecular weights between 500 and 5000 Da. The sensation of astringency is the result of the binding of plant polyphenols to salivary proline-rich-proteins (PRP). The main binding interaction is a hydrophobic stacking of a phenolic ring belonging to a polyphenol over a prolyl ring of a salivary PRP. The PRPs lack any secondary structure and exist as random coils in the saliva. The studies presented suggest that upon binding of polyphenols the molecular dimensions of the proline-rich proteins decrease; this may be due to multiple binding of one protein to one polyphenol. The proline-rich protein (PRP) is able to wrap around and bind very tightly to the phenolic compounds, the random coiled structure becomes therefore more dense and compact.

In this project dephosphorylated b-casein is used as a model for salivary proline-rich protein and (-)-epigallocatechin gallate (EGCG) as a representative for tannins. The effect of the binding event on the structure of b-casein is investigated using small angle X-ray scattering (SAXS), nuclear magnetic resonance (NMR) pulsed gradient spin echo methods, analytical ultracentrifugation, dynamic laser light scattering (DLS) and transmission electron microscopy (TEM).

## Kinetics of Phase separation in Non-ionic Systems

Patrick Fairclough, Alex Norman

Department of Chemistry, University of Sheffield, Sheffield S3 7HF

We will report on studies of the phase separation in non-ionic block copolymer systems. The structure formation in these systems evolves rapidly from a disordered mixed state to a microphase separated state, with a length scale ideal for SAXS and SANS studies. We will present recent results on the evolution of structure within these systems after a temperature quench.

## Using Hydrogenated Polybutadienes with Novel Architectures to Learn about Polymer Crystallisation

Ariana Morgovan, E. Heeley, C.M. Fernyhough and A.J. Ryan

The Department of Chemistry, Dainton Building, the University of Sheffield, Brook Hill, Sheffield, S3 7HF, England

During processing, crystallisation is the essential step that determines the quality of the final product (*i.e.* toughness, smooth surface, elasticity, *etc.*). Thus, in order to develop more useful, job specific, materials, the crystallisation process has to be controlled. To do this, model compounds with well-defined architectures are required. They can facilitate the understanding and prediction of the relationships between polymer properties and their structure.

Polyethylene-like materials from hydrogenated polybutadienes with well-controlled molecular architecture, a range of molecular weights and very narrow polydispersities have been made, using anionic polymerisation techniques. Small- and Wide-angle X-ray Scattering (SAXS/WAXS) are excellent tools to look at the macrostructure development or long range ordering (lamellae stacking) (SAXS) and the microstructure development or crystalline atomic ordering (WAXS). Here we investigated the quiescent crystallization of hydrogenated polybutadienes by means of time-resolved, simultaneous SAXS/WAXS/DSC techniques at synchrotron sources (SRS CLRC Daresbury Laboratory, UK and at ESRF, Grenoble, France). These allowed the kinetics of crystallisation to be analysed and the morphological parameters of the samples to be determined (using correlation function analysis).

Results obtained from scattering were also confirmed by other laboratory techniques, such as Differential Scanning Calorimetry (DSC) and polarised optical microscopy. Avrami exponents, which are a measure of the dimensionality of growth, were obtained and compared.

Future work will involve using shear regimes during scattering and optical microscopy experiments. Also, rheology measurements will be performed.

## References

1. G. Ungar, Xiang-bing Zeng, *Chem. Rev.* 2001, **101**, 4157-4188
2. B. Chu, B.S. Hsiao, *Chem. Rev.* 2001, **101**, 1727-1761

## Progress in the evaluation of SAXS data from dense and partially ordered systems

Otto Glatter

Institute of Chemistry, University of Graz, Austria

During the last years we have developed the so-called generalized indirect Fourier transformation method. It allows the separation of the form factor and structure factor from SAXS and SANS data from interacting dense systems. The most recent development concerns the evaluation of scattering data from lamellar systems. The basics of the method will be explained and some applications will be demonstrated.

## Beamline 11 on Diamond for the Non-Crystalline Diffraction Materials and Life Sciences Communities

N.J. Terrill

Diamond Light Source Ltd, Rutherford Appleton Laboratory, Chilton, Didcot, Oxon, UK, OX11 0QX

Beamline I22 has been approved for year 2 on DIAMOND. The beamline is to include features for standard Small Angle scattering and fibre diffraction as well as a microfocus capability. The latest technical design ideas for the beamline will be presented.

## Nucleation of thermodynamically stable structures for polyglutamine amyloid fibres

J.A. Elliott<sup>1</sup>, J. Starikow<sup>2</sup>, J. Crawshaw<sup>1</sup>, P.R. Claiden<sup>1</sup>, A.H. Windle<sup>1</sup>

[1] Department of Materials Science and Metallurgy, University of Cambridge, Cambridge, UK;

[2] Department of Chemistry, Freie University, Berlin, Germany.

It has been recently suggested [1] that the formation of amyloid plaques, which are implicated in the pathology of a wide range of neurodegenerative disorders, may be related to nucleation of protein aggregates. In one particular case, Huntington's disease, it is known that the age of onset depends exponentially on the length of a sequence of glutamine residues in the Huntingtin protein. This can be explained if the rate-determining step in the disease process is the formation of a stable nucleus for a fibrillar amyloid structure. In order to test this hypothesis, we have examined a number of proposed structural models for polyglutamine fibres using canonical molecular dynamics

simulations [2]. We discuss the thermodynamic stability of these models as a function of time, temperature and glutamine repeat length, and use these results to parameterise a simple model for the aggregation process. We also present simulated X-ray fibre diffraction patterns from the polyglutamine amyloid nuclei that show similar features to experimental patterns.

## References

- [1] M. F. Perutz and A. H. Windle *Nature*, **412**, 143-144, 2001.  
 [2] J. A. Elliott, J. Starikow, J. Crawshaw, P.R. Claiden and A.H. Windle, in *Nucleation Control* (eds. G. W. Greenwood, A. L. Greer, D. M. Herlach, K. F. Kelton), CUP, Cambridge, in press 2003.

## SAXS ANALYSIS OF POLYURETHANE MORPHOLOGY AND ITS RESPONSE TO DEFORMATION.

P.R. Laity<sup>1</sup>, J.E. Taylor<sup>1</sup>, S.S. Wong<sup>2</sup>, P. Khunkamchoo<sup>2</sup> and A.F. Johnson<sup>2</sup> and R.E. Cameron<sup>1</sup>.

- [1] Department of Materials Science and Metallurgy, University of Cambridge;  
 [2] IRC in Polymer Science, University of Leeds.

Thermoplastic polyurethanes (TPU) are usually copolymers, composed of alternating urethane-containing hard segments (HS) and more flexible soft segments (SS). As a result of immiscibility between the HS and SS parts of the polymer, microphase-separated morphologies can develop, with characteristic lengths on the nanometre scale, which depend on the overall polymer composition and processing history. In this structure, the dispersed, HS-enriched, microdomains act as physical cross-links within the surrounding SS-enriched matrix, which gives rise to the elastomeric properties of TPU.

In the present work, the morphological responses of several TPU formulations were studied during deformation, using real-time measurements of two-dimensional small-angle X-ray scattering (2D-SAXS). The results were analysed on the basis of the model proposed recently by Blundell *et al.* [1,2], in which the 2D-SAXS patterns were interpreted as arising from rigid particles on a deformable statistical lattice. By curve-fitting this model to the experimental data, it was found that the morphological responses involved a combination of HS-enriched microdomain rotation, fragmentation and approximately affine deformation of the SS-enriched matrix.

This work forms part of a larger project to develop polyurethanes for medical applications. A thorough understanding of the mechanical behaviour of TPUs is, clearly, of key importance. Moreover, the morphology may also affect the biostability of these polymers.

## References

- [1] Blundell, D.J. Eeckhaut, G. Fuller, W. Mahendrasingam, A. and Martin, C. *Polymer* 2002; **43**: 5197-5207.  
 [2] Blundell, D.J. Martin, C. Mahendrasingam, A. Fuller, W. and Eeckhaut, G. *Fibre Diffraction Review* **2002**; 10: 50-56.

## A North American Research Coordination Network for Fiber Diffraction

Gerald Stubbs<sup>2</sup>, R. Chandrasekaran<sup>1</sup>, Thomas C. Irving<sup>2</sup>, Daniel A. Kirschner<sup>2</sup>, Joseph Orgel<sup>2</sup>, and Trevor Forsyth<sup>3</sup>

- [1] Vanderbilt University, Purdue University,  
 [2] Illinois Institute of Technology, Boston College, Chicago Medical School,  
 [3] Keele University / Institut Laue Langevin

A network of fibre diffraction groups has been established to coordinate activities in the USA. The goal of the network is to develop biological fibre diffraction methods, particularly computational methods. This will be done through a program of software development, and through a series of retreats and workshops. The network software will be complementary to CCP13 software; together, they will eventually cover all aspects of biological fiber diffraction.

A major focus of activity will be cooperation between fibre diffractionists in the USA and others, particularly those in Britain. A second focus will be the coordinated use of the BioCAT X-ray beamline facility at the Advanced Photon Source, Argonne National Laboratory. Network meetings will include three types of activity: retreats that will formalize a successful informal series held sporadically since 1989, workshops at BioCAT, and partial sponsorship of sessions organized by the fiber diffraction Special Interest Group of the American Crystallographic Association.

## Towards the complete atomic structure of the bacterial flagellum

Keiichi Namba

Graduate School of Frontier Biosciences, Osaka University, & Dynamic NanoMachine Project, ICORP, JST, 3-4 Hikoridai, Seika, Kyoto 619-0237 Japan

The bacterial flagellum is made of a rotary motor and a long helical filament by means of which bacteria swim. The flagellar motor at its base rotates at around 300 Hz and drives the rapid rotation of each flagellum to propel the cell's movements in viscous environments. The filament is a tubular structure with a diameter of about 20 nm and made of 20,000 to 30,000 copies of a single protein flagellin, and yet the filament can form left-handed or right-handed helical forms and switch between these two in response to the twisting force produced by quick reversal of the motor rotation. This allows bacteria to alternate their swimming pattern between run and tumble for taxis. The filament is connected to the motor through a highly curved short segment called the hook. Its bending flexibility makes it function as a universal joint, while the filament is relatively

more rigid to work as a propeller. A very short segment called the hook-filament junction, made of HAP1 and HAP3, is a mechanical buffer to connect these two mechanically distinct structures. The flagellum is constructed through various self-assembly processes, in which all the axial structures growing in the cell exterior are constructed by proteins translocated from the cytoplasm to the distal end of the growing structure, where three different cap complexes help efficient self-assembly of these proteins in different stages.

We have been trying to visualize the structure of the flagellum in atomic detail to understand how it self-assembles and works. We solved the crystal structures of core fragments of the flagellar axial component proteins by X-ray crystallography. X-ray fibre diffraction gave high-resolution structural information. Electron cryomicroscopy also visualized the structures of the filament, cap and cap-filament complex, and recently enabled us to build an atomic model of the filament based on a density map at 4 Å resolution. All these structures have given interesting implications for the function of each molecule, demonstrating the importance of the dual nature of protein molecules, flexibility and precision.

### Examining the structure of amyloid fibrils

Louise Serpell, O Sumner Makin

Cambridge Institute for Medical Research, Structural medicine unit, University of Cambridge, Hills Rd, Cambridge, CB2 2XY

Amyloid fibrils deposited in the tissue in a number of diseases are known collectively as the Amyloidoses. This group of diseases includes Alzheimer's disease as well as the Spongiform encephalopathies. Each disease is characterised by a different protein that aggregates to form amyloid fibrils. The normally functional protein undergoes considerable conformational change associated with the fibrillogenesis.

We have examined the structure of amyloid fibrils using X-ray diffraction as well as electron microscopy. Using short peptides to make ordered amyloid fibrils in vitro, we have been able to collect ordered diffraction patterns and electron microscopy images to enable us to construct a model for the beta-sheet core structure of the amyloid fibril.

### Liquid crystalline aspects of starch structure

Athene M Donald

Cavendish Laboratory, University of Cambridge

Small Angle X-ray Scattering (SAXS) and Small Angle Neutron Scattering (SANS) have been used to study the internal supramolecular packing within starch granules. These small angle scattering techniques are able to provide information on the packing of the semicrystalline lamellae and the amorphous growth rings. Rationalising the changes in the lamellae that occur under different conditions (such as temperature and extent of plasticisation) it is useful to consider the constituent highly branched amylopectin molecule within the framework of side chain liquid crystalline polymers. The side chains are

known to form double helices which then order laterally, and these double helices are considered as the mesogens. In unplasticised starches the mesogens are disordered forming a nematic phase, but upon solvent ingress their packing improves and a smectic phase is formed. Furthermore, by comparing the SAXS from different species of starch, it becomes apparent that the nature of the lamellae themselves varies between species. Those which have a significant length of flexible spacer can form rather flat lamellae, but undulations of the lamellae are present if the antagonistic effects of side chain and backbone organisation dominate.

### Structures of classical and therapeutic antibodies by constrained solution scattering modelling

Stephen J. Perkins

Structural Immunology Group, Dept Biochemistry and Molecular Biology, Darwin Building, University College London, Gower St, London WC1E 6BT

Highly constrained scattering curve modelling potentially offers many advantages for determining solution structures for antibodies. Crystal structures for the antibody Fab and Fc fragments are often known for scattering modelling purposes. The main unknown is the averaged structure of the hinge peptide that connects each Fab fragment to the Fc fragment. A trial and error strategy based on the generation of as many as 10,000 random conformations of the hinge peptide generally results in the identification of a few structures that fit the scattering data. The results are biologically significant in explaining the several unique features of the antibody in question. Two examples will be discussed. (1) Two classic 12-domain antibody structures are exemplified by the monomeric forms of the IgA1 and IgA2 subclasses. The applications and adaptations of the above strategy to determine their solution structures will be discussed. IgA1 is notable for possessing a long glycosylated hinge, while IgA2 possesses a short hinge and a disulphide bridge connecting the two Fab fragments. (2) Antibodies designed for therapeutic treatments have their Fab fragments replaced by an active protein reagent, thereby doubling the concentration of the reagent, and coupling this with antibody effector function. The activity of the chimeric antibodies thus created will depend on its solution structure. The case of the five-domain rodent complement-related receptor protein/gene  $\gamma$  (Crry) will be discussed. The determination of the solution structure for the Crry chimera with an Fc fragment was able to account for its reactivity.

### Grazing-incidence X-ray diffraction studies of polyfluorenes

Matti Knaapila<sup>1</sup>, Benjamin P. Lyons<sup>2</sup>, Kaisa Kisko<sup>1</sup>, Joel P. Foreman<sup>2</sup>, Ulla Vainio<sup>1</sup>, Milena Mihaylova<sup>1</sup>, Oliver H. Seeck<sup>1</sup>, Lars-Olof Palsson<sup>2</sup>, Ritva Serimaa<sup>1</sup>, Mika Torkkeli<sup>1</sup>, and Andrew P. Monkman<sup>2</sup>

[1] Division of X-ray Physics, Department of Physical Sciences, P.O. Box 64, FIN-00014 University of Helsinki, Finland

[2] Department of Physics, University of Durham, South Road, Durham, DH1 3LE, United Kingdom

[3] Institut für Festkörperforschung, Forschungszentrum Jülich GmbH, D-52452, Jülich, Germany

We report on grazing-incidence X-ray diffraction and reflectivity studies of aligned pi-conjugated polymers. Since both the applications and basic research of pi-conjugated polymers are concentrated on thin films, the thin film structures instead of the fibre structures are the focus of interest here. Among them, we have studied the important polyfluorene class of materials. We present excellent data concerning the film quality and we find interesting and novel results on the molecular ordering in the films with highly aligned molecules forming different phases in different orientations. These properties are dependent on the processing conditions.

### Rheology and structure of hydrophobically modified polyacrylamide solutions in the semidilute regime

Valeria Castelletto<sup>1</sup>, Ian W Hamley<sup>1</sup>, Wei Xue<sup>1</sup>, Cornelia Sommer<sup>2</sup> and Jan Skov Pedersen<sup>2</sup>

[1] Department of Chemistry, University of Leeds, Leeds LS2 9JT, UK.

[2] Department of Chemistry, University of Aarhus, Langelandsgade 140 DK-8000 Aarhus C, Denmark.

The ordering of hydrophobically modified polyacrylamide polymers, with disubstituted acrylamides di-n-propylacrylamide and di-n-octylacrylamide used as hydrophobic comonomers, has been studied by small angle scattering (SAXS) and rheology. The overall content of hydrophobe and length of hydrophobic sequences in the random copolymer was varied using a micellar copolymerization technique. Changes in the correlation length of the semidilute solutions as a function of the temperature are analyzed, and evidence is presented for cluster formation due to an increasing association between hydrophobic groups at high temperature. Information on the solution from SAXS is compared to that extracted from rheology experiments, and comparisons are made to scaling theories for associating polymers.

### Two-dimensional maps of archaeological bone nanotexture: variation across bone features.

J.C. Hiller<sup>1</sup>, M. Drakopoulos<sup>2</sup>, I.L. Alberts<sup>3</sup>, A.C. Chamberlain<sup>4</sup>, M.J. Collins, T.J. Wess<sup>1</sup>

[1] Centre for Extracellular Matrix Biology, University of Stirling, Stirling, UK

[2] European Synchrotron Radiation Facility, Grenoble, France

[3] Department of Archaeology, University of Sheffield, Sheffield, UK

[4] School of Civil Engineering and Geosciences, University of Newcastle, Newcastle upon Tyne, UK

The prediction of the survival of biomolecular material in retrievable form over archaeological time-scales has been a long-standing problem for archaeology and paleontology alike. Recent studies have shown that an intact mineral phase in bone can shelter biomolecules such as DNA and osteocalcin that can subsequently be extracted for analysis. We describe here a method of visualizing bone mineral nanotexture in modern and archaeological bone using microfocus small-angle X-ray scattering, in an attempt to determine areas of mineral alteration. Two-dimensional maps of bone crystallite shape and thickness have been produced here. These show both the variation present in modern bone due to histological features and the changes to the biogenic mineral structure following processes of diagenesis.

### High Resolution Wide Angle X-ray Scattering of Protein Solutions

Robert F. Fischetti<sup>1,2</sup>, Ahmed Mirza<sup>3</sup>, Diane J. Rodi<sup>2</sup>, Thomas C. Irving<sup>3</sup>, Richard F. Heurich<sup>3</sup>, Elena Kondrashkina<sup>3</sup> and Lee Makowski<sup>2</sup>

[1]. GM/CA-CAT, Advanced Photon Source, Argonne National Lab, Argonne IL USA 60439

[2]. Biosciences Division, Argonne National Lab, Argonne IL USA 60439

[3]. BioCAT, Dept. BCPS, Illinois Institute of Technology, Chicago IL 60616.

Wide angle X-ray scattering patterns from proteins in solution contain information relevant to the determination of protein fold. But at relevant scattering angles these data are weak, and the degree to which they might be used to categorize the fold of a protein is unknown. Preliminary work has been performed at the BioCAT insertion device beamline at the Advanced Photon Source which demonstrates that one can collect X-ray scattering data from proteins in solution to spacings of 0.22 nm. These data are sensitive to protein conformational states, and are in good agreement with data modelled using the program CRY SOL and the known three-dimensional atomic coordinates of the protein. An important issue in the exploitation of this technique as a useful tool for structural genomics is the extent to which the high-intensity X-rays of a third generation synchrotron source chemically or structurally

damage proteins. Various data collection protocols have been investigated demonstrating conditions under which structural degradation of even sensitive proteins can be minimized, making this technique a viable tool for protein fold categorization, the study of protein folding, unfolding, protein-ligand interactions and domain movement.

### Further Research Into Breast Cancer Diagnosis Using Small Angle X-Ray Scattering SAXS

A.R. Round, C.J. Hall, K. D. Rogers

C.L.R.C. Daresbury Laboratory, Daresbury, Cheshire  
Cranfield University, R.M.C.S., Shrivvenham

Preliminary research investigating the SAXS pattern obtained from breast tissue with a view to using the information as a marker for cancer, is present in the literature (K. D. Rogers *et al* 1999, R.A. Lewis *et al* 2000 and M. Fernandez *et al* 2002). These works compared the subtle changes in the SAXS pattern of normal, malignant and benign samples using synchrotron radiation. Changes are correlated with the disease state of the sample, which is determined by standard histo-pathological analysis. Our findings suggest that the structural organisation of the collagen within the connective tissue of the breast is disrupted in areas of tumour genesis. These changes were evident at some distance from the centre of the tumour. However, before this technique could be considered for diagnosis further work is required to ensure accuracy, repeatability, sensitivity and specificity.

### The supramolecular characteristics and mechanical properties of elastic fibrillin-rich tissues

J.L. Haston<sup>1</sup>, S.B. Engelsen<sup>2</sup>, M. Roessle<sup>3</sup>, J. Clarkson<sup>4</sup>, E.W. Blanch<sup>5</sup>, C. Baldock<sup>6</sup>, C.M. Kielty<sup>6</sup>, T.J. Wess<sup>1</sup>

[1] Department of Biological Sciences, University of Stirling, U.K.;

[2] The Royal Veterinary and Agricultural University, Frederiksberg, Denmark;

[3] European Synchrotron Radiation Facility, Grenoble, France;

[4] Department of Pure and Applied Chemistry, University of Strathclyde, Glasgow, U.K.;

[5] Department of Biomolecular Sciences, UMIST, Manchester, U.K.;

[6] Schools of Biological Sciences and Medicine, University of Manchester, U.K.

Fibrillin-rich microfibrils are essential elastic structures contained within the extracellular matrix of a wide variety of connective tissues. Microfibrils have been characterised as macromolecular structures with a regular beaded appearance and fundamental axial periodicity of approximately 56nm in the untensioned state. Small-angle X-ray scattering studies have proven to be pivotal in the understanding of these structures.

Despite extensive investigation, however, the basis of this elasticity remains unknown. This study combined small-angle X-ray scattering and Raman microscopy for the first time to investigate the packing of microfibrils within the intact tissue and to determine the role of molecular reorganisation in the elasticity of microfibrils.

The application of relatively small strains produced no overall change in either molecular or macromolecular microfibrillar structure. In contrast, the application of large forces to the tissue resulted in a markedly different structure, as observed by both small-angle X-ray scattering and Raman microscopy. These changes occurred at different levels of architecture and are interpreted as ranging from alterations in peptide bond conformation to domain rearrangement. This study demonstrates the importance of molecular elasticity in the mechanical properties of fibrillin-rich microfibrils in the intact tissue.

### Molecular packing interactions in type I collagen as revealed by X-ray diffraction of cryo-cooled tendon

Laing, J.H., Orgel, J.P.O., Wess, T.J., Cameron, G.J., Laurie, C.

Centre for Extracellular Matrix Biology, Department of Biological Sciences, University of Stirling, Stirling, Scotland, UK

Regular crystalline-like three-dimensional (lateral) packing interactions between type I collagen molecules in rat tail tendon produce discrete Bragg peaks that intersect the equatorial plane of the X-ray diffraction pattern as a series of row-lines. These rowlines are overlain by a slowly varying layer of diffuse scatter that is thought to arise from liquid-like thermal and static molecular disorder. We show here that cryo-cooling the sample during data collection alters the profile of this diffuse scatter without disrupting the triclinic lattice of type I collagen. There is a lower overall intensity of diffraction in the cryo-cooled samples, both in the diffuse scatter and Bragg peak profiles and particularly in the near-equatorial region, where there are strong contributions from the gap region. Any diffuse scatter remaining after cryo-cooling may arise from a combination of static (positional) molecular disorder and residual thermal movement. Results are also shown of progress made towards successfully diffracting a single fibril of collagen, of typical diameter 100-500 nm. This is a technically challenging project, but one that will present a unique opportunity to track molecular paths through the gap and overlap regions at a more fundamental level of structure.

## Collagen Organisation in Adult and Foetal Marmoset Cornea

C. Boote, S. Dennis, K.M. Meek

Dept. Optometry and Vision Sciences, Cardiff University, Redwood Building, King Edward VII Ave, Cardiff CF10 3NB, Wales, UK.

**Purpose:** The precise arrangement of fibrillar collagen in the corneal stroma influences the tissue's transparency and dioptric power. The purpose of this study was to examine fibril organisation in adult and foetal marmoset cornea in order to assess their potential as animal models for exploring corneal structure/function relationships.

**Methods:** WAXS methods were used to map the orientations and proportions of aligned collagen fibrils over 3 whole adult and 2 whole (age-matched) foetal corneas at a maximum spatial resolution of 0.5 X 0.5 mm. SAXS methods also provided information on the average diameter and separation of the fibrils at 0.5 mm intervals along 2 orthogonal corneal diameters.

**Results:** Collagen orientation maps of all adult and 130 day (of a 144 day gestation term) foetal marmoset corneas clearly showed a circumferential annulus of fibrils at the limbus, similar to that observed previously in humans and some other vertebrate species. More centrally, the foetal corneas exhibited a predominantly orthogonal arrangement of fibrils reminiscent of that seen in mature human cornea and in immature tissue from some lower vertebrates. The current data suggest that the preferred orientation in the foetal marmoset cornea may be preserved in the adult tissue; a situation which has thus-far only been seen in humans. An index of X-ray scattering intensity from aligned collagen as a fraction of total scattering intensity from all fibrillar collagen showed that in the foetal tissue approximately 20% of fibrils were preferentially aligned in the central cornea, compared to 45% at the limbus. For the adults the corresponding values were 19% and 38%. SAXS results revealed fibril separations and diameters for the adult and foetal tissues in the normal range for monkey cornea. Both parameters remained fairly constant across the cornea before increasing sharply at the limbus; a pattern similar to that observed in human cornea.

**Conclusions:** This work represents the most comprehensive study of collagen organisation so far performed across whole, intact non-human corneas. The results suggest that, structurally, the human cornea may mirror that of the marmoset more closely than that of any other animal so far studied. By this token, the results reconcile with the established view, gained from optical and retinal studies, that the marmoset eye is well represented as a scaled-down version of the human eye. The marmoset could potentially make a useful animal model for corneal pathologies.

## Diffraction from Small Crystals

Simon Hanna

H.H. Wills Physics Laboratory, University of Bristol, Tyndall Avenue, Bristol, BS8 1TL.

Recently, much attention has been focused on spinodal decomposition as a possible mechanism for nucleation in a number of semi-crystalline polymer systems. In many cases, the data presented are from simultaneous small and wide-angle X-ray scattering (SAXS and WAXS) experiments carried out during isothermal crystallization. A common feature of these measurements is that a build-up of small-angle intensity is observed some time before any wide-angle trace is discernible. On this basis it has been suggested that long-range density fluctuations are present, in the melt, before the onset of crystallisation, and which may promote the nucleation of crystals.

We have calculated the SAXS and WAXS patterns from randomly oriented stacks of ideal lamella crystals of iPP, at various stages during a hypothetical growth process. It can be shown that, when the crystals have a small lateral width, it is possible to detect a long-period peak in the SAXS pattern under conditions when the crystalline WAXS trace is too weak to be detected above the background noise. This finding has important implications for the interpretation of simultaneous SAXS and WAXS data, and in particular, it casts doubt on suggestions that such measurements, alone, can provide conclusive evidence for nucleation induced by spinodal decomposition.

## Modelling based on Monte Carlo simulations

Jan Skov Pedersen

Department of Chemistry and iNANO Interdisciplinary Nanoscience Center, University of Aarhus, Langelandsgade 140, DK-8000 Aarhus C, Denmark

SANS and SAXS studies of block copolymer micelles:

Block copolymers dissolved in a selective solvent form micelles with the insoluble blocks in the core and the soluble blocks in a solvated corona. Such micelles can be studied by small-angle neutron and X-ray scattering (SANS and SAXS, respectively). The data can be analysed by scattering functions recently derived from Monte Carlo simulations for a model with a spherical core and a corona of semi-flexible chains interacting with a hard-core potential. Least-squares fit to the data of this model gives very detailed information. It provides information on aggregation number, polydispersity, core size, core solvation, corona shape/size, intermicellar interactions, and on the interactions between the chains in the corona. Micelles of  $\text{PS-}i\text{P}$  (polystyrene-polyisoprene) of relatively high molecular weight in *n*-decane have been studied. Contrast variation SANS was performed using mixtures of hydrogenated and deuterated decane and by inclusion of SAXS data on the same samples. The results are in very good

agreement with simulation results on the same systems. In another study micelles of a Brij surfactant with a C18-chain and a poly(ethylene oxide) (PEO) block with 100 EO units have been studied in water as a function of temperature and concentration. In this study SANS and SAXS were done on the same sample to provide two different contrast conditions. The variation of the temperature results in a variation of the solvent quality of the PEO blocks and it is clearly observed that the interactions are reduced at elevated temperatures.

### Simultaneous determination of structure and tensile properties of wood

Marko Peura<sup>1</sup>, Tiina Koponen<sup>1</sup>, Seppo Andersson<sup>1</sup>, Ingo Grotkopp<sup>2</sup>, Klaas Koelln<sup>2</sup>, Martin Mueller<sup>2</sup>, Pekka Saranpaa<sup>3</sup>, Ritva Serimaa<sup>1</sup>

[1] University of Helsinki, Department of Physical Sciences, Division of X-ray Physics, P.O. Box 64, FIN-00014 University of Helsinki, Finland

[2] Institut fuer Experimentelle und Angewandte Physik der Christian-Albrechts Universitaet zu Kiel, Leibnizstr. 19, D-24098 Kiel, Germany

[3] Finnish Forest Research Institute (METLA), P.O. Box 18, FIN-01301 Vantaa, Finland

The purpose of this work was to investigate the behaviour of normally grown wood when subjected to tensile deformation. Small pieces of Norway spruce (*Picea abies* [L.] Karst.) were stretched and in situ WAXS (Wide Angle X-ray Scattering) measurements were made. This was done in order to simultaneously determine both the structure and the tensile properties of this material. The tensile properties of the samples can be determined from the stress/strain -curves while X-ray diffraction gives information on cellulose crystallisation, crystal structure and fibre texture. Diffraction patterns recorded before stretching and right before fracture were compared and from these patterns the reflections *004* and *200* of cellulose were investigated. The reflection *004* gives information on the dimension of the cellulose unit cell parallel to the cellulose chains, whereas the reflection *200* gives dimensional information perpendicular to the chains.

In order to achieve sufficient time resolution for the tensile test, a high intensity X-ray beam was needed. Therefore the use of synchrotron radiation was essential. Measurements were carried out at beamline A2 of HASYLAB, Hamburg. Samples were stretched with a constant rate of  $2 \cdot 10^{-4}$  mm/s or  $4 \cdot 10^{-4}$  mm/s and diffraction patterns were measured simultaneously using a MAR CCD detector. The exposure time was either 24 or 34 seconds per sample, depending on the scattered intensity. When the dead time of the detector is taken into account, the time resolution of the tests was 30 or 40 seconds, respectively. The results presented are from two early wood samples from different stems grown in southern Finland. Sample A is from the 22nd annual ring of stem 1 and sample B is from the 23rd annual ring of stem 2. Both samples represent wood material in mature phase. In stem 1, the average density was  $341 \text{ kg/m}^3$  and in stem 2 it was  $392 \text{ kg/m}^3$ , the average width of annual rings was 5.16 mm in stem 1 and 3.07 mm in stem 2.

To obtain more information on the structure of the samples in a non-strained state, other WAXS measurements were made using a reference sample set of the same material at the University of Helsinki using a diffractometer with Bragg-Brentano geometry and  $\text{CuK}\alpha_1$  radiation. The orientation of cellulose microfibrils (Microfibril Angle, MFA) was determined by using X-ray diffraction arising from the lattice planes *200* and *004* of cellulose, the crystallinity of the samples was determined both with symmetrical reflection and symmetrical transmission geometry [1]. The mean MFA was determined to be  $(6 \pm 2)$  degrees in sample A and  $(10 \pm 2)$  degrees in sample B. Crystallinity of the samples was  $(34 \pm 4)$  per cent in sample A and  $(33 \pm 4)$  per cent in sample B.

In the tensile experiments, the maximum stress of sample A was  $(95 \pm 5)$  MPa, while with sample B it was  $(47 \pm 2)$  MPa. Fracture occurred at a strain of 6.7 per cent in sample A and at 1.4 per cent in sample B. Sample A was stretched with a rate of  $2 \cdot 10^{-4}$  mm/sec, sample B with a rate of  $4 \cdot 10^{-4}$  mm/sec. The intensities of the reflections became lower as a consequence of the applied strain, but the effect was not uniform in the samples. Changes in the shapes of the reflections occurred as well, but the changes were not unambiguous among the samples. Upon stretching, the reflection *004* shifted towards smaller and *200* towards larger scattering angles, which indicates changes in the dimensions of the unit cell. In the direction of the cellulose chains the unit cell elongated by  $(0.4 \pm 0.1)$  per cent in sample A and by  $(0.1 \pm 0.1)$  per cent in sample B. Perpendicular to chain direction the unit cell became thinner in sample A and remained unchanged in sample B, but the observed changes were much smaller in magnitude than in the direction parallel to the chains. No significant effect on the orientation of cellulose microfibrils was observed during stretching. A similar type of shift of the reflection *004* towards smaller scattering angles has been reported earlier on thin foils of wood [2], but in that study the microfibril angle was also affected. One reason for the difference can be that the wood foils used in [2] had much larger MFA than the samples used in this study.

### References

- [1] Andersson, S., R. Serimaa and P. Saranpaa. 2003. The crystallinity of wood and the size of cellulose crystallites in Norway spruce. *J. Wood Sci.*, in press
- [2] Keckes, J., P. Fratzl and M. Hamilton. 2002. *ESRF Newsletter* 36: 13.

## X-RAY AND NEUTRON DIFFRACTION STUDIES OF FIBROUS BIOLOGICAL MOLECULES

Ingrid Parrot<sup>1,2</sup>, Valerie Laux-Lesourd<sup>1</sup>, Michael Haertlein<sup>1</sup>, Guy Schoen<sup>3</sup>, Trevor Forsyth<sup>1,2</sup>

[1] Institut Laue Langevin, Rue Jules Horowitz, BP 156, F-38042 Grenoble Cedex 9, France

[2] School of Chemistry and Physics, Keele University, Staffordshire ST5 5BG, U.K.

[3] Institut de Biologie Structural, Rue Jules Horowitz, F-38027 Grenoble Cedex 1, France

Fibre diffraction is an extremely powerful technique for investigating the structure of biological polymer systems. The work described in this poster illustrates how X-ray and neutron diffraction methods can be used to provide highly complementary information that is not accessible to either method alone.

X-ray fibre diffraction methods have provided a major contribution to our understanding of a wide variety of biological polymers. However they are less effective for study of location of water and hydrogen atoms. Here neutron methods can provide vital information. The ability to deuterate the biopolymers either throughout the entire molecule or in a more specific way adds a powerful dimension to work aimed at investigating hydration patterns or hydrogen positions and changes that occur during water-driven transitions.

This poster also describes new facilities for sample preparation that are being developed between the ILL and the EMBL Grenoble Outstation. These facilities include a Deuteration Laboratory that will be dedicated to the production of deuterium labelled molecules for use in biological neutron scattering experiments.

## New or updated versions of XCONV, XFIX, FTOREC & LSQINT for Windows and Unix platforms

Ganeshalingam Rajkumar<sup>1</sup>, Andrew He<sup>1</sup>, Trevor Forsyth<sup>1</sup>, John Squire<sup>1</sup>

[1] Biological Structure and Function Section, Biomedical Sciences Division, Imperial College London, London SW7 2AZ, UK

[2] ILL, BP 156 F-38042, Grenoble, France.

During the past decade many CCP13 related computer programs have been developed for stripping and analysing fibre diffraction patterns. However, most of this software was implemented on Unix platforms. Because of the increasing popularity of Microsoft Windows, we have recently redeveloped these programs, which include XCONV, XFIX, FTOREC and LSQINT, for Windows platforms. The

presentation will show how the four programs mentioned above have been redeveloped and how they work under Microsoft Windows.

Basically, XCONV is used to provide for the conversion of various image data files supported by the scanner to either a common format, BSL, that is used by other CCP13 software, or to TIFF format. XFIX is designed to display BSL files and to help to determine such things as the pattern centre, detector orientation and fibre tilt of a fibre diffraction pattern. It also allows the use of three different background subtraction tools. FTOREC is designed to transform image data from detector space to reciprocal space once provided with the specimen to film distance, the orientation of the image, the wavelength and the tilt of the specimen as determined in XFIX. LSQINT provides an automatic method for the integration of intensities for fibre diffraction data. It also allows four background subtraction options.

As well as implementation for Windows, several modifications and improvements have been made to existing programs to enhance the performance and capability of the CCP13 suite across different computer platforms.

## Heavy water inhibits the super-aggregation process of $\alpha$ -crystallin in response to increasing temperature

JW Regini<sup>1</sup>, JG Grossmann<sup>2</sup>, AJ Quantock<sup>1</sup>, A Thomas<sup>1</sup>, PA Timmins<sup>3</sup>, SA Hodson<sup>1</sup> and GF Elliott<sup>1</sup>

[1] Department of Optometry & Vision Sciences, Cardiff University, Cardiff, UK

[2] Synchrotron Radiation Department, CCLRC Daresbury Laboratory, Daresbury, UK

[3] Institut Laue-Langevin, Grenoble, France

In our previous X-ray diffraction studies we have observed the super-aggregation of  $\alpha$ -crystallin with increasing temperature both in the solution and the gel state (Regini *et al.*, 2003, *J. Mol. Biol.*, in press; Regini & Grossmann, 2003, *Fibre Diffraction Review*, 11, 95-101). The aim of our subsequent study was to determine possible changes in the hydration shell surrounding these super-aggregates during heating using both neutron and X-ray solution scattering techniques. Surprisingly, we found that in the presence of D<sub>2</sub>O the super-aggregation process is significantly reduced with increasing temperature. This finding was established using both scattering techniques.

**Fibre Diffraction Review On-line**

Andrew He &amp; John Squire

Biological Structure and Function Section, Biomedical Sciences Division, Imperial College London, London SW7 2BZ, UK

Fibre Diffraction Review (FDR) is a scientific journal with a specific interest in the fibre diffraction and non-crystalline diffraction fields. It includes original papers, technical reports, reviews, comments/letters and meeting reports. To disseminate FDR as widely as possible, an on-line version of Fibre Diffraction Review has been developed. From now on, all the published FDR papers, including papers in back issues, are being made available in PDF format for downloading from the CCP13 websites. To further maximise broad publicity and accessibility for authors and readers, the journal has joined CrossRef, which is the citation-linking backbone for on-line publications. Established in 2000 by scholarly publishers as an independent, non-profit entity, CrossRef enables researchers to navigate electronic journals across publishers, based on open-standards technology. Each document is tagged with a Digital Object Identifier (DOI). Here we report the progress on the preparation of DOI metadata. As soon as this has been done, each article in FDR will have a DOI for cross-referencing throughout the on-line environment. Finally, an example of how to search an article by DOI is also presented.

**Development of a CCP13 Front-End GUI Program**Andrew He<sup>1</sup>, Ganeshalingam Rajkumar<sup>1</sup>, David Dover<sup>1</sup>, Trevor Forsyth<sup>2</sup>, John Squire<sup>1</sup>

- [1] Biological Structure and Function Section, Biomedical Sciences Division, Imperial College London, London SW7 2AZ, UK  
 [2] ILL, BP 156 F-38042, Grenoble, France.

CCP13 is the Collaborative Computational Project for fibre diffraction started on 1st January, 1992. Its primary interests are to develop software used to strip, analyse and model data from fibre diffraction patterns. Since then, CCP13 has made a set of programs available. What we present here is the development of a Front-end graphical user interface (GUI) program called CCP13 Front-End (now known as ICE) as an attempt to integrate these programs together. Apart from the standard windows menus, this program consists of a program start-up panel, a file display panel and a file and directory panel. For example, the program start-up panel can dynamically load a number of CCP13 programs and launch any of them by clicking the loaded program image icon. The file display panel is a client windows container that holds the CCP13 program editor and common image display windows. When we click on a text file or an image file on the file and directory panel, a CCP13 program editor or common image display window will be launched as a separate client window inside the container. The main purpose of developing this program is to increase user productivity and to provide a user-friendly environment to the CCP13 software user.

**NEW OPPORTUNITIES IN NEUTRON SINGLE CRYSTAL AND FIBRE DIFFRACTION ON D19 AT THE INSTITUT LAUE LANGEVIN**V.T. Forsyth<sup>1,4</sup>, S.A. Mason<sup>1</sup>, J.A.K Howard<sup>2</sup>, M. Davidson<sup>3</sup>, W. Fuller<sup>4</sup>, D.A.A. Myles<sup>5</sup>

- [1] Institut Laue Langevin, 6 Rue Jules Horowitz, 38042 Grenoble Cedex 9, France  
 [2] Chemistry Department, Durham University, Durham, U.K.  
 [3] Chemistry Department, Bath University, Bath, UK  
 [4] School of Chemistry and Physics, Keele University, Staffordshire, UK  
 [5] EMBL Grenoble Outstation, 6 Rue Jules Horowitz, 38042 Grenoble Cedex 9, France

Neutron diffraction has proven applications in biology, chemistry, physics, materials science and polymer science [1,2]. D19 is the only instrument at the ILL that can record monochromatic single crystal diffraction data to atomic resolution from small samples with relatively large unit cells; it is also without doubt the best instrument in the world for neutron fibre diffraction. Until now the limited size of its detector has restricted applications in the most challenging fields.

D19 is currently undergoing a complete rebuild that will yield a factor of ~25 in performance. This upgrade, which is funded in large part by a major EPSRC award, will have a real impact on the quality of experiments, combining all the advantages of monochromatic data with new opportunities arising from multiparametric experiments, smaller samples and the ability to study larger unit cells. It will considerably widen the scope of both single crystal and fibre diffraction experiments [3].

In chemical crystallography, new fields will be opened up in charge density analysis [4], accurate structure determination for crystal engineering [5], studies of transition metal catalysis [6,7], structural studies of new organic materials [8], characterisation of weak intermolecular interactions involving hydrogen [9], and structure-property studies of optoelectronic/magnetic materials [1]. In biological crystallography, there will also be strong impact for the study of oligonucleotides and small proteins. Of particular interest are situations where data at moderate resolution (~2Å) can yield definitive information on H atom and water positions, or even where high resolution data are available but where large thermal displacement parameters (>10Å<sup>2</sup>) make their visualisation by X-ray diffraction very difficult. Other applications include fibre diffraction studies of biopolymers (nucleic acids, filamentous viruses, cellulose & other polysaccharides, chitin, amyloid fibres etc) [10,11,12].

**References**

- [1] Wilson, C.C., *Single Crystal Neutron Diffraction from Molecular Materials*, World Scientific Publishing (2000);  
 [2] G. Stubbs, *Current Opinions in Structural Biology* **9**, 615-619 (1999);

- [3] Forsyth, V. T., Mason, S. A., Howard, J. A. K., Davidson, M. G., Fuller, W. and Myles, D. A. A., *Neutron News* **12** (4), 10 (2001);
- [4] Coppens, P., *X-ray Charge Densities and Chemical Bonding* IUCr/Oxford University Press (1997);
5. Desiraju, G., and Steiner, T., *The Weak Hydrogen Bond* OUP (1999);
6. Howard, Johnson, Koetzler, Spencer, *Inorg. Chem* **26**, 2930 (1987);
7. Bakhmutov, Howard, Keen, Kuzmina, Leech, Nikonov, Vorontsov and Wilson, *J. Chem. Soc., Dalton Trans.* 1631-1635 (2000);
8. Mackenzie Gravett, Howard, Astin and Tomlins, *J. Chem. Soc., Perkin Trans.* **2**, 1233-1242 (1996);
9. Davidson, Goeta, Howard, Lamb and Mason, *New J. Chem.* **24**, 477-479 (2000);
10. M. W. Shotton, L.H. Pope, V.T. Forsyth, R.C. Denny, J. Archer, P. Langan, H. Ye, C. Boote, *J. Appl. Cryst.* **31** (5), 758-766 (1998);
11. M.W. Shotton, L.H. Pope, T. Forsyth, P. Langan, R.C. Denny, U. Giesen, M.-Th. Dauvergne, W. Fuller, *Biophysical Chemistry* **69** (1), 85-96 (1997);
12. Y. Nishiyama, T. Okano, P. Langan, H. Chanzy, *Int. J. Biol. Macr.* **26** (4), 279-283 (1999).

# CCP13 PROGRAM STATUS AND PLATFORMS

## Program Description

XOTOKO	1-D data manipulation	CONV	file format conversion (cmd line)
BSL	2-D data manipulation	FTOREC	reciprocal space transformation
V2A	vax to unix data conversion	LSQINT	2-D integration and background fitting
A2V	unix to vax data conversion	CORFUNC	correlation function analysis
OTCON	ascii to otoko data conversion	SAMPLE	Fourier-Bessel smoothing
RECONV	otoko to ascii data conversion	FDSCALE	scaling and merging of intensities
TIFF2BSL	image plate (tiff) to bsl conversion	FD2BSL	intensity to bsl conversion
I2A	ieee to ansi data conversion (DEC)	ICE	An Integrated CCP13 Environment
XCONV	file format conversion (GUI-driven)	Image Viewer	CCP13 ImageViewer
XFIT	1-D fitting and plotting (GUI-driven)	Online Help	CCP13 Online Help

Program	Solaris 2.7	Irix 6.2	OSF 3.2	Linux	Windows
XOTOKO	17/10/03	30/05/96	29/04/97	17/10/03	-
BSL	31/03/03	21/03/97	27/04/97	12/09/03	-
V2A	19/05/95	-	-	-	-
A2V	19/05/95	-	-	-	-
OTCON	06/06/95	08/07/94	-	08/05/97	-
RECONV	06/06/95	31/10/94	-	08/05/97	-
TIFF2BSL	01/2002	01/2002	-	01/2002	-
BSL2TIFF	21/03/97	-	-	-	-
I2A	n/a	n/a	29/04/97	02/05/97	-
XCONV	15/01/04	15/01/04	15/01/04	15/01/04	14/01/04
XFIT	06/12/99	17/08/99	17/08/99	17/08/99	-
XFIX	06/12/99	17/08/99	17/08/99	17/08/99	14/01/04
CONV	25/05/99	25/05/99	25/05/99	25/05/99	05/02/03
FTOREC	10/07/99	10/07/99	10/07/99	10/07/99	14/01/04
LSQINT	09/01/03	08/01/03	08/01/03	09/01/03	05/02/03
CORFUNC	25/05/99	22/04/99	-	22/08/99	01/07/03
SAMPLE	22/04/99	22/04/99	15/07/99	22/04/99	04/06/03
FDSCALE	22/04/99	22/04/99	22/04/99	22/04/99	04/06/03
FD2BSL	22/04/99	22/04/99	19/02/02	19/02/02	04/06/03
ICE	-	-	-	-	14/01/04
ImageViewer	-	-	-	-	14/01/04
Online Help	-	-	-	-	14/01/04

## ***Fibre Diffraction Review: Instructions to Authors***

Submitted original papers, technical reports, Reviews, comments/letters and meeting reports for inclusion in *Fibre Diffraction Review* are welcome.

### Technical Reports:

These include presentations of the latest developments in CCP13 and other fibre diffraction/non-crystalline diffraction software and their scientific justification and also, for example, reports on developments at synchrotron beamlines used for fibre diffraction and non-crystalline diffraction studies.

### Reviews:

These include summary presentations of the 'state of the art' in the structural analysis of particular fibrous or non-crystalline systems.

### Original Papers:

These present previously unpublished results from fibre diffraction or small-angle scattering experiments using either X-ray, neutron or electron diffraction.

### Expanded Poster-Prize Abstracts:

At each of the CCP13/ NCD Annual Workshops cash prizes are presented to the best poster presentations. The judges are always senior scientists in the field and are often from overseas. Winners of the Poster Prizes are invited to expand their abstracts into short papers for inclusion in *Fibre Diffraction Review*.

### Refereeing:

All papers, of whatever category above, will be refereed by at least two people (from the CCP13 Committee or their nominated referees) and may be either (a) accepted as they stand, (b) returned for rapid revision, or (c) rejected. As well as their scientific content, papers will be judged on their clarity of presentation and the quality of their figures.

### Meeting Reports:

*Fibre Diffraction Review* includes reports on relevant meetings and conferences which include an element of fibre diffraction or small-angle scattering and which will be of general interest to our readers. Such reports will often be solicited by the Editor from known meeting participants. Other potential contributors to this part of the Journal should contact the Editor prior to writing their report.

### Comments/Letters:

Feedback from readers about CCP13, about the NCD community and about the Journal itself are welcome. These could be in the form of comments or letters to the Editor. Suitable contributions will be published in the Journal.

### Advertisements:

Industrial/commercial adverts of interest to our readers are welcome. Potential advertisers should contact the Editor for details of current rates.

### Submission:

Contributions should be sent to the Editor before the annual deadline (December 31st) for each issue. Contributions submitted after this date may be held over for the following issue.

Colour illustrations are welcome and are included without charge. Contributions should be submitted both in hardcopy (ONE complete copy) and in electronic format to the Editor ([j.squire@ic.ac.uk](mailto:j.squire@ic.ac.uk)).

Text should be in Word 6 format and illustrations should be submitted as separate files at high resolution in TIFF or JPG format.

References should be in the format specified for *J. Molecular Biology*, and should be complete with title. Please find more details from our website.

### Reprints:

It is not economic for us to produce reprints of articles. However, in future, papers will be made available on the CCP13 website in downloadable pdf format.

Those wishing to purchase extra copies of the whole Journal should contact the Editor to find out costs.

### Editor's Address:

Professor John M. Squire,  
Head, Biological Structure and Function Section,  
Biomedical Sciences Division,  
Imperial College of Science, Technology  
& Medicine,  
London SW7 2AZ, UK.

Editor '*Fibre Diffraction Review*' (ISSN 1463-8401).

# The CCP13 Committee Members (As at April 2004)

## Chairman

Prof John Squire (to 2005)  
Biological Structure and Function Section  
Biomedical Sciences Division, Imperial College London, London SW7 2AZ, UK  
Editor "*Fibre Diffraction Review*".  
**Phone** 0207 594 3185 **Fax** 0207 594 3169 **Email** j.squire@imperial.ac.uk

## Vice Chairman

Dr Trevor Forsyth (to 2005)  
Institut Laue-Langevin, BP 156 F-38042, Grenoble Cedex 9, France, and Physics Dept, Keele University, Staffordshire ST5 5BG, UK  
**Phone** +33 4 (0) 76207158 **Fax** +33 4 (0) 76483906 **Email** tforsyth@ill.fr

## Secretary

Dr. Patrick Fairclough (to 2005)  
Department of Chemistry, The University of Sheffield,  
Dainton Building, Brookhill, Sheffield, S3 7HF  
**Phone** 0114 222 9411 **Fax** 0114 273 8673 **Email** p.fairclough@sheffield.ac.uk

## Research Assistants

Dr Jane Crawshaw  
Polymer Group, Department of Materials Science and Metallurgy, University of Cambridge, Pembroke St., Cambridge CB2 3QZ  
**Phone** 01223 334335, **Email** jc10027@hermes.cam.ac.uk

Dr Andrew He  
Biological Structure and Function Section, Biomedical Sciences Division, Imperial College London, London SW7 2AZ,  
**Email** andrew.he@imperial.ac.uk

Ganeshalingam Rajkumar  
Biological Structure and Function Section, Biomedical Sciences Division, Imperial College London, London SW7 2AZ,  
**Email** g.rajkumar@imperial.ac.uk

Dr Matthew Rodman  
Daresbury Laboratory, Daresbury, Warrington WA4 4AD,  
**Phone** 01925 603626 , **Email** m.j.rodman@dl.ac.uk

## Members

Dr David Blundell (to 2005)  
Physics Department, Keele University, Keele, Staffordshire, ST5 5BG,  
**Phone** 01782 583330

Dr Mike Ferenczi (to 2004)  
Biological Structure and Function Section, Biomedical Sciences Division, Imperial College London, London SW7 2AZ,  
**Phone** 0207 594 3139, **Fax** 0207 594 3169, **Email** m.ferenczi@imperial.ac.uk

Dr Steve King (to 2004)  
Rutherford Appleton Laboratory, Chilton, Didcot, OX11 0QX,  
**Phone** 01235 446437, **Fax** 01235 445720, **Email** s.m.king@rl.ac.uk

Professor Tim Wess (to 2005)  
Biophysics Group, Dept of Optometry and Vision Sciences, Redwood Building, Cardiff University, Cardiff CF10 3NB.  
**Phone** 029 2087 0117 **Fax** 029 2087 4859 **Email** WessTJ@cardiff.ac.uk

Prof. Alan Windle FRS (to 2004)  
Department of Materials Science and Metallurgy, University of Cambridge, Pembroke Street, Cambridge CB2 3QZ.  
**Phone** 01223 334335 **Fax** 01223 335637, **Email** ahw1@cam.ac.uk

Prof. Struther Arnott FRS (to 2004)  
Biological Structure and Function Section, Biomedical Sciences Division, Imperial College London, London SW7 2AZ,  
**Phone** 0207 594 3185, **Fax** 0207 594 3018, **Email** s.arnott@imperial.ac.uk

## Members (Co-opted)

Dr Greg Diakun

Daresbury Laboratory, Daresbury, Warrington WA4 4AD,

**Phone** 01925 603343 **Email** g.diakun@dl.ac.uk

Dr Tom Irving

CSRRI, Dept BCPS, Illinois Institute of Technology, 3101 s. Dearborn, Chicago IL. 60616, USA.

**Phone** (312) 567-3489 **Fax** (312) 567-3494 **Email** irving@biocat1.iit.edu

Dr. K. H. Gardner

DuPont CR&D, P.O. Box 80228, Experimental Station, Wilmington, Delaware, DE 19880-0228, USA

**Phone** +1 302 695 2408 **Email** kenn.h.gardner@usa.dupont.com

Dr. Carlo Knupp

Biophysics Group, Dept of Optometry and Vision Sciences, Redwood Building, Cardiff University, Cardiff CF10 3NB.

**Phone** 029 2087 0118 **Fax** 029 2087 4859 **Email** KnuppC@cardiff.ac.uk

Dr Geoff Mant

Daresbury Laboratory, Daresbury, Warrington WA4 4AD

**Phone** 01925 603169 **Email** g.r.mant@dl.ac.uk

Prof. Rick Millane

Dept of Electrical and Computer Engineering, University of Canterbury, Christchurch, New Zealand.

**Email** rick@elec.canterbury.ac.nz

Dr Keiichi Namba

Matsushita Electric Industrial Co. Ltd., 3-4 Hikaridai, Seika 619-0237, Japan.

**Phone** 81-774-98-2543 **Fax** 81-774-98-2575 **Email** keiichi@crl.mei.co.jp

Dr. Christian Riekkel

ESRF, BP 220, F38043 Grenoble Cedex, France.

**Phone** (33) 4 76 88 20 51 **Fax** (33) 4 76 88 21 60 **Email** riekkel@esrf.fr

Prof. Gerald Stubbs

Dept of Molecular Biology, Vanderbilt University, 2200 West End Avenue, Nashville, TN 37235

**Phone** (615) 322-7311 **Email** stubbsgj@ctrvax.vanderbilt.edu

Dr N.J. Terrill

Diamond Light Source Ltd, Rutherford Appleton Laboratory, Chilton, Didcot, Oxfordshire OX11 0QX, UK

**Phone** +44 1235 778047 **Fax** +44 1235 778052 **Email** Nick.Terrill@diamond.ac.uk

## From the Editor

To complement the tremendous advances that are taking place in CCP13, *Fibre Diffraction Review*, our own Journal, is also we believe getting better and better. As usual, in this current volume, we have many excellent scientific reports both on hardware developments, on software developments and on their applications to a wide range of scientific problems. However, the style is gradually changing so that, in addition to everything now being available in PDF format on the CCP13 Website and having Digital Object Identifiers (DOIs) for use in search engines, all thanks to the efforts of Andrew He, every paper will now carry full publication details on its first page and running headers on subsequent pages carrying a brief title and the paper's authorship. In the interests of economy the general print size has been reduced this year from 12 point to 10 point, but we still retain the unusual and much appreciated facility of including images in full colour without charge. Also in this Volume, for the first time, we are including adverts from

companies that have a significant role in the Non-Crystalline Diffraction field. We welcome more. Remember that *Fibre Diffraction Review* is your Journal. We appreciate the many high quality papers that are submitted to us each year, but please also feel free to contribute short comments on meetings of interest which you have attended. As you would expect, all contributions are refereed and scrutinised for clarity of expression and the usefulness of the submitted figures. We will do everything that we can to maintain this high production standard, but in the end it is your contributions that make the Journal what it is. Remember - material for the 2005 Volume can be submitted to me at any time in 2004.

John Squire - Imperial College London - April 2004



# CCP13



## 13<sup>th</sup> Annual Fibre Diffraction and Non-Crystalline Diffraction Workshop 2<sup>nd</sup> - 4<sup>th</sup> June 2004 ILL/ESRF, Grenoble, France

- |                                   |                               |
|-----------------------------------|-------------------------------|
| W. Bras (ESRF, France)            | D. Kirschner (Boston, USA)    |
| J. Crawshaw (Cambridge, UK)       | J. Ma (Rice, USA)             |
| P. Callow (ILL/Keele)             | R. May (ILL, Grenoble)        |
| M. Ferenczi (Imperial, UK)        | G. Rajkumar (Imperial, UK)    |
| P. Fratzl (MPI Potsdam, Germany)  | C. Riekkel (ESRF, France)     |
| M. Haertlein (ILL, Grenoble)      | J. Squire (Imperial, UK)      |
| A. Hammersley (ESRF, France)      | G. Stubbs (Vanderbilt, USA)   |
| A. He (Imperial, UK)              | D. Svergun (EMBL, Hamburg)    |
| E. Heeley (Sheffield, UK)         | K. Wakabayashi (Osaka, Japan) |
| M. Irving (KCL, UK)               | N. Yagi (Spring8, Japan)      |
| T. Irving (BioCAT, Illinois, USA) | X. Zeng (Sheffield, UK)       |

Software development & demonstration  
Visits to/demonstration of ESRF & ILL instrumentation  
ILL-EMBL Deuteration Laboratory  
Poster Session

For further information and registration, see the web pages at  
<http://www.ccp13.ac.uk/> or contact [a.mutch@dl.ac.uk](mailto:a.mutch@dl.ac.uk)

Supported by CCP13, Daresbury Laboratory, Institut Laue  
Langevin, ESRF, Stable Isotopes, Bruker AXS



### Useful World Wide Web addresses (URL)

- |                          |   |
|--------------------------|---|
| Fibre Diffraction Review | <a href="http://www.fibrediffractionreview.org">http://www.fibrediffractionreview.org</a>   |
| CCP13                    | <a href="http://www.ccp13.ac.uk">http://www.ccp13.ac.uk</a>   |
|                          | <a href="http://www.ccp13.org">http://www.ccp13.org</a>   |
|                          | <a href="http://www.bio.aps.anl.gov/biocat/mirror/www.ccp13.ac.uk/">http://www.bio.aps.anl.gov/biocat/mirror/www.ccp13.ac.uk/</a> |
|                          | <a href="http://www.ill.fr/ccp13">http://www.ill.fr/ccp13</a>   |
| NCD                      | <a href="http://www.srs.dl.ac.uk/NCD">http://www.srs.dl.ac.uk/NCD</a>   |
| SRS                      | <a href="http://www.srs.ac.uk/SRS">http://www.srs.ac.uk/SRS</a>   |



## CCP13 14<sup>th</sup> Annual Fibre Diffraction and Non-Crystalline Diffraction Workshop July 2005 CARDIFF UNIVERSITY

